DOCTOR OF PHILOSOPHY

Controls on stratification in the Rhine ROFI system

Souza, Alejandro Jose Gerardo

Award date:
1994

Awarding institution:
Bangor University

Title: Controls on stratification in the Rhine ROFI system.

A thesis submitted in accordance with the requirements of the University of Wales for the degree of Doctor of Philosophy.

by Alejandro José Gerardo Souza.

University College of North Wales,

School of Ocean Sciences,

Menai Bridge,

Gwynedd LL59 5EY,

U.K.

September 1994.

ABSTRACT

The nature of the physical regime in the vicinity of the Rhine ROFI(**R**egion **O**f **F**reshwater **I**nfluence) has been determined in a series of collaborative observations. Extensive surveys with shipboard profiling and undulating CTD systems have been used to complement time series observations with an array of moorings instrumented with current meters, transmissometers and fluorimeters to determine the time evolution of flow and structure.

The observations reveal a highly variable system in which the influence of the freshwater input from the Rhine extends northeastwards from the source and out to 30km from the coast.

The mean water column stability is controlled by the combined effect of tidal, wind and wave stirring which brought about complete vertical homogeneity. During periods of low stirring the water column is observed to re-stratify over the whole inshore region through the relaxation of the horizontal gradients under gravity and with the influence of rotation as in the model of Ou(1983).

Strong semi-diurnal oscillations are superimposed on the mean stratification, occurring throughout the stratified region at times of reduced mixing. The amplitude of this semi-diurnal variation is of the same order as the mean stability and frequently results in conditions being mixed or nearly mixed once per tide. It is inferred that this semidiurnal variation results primarily from cross-shore tidal straining which interacts with the density gradient to induce stratification. This conceptual picture of the contributing processes is tested in a 1-d point model forced by the observed slopes and the local density gradients. The model exhibits the same qualitative behaviour as the observations, produces oscillations in stratification of the amplitude observed and confirms the critical role of cross-shore tidal straining. The large cross-shore shear under stratified conditions is identified with the change in ellipse configuration which is observed to occur between mixed and stratified conditions. The occurrence of semi-diurnal variations in stability in the Rhine ROFI is thus inferred to be a consequence of the development of mean stability whenever the horizontal density gradients relax in conditions of low stirring.

The flow in the Rhine ROFI is dominated by tides with the M_2 semi-major axis of the order of 0.8 ms^{-1}. The wind-driven flow has a transfer factor between ~1 and 3 % and the rotation varies with depth closely to Ekman theory. Stratification intensifies the wind response at the surface while the explained variance is reduced near the pycnocline. The density driven flow within this region is generally parallel to the coast (northeastwards) and with surface speeds, determined by the HF radar, of about 10 cms^{-1}, while the vertical distribution closely follows the Heaps (1972) profile.

ACKNOWLEDGEMENTS

I want to express my appreciation to my supervisor, Professor John H. Simpson, for initially suggesting this project and his continuous advice, critical comments and encouragement throughout all my work. But above all I will like to thank him for the discussion sessions, that, although there were heated at times, I think they were the times when I learnt more from him.

During my research work I was assisted by many people. I express my thanks to the officers and crew of the R.R.S Challenger during cruises CH72B and CH96, with special acknowledgments due to Kate for making my life easier by setting up the cruise files in a very "user friendly" manner. I will also like show my appreciation to Dave Boon from the School of Ocean Sciences and Phill Taylor from R.V.S. for the design and deployment of the moorings. A key player on the CH96 cruise was the SEAROVER and this was only possible thanks to the kind work of Nigel Mathers from SOS.

I will also like to thank to everybody in the Ph.D. (coffee) room for all their moral support and for making life much easier during my stay in Menai Bridge. Special thanks are due to Dr. T.P. Rippeth who very kindly in calibrated the CH72 mooring data and taught me how to do it for the CH96 data, to Dr. Jonathan Sharples for letting me have a copy of his point model and to A. Campbell for reading a final version of this work. I am much obliged to Dr. Reginaldo Durazo for his unconditional friendship, his invaluable help with UNIRAS and the brilliant discussion sessions, from which I always learnt something, Gracias Compadre.

I also thank the PROFILE group, in particular Pim Bos and Dr. Andy Visser for their interesting comments and their kind attentions during my stay in Holland. I am thankful to Dr. Ian James for providing the 2-d version of his model.

This work was supported by the EEC through the MAST program under the MAST_0050C contract while the studentship was provided by CONACyT, Mexico

It will be spoken when I have gone.
I shall leave my song-image on earth ...
My heart shall live, it will come back,
My memory will live and my fame ...
My song is heard and flourishes.
My implanted word is sprouting,
our flowers stand up in the rain.
The Cocoa flower gently opens his aroma,
the gentle Peyote falls like rain.
My song is heard and flourishes.
My implanted word is sprouting,
our flowers stand up in the rain. *(Nahuatl poem, from Cantares Mexicanos)*

As white and yellow maize I am born,
The many-coloured flower of living flesh rises up
and opens its glistening seeds before the face of our mother.
In the moisture of Tlalocan, the quetzal water-plants open their corollas.
I am the work of the only god, his creation.

Your heart lives in painted page,
you sing the royal fibres of the book,
you make the princes dance,
there you command by the water's discourse.

He created you,
he uttered you like a flower,
he painted you like a song:
a Toltec artist.
The book has come to an end
your hart is complete. *(Nahuatl poem, from Cantares Mexicanos).*

A mi Padres,

Noel y Amada

Gracias por todo ya que sin ustedes esto no hubiera sido posible.

Table of contents

List of figures v

Chapter one. Introduction. 1

1.1 Rationale and motivation for shelf sea studies. 1

1.2 Introduction to the ROFI regime. 3

1.3 The Rhine ROFI system. 6

1.4 Aims of the thesis. 9

Chapter two. Theoretical background. 12

2.1 Theory of the heating-stirring problem. 12

2.2 Freshwater buoyancy input. 15

2.3 Density current dynamics. 20

2.4 Tidal dynamics. 23

Chapter three. Observational techniques. 25

3.1 Experiment strategy. 25

3.1.1 The 1990 Experiment. 25

3.1.2 The 1992 Experiment. 27

3.2 Instrumentation. 28

3.2.1 Profiling CTD. 28

3.2.2 Undulating CTD SEAROVER. 29

3.2.3 HF radar CODAR. 30

3.2.4 Current meter temperature and salinity calibration. 31

3.2.5 Acoustic Doppler Current meter Profiler (ADCP). 35

3.2.5.1 Theory of operation. 37

Chapter four. data analysis. 39

4.1 Current analysis 39

4.1.1 Harmonic analysis 39

4.1.1.1 Moving average harmonic analysis. 42

4.1.2 Residual currents. 43

4.2 Empirical Orthogonal Functions (EOF). 44

4.2.1 The analysis 44

Chapter five. Density field and stratification in the Rhine ROFI. 47

5.1 Introduction. 47

5.2 September-October 1990 experiment. 48

5.2.1 Time series of water column characteristics. 48

5.2.2 Spatial distribution of water column structure. 50

5.3 September 1992 experiment. 52

5.3.1 Time series of water column structure. 52

5.3.2 Spatial distribution of water column structure. 54

5.4 Interpretation and discussion. 55

Chapter six. Tidal flow. 57

6.1 Introduction. 57

6.2 Spatial mapping of ellipse properties. 57

6.3 Vertical structure of the tidal currents 58

6.4 The effect of stratification on the tidal current profiles. 60

6.5 Interpretation. 64

6.6 Summary. 65

Chapter seven. Wind-driven flow. 67

7.1 Introduction. 67

7.2 Surface currents. 67

7.3 Vertical structure. 68

7.4 Discussion. 68

Chapter eight. Density-driven flow. 71

8.1 Introduction. 71

8.2 Horizontal distribution of the residual currents. 72

8.3 Vertical structure of the residual currents. 73

8.4 Summary 75

Chapter nine. Synthesis. 77

9.1 Introduction. 77

9.2 Space-time evolution of stratification. 77

9.3 Interaction between mean water column stability and tidal shear in the production of semi-diurnal switching of stratification in the Rhine ROFI. 79

9.4 Conceptual model. 81

Chapter ten, Modelling of processes in the Rhine ROFI. 84

10.1 Introduction. 84

10.2 The numerical model. 84

10.2.1 The equations of motion. 84

10.2.2 The Forcing. 87

10.3 Results. 87

10.3.1 1990 simulation. 87

10.3.2 1992 simulation. 87

10.4 Discussion. 90

Chapter 11. Discussion. 92

11.1 Introduction. 92

11.2 Summary of principal findings. 92

11.3 Discussion. 94

11.3.1 Current. 94

11.3.2 Effect of stratification on the tidal ellipses 95

11.3.3 Controls on stratification on the Rhine ROFI system 97

11.3.4 Contrast with other ROFIs 98

11.4 Generalization of processes in a 2-dimensional model 99

11.5 Future work 100

References. 102

List of figures.

Figure 1.1 Schematic in the cross-shore direction showing ROFI and other shelf regimes.

Figure 1.2 The Liverpool Bay ROFI (from Sharples and Simpson, 1993).

Figure 1.3 The Rhine discharge in m^3s^{-1} as measured in Lobith between 1985 and 1987.

Figure 1.4 Large scale salinity distribution from North Sea project data between the 27 April and the 9 May 1989.

Figure 1.5 Co-tidal maps of the southern North Sea, generated using the output of the Proudman Oceanographic Laboratory tidal prediction model (Proctor, personal communication). a and b are the co-range and co-phase maps for M_2 and c and d for S_2 respectively.

Figure 1.6 M_2 tidal ellipses from the southern North Sea generated using the output of the vertically integrated tidal prediction model from the Proudman Oceanographic Laboratory (Proctor, personal communication).

Figure 1.7 SPOT image of the Rhine outflow for the 17 January 1991 at 11:20 hrs. Note that Rhine water (green) appears to be turning southwards, due to the fact that the satellite image was taken at low water. The image is a composite using the green, red and near infra-red channels.

Figure 1.8 Surface currents and salinity in the Rhine ROFI as simulated by the Ruddick *et al.* (1994) three-dimensional model; a at high tide and b at low tide.

Figure 1.9 Along-shore transects at the rising turn of the tide; a) velocity and salinity from the Ruddick *et al.* (1994) model and b) salinity from CTD measurements from van Alphen *et al.* (1988).

Figure 1.10 Distribution of the mean and standard deviation of salinity over 8 cruises between 1985 and 1987; a) Ter Heijde, b) Noordwijk, c) Egmond and d) Callantsoog.

Figure 1.11 Average salinity over 8 cruises; a) at 1m and b) at 10m depth. Every tick-mark represents 10 km in distance (from de Ruijter *et al.*, 1992).

Figure 1.12 Horizontal distribution of mean salinity stratification, defined as the difference between average salinities at 1m and 10m deep. Every tick-mark represent 10 km (from de Ruijter *et al.*, 1992).

Figure 1.13 Calculated mean residual flows in the southern North Sea, from a vertically integrated numerical model (Voogt, 1984).

Figure 1.14 Mean currents in a transect in front of Noordwijk. The average was taken

for the period between August 1985 and September 1986 (from de Ruijter *et al.*,1992).

Figure 2.1 Schematic of the competition between seasonal heating and tidal stirring (from Simpson and James, 1986).

Figure 2.2 Schematic of the competition of the stratifying forces of the density driven current; tidal straining of the density field due to shear in the tidal current and the stirring forces of winds and tides (from Simpson *et al.*, 1991).

Figure 2.3 Comparison of stratification in Liverpool Bay with the simulation of a turbulence closure level 2 point model (Simpson and Sharples, 1992). a) depth mean tidal current in ms^{-1}, b) observed stratification, c) modelled stratification, both calculated as the bottom-surface density difference in kgm^{-3}, c) observed variation of density gradients in m^{-1}.

Figure 2.4 Heaps (1972) velocity profile for typical values of the Rhine ROFI: $N_z=0.01m^2s^{-1}$ and $1/\rho(\partial\rho/\partial x)=2 \times 10^{-7}$ m^{-1}.

Figure 3.1 Rhine ROFI study area for the 1990 campaign. (·) represent CTD stations, (♦) and (◊) represent UCNW and RWS moorings respectively. (★) are the ground CODAR stations and the square shows the HF radar coverage.

Figure 3.2 RWS moorings schematic, where (■) are pressure gauges, (□) are Hydrolab water quality sensors and (⊕) are current meters.

Figure 3.3 Schematic of the UCNW U-mooring used in 1990.

Figure 3.4 Rhine ROFI study area for 1992. Bathymetry in metres with mooring positions (■) and Searover tracks for the study period.

Figure 3.5 Schematic of the UCNW U-mooring used in 1992.

Figure 3.6 Schematic of how the HF radar generates the velocity field (from Prandle, 1990).

Figure 4.1 Characteristics of the 19 hour Doodson filter. Reproduced from Pugh (1987, page 418).

Figure 5.1 Salinity time series from mooring A during the 1990 campaign; a) surface, b) bottom.

Figure 5.2 Temperature time series from mooring A during the 1990 campaign; a) surface, b) bottom.

Figure 5.3 Time series of bottom - surface characteristics for mooring A during the 1990 campaign. a) temperature, b) salinity and c) density.

Figure 5.4 Mooring A time series: A) east-west tidal currents 4 m above the bed; b) windstress from the Hook of Holland; c) salinity difference between 1 and 16 m below the surface; d) transmittance black line 1m deep dotted line 16 m deep.

Figure 5.5 Sea surface temperature distribution for post-springs (a) and post-neaps (b).

Figure 5.6 Surface salinity distribution for post-springs (a) and post-neaps (b).

Figure 5.7 Surface Nitrate concentrations for the entire observation period.

Figure 5.8 Temperature sections on the N (Noordwijk) transect. a) post-springs; b) post-neaps.

Figure 5.9 Salinity sections on the N (Noordwijk) transect. a) post-springs; b) post-neaps.

Figure 5.10 Density sections on the N (Noordwijk) transect. a) post-springs; b) post-neaps.

Figure 5.11 Distribution of potential energy anomaly ϕ in Jm^{-3}; a) post-springs; b) post-neaps.

Figure 5.12 Surface total seston in mgl^{-1}. a) post-springs; b) post-neaps.

Figure 5.13 Salinity time series for 1992. a) Mooring A; b) Mooring B; c) Mooring D; d) Mooring D. i) Surface (1 m), ii) Bottom (16m).

Figure 5.14 Temperature time series for 1992. a) Mooring A; b) Mooring B; c) Mooring D; d) Mooring D. i) Surface (1 m), ii) Bottom (16m).

Figure 5.15 Time series of bottom - surface difference for the 1992 campaign. a) mooring A; b) Mooring B; c) Mooring D; d) Mooring D. i) temperature; ii) salinity; ii) density.

Figure 5.16 Time series of stirring power and stratification. a) tidal stirring power: instantaneous value (dashed) and daily mean (continuous) computed from current meter velocity at mooring A (4 m above the bed); b) wind stirring power calculated using data from Noordwijk tower; c) stratification $\Delta\rho$, density difference between 1m and 16 m deep, continuous mooring A dashed mooring D.

Figure 5.17 Sea surface temperature distribution in the Rhine ROFI for the 1992 campaign. a) 8 to 10 September (jdays 252-254); b) 11 September (jday 255); c) 12 September (jday 256); d) 15 September (jday 259).

Figure 5.18 Surface salinity distribution in the Rhine ROFI for the 1992 campaign. a) 8 to 10 September (jdays 252-254); b) 11 September (jday 255); c) 12 September (jday 256); d) 15 September (jday 259).

Figure 5.19 Surface density distribution in the Rhine ROFI for the 1992 campaign. a) 8 to 10 September (jdays 252-254); b) 11 September (jday 255); c) 12 September (jday 256); d) 15 September (jday 259).

Figure 5.20 Potential energy anomaly (ϕ) distribution in the Rhine ROFI for the 1992 campaign. a) 8 to 10 September (jdays 252-254); b) 11 September (jday 255); c) 12 September (jday 256); d) 15 September (jday 259).

Figure 5.21 Density sections on jday 261 (17 September 1992). a) between 00:34 and 02:26 hrs; b) at low water, between 02:26 and 03:58 hrs; c) between 04:28 and 06:06; d) at high water between 06:36 and 08:02.

Figure 6.1 Surface distribution of tidal ellipses from CODAR observations, between 7 and 18 October 1990 (Julian days 280 to 291). a)M_2, b) S_2.

Figure 6.2 M_2 tidal ellipse profiles, from bottom-mounted ADCPs at mooring A (continuous) and mooring B (dashed), from 2 to 17 September 1992 (Julian days 248 to 261). a) semi-major axis, b) ellipticity, c) phase and d) orientation.

Figure 6.3 S_2 tidal ellipses profiles, from bottom-mounted ADCPs at mooring A (continuous) and mooring B (dashed), from 2 to 17 September 1992 (Julian days 248 to 261). a) semi-major axis, b) ellipticity, c) phase and d) orientation.

Figure 6.4 Tidal ellipses distribution along line N from ship-mounted ADCP on Julian day 261. a) semi-major axis; b) ellipticity; c) orientation; d) phase.

Figure 6.5 Spatial distribution of the surface semi-diurnal tidal ellipses during mixed (a) and stratified (b) conditions, as mapped by the HF radar CODAR.

Figure 6.6 Vertical structure of tidal ellipses at a location 19 km from the coast on the Scheveningen transect during the 1990 campaign. Surface currents are from CODAR and subsurface from current meters at mooring B. Note the change between mix and stratified conditions on day 285.

Figure 6.7 Cross-shore evolution of the tidal ellipses from CODAR data at 5 20 and 30 km off-shore, from CODAR observations.

Figure 6.8 Time series of ellipse characteristics and water column stratification at mooring A (20 m deep). (a) The density difference between bottom and top current meters; the continuous line represent the mean stratification averaged over two tidal periods while the dashed line is the instantaneous value. (b) Ellipticity (ε) from bottom mounted ADCP data. (c) Semi-major axis of the ellipse in ms^{-1}. (d) Orientation of the ellipse major axis in degrees (positive anti-clockwise from the east).

Figure 6.9 Time series of ellipse characteristics and water column stratification at mooring b (20 deep). (a) The density difference between bottom and top current meters. (b) Ellipticity ε from bottom mounted ADCP data. (c) Semi-major axis of the ellipse in ms^{-1}. (d) Orientation of the ellipse major axis in degrees (positive anti-clockwise from the east).

Figure 6.10 Schematic of the vertical profile of the clockwise and anti-clockwise rotary components and ellipse configuration. a) for the homogeneous case when N_z is constant. b) for the stratified case when N_z is reduced at the pycnocline.

Figure 7.1 Wind analysis for surface currents mapped by CODAR, from 7 to 23 October 1990. a) Transfer factor; b) rotation.

Figure 7.2 Percentage of variance, of the non-tidal currents, explained from the wind analysis.

Figure 7.3 Vertical profile of the wind transfer function from moorings A (continuous) and B (dashed) bottom-mounted ADCPs, from 2 to 17 September 1992. a) transfer factor; b)rotation.

Figure 7.4 Vertical distribution of the explained variance from the wind analysis of non-tidal currents at moorings A (continuous) and B (dashed), from 2 to 17 September 1992.

Figure 7.5 Time series 3 km from the coast from 3 to 18 October 1990. a) wind vector at Noordwijk, 10 m above the ground; b) Salinity difference between 5 and 9 m deep; c) Current residuals at 4 and 12 m deep. Both wind and currents have been rotated clockwise through 39.5°, so that the vectors lie parallel and perpendicular to the coast, as indicated in panel c.

Figure 8.1 Surface velocity vectors mapped by IFM CODAR from 7 to 23 October 1990. a) total long term residual; b) after removing the wind driven flow.

Figure 8.2 Surface velocity components after removing the wind driven component, between 7 to 23 October 1990. a) off-shore; b) along-shore.

Figure 8.3 Vertical distribution of velocity as observed by the POL bottom-mounted ADCP at mooring A, between 2 and 17 September 1992; a) cross-shore component; b) the along-shore component. Continuous line is the Heaps profile; octagons are the observed total long term residual; triangles are the observed long term residuals after removing the wind component.

Figure 8.4 Vertical distribution of velocity as observed by the POL bottom-mounted ADCP at mooring B, between 2 and 17 September 1992; a) cross-shore component; b) along-shore component. Continuous line is the Heaps profile; octagons are the observed total long term residual; triangles are the observed long term residuals after removing the wind component.

Figure 8.5 Vertical distribution of velocity as observed by the POL bottom-mounted ADCP at mooring B, between 2 and 17 September 1992; a) cross-shore component; b) along-shore component. Continuous line is the Heaps profile; octagons are the difference between observations at mooring A and at mooring B after removing the wind component; triangles are the observed long term residuals after removing the wind component.

Figure 8.6 Geostrophic velocity calculated using the density structure from the 25 hours SEAROVER survey at line N on days 260 and 261 1992, referenced to the bottom. a) mean geostrophic velocity; b) mean density structure.

Figure 8.7 Velocities from the ship-mounted ADCP at line N between days 260 and 261 1992. a) cross-shore component; b) along-shore component.

Figure 9.1 Time series of stratification expressed as the density difference between 1 m and 12 m deep. The continuous line correspond to data from mooring A and the dots correspond to data from the SEAROVER inside the stratified area (15 km from the coast).

Figure 9.2 EOF mode 1, with 75.3 % of the variance explained, from the cross-shore density stratification as observed by the SEAROVER. a) Temporal function; b) eigenvector.

Figure 9.3 Tidal straining and periodic stratification:
(a) time series of stratification (continuous line) and tidal displacement (dashed line); the displacement is calculated using 6 tidal constituents (M2, S2, N2, O1, K1, M4) from the top bin (3m deep) relative to the bottom bin (17m deep) from a 1.2 MHz ADCP at mooring A; positive displacement is off-shore;
(b) as (a) but the displacement is calculated from the high-pass-filtered velocities.
(c) estimates of the combined wind and stirring power for the same period.

Figure 9.4 The relation between straining and the propagation of the tidal wave from measurements at mooring A:
(a) tidal elevation
(b) alongshore velocity v
(c) relative displacement between 4m and 16m.
(d) density difference

Figure 9.5 Process summary schematic showing the changes in ellipse format at surface and bottom due to the onset of stratification and the resulting semi-diurnal oscillations in stability driven by tidal straining. The symbolic windstress is shown in an arbitrary direction.

Figure 10.1 Time series of stratification for the 1990 campaign. a) observed; b) simulated.

Figure 10.2 Density evolution over 1 tidal cycle. a) observed; b) modelled.

Figure 10.3 Tidal ellipses time series from model simulations for the 1990 data.

Figure 10.4 Stratification and displacement from the 1-dimensional turbulence closure model, for the 1992 observations:
Density stratification from the model (a) and observations (b)
Relative displacement from the model (c) and observation (d)

Figure 10.5 Stratification and tidal ellipses from the 1-dimensional turbulence closure model, for 1992 observations. i) observations and ii) model results.
a) stratification; b) semi-major axis; c) ellipticity; d) phase and e) orientation.

Figure 11.1 Relationship between bottom-surface ellipticity difference ($\Delta\varepsilon$) and bulk Richardson number Ri_0 for September 1992 data (▾) and October (Jdays 280 to 290) 1990 data (·).

Figure 11.2 Salinity distribution from the slice model at different times in a tidal cycle. (a) 3 hours after high water, (b) at low water, (c) 3 hours after low water and (d) at high water. Simulation times are above each pane. Note that the tidal states are chosen to be comparable to those of the SEAROVER sections.

Figure 11.3 Same as figure 6 but for the current field. Contours show the along-shore component of velocity, while the vectors show the cross-shore and vertical components, all in ms^{-1}.

Figure 11.4 Relation between stratification (a), cross-shore wind (b); and waves (c).

CHAPTER ONE

INTRODUCTION

1.1. Rationale and motivation for shelf sea studies

In recent years there has been growing interest in shelf sea oceanography. This has been due to the realization that we need better management of our local marine environment, combined with the intellectual challenge of understanding the processes that control this environment. Such understanding is the key that will allow us to create models of the shelf system, which should become a basic tool for the management of these areas.

The rapid expansion of the exploitation of the coastal and shelf sea region for its natural resources, such as hydrocarbons, aggregates and fisheries, and the increased use of these areas as dumping grounds for industrial, agricultural and sewage wastes, has proceeded with little knowledge and consideration of the impact on the ecosystem. The shelf seas are highly productive regions, where the dumping of excess nutrients or pollutants can disrupt the environmental balance and result in both an environmental and economic disaster.

A number of potential problems have become apparent in the last few years which serve to highlight an earlier lack of consideration of the likely consequences of these actions and the need to fully investigate future exploitation in an attempt to prevent more serious damage to the shelf sea environment. One large scale example of such a problem is the increasing frequency of 'nuisance' blooms in the European Shelf seas, caused by input of agricultural and sewage nutrient material. This excess

nutrients burden results in eutrophication of the environment that leads to the rapid growth of phytoplankton, which may even cause hypoxia, affecting the local benthic ecology with toxic effects on fish and even on human population via the consumption of shellfish.

The above example highlights the necessity of creating water quality models and using them in an informed manner to manage the shelf sea ecosystem. A first step in this direction was the Natural Environment Research Council North Sea project, which, for the first time, made a systematic interdisciplinary study of the North Sea and has developed the scientific basis for a useful water quality model.

From the purely intellectual point of view, oceanography of shelf seas presents an interesting challenge due to the fact that it involves problems that do not occur in the deep ocean. Tides are small in deep waters, while they are amplified in the shelf seas due to change in the group velocity of the tidal wave, wave reflection and resonance. The water column in the deep ocean is permanently stratified in contrast with the shelf seas where only seasonal stratification is observed. The flow in deep waters is basically geostrophic in contrast with the tidally dominated flow of shallow waters which involve strong frictional effects. The understanding and modelling of shelf sea processes thus presents a very different challenge from the deep ocean and, combined with the advances in measurement techniques and in computer technology this has stimulated modern oceanographers in to trying to understand the dynamics of the shelf sea.

1.2 Introduction to the ROFI regime.

A particular focus in recent years has been in the study of the Regions Of Freshwater Influence (ROFIs). A ROFI is an area of the shelf seas where the dynamics are modified by the presence of freshwater from the discharge of one or more adjacent rivers, which generate strong horizontal density gradients (fig. 1.1). A coupled circulation is then present between the shelf seas and the adjacent estuaries, driven by the horizontal density gradients.

When the tidal flows are relatively weak, it allows the low salinity water leaving the estuaries to spread seawards as a thin surface layer in response to the buoyant force. Once the buoyant flow leaves the estuary, the effect of rotation becomes apparent deflecting the flow to the right (Northern hemisphere), generating plumes and coastal currents, as observed in laboratory experiments (Griffiths and Linden, 1981). These plumes and coastal currents are characterized by frontal regions. Several of them have been observed in nature, *e.g.* the Mississippi discharge (Wright and Coleman, 1971) and on a much smaller scale in the Norwegian fjords (McClimans, 1978). A well documented example of such frontal behaviour is the plume generated by the Connecticut River discharge into the Long Island Sound as first reported by Garvine and Monk (1974). In this case there is a shallow surface layer of the order of 2m thick and an offshore plume characterised by extreme salinity gradients with obvious colour changes and accumulation of surface material. Strong convergent velocities (20-50 cms^{-1}) are found at the surface on both sides of the front, with vigorous sinking motions at the front. This vertical plane motion induces a downward entrainment of fluid from the surface brackish layer, leading to vertical mixing and the eradication of the frontal structure over a period of several hours.

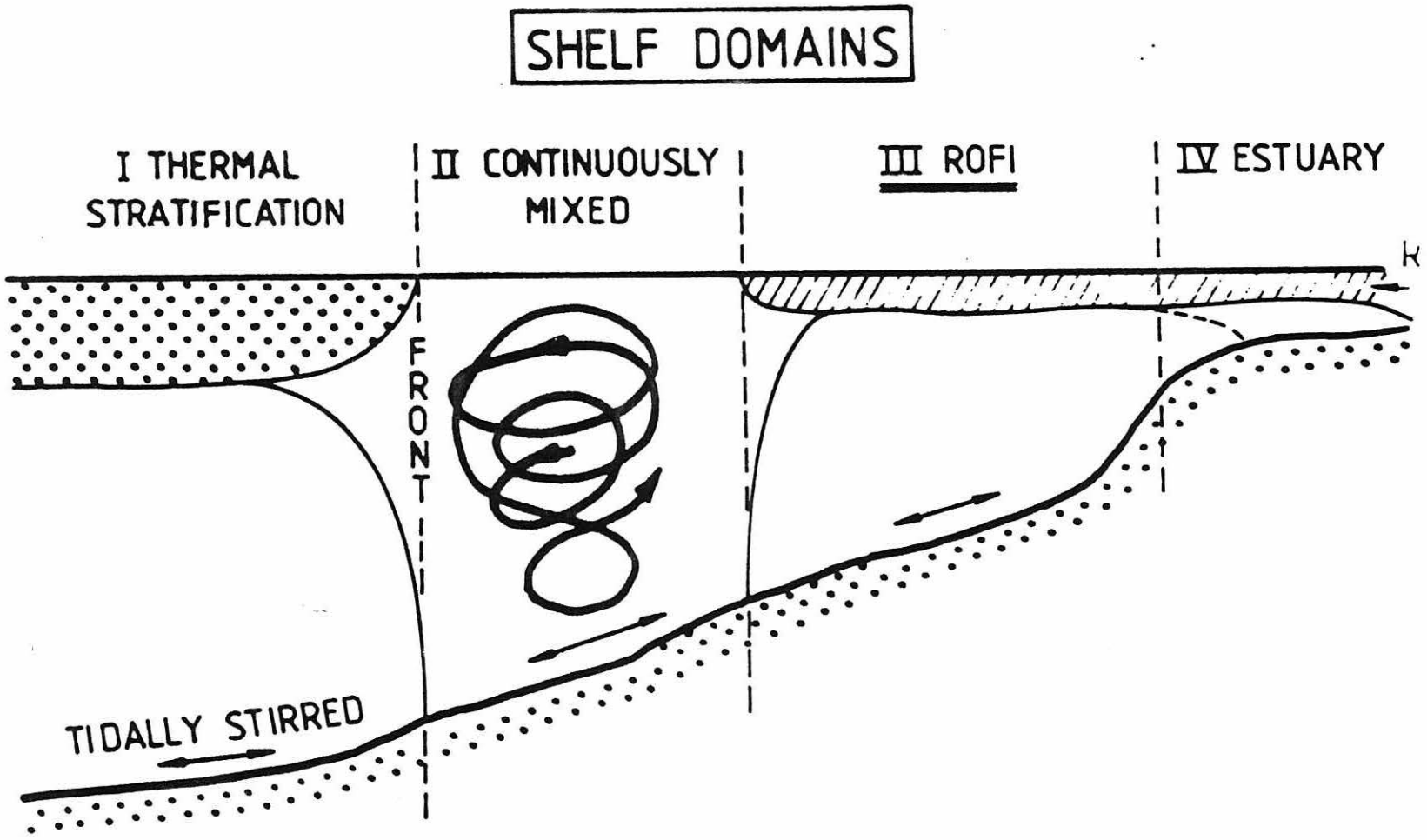

Figure 1.1 Schematic in the cross-shore direction showing ROFI and other shelf regimes.

The best documented example to date of a ROFI is that of Liverpool Bay. It is located in the eastern part of the Irish Sea, bounded to the east by coast of Northwest England and to the south by the coast of North Wales (fig 1.2). The horizontal density gradient is typically 2.0 - 7.0 $\times$ 10^{-5} kgm^{-4} and it is maintained throughout the region by the freshwater inflow from the rivers Dee, Mersey and Ribble in the south, and the Wyre and Lune further north in Morecambe Bay. The general trend of the isopycnals, as shown in figure 1.2, is oriented north-south, turning in the south to follow the North Wales coast. The tidal oscillation in Liverpool Bay is almost a standing wave, with flood currents moving eastward and slack waters occurring at about the same time as high water and low water (Sharples, 1992). Bowden and Sharaf El Din (1966) analyzed current and salinity data from a number of positions off the Mersey estuary, showing that the salinities at all depths tended to reach a maximum value at high water and a minimum at low water, consistent with tidal advection of a freshwater-induced horizontal density gradient. A recent study by Simpson *et al.* (1990) extended this study of the semi-diurnal variability of stratification and concluded that it is the result of the differential advection of the horizontal density gradients a process that they termed tidal straining. They also found an important semi-monthly component of stratification, due to the spring-neaps tidal cycle, which modulates the tidal energy.

Heaps (1972) studied the steady density driven circulation in the area, and found an analytical solution for a density driven circulation in the presence of frictional and inertial forces, which was successful in explaining the currents observed by drifters (Halliwell, 1973 and Ramster, 1971).

Tidal currents in the region have a major axis lying approximately east-west

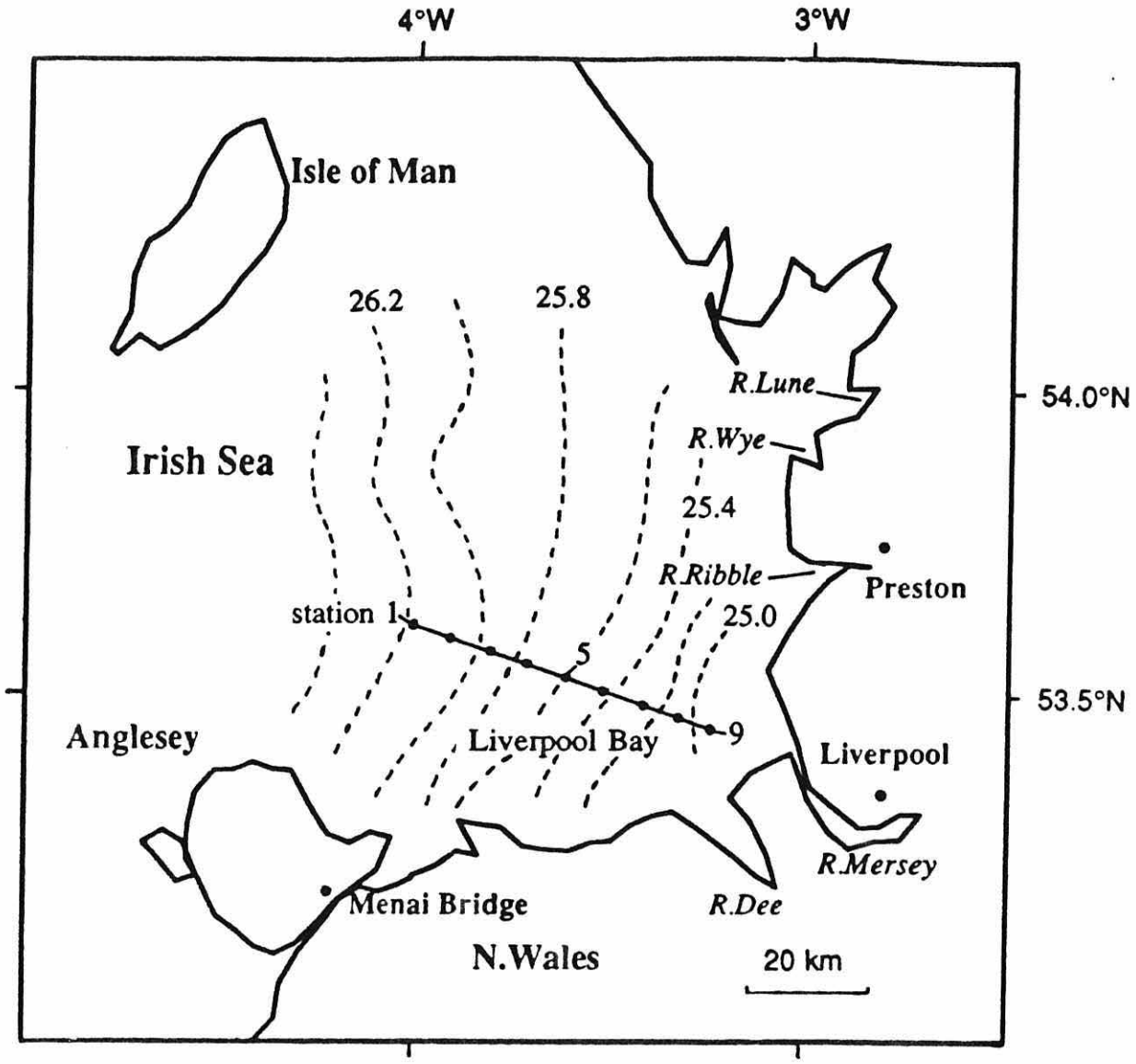

Figure 1.2 The Liverpool Bay ROFI (from Sharples and Simpson, 1993).

with an ellipticity of about 0.1. Typical depth-averages currents are of the order of 0.6 and 0.3 ms^{-1} for the M_2 and S_2 components respectively, with non-linear tidal residuals of the order of 3 cms^{-1} (Johns and Dyke, 1972).

An extreme case of a ROFI is that associated with the Amazon, whose outflow is so great as to permanently exclude salt water from its estuary. The brackish water produced by tidal mixing in shallow waters near the river mouth, spreads as a plume and is at the same time advected along the coast of the Guianas, forming an extensive complex system of fronts (Simpson and James, 1986). Another extreme example of a ROFI is that generated by the Changjiang River discharge in the East China Sea (Beardsley *et al.*, 1994), with an average outflow of 30000 m^3s^{-1}.

The largest ROFI in Europe, although much smaller than that of the Amazon, is that generated by the Rhine outflow. This high energy ROFI (table 1.1), which is the subject of the present study, results from an average outflow of 2200 m^3s^{-1} by the Rhine into the North Sea. The horizontal density gradients tend to drive an estuarine circulation limited by the earth's rotation, which results in a coastal current and an associated ROFI.

Table 1.1 ROFI classification.

ROFI	Run-off (m^3s^{-1})	Depth (m)	Tidal U (ms^{-1})	SH ($\log(h/U^3)$)	Energy
Liverpool Bay	~ 200	35	~0.8	1.83	Very High
Connecticut River Plume	~ 560	20	~1.0	1.03	Very High
Rhine outflow	~ 2200	20	~0.5	2.2	High
Changjiang River plume	~ 30000	50	,0.5	2.6	High
Delaware Coastal Current	~ 650	20	~0.2	3.4	Moderate
Clyde Sea	~ 200	150	,0.1	5.2	Low
Thermaikos Gulf	~ 200	30	~0.03	6.0	Very low

The problem of analyzing the interaction of freshwater buoyancy input with stirring processes in these ROFI regimes is generally a different and complex one. We shall approach it in the following chapter through the somewhat simplified analysis of the self sea thermal regime in which the buoyancy exchange is in the form of a heat flux at the surface. The important simplification here is that the surface fluxes may be assumed spatially uniform in contrast to the ROFI regime where we have to take account of the fact that the buoyancy is input at one or more sources at the lateral boundary.

1.3 The Rhine ROFI system.

The Dutch coastal zone has been subject of interest to the Dutch scientists for some time, because of the need for coastal zone management of an area subject to increasing environmental pressure. The approach to the giant port of Rotterdam experiences very heavy maritime traffic much of it involving cargoes which pose a potential threat to the environment either through a catastrophic release in a major accident or by long-term low-level leakage into the estuarine environment during unloading operations.

The Rhine itself, flowing as it does through some of the most densely populated and industrialised areas of Europe, brings a rich mixture of nutrients and pollutants including heavy metals and xenobiotics to the coastal zone. The high level of nutrients (notably nitrates and phosphates) carried by the Rhine outflow has been implicated in the generation of nuisance blooms.

The discharge of the Rhine river varies considerably. It ranges between 600 and

13000 m^3s^{-1} with a long-term average of 2200m^3s^{-1} (fig. 1.3). The river discharge exhibits a seasonal periodicity with low discharges during late summer and autumn, while high water discharge are typical of winter and spring (de Ruijter, 1992).

In terms of the physics of the coastal zone, the average inflow of 2200 m^3s^{-1} represents a major buoyancy source for the adjacent region of the North Sea . This buoyancy input, which has a magnitude of ~ 5.4 x 10^5 Ns^{-1}, is equivalent to peak summer heating over an area of ~10^4 km^2. It creates a ROFI system which extends along the Dutch coast and continues into the German Bight, where it combines with other large buoyancy inputs from the Weser and Elbe to maintain a substantial ROFI in the German Bight. The further continuation of this ROFI is evident along the Danish coast and into the Skaggerak where it gets incorporated in the Baltic outflow, as observed in synoptic salinity distributions like that of fig. 1.4.

The tides in the Dutch Coastal zone are dominated by the semi-diurnal components. At the Hook of Holland, the M2 amplitude is 0.77 m, while S2 has an amplitude of 0.19m. To a first approximation the tides propagate to the north along the Dutch coast as a Kelvin wave (fig. 1.5), with surface currents ranging between 0.7 and 1.0 ms^{-1}. Tidal Currents are mainly directed parallel to the coast (fig. 1.6), with flood currents north-eastward and ebb currents directed south-westward and tidal excursion between 8 and 12 km.

As the freshwater leaves the Rotterdam waterway it forms a strong plume bounded by a front; this front is visible as a sharp gradient in colour and turbidity (fig. 1.7), while a strong line of foam and debris suggests a strong convergence. This near source region is limited in scale by the inertial radius (r_i=u/f ~ 10 km) and is

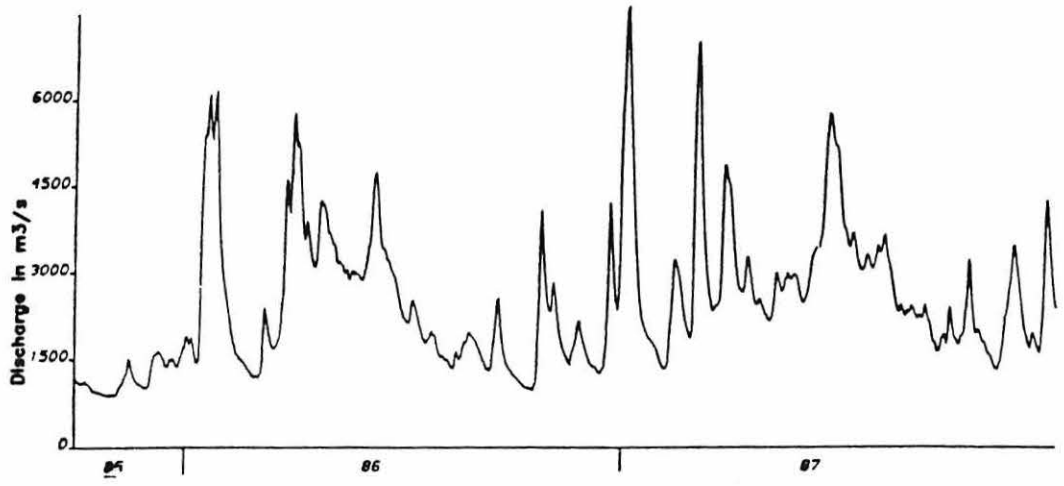

Figure 1.3 The Rhine discharge im m^3s^{-1} as measured in Lobith between 1985 and 1987.

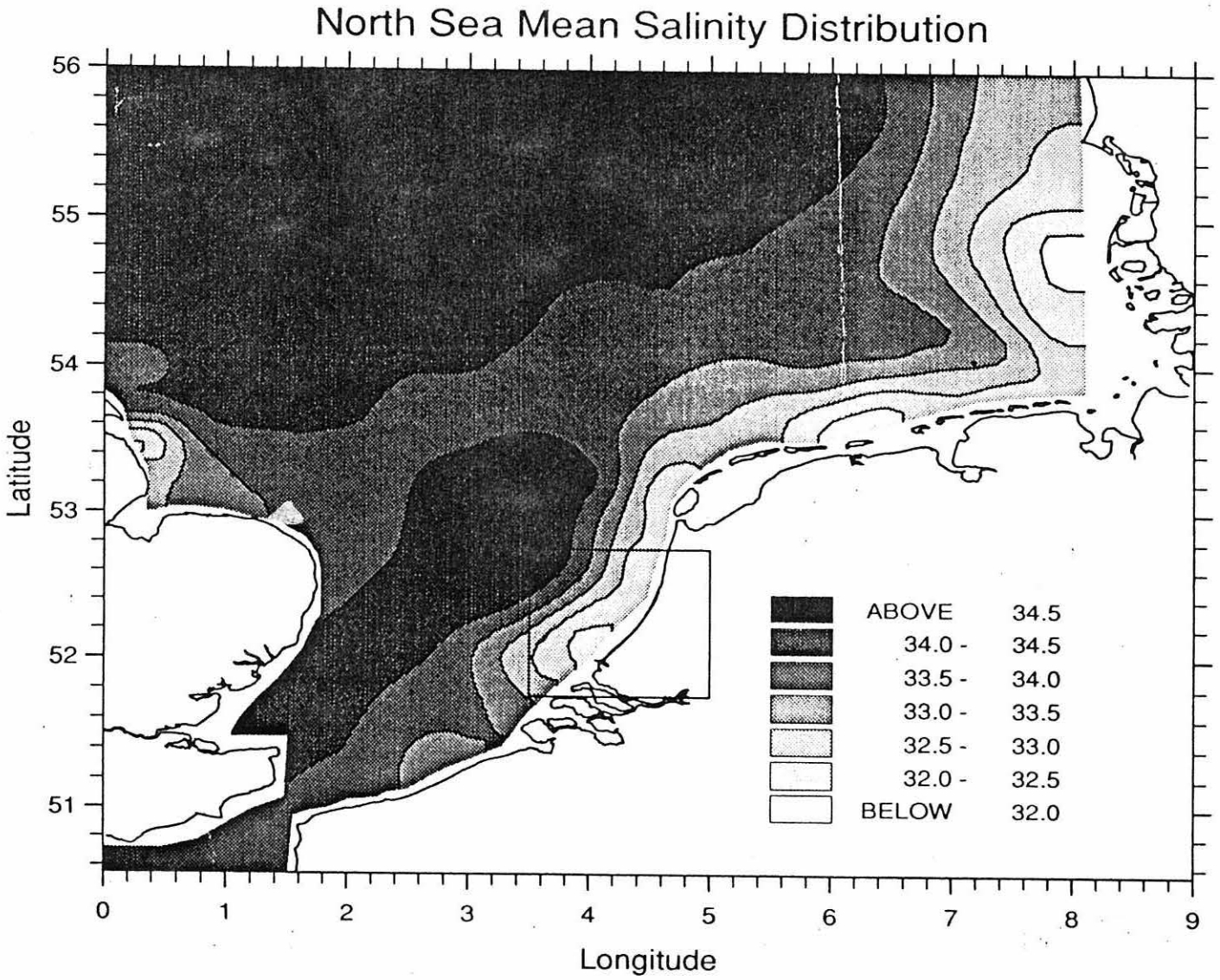

Figure 1.4 Large scale salinity distribution from North Sea project data between the 27 April and the 9 May 1989.

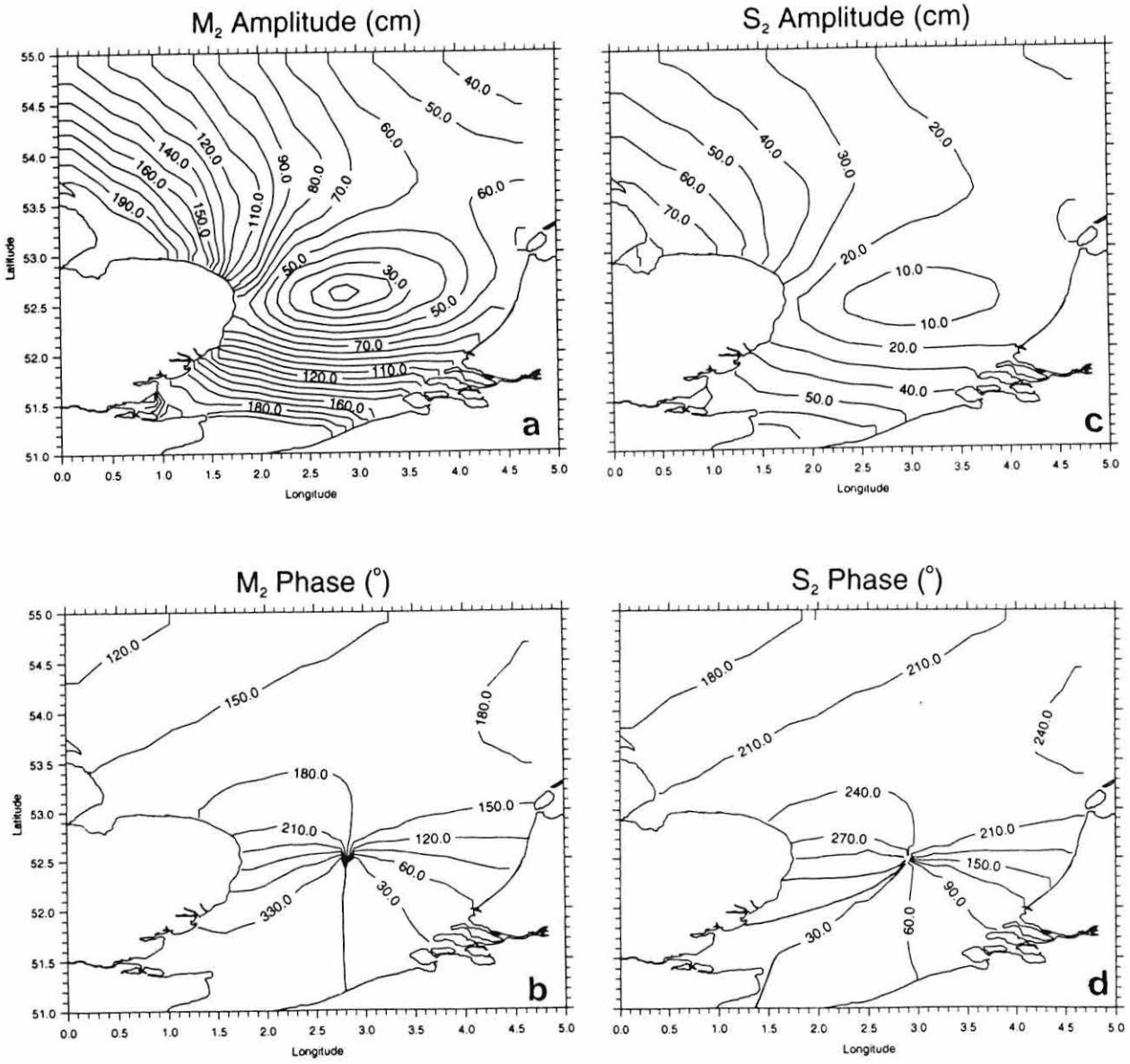

Figure 1.5 Co-tidal maps of the southern North Sea, generated using the output of the Proudmal Oceanographic Laboratory tidal prediction model (Proctor, personal comunication). a and b are the co-range and co-phase maps for M_2 and c and d for S_2 respectively.

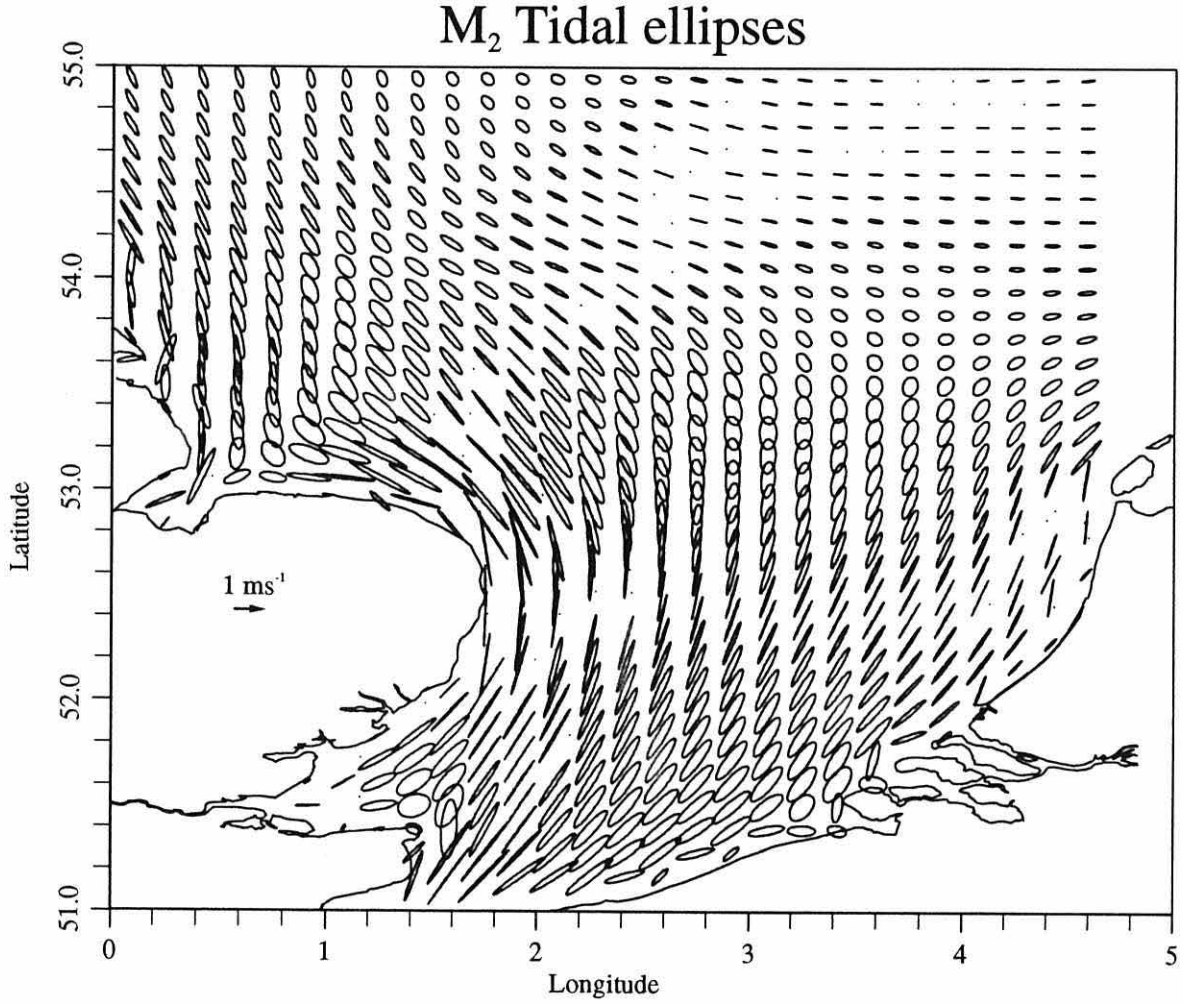

Figure 1.6 M_2 tidal ellipses from the southern North Sea generated using the output of the vertically integrated tidal prediction model from the Proudman Oceanographic Laboratory (Proctor, personal comunication).

Figure 1.7 SPOT image of the Rhine outflow for the 17 January 1991 at 11:20 hrs, note that Rhine water (green) appears to be turning southwards, this is due to the fact that the satellite image was taken at low water. The image is a composite using the green, red and near infra-red channels.

clearly influenced by the strong currents, as in the Connecticut River plume, advecting the plume backwards and forwards (fig 1.8). The interaction between the outflow and along-shore southward tidal currents creates a strong frontal convergence upstream (fig. 1.9), as suggested by SLAR observations and numerical simulations (Ruddik *et al.*, 1994).

The average salinity distribution of several sections, shows that as we move northwards from the source, the stratification and variability decrease (fig. 1.10) although it is important to note that the effect of freshwater stratification is still present in the Callantsoog transect 100 km from the river source. On this section, the frontal position is between 10 and 15 km from the coast (fig. 1.10). This outer front that limits the ROFI, will be referred from now on as the ROFI frontal region. The mean horizontal distribution of salinity, as observed from de Ruijter (1992), indicates that although stratification may decrease as we move along-shore from the source, the dominant horizontal density gradients are in the cross-shore direction (fig. 1.11), while the along-shore density gradients are by comparison negligible.

Figure 1.12 shows the mean stratification over 8 cruises, determined as the difference between the average salinity at 1 and 10 m deep. It indicates a buoyant plume extending from the river mouth in a relatively coastal area within 20 km from the coast, bounded by the ROFI frontal region.

The origin and nature of residual flows through the ROFI is notcompletely understood. According to van der Giessen *et al.* (1990) the main transport in the Rhine ROFI is associated with inflow through the English Channel. They suggest that about a quarter of the water entering the North Sea through the Dover Strait passes through

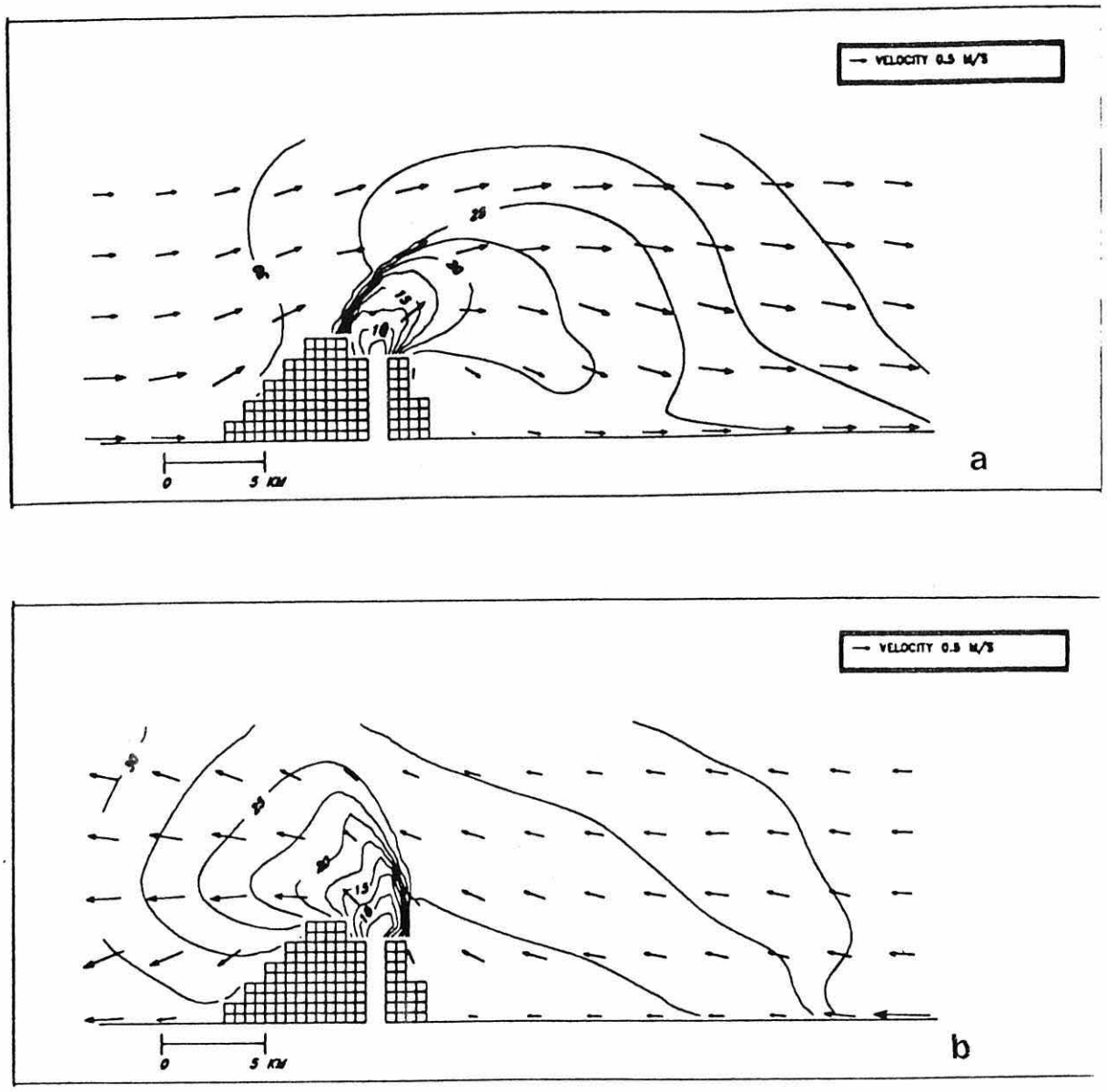

Figure 1.8 Surface currents and salinity in the Rhine ROFI as simulatted by Ruddick *et al.* (1994) three-dimensional model; a at high tide and b at low tide.

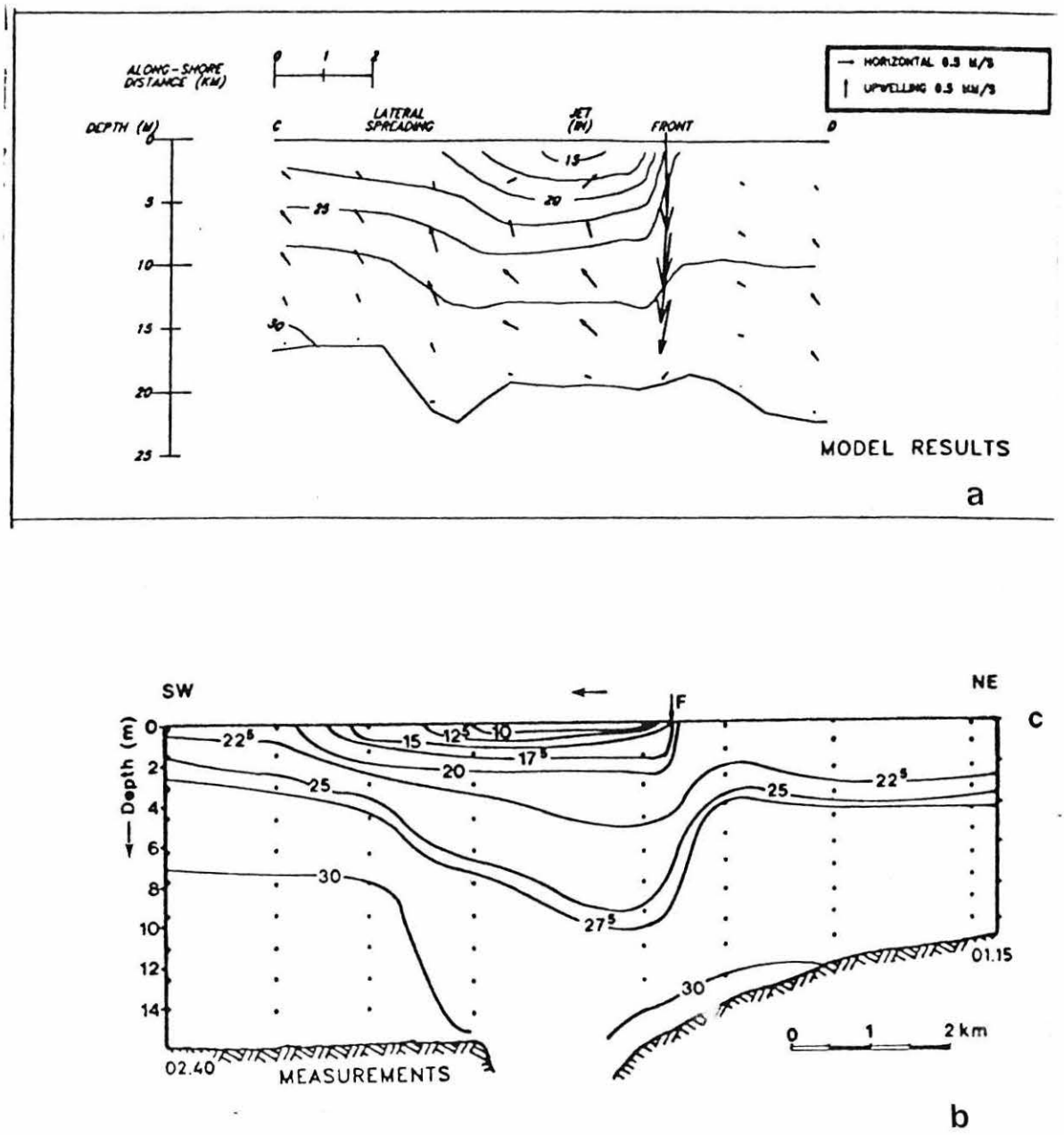

Figure 1.9 Along-shore transects at the rising turn of the tide; a) Shows the velocity and salinity from Ruddick *et al.* (1994) model and b) is the salinity from CTD measurements from van Alphen *et al.* (1988).

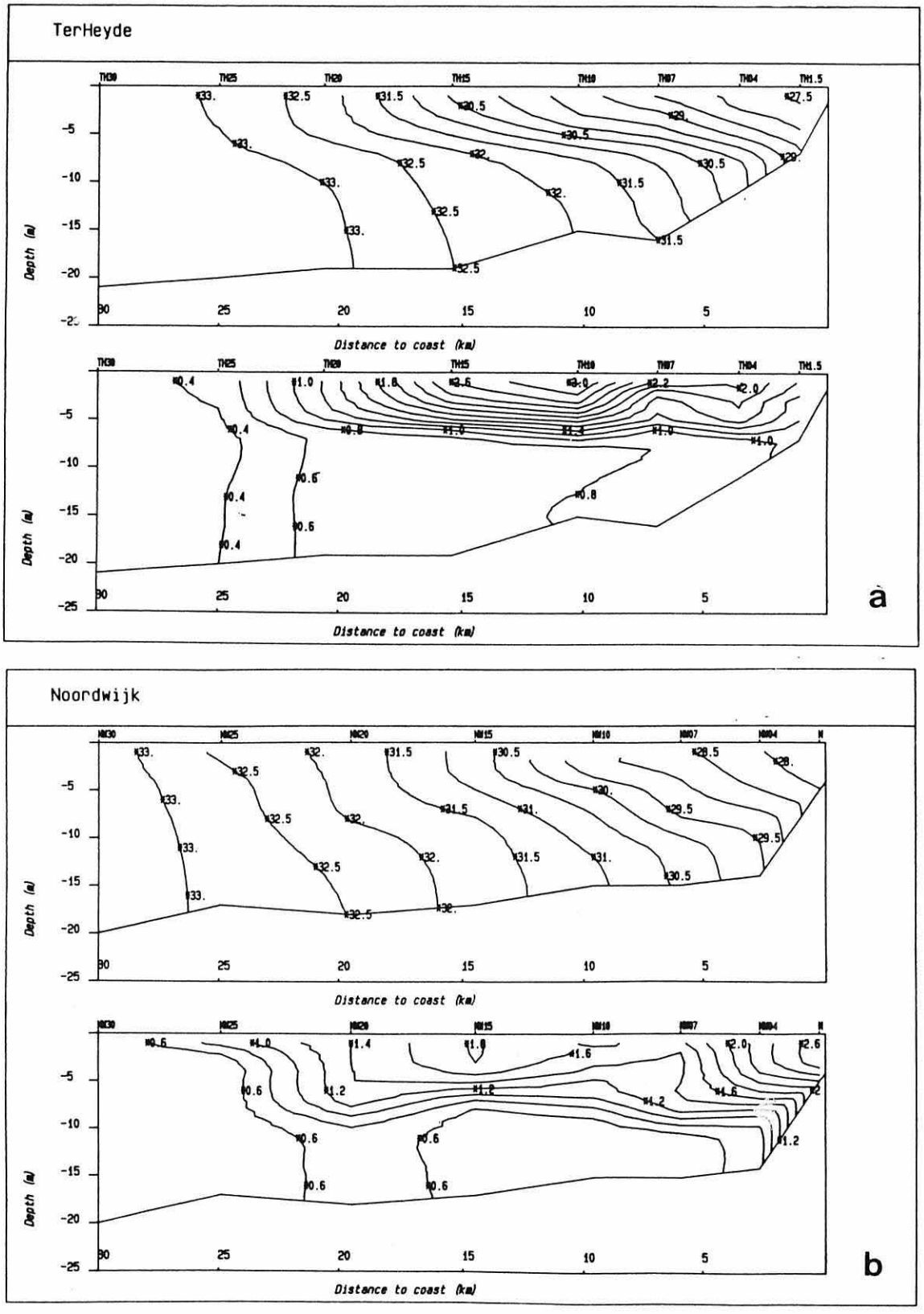

Figure 1.10 Distribution of the mean and standard deviation of salinity over 8 cruises between 1985 and 1987; a) Ter Heijde, b) Noordwijk, c) Egmond and d Callantsoog.

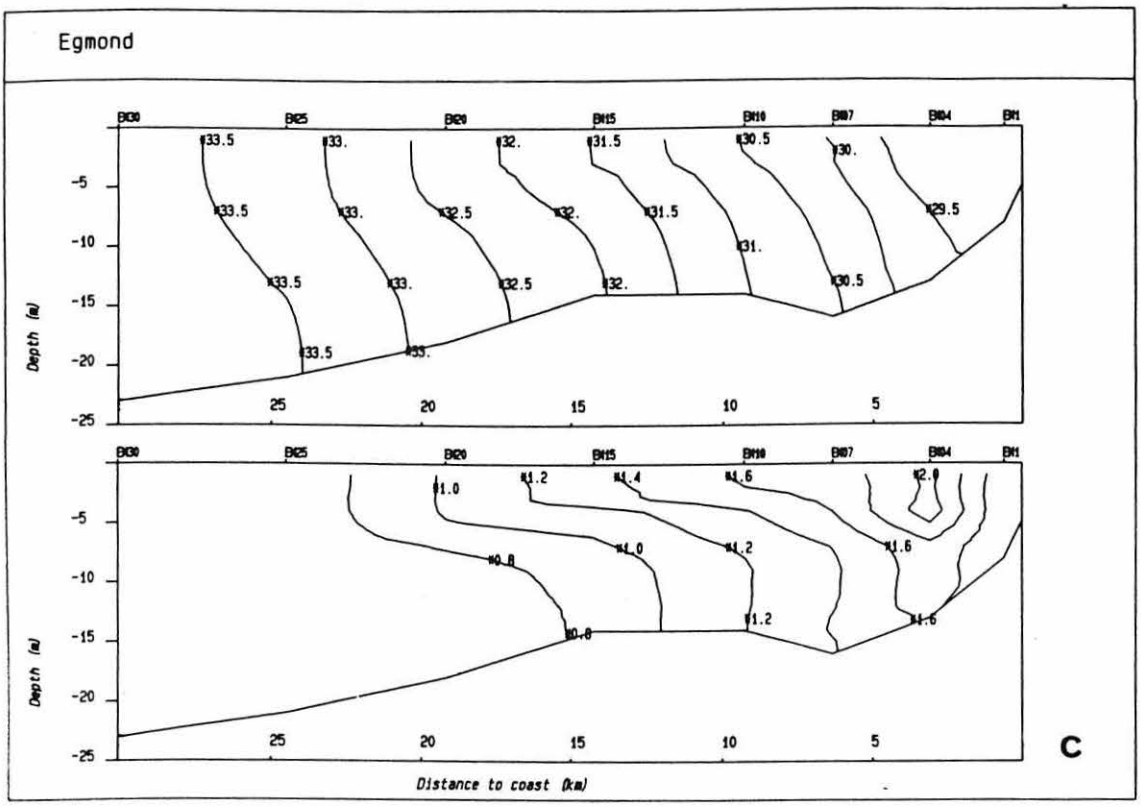
Egmond
Depth (m)
Distance to coast (km)
c

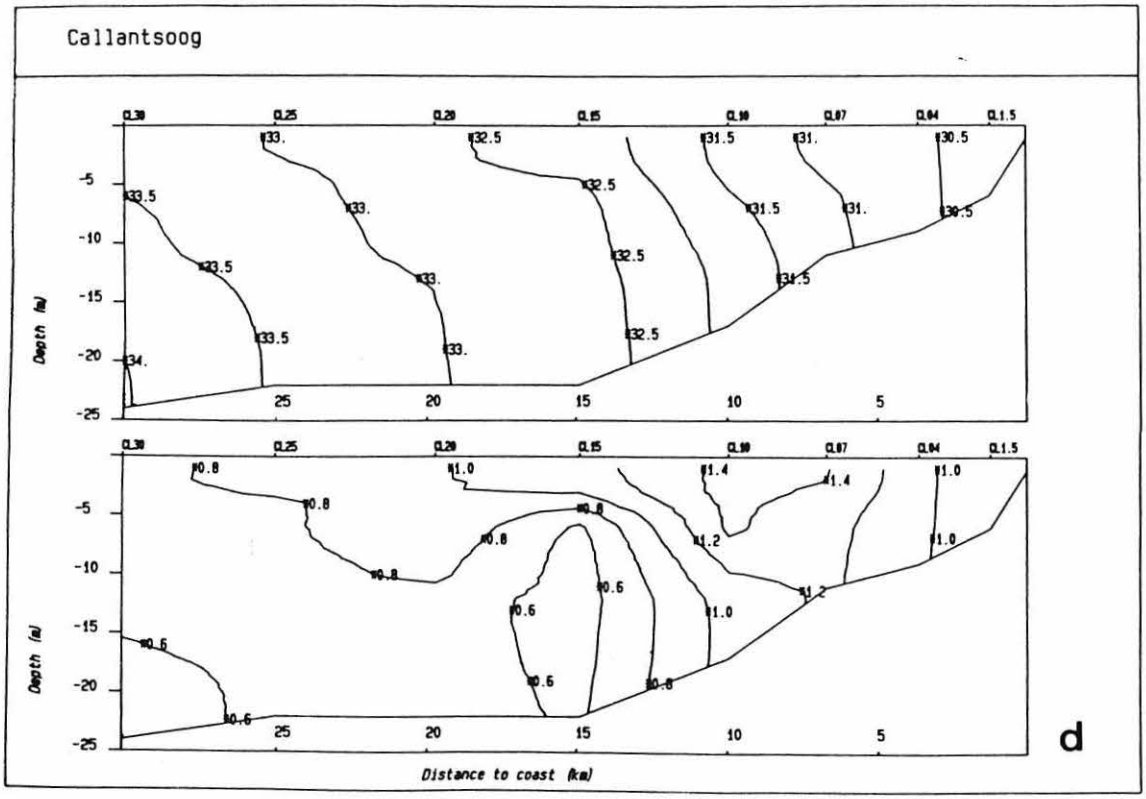
Callantsoog
Depth (m)
Distance to coast (km)
d

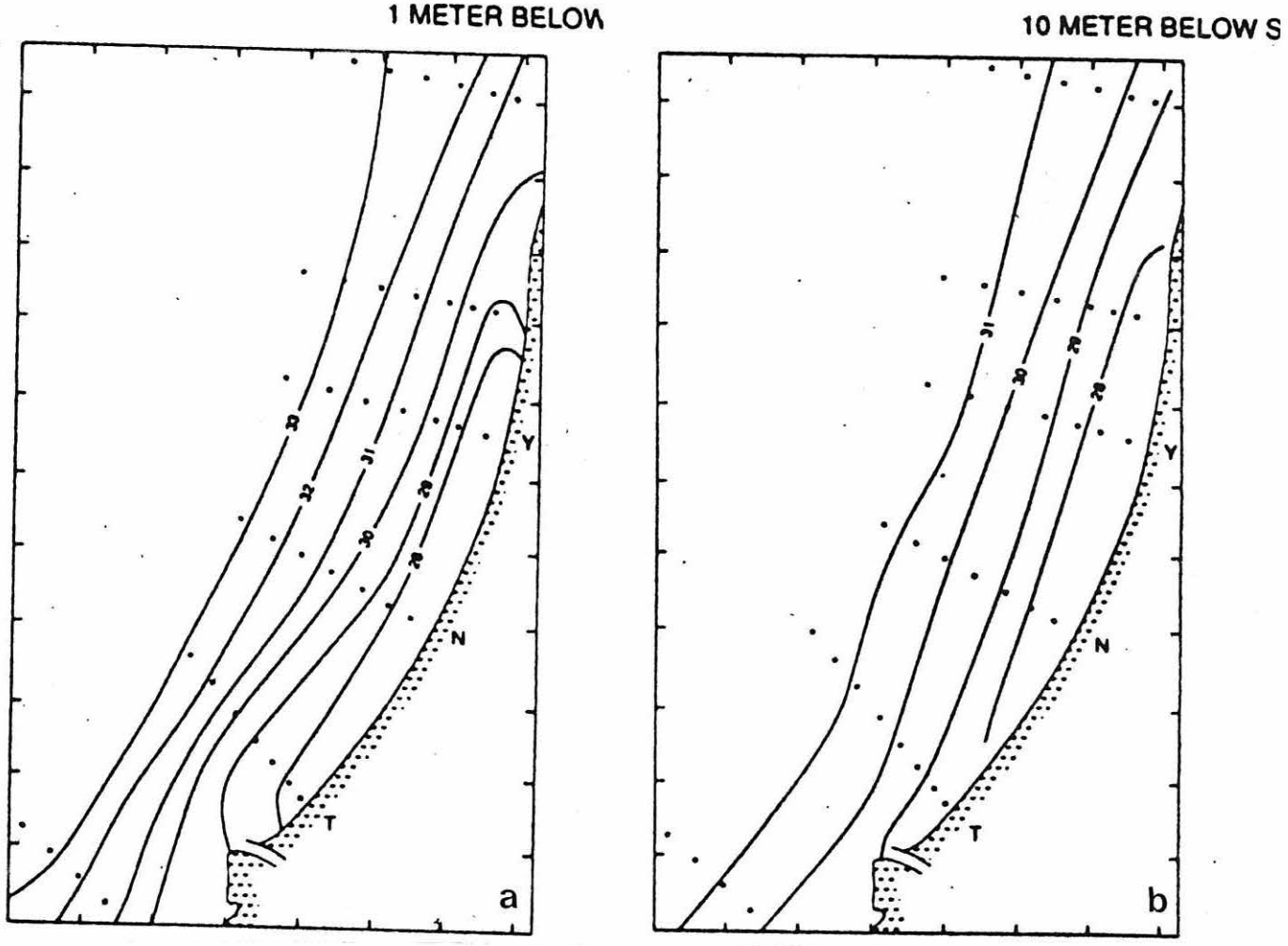

Figure 1.11 Average salinity over 8 cruises; a) at 1m and b) at 10m depth. Every tick-mark represent 10 km in distance (from de Ruijter *et al.*, 1992).

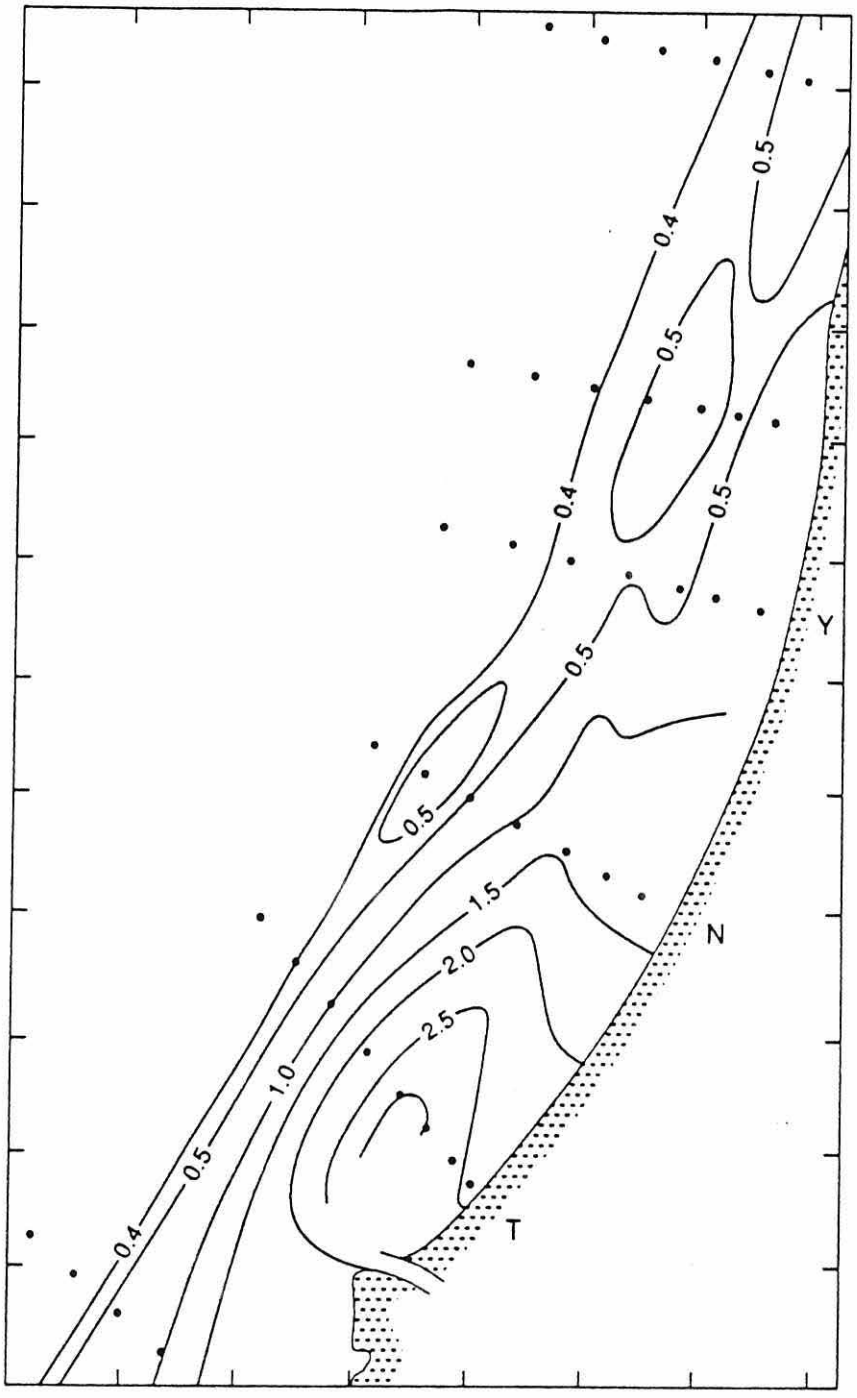

Figure 1.12 Horizontal distribution of mean salinity stratification, defined as the difference between average salinities at 1m and 10m deep. Every tick-mark represent 10 km (from de Ruijter *et al.*, 1992).

the Rhine ROFI, this transport is approximately twenty times the average inflow of riverine water, while the influence of North Atlantic water from other sources is negligible (van Pagee, 1986).

Residual flows arise from the interaction of the tides with topography, wind forcing and cross-shore density gradients. The long term average wind stress from predominantly north-eastward winds drives a mean residual current of the order of 0.05 ms^{-1} (fig. 1.13). However changes in wind speed and direction can considerably modify the mean flow. In extreme conditions persistent south-westward winds may even reverse the residual flow (de Ruijter *et al.*, 1987).

The effect of residual currents driven by cross-shore density gradients are also important as suggested by long term observations of the currents. The bottom currents are of the order of 3 cm^{-1} towards the coast (fig. 1.14), with a maximum located between 5 and 10 km offshore from Noordwijk. This same region exhibits the strongest along-shore flow (~10 cms^{-1}) and it is suggested by de Ruijter *et al.* (1992) that this may be the core of the coastal current.

1.4. Aims of the thesis.

This thesis reports a substantial new series of observations of the ROFI generated by the Rhine in the North Sea. This area was selected as a prototype area to study the processes in regions of freshwater influence as part of the MAST PROFILE project. The study is based on two observational campaigns, one in September-October 1990 and another in September 1992. During these observational periods, state-of-the-art instrumentation was available thanks to extensive European

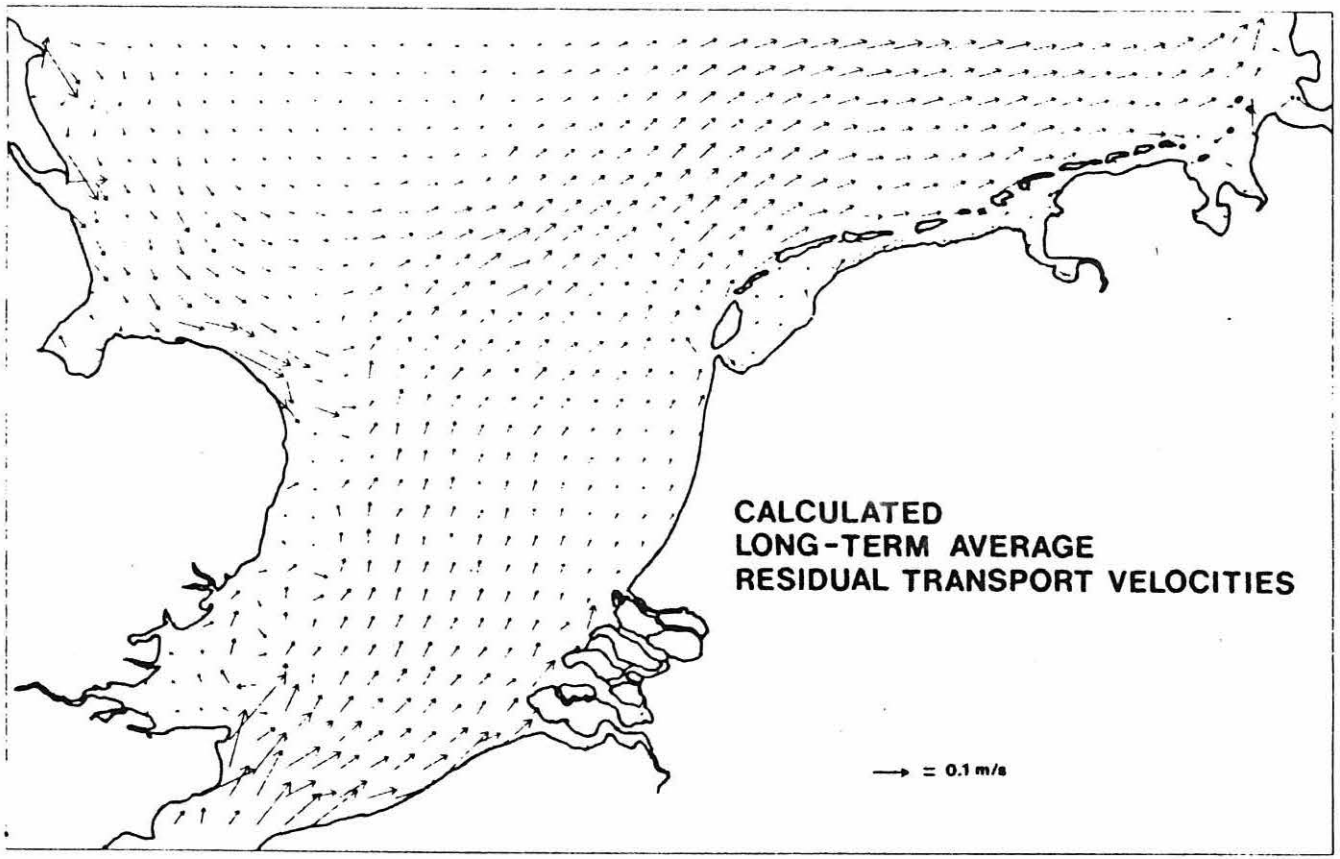

Figure 1.13 Calculated mean residual flows in the southern North Sea, from a vertically integrated numerical model (voogt, 1984).

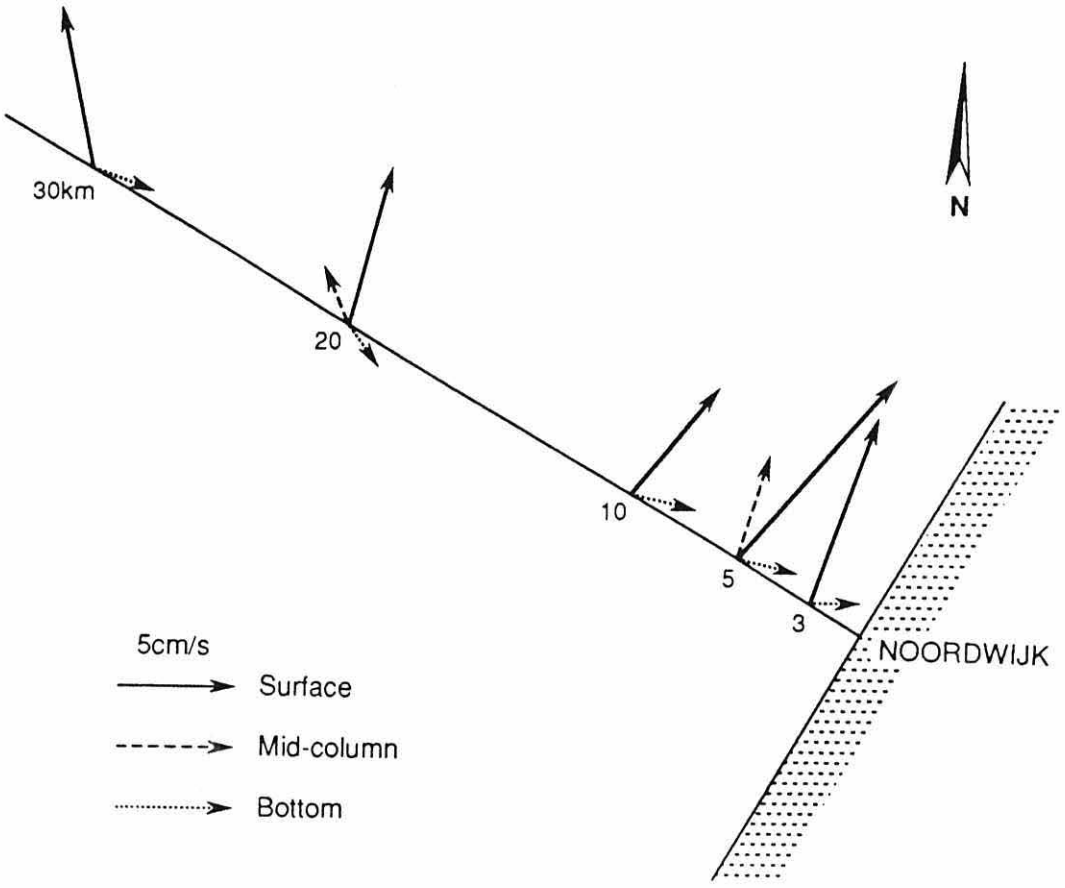

Figure 1.14 Mean currents in a transect infront of Noordwijk. The average was taken for the period between August 1985 and September 1986 (from de Ruijter *et al.*,1992).

cooperation. Although much of the study was based in current meter moorings, there were also spatial surveys, using a profiling CTD in 1990 and an undulating CTD (SEAROVER) in 1992. During the 1990 campaign the IFM-Hamburg CODAR was also deployed, while in 1992 current measurements were supplemented with bottom and hull-mounted ADCPs.

The principal aim of the thesis is to increase our understanding of the structure and flow in a high energy ROFI system. To this end the following specific goals have been set:

(i) To observe the space-time variations in structure and flow in the Rhine ROFI over periods of at least 15 days.

(ii) To interpret the observations in terms of the processes operating and to better define the nature of those processes and the way they interact.

(iii) To develop a 1-d model of vertical structure incorporating the principal physical processes to demonstrate processes understanding and lay a foundation for predictive models.

The following chapter will explain the theoretical background needed to understand the processes in ROFIs, while chapter 3 explains the observational techniques and the data analysis is in chapter 4.

The results for the stratification and mixing processes are considered in chapter 5, while the dynamics are presented in chapter 6, 7 and 8. A summary of observations

in chapter 9 explains the interaction of stratification and dynamics as inferred from the observations and highlights the importance of the generation of cross-shore shear, in the forcing of tidal straining. I shall seek to confirm the interpretation in chapter 10 by the use of a one-dimensional dynamic model which will lead to the final conclusions presented in chapter 11.

CHAPTER TWO

THEORETICAL BACKGROUND

2.1. Theory of the heating-stirring problem.

Following an extended series of investigations over the last 25 years, the development and decay of stratification in the shelf seas is now widely recognised to be the result of competition between the stratifying influence of buoyancy input on the one hand and mechanical stirring by tidal and wind stresses on the other. This competition was first clearly elucidated in relation to the problem of the formation of tidal mixing fronts whose locations were successfully predicted by an energy argument (Simpson and Hunter, 1974) based solely on buoyancy input by heating and stirring by the tides.

This argument can be generalized to include wind stirring and to explain the seasonal cycle of thermal structure in the shelf seas using the parameter ϕ defined as

$$\phi = \frac{1}{h}\int_{-h}^{0} (\bar{\rho} - \rho)\, gz\, dz; \qquad \bar{\rho} = \frac{1}{h}\int_{-h}^{0} \rho\, dz, \tag{2.1}$$

where h is the water depth, ρ is the water density, g is the acceleration due to gravity and z the vertical coordinate, positive upwards. For $\phi=0$ the water column is homogeneous and $\phi>0$ corresponds to a stable water column. Using this state variable ϕ, Simpson *et al.* (1978) derived a simple energy model in which the stratification arises as a result of the competition between stirring due to tides and wind, with the only buoyancy input due to solar heating and neglecting the effect of advection (fig.

2.1).

The rate of change of the potential energy anomaly ϕ due to surface heating is given by:

$$\left(\frac{d\phi}{dt}\right)_H = \frac{\alpha g \dot{Q}}{2C_p} \qquad (2.2)$$

where α is the thermal expansion coefficient, $\dot{Q}$ is the heat input rate at the surface, and C_p is the specific heat of seawater.

If the bottom stress is represented by a quadratic drag law, the mean dissipation over a tidal cycle is $\frac{4}{3\pi} k_b \rho U_b^3$, where U_b is the amplitude of the tidal velocity and k_b is the bottom drag coefficient. If it is assumed that a fixed fraction ε of the tidal dissipation is used to work against buoyancy forces the change in ϕ due to tidal stirring is

$$\left(\frac{d\phi}{dt}\right)_{TS} = -\frac{4}{3\pi} \epsilon k_b \rho \frac{|U_b|^3}{h} \qquad (2.3)$$

By analogy, the wind stirring effect is calculated from the wind stress drag law $\tau_s = \rho_a k_s W|W|$, where ρ_{air} the air density, W the wind velocity and $k_s = C_d \times \gamma$, where C_d is the surface drag coefficient and γ is the ratio of surface current to wind speed.

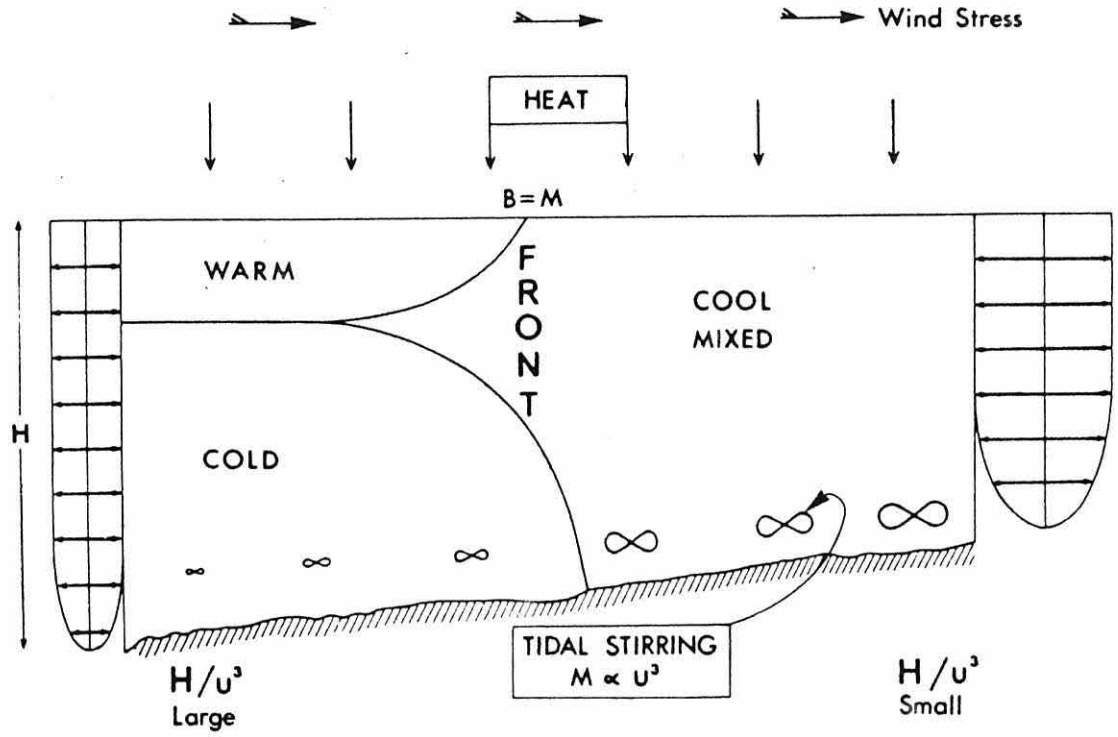

Figure 2.1 Schematic of the competition between seasonal heating and tidal stirring (from Simpson and James, 1986).

The rate of work done by the wind stress on the sea surface that goes to generate turbulent kinetic energy is $\delta \rho_a k_s |W|^3$, where δ is the wind efficiency. So the rate of change in ϕ due to wind stirring is

$$\left(\frac{d\phi}{dt}\right)_{WS} = - \delta \rho_a k_s \frac{|W|^3}{h} \qquad (2.4)$$

The total rate of change of the potential energy anomaly is then given by

$$\frac{d\phi}{dt} = \left(\frac{d\phi}{dt}\right)_H + \left(\frac{d\phi}{dt}\right)_{TS} + \left(\frac{d\phi}{dt}\right)_{WS}$$

$$\frac{d\phi}{dt} = \frac{\alpha g \dot{Q}}{2C_p} - \frac{4}{3\pi} \epsilon k_b \rho \frac{|U_b|^3}{h} - \delta k_s \rho_a \frac{|W|^3}{h} \qquad (2.5)$$

In the frontal region, which is the transition between the mixed and stratified waters, $\frac{d\phi}{dt}=0$ and, if the tidal mixing dominates, so that the wind mixing can be neglected, equation (2.5) simplifies to

$$\frac{h\dot{Q}}{U_b^3} = \frac{8C_p \rho k_b \epsilon}{3\pi \alpha g} \qquad (2.6)$$

To a first approximation, the quantities $\dot{Q}$, C_p, K_b, ρ, α and ε may be regarded as constants. The frontal position is then defined by the stratification parameter h/U^3.

Simpson and Hunter (1974) used this relation to predict the positions of fronts which should lie along a critical contour. The parameter h/U^3 has been calculated using numerical hydrodynamic tidal models in several regions of the world to find the mean position of frontal regions (Garret *et al,* 1978; Pingree and Griffith, 1978; Schumacher *et al.*, 1979; Yanagi, 1980; Argote *et al.*, 1985; Glorioso, 1987).

The heating-stirring model was then extended (Simpson and Bowers, 1984) to produce a full profile and allow for the control of heat flux by the sea surface temperature. The stirring power is calculated using wind and tidal stresses as described above. The model works allowing the heat exchange for one time step and then mixing downwards from the surface, to produce a new surface mixed layer, until the increase of potential energy of the water column equals the effective stirring energy input of wind. The resulting profile is then modified by similar mixing of the bottom structure until the increase in potential energy equals the effective stirring energy input from the tide.

When the model was driven by climatological cycles of heat flux, it resulted in fair agreement with the observations, but with some discrepancies probably due in part to advection, which is not considered in these models.

2.2 Freshwater buoyancy input.

It is important to note that the models like that discussed above neglect the effects due to horizontal changes in density. They therefore cannot be directly applicable to ROFIs, which as discussed earlier, are regions in which there are strong density gradients, and the stratification tends to be dominated by the density driven

circulation.

To be able to predict the estuarine stratification with an energy approach, the model will have to include the additional stratifying influence of the density circulation. The main problem that arises in this approach is that this stratifying process is not horizontally uniform, since it enters as one or more localized inputs of freshwater at a lateral boundary (Simpson *et al.*, 1990; Uncles *et al.*, 1990).

In order to quantify this process Simpson *et al.* (1990) assumed that the buoyancy input will maintain a horizontal density gradient which will drive a density circulation. They also introduced the idea of tidal straining, in which the semi-diurnal tidal shear interacts with the horizontal density gradient to produce transient stratification. During the part of the tidal cycle when flow is off-shore, the faster surface currents tend to move the fresher water on top of the lower, and therefore, relatively denser bottom water. During the shoreward part of the tidal cycle the process reverses to restore the initial mixed density profile (fig 2.2).

To determine the contribution of these shear flows (estuarine circulation and tidal straining) to ϕ, Simpson *et al.* (1990) first took the derivative of ϕ from equation (2.1) with respect of time

$$\frac{\partial \phi}{\partial t} = \frac{g}{h} \int_{-h}^{0} \left(\frac{\partial \bar{\rho}}{\partial t} - \frac{\partial \rho}{\partial t} \right) z \, dz$$

where the changes in ϕ due to the tidal elevation have been neglected. Considering the flow to be in the x direction and the density gradients uniform in depth the

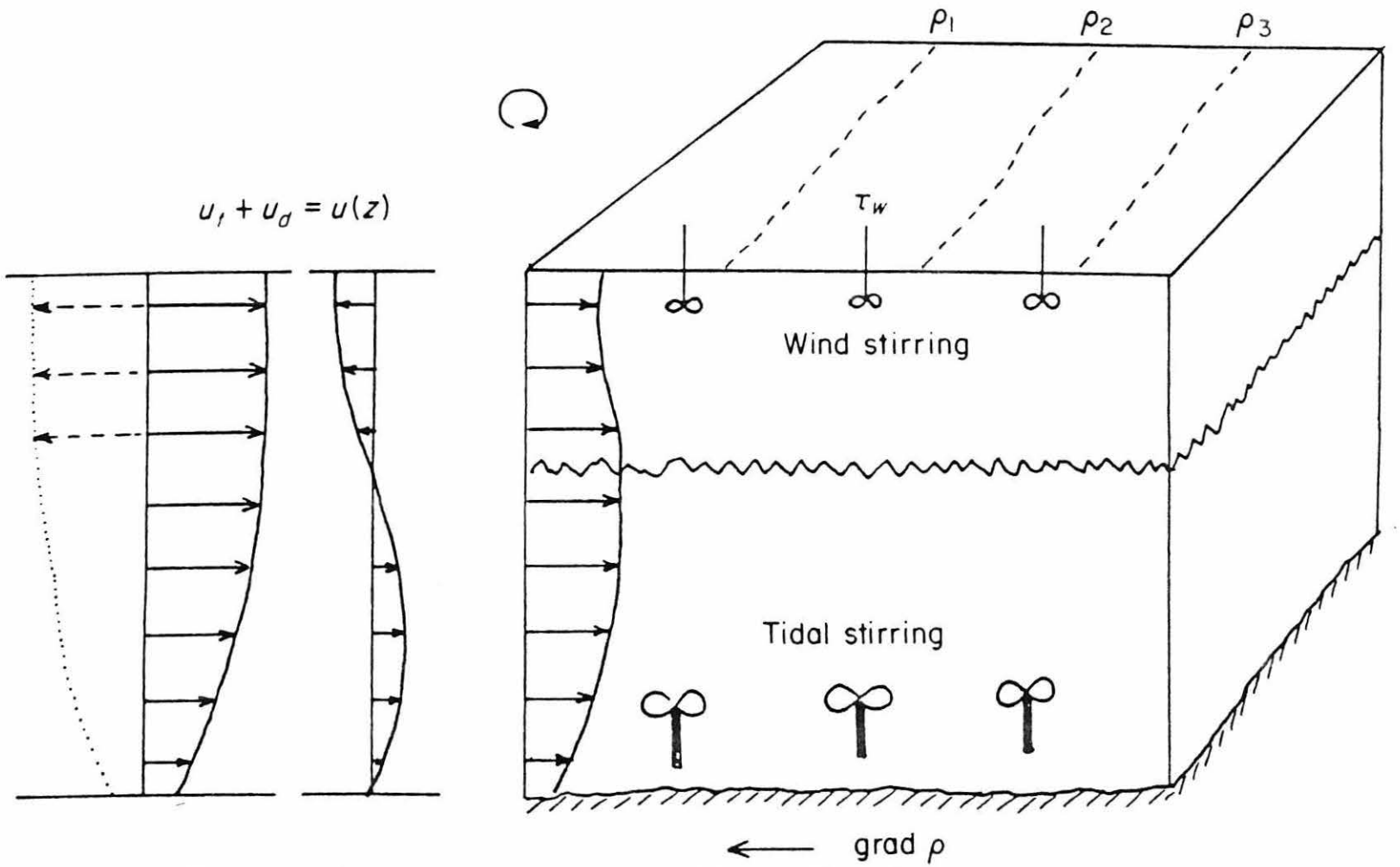

Figure 2.2 Schematic of the competition of the stratifying forces of the density driven current; tidal straining of the density field due to shear in the tidal current and the stirring forces of winds and tides (from Simpson *et al.*, 1991).

density advection equation gives

$$\frac{\partial \phi}{\partial t} = \frac{g}{h}\frac{\partial \rho}{\partial x}\int_{-h}^{0}(u - \bar{u})\,z\,dz \qquad (2.7)$$

This result allows the evaluation of the input to ϕ for any known velocity profile u(z).

For example, using the Hansen and Rattray (1965) velocity profile

$$u(\zeta) = \frac{g h^3}{48 N_z \rho}\frac{\partial \rho}{\partial x}(1 - 9\zeta^2 - 8\zeta^3); \quad \zeta = \frac{z}{h} \qquad (2.8)$$

and substituting in equation (2.7), the change of ϕ due to the estuarine circulation is found to be

$$\left(\frac{\partial \phi}{\partial t}\right)_E = 3.1\times10^{-3}\frac{g^2 h^4}{N_z \rho}\left(\frac{\partial \rho}{\partial x}\right)^2 \qquad (2.9)$$

This is an interesting result that shows how the estuarine stratification will be sensitive to any change in the density gradient, due to the fact that the time derivative of stratification is directly proportional to the square of the density gradients. It also shows an inverse dependence of $\left(\frac{\partial \phi}{\partial x}\right)_E$ on the eddy viscosity, Nz, which will vary as described by Bowden (1953) $N_z = \gamma|\bar{u}|$. Large values of N_z during the main part of flood and ebb when mixing is strong, may suppress the density current and restrict its stratifying action to near slack water. This alternation of periods of density current flow and strong vertical mixing have been reproduced in laboratory experiments by

Linden and Simpson (1988). The density current regime set up by the removal of a barrier between different density fluids is disrupted by mixing induced by bubbles. The vertical structure is largely destroyed and what horizontal transport there is, in response to the horizontal gradient, may be regarded as a shear diffusion process. When the mixing is switched-off, the density current regime is rapidly restored with a consequent increase in the horizontal fluxes and rapid development of a stratified structure. At the ROFI scale, the flow is further complicated by the influence of the earth's rotation which limits the cross-shore movement of density currents to about 1.5 times the internal Rossby radius of deformation, as indicated by the geostrophic two-layer model of Ou (1983).

In the real world, apart from these changes in mixing, there are further complications due to "tidal straining", described above, which drives a semi-diurnal variation in water column stability. Simpson *et al.* (1990) have estimated the contribution from straining using the tidal velocity profile given by Bowden and Fairbairn (1952)

$$\mathbf{u(\zeta) = \bar{u}(a - b\zeta^2)} \qquad \mathbf{a = 1.15 \; ; \; b = 0.425} \qquad \textbf{(2.9)}$$

which was substituted into equation (2.7) to give

$$\left(\frac{\partial \phi}{\partial t}\right)_{ST} = \mathbf{0.031\, gh\bar{u}} \frac{\partial \rho}{\partial x} \qquad \textbf{(2.10)}$$

The total rate of change of ϕ including tidal mixing as given by Simpson *et al.* (1990) is

$$\frac{\partial \phi}{\partial t} = \left(\frac{\partial \phi}{\partial t}\right)_{ST} + \left(\frac{\partial \phi}{\partial t}\right)_{E} - \left(\frac{\partial \phi}{\partial t}\right)_{TS}$$

$$\frac{\partial \phi}{\partial t} = 0.031 g h \bar{u} \frac{\partial \rho}{\partial x} + 0.0031 \frac{g^2 h^4}{N^z \rho} \left(\frac{\partial \rho}{\partial x}\right)^2 - \epsilon k \rho \frac{|\bar{u}|^3}{h}, \qquad (3.11)$$

Simulation for Liverpool Bay showed a fair qualitative agreement with the observations, with a fortnightly stratification due to the variation in tidal mixing energy in the spring-neap tidal cycle and a semi-diurnal oscillation in stratification due to the tidal straining, which appears as an important control of stratification.

Improvements of this model were made by Simpson *et al.* (1991), using a prescriptive profile model, of the similar kind to that developed by Simpson and Bowers (1984) for the heating stirring problem. The main improvements of the model, were the inclusion of wind stirring, the use of the tidal velocity profile given by Prandle (1982) and a density current profile which takes rotation into account (Heaps, 1972, explained in more detail later). The latter improvement is important for regions such as Liverpool Bay and the Rhine ROFI, where the study area is larger in scale than the internal Rossby radius of deformation and hence the earth's rotation become important in modifying the stratification processes and the frontal position (Ou, 1983).

The next step forward from these relatively simple energy models is the use of fully dynamical point models, which have been a valuable tool in developing the understanding of the ROFI system. The advantage of these models is that they allow a feedback between the density structure, frictional coupling and the flow. The requirement of all such models is that they have to find a way to close the equations of motion. Generally this is done by specifying a turbulence closure prescription to

determine the eddy coefficients N_z and K_z.

In the approach that is to be adopted in chapter 10 we shall use a point model with a level 2 turbulence-closure scheme, in much the same way as it was described for Liverpool Bay (fig. 2.3) by Simpson and Sharples (1992).

2.3 Density current dynamics.

It is frequently observed that water transport in coastal margins is confined to a narrow zone, called coastal current. The driving force is due to density gradients due to one or more buoyancy inputs from land, which will be balanced by the Coriolis force, as observed in the Dutch Coastal region.

The dynamics of the coastal currents can be explained using the Navier-Stokes equation. Consider the flow for a rotating incompressible fluid with negligible viscous or diffusive forces (Gill, 1982)

$$\frac{Du}{Dt} - fv = -\frac{1}{\rho}\frac{\partial P}{\partial x} + F_x \qquad (2.13)$$

$$\frac{Dv}{Dt} + fu = -\frac{1}{\rho}\frac{\partial P}{\partial y} + F_y \qquad (2.14)$$

$$-\frac{1}{\rho}\frac{\partial P}{\partial z} + g = 0 \qquad (2.15)$$

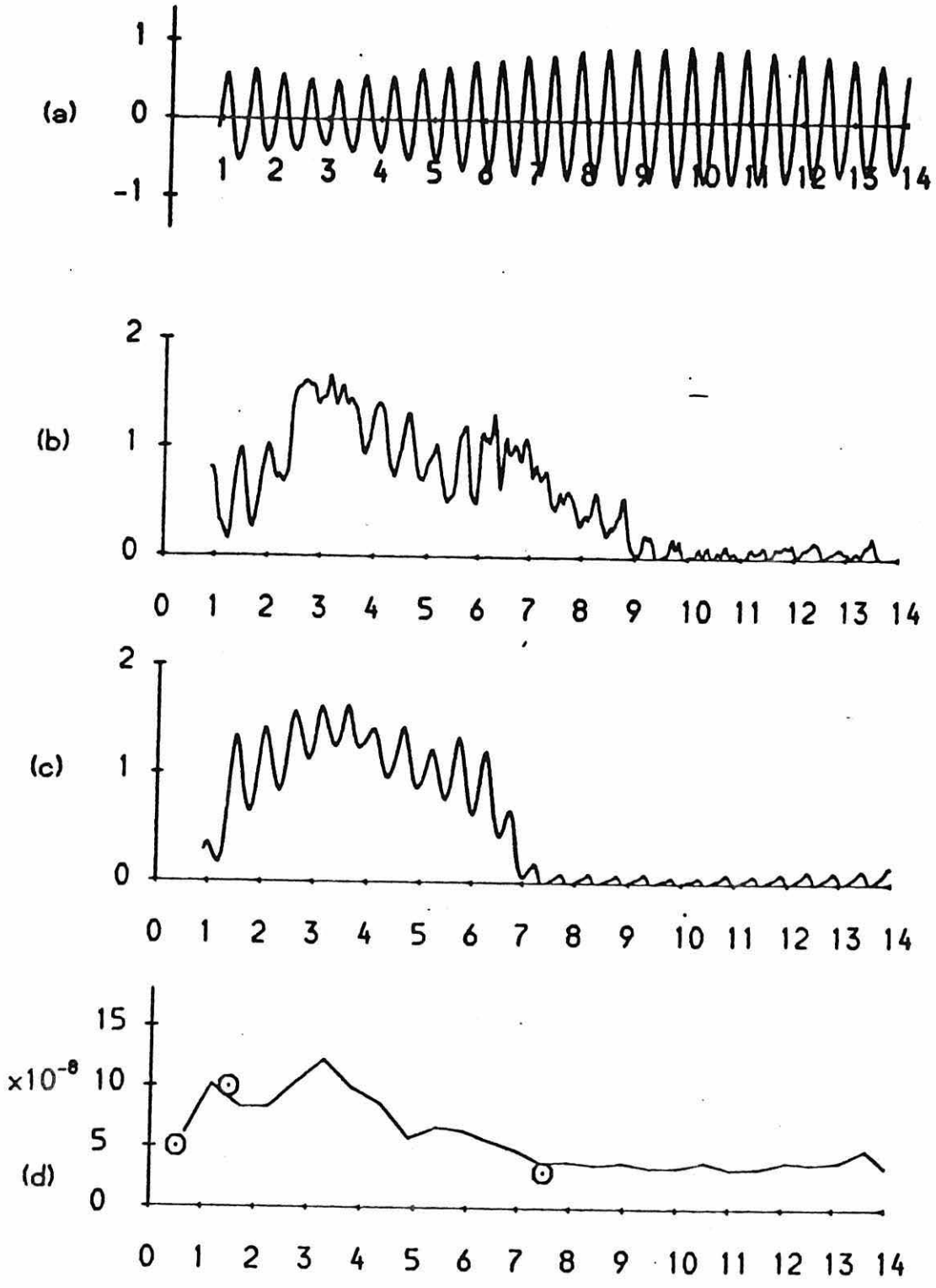

Figure 2.3 Comparison of stratification in Liverpool Bay with the simulation of a turbulence closure level 2 point model (Simpson and Sharples, 1992). a) depth mean tidal current in ms^{-1}, b) observed stratification, c) modelled stratification, both calculated as the bottom-surface density difference in kgm^{-3}, c) observed variation of density gradients in m^{-1}.

$$\frac{\partial u}{\partial x} + \frac{\partial v}{\partial y} + \frac{\partial w}{\partial z} = 0 \qquad (2.16)$$

where (u,v,w) are the velocity components in cartesian coordinates (x,y,z), f is the Coriolis parameter, P is pressure and F_x, F_y are external forces in the x and y direction respectively.

In the case of shallow seas, where the effects of friction become important, Heaps (1972) derived a velocity profile for the density driven flow. The frictional forces are given by

$$F_x = \frac{1}{\rho}\frac{\partial \tau_x}{\partial z} = N_z \frac{\partial^2 u}{\partial z^2}$$

$$F_y = \frac{1}{\rho}\frac{\partial \tau_y}{\partial z} = N_z \frac{\partial^2 v}{\partial z^2}$$

and the pressure terms derived from the hydrostatic law (equation 2.15)

$$P = g\rho(z + \eta)$$

With no pressure changes along the coast and specifying that the net transport must be equal to the river transport, the equations of motion and continuity given by equations (2.13) to (2.15), in the steady state become

$$fv = g(z + \eta)\frac{1}{\rho}\frac{\partial \rho}{\partial x} + g\frac{\partial \eta}{\partial x} - N_z \frac{\partial^2 u}{\partial z^2} \qquad (2.17)$$

$$fu = N_z \frac{\partial^2 u}{\partial z^2} \tag{2.18}$$

$$\int_{-h}^{\eta} u dz = q \tag{2.19}$$

to which Heaps (1972) found the analytical solution

$$u = \frac{gH}{f}\left(\frac{1}{\rho}\frac{\partial \rho}{\partial x}\right) F(\zeta,a,b) \tag{2.20}$$

$$v = \frac{gH}{f}\left(\frac{1}{\rho}\frac{\partial \rho}{\partial x}\right) G(a,b,\zeta) \tag{2.21}$$

where

$$H = h + \eta, \quad \zeta = \frac{Z}{H}$$

and

$$a = \frac{H}{\sqrt{2N_z/f}}, \quad b = \frac{kH}{N_z}$$

while $F(\zeta,a,b)$ and $G(\zeta,a,b)$ are complicated analytical functions too extensive to reproduce here but defined explicitly in Heaps (1972, equations (27) and (28)).

Figure 2.4 shows the velocity profile using the above analysis for typical values for the Rhine ROFI: N_z=0.01 m^2s^{-1}; $1/\rho(\partial\rho/\partial x)$=2 x 10^{-7} m^{-1}. It is evident in this case how the presence of friction produces strong cross-shore estuarine flow. In comparison with geostrophy where the frictional forces are negligible and the flow is purely along-shore.

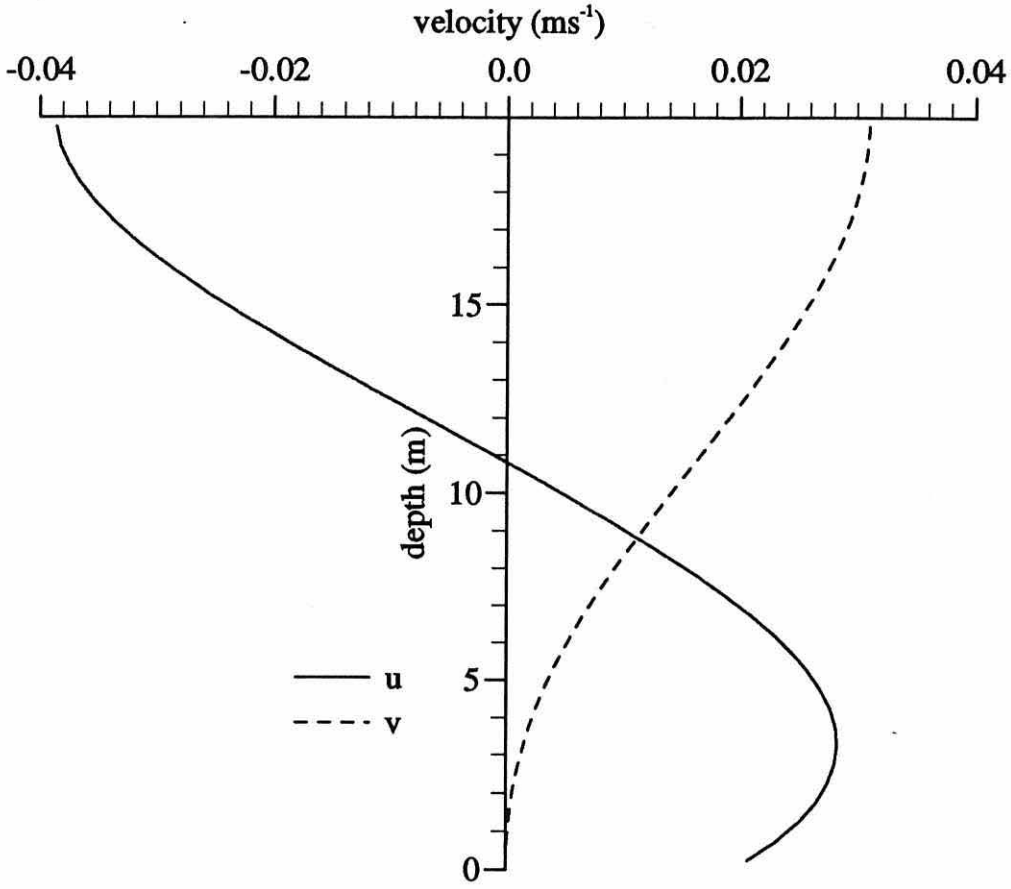

Figure 2.4 Heaps (1972) velocity profile for typical values of the Rhine ROFI: N_z=0.01m^{2}s^{-1} and $1/\rho(\partial\rho/\partial x)=2 \times 10^{-7}$ m^{-1}.

2.4. Tidal dynamics

Although in much of this study we will refer to observations of tidal velocities in stratified waters, we need to use the homogenous solution as a reference, due to the lack of a theoretical solution for stratified water. The vertical distribution of tidal currents for an homogenous water column can be explain using boundary layer theory following Prandle, 1982:

$$\frac{U(z)}{\bar{U}} = \frac{\left(e^{bz} + e^{-bz+2y}\right)}{T} + Q\,, \tag{2.22}$$

where

$$T = (1 - e^{2bH})\,\frac{j - 1}{bH - 1} - 2e^{2bH} \tag{2.23}$$

$$Q = \frac{j(1 - e^{2bH}) - 1 - e^{2bH}}{T} \tag{2.24}$$

$$j = \frac{3\pi N_z}{8k|\bar{U}|} \tag{2.25}$$

and

$$b = \left(\frac{i(f + w)}{N_z}\right)^{\frac{1}{2}} \tag{2.26}$$

for the anticlockwise component, while

$$b = \left(\frac{i(f - w)}{N_z}\right)^{\frac{1}{2}} \qquad (2.27)$$

for the clockwise. N_z is the eddy viscosity, ω is the tidal frequency, f is the Coriolis parameter, k is the bottom drag coefficient, $\bar{U}$ is the depth mean average, H is the total depth, z=h/H and i is $(-1)^{1/2}$.

Studies of velocity profile in shallow waters have shown that the elliptic properties of tidal currents vary with depth: near surface currents are generally stronger than near bottom currents; their rotational sense and orientation may also vary with depth. This has been successfully explained in terms of the bottom Ekman dynamics with constant or linear variations of eddy viscosity using the theory discussed above. The greater length scale of the boundary layer associated with clockwise motion (in the Northern hemisphere) causes the currents to become increasingly clockwise with increasing height above the seabed. Recent observations (Maas and van Haren, 1987; Lwiza *et al.*, 1991, Visser *et al.*, 1994) suggest that the presence of stratification modifies the tidal dynamics and produces significant deviations from the predicted profiles for the homogeneous rotating case. In chapter 6, we report on new observations in the Rhine ROFI demonstrating the direct influence of stratification on the tidal ellipse shape.

CHAPTER THREE

OBSERVATIONAL TECHNIQUES

3.1 Experiment strategy.

The observational programme in the Rhine ROFI was designed to determine the structure of the water column and flow and to measure the horizontal density gradients which form an important part of the dynamical forcing.

The measurements were planned to include at least one spring-neap tidal cycle, and hence to determine the water column stability during conditions of high and low tidal stirring. To achieve this, an array of instrumented moorings were deployed, while ship surveys were carried out to establish a spatial context.

The data were collected during two cruises onboard the RRS Challenger, the first one in September-October 1990 and the second in September 1992. Although the basic aims of the two observational periods were practically the same, there were some significant differences between the two campaigns. During part of the 1990 survey the IFM HF radar CODAR was measuring surface velocities, while in the 1992 campaign, an undulating CTD SEAROVER was used to generate quasi-synoptic density sections.

3.1.1 The 1990 Experiment.

This first survey, in the period 23/9/90 to 23/10/90, was a co-operative effort

between the Institute für Meereskunde Hamburg, Germany (IFM), the Rijkwaterstaat, Netherlands (RWS) and the University of North Wales, U.K. (UCNW) and consisted of three major elements: ship hydrographic surveys; current, temperature and conductivity time series from moorings; an HF radar (CODAR) for mapping the surface currents.

Two arrays of moorings (fig. 3.1) were deployed from the 23 September to the 18 October: (i) cross-shore from Scheveningen, with moorings at 2, 3, 5, 8, 13 and 33 km from the coast, with current meters at 4 m above the bed and 4 m below the surface to observe the transverse section of the alongshore flow field (fig. 3.2) and (ii) a diamond array centred on the Scheveningen line 13 km from the coast (fig. 3.1). Each of the diamond moorings were equipped with three current meters, at approximate depths of 8, 12 and 16 m and the majority of instruments also recorded temperature and salinity. In addition a TS recorder and a recording transmissometer were attached to the toroidal marker buoy. A fifth transmissometer was located near the bottom in mooring A (fig. 3.3).

From the 7 October to the 23 October 1990, surface currents were measured using an HF radar (CODAR) with ground stations located at Gravenzande and Noordwijk. This gave a coverage out to ~ 40 km, equivalent to a grid of more than 100 current meters spaced at intervals of ~ 3 km.

Two spatial hydrographic surveys were carried out by the RRS Challenger (fig. 3.1). The timing of these surveys was chosen to coincide with the post-springs and post-neaps periods to provide a maximum contrast in tidal stirring. Profiles of temperature, salinity, optical beam transmittance and chlorophyll fluorescence were

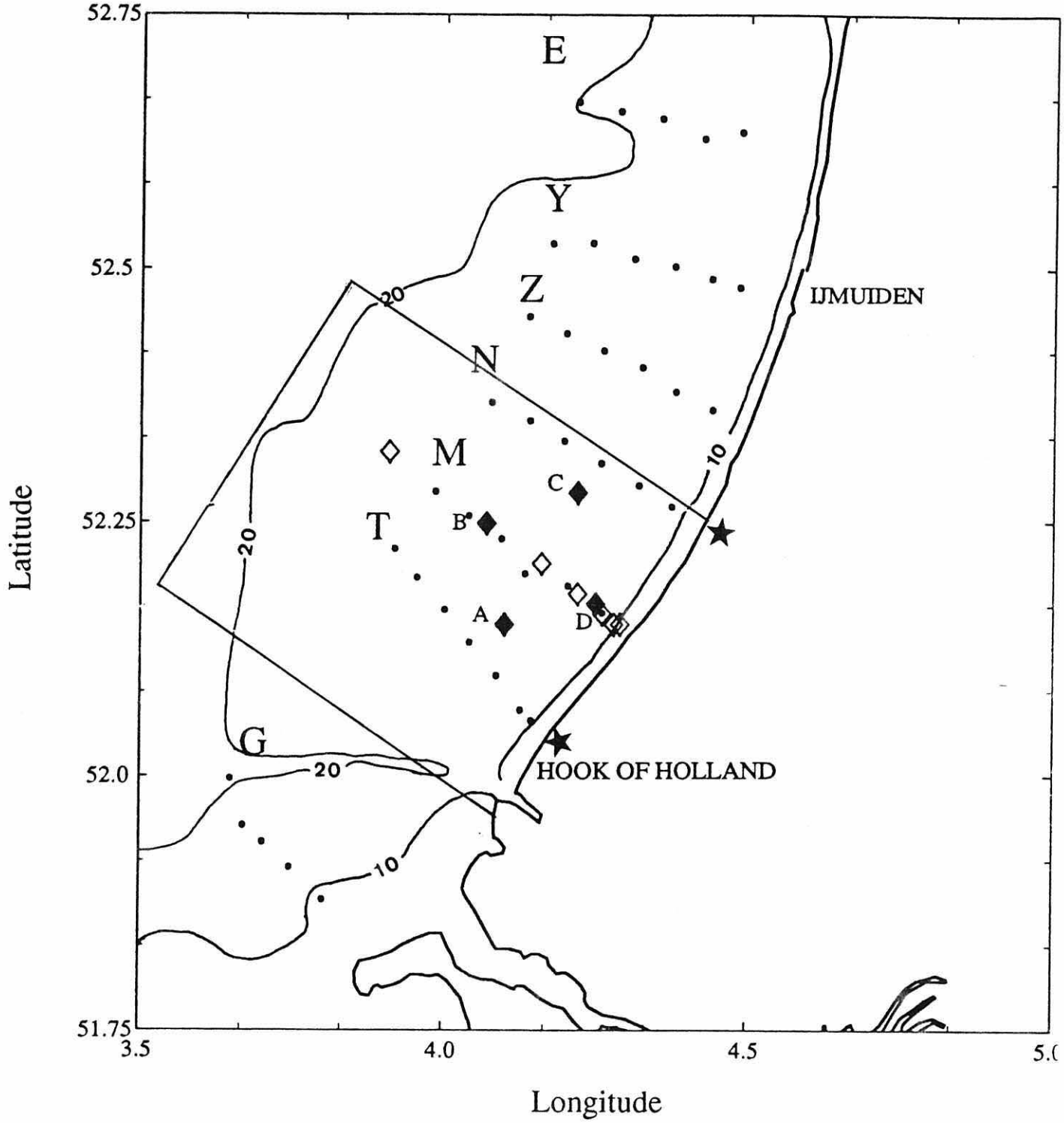

Figure 3.1 Rhine ROFI study area for the 1990 campaign. (·) represent CTD stations, (♦) and (◊) represent UCNW and RWS moorings respectively. (★) are the ground CODAR stations and the square shows the HF radar coverage.

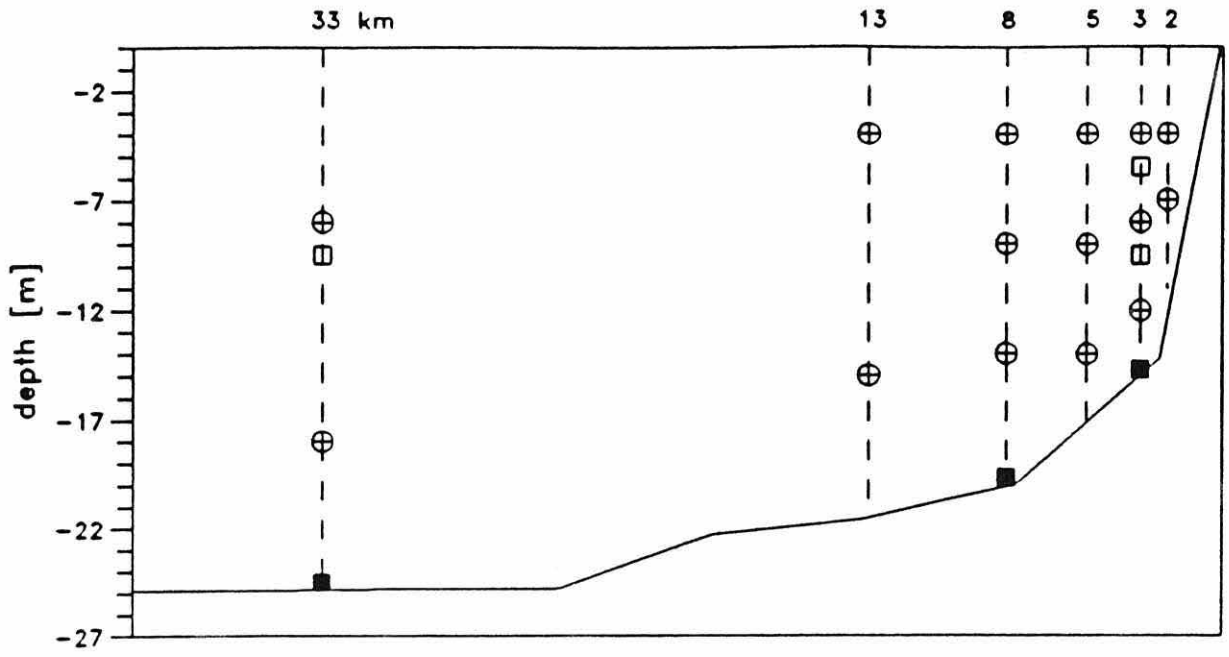

Figure 3.2 RWS moorings schematic, where (■) are pressure gages, (□) are Hydrolab water quality sensors and (⊕) are current meters.

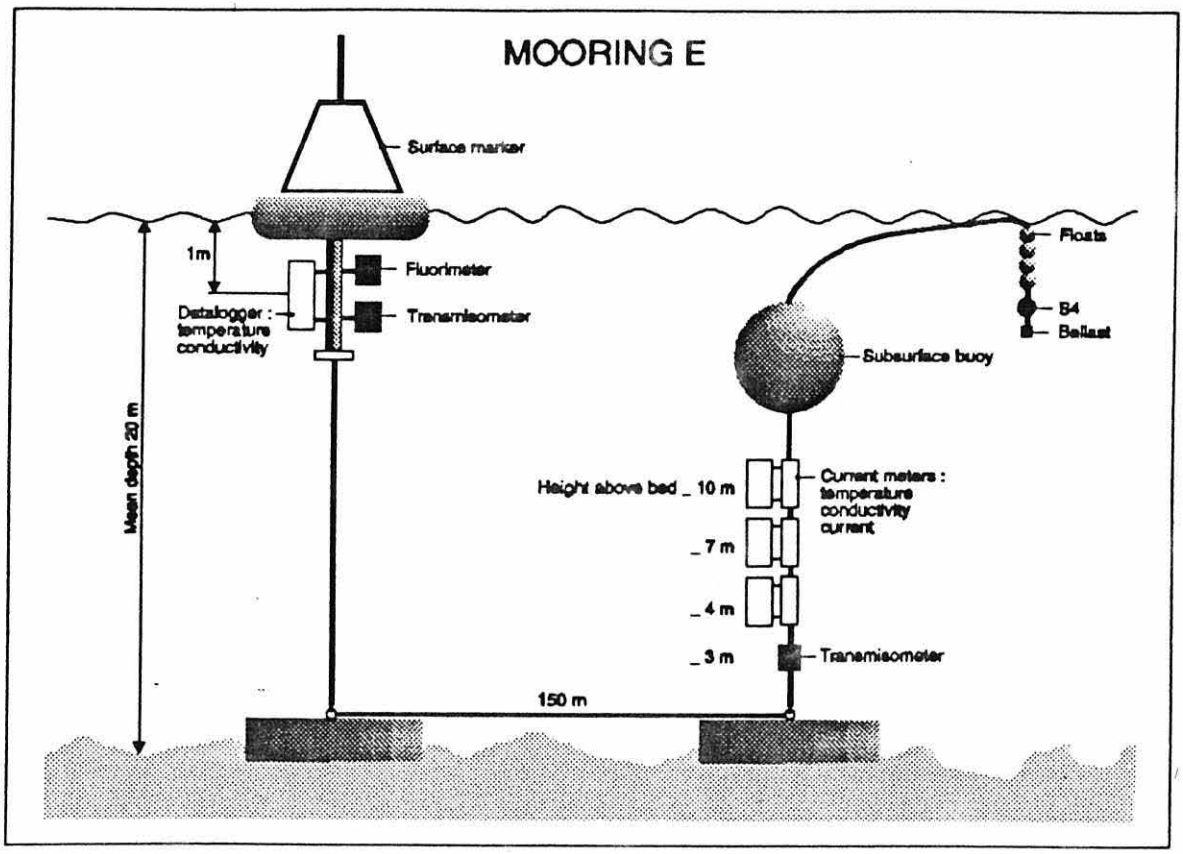

Figure 3.3 Schematic of the UCNW U-mooring used in 1990.

recorded at each station using a NBIS Mk 3 CTD system equipped with auxiliary sensors.

3.1.2 The 1992 Experiment.

A second collaborative study, between UCNW and RWS, was carried out between the 2 and 17 September 1992. In this case the mooring array formed a square with a centroid, located on the Noordwijk line 16 km from the coast and with corner moorings at 13 km from each other (fig. 3.4). The moorings were moved northward relative to the 1990 positions to avoid any possible effect from the near source region. As in the 1990 campaign, the moorings were designed to determine the water column structure and flow and to measure the horizontal density gradients. For this purpose the moorings were equipped with 4 current meters (3 Aanderaa and 1 S4), at 1, 10, 13, 16 m deep; all the Aanderaa current meters were capable of measuring temperature and salinity. At the same time, bottom mounted ADCPs were recording velocities throughout most of the water column. The toroid marker buoys were fitted with a TS logger, a fluorimeter and a transmissometer, while another transmissometer was located near the bottom (fig. 3.5).

From the 8 September 1992 a continuous hydrographic spatial survey was carried out by the RRS Challenger. The survey was done using an undulating CTD (SEAROVER) and followed three different strategies (fig. 3.4): the first was a series of alongshore lines to determine the alongshore density structure; the second was a zig-zag survey, using the historical survey lines in figure 3.1 as the main axes, to study the three dimensional structure of the Rhine ROFI; and the third one was a 25 hours cross-shore section in front of Noordwijk, during which the 150 kHz ship-

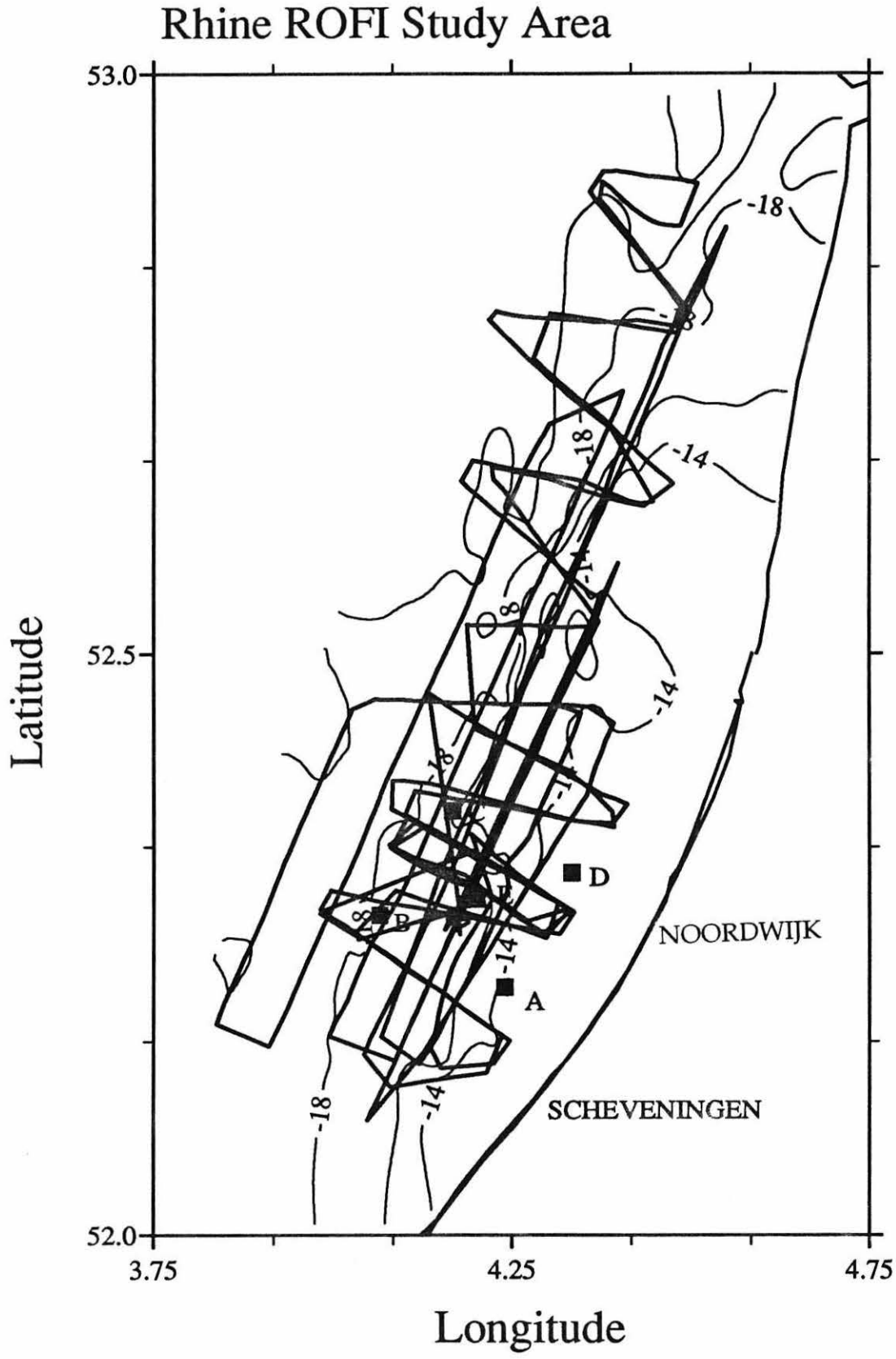

Figure 3.4 Rhine ROFI study area for 1992. Bathymetry in metres with mooring positions (■) and Searover tracks for the study period.

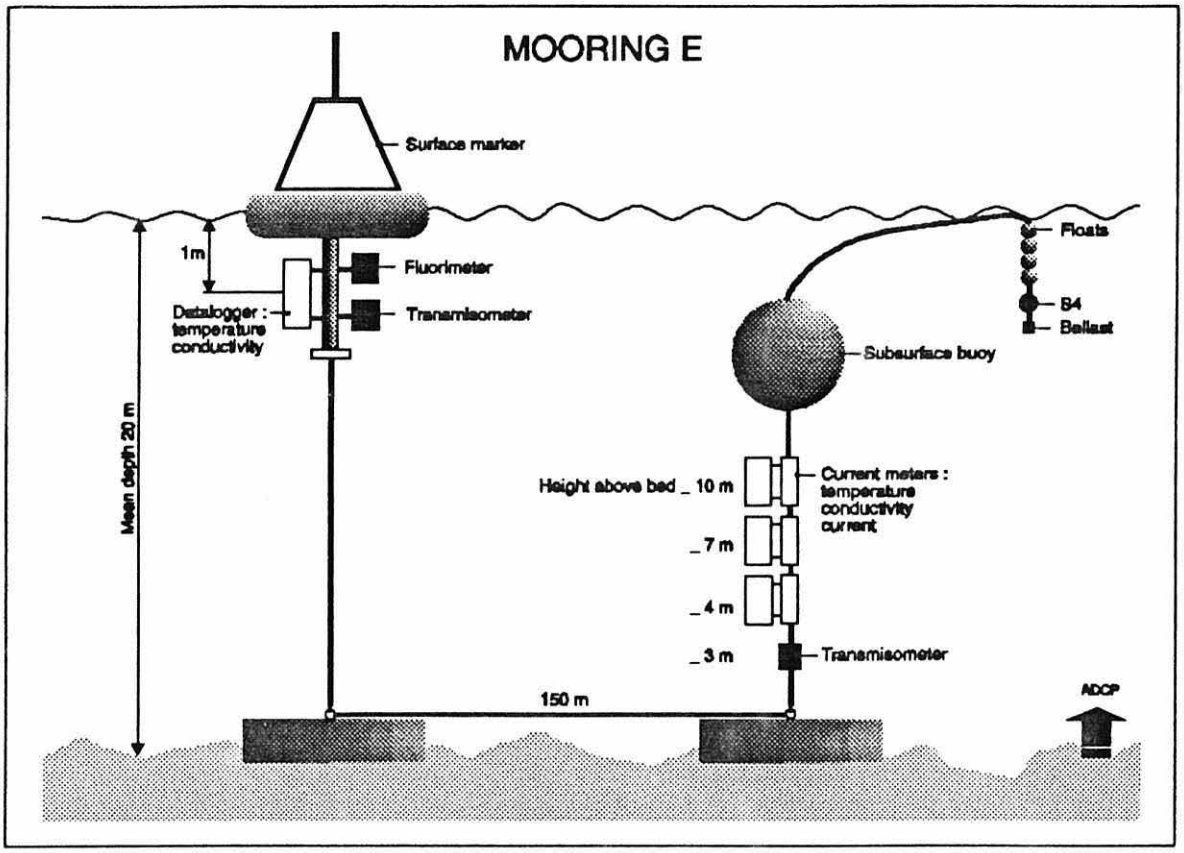

Figure 3.5 Schematic of the UCNW U-mooring used in 1992.

mounted ADCP on the Challenger was operated continuously.

3.2 Instrumentation.

During these studies it was possible to use some of the most advanced instruments available. This was, in part thanks to the co-operative nature of the project. Currents were measured throughout the water column, using Aanderaa and S4 current meters as well as bottom and hull-mounted ADCPs, while horizontal spatial coverage of surface currents was made possible by using HF radar (CODAR). Complementary measurements of the spatial water column structure were obtained with the aid of profiling and undulating CTDs.

3.2.1 Profiling CTD.

During both cruises vertical profiles of pressure, conductivity and temperature as well as optical beam transmittance and chlorophyll fluorescence were recorded using a Neil Brown Mk IIIb CTD equipped with auxiliary sensors. When lowered, the unit transmits data in real time to a micro-computer via a single conductor armoured cable. The pressure measurements are made by a high performance strain gauge bridge transducer, while the temperature is assessed with a platinum resistance sensor and the conductivity is obtained using a four-electrode conductivity cell. Salinity and σ_t were calculated using the international standard formulas for seawater (UNESCO, 1981). The specifications of the Neil Brown Mk IIIb CTD are listed in table 3.1.

Table 3.1 Specifications for individual sensors on the NBIS Mk IIIb CTD.

Sensor	range	accuracy	resolution	response time (ms)
Pressure (dbar)	0-320	±0.5	0.005	
Temperature (°C)	-3 to +32	±0.005	0.0005	200
Conductivity (mmho/cm)	1-65	±0.005	0.001	30

The CTD temperature sensor was calibrated against two independent temperature measurements, made using SIS RTM4002 reversing thermometers, with an accuracy of ±0.001 °C. The salinity measurements were calibrated by water samples taken during each profile; salinity of the samples was determined using a Guildline Autosal.The CTD calibration was performed by comparing CTD measurements of salinity and temperature against those observed. Plots of temperature and salinity differences against station number, indicated that no significant drift occurred during either of the cruises. The mean value correction were used, as shown in table 3.2.

Table 3.2 temperature and salinity calibrations

Experiment	Salinity (psu)	Temperature (°C)
1990	0.013 ± 0.005	-0.008 ± 0.005
1992	0.002 ± 0.003	-0.100 ± 0.03

3.2.2 Undulating CTD SEAROVER.

The undulating CTD used during the 1992 cruise, was the Seasonal and Regional Ocean Variability Explorer (SEAROVER). The SEAROVER is a modified version of the IOS Wormley SEASOAR, and was constructed by IFM Kiel. The main difference from the SEASOAR is that it carries a Meerestechnik Electronik (ME) CTD. The pressure is measured by a piezo resistive cell, conductivity by a seven pole conductivity cell and temperature by a PT 100 Platinum resistance thermometer. The

specifications of the above sensors are shown in table 3.3.

Table 3.3 Specification of SEAROVER sensors

Sensor	range	accuracy	resolution	response time (ms)
Pressure (dbar)	0-600	±0.5	0.5	20
Temperature (°C)	-2 to +40	±0.005	0.001	160
Conductivity (mS/cm)	5-55	±0.005	0.001	100

The calibrations of the SEAROVER were made by comparing the temperature and salinity against measurements of the Neil Brown CTD at the same depth, hence in the same water mass. The Neil Brown and ME values were then compared and the SEAROVER constants were modified, so that values of temperature and salinity were the same for the two instruments.

The advantage of using an undulating CTD is that of the rapid sampling of the water column, so that the observations will be more synoptic than in the case of the profiling CTD. The SEAROVER follows a saw-tooth-like track while the ship is moving. If the ship is cruising at a speed of 6 knots and the SEAROVER diving depth is about 20 m, the undulator will complete a full surface to surface cycle every 600 m, this is a vertical profile every 300 m.

3.2.3 HF radar CODAR.

HF radar has successfully been used in mapping surface currents since the 70's (*e.g.* Barrick *et al.*, 1977). The technique uses the radar backscatter from surface waves, at one specific frequency which enables the radar to "see" surface waves of a particular wavelength. The radar echo exhibits a Doppler shift due to the combined

effect of the phase velocity of the surface waves, and the surface currents. The phase velocity however, is known from linear wave theory and so the radial component of the surface currents can be calculated from the difference of observed and expected Doppler shift. As one station measures only the radial component of the currents, a second station is required to create a full vector field (fig. 3.6).

The system used in the Rhine ROFI 1990 experiment, was the IFM Hamburg CODAR, which has an operating wavelength of 10 m and senses waves with a wavelength of 5 m. It has a range of about 50 km, with a radial resolution of 3 km, an azimuthal resolution of ± 1.5°, a speed resolution of ± 3 cms^{-1} and an accuracy of ± 5 cms^{-1}. The original set up for the Rhine ROFI had one station in Gravenzande and the other 30 km away in Noordwijk. The data recorded consisted of a grid of 17 by 17 points, with a two-dimensional vector field integrated over 18 minutes and 28 km^2, and recorded every 30 minutes.

3.2.4 Current meter Temperature and Salinity calibration.

It is important to calibrate any instrument against an accurate standard and against each other, so that comparisons between different instruments can be made, without the uncertainty of the intrinsic differences in the instruments used. This is especially important in the study of frontal regions, where accurate measurements of the water column structure and horizontal density gradients are needed and inter-comparisons between moorings and spatial surveys are often carried out.

The technique used for the calibration of the instruments in the moorings was to attach the RCMs to the CTD , in a specially made calibration frame and to lower

the frame into a mixed layer where the instruments were left to simultaneously record the water column characteristics for at least 3 RCM sampling intervals. The data collected provided a direct calibration of temperature and salinity for all RCMs relative to each other and to the CTD. This procedure was carried out at deployment and recovery of each mooring.

The calibrations for salinity and temperature need slightly different approaches, as will be described next:

(i) Calibrations of the conductivity cell: Discrepancies in measurements made by the conductivity cell arise from small changes in the cell geometry so it is necessary to use a form factor, *ff*, to relate the conductivity measured by the cell to the *true* conductivity measured using the CTD (Aanderaa instruments, 1992). Hence,

$$C_{CTD} = ff \times C_{RCM} \qquad (3.1)$$

The conductivity measurements are calibrated by multiplying the mean value of the form factor calculated for each instrument.

(ii) Calibrations of temperature: The thermistor used on RCMs does not require a geometrical based calibration technique and can be calibrated simply by using the mean difference, ΔT, between the RCM and CTD recorded temperatures.

The main error in values for salinity and temperature given by the RCMs are

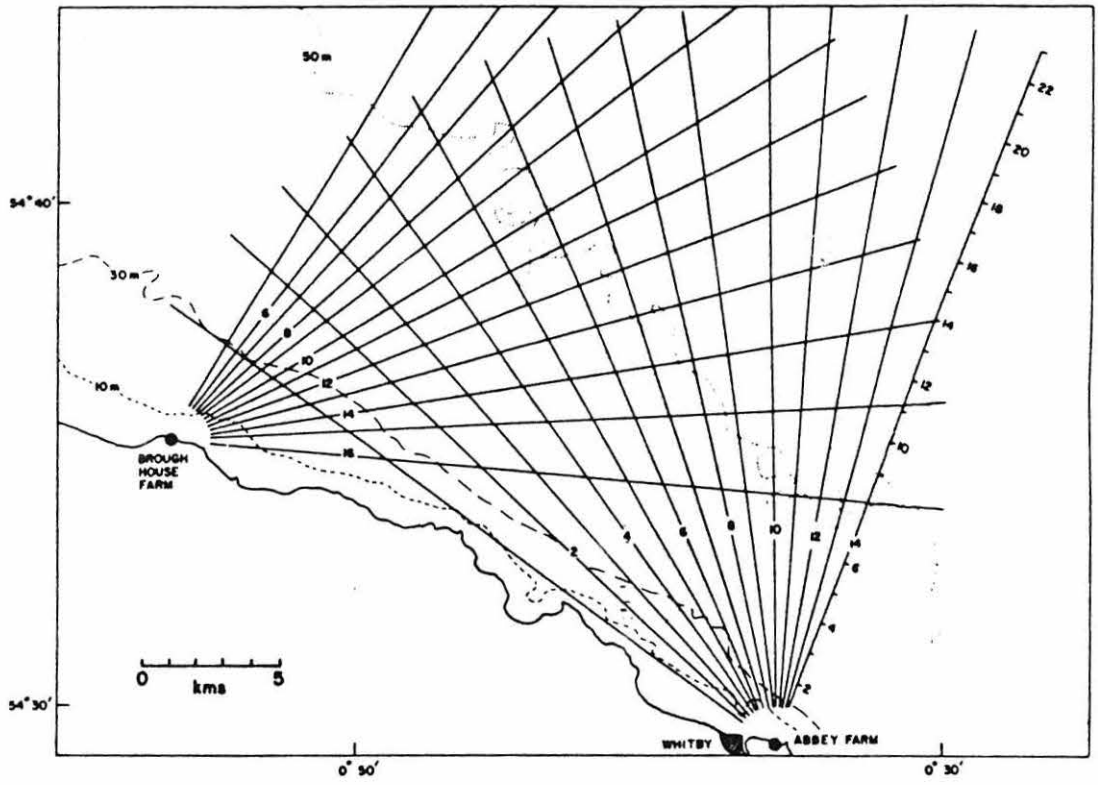

Figure 3.6 Schematic of how the HF radar generate the velocity field (from Prande, 1990).

due to the resolution of the recording system and the uncertainty in ΔT and *ff*. The combined error was of the order ± 0.05 °C in temperature and ± 0.07 psu in salinity. A summary of RCM temperature and salinity calibrations calculated for both deployments are given in tables 3.4 and 3.5.

Table 3.3 Current meter details for 1990 survey

Mooring	Position	Height above bed (m)	Current meter No	*ff*	ΔT	Comments
A	52.15° N 4.10° E	Toroid	8240	0.9972	-0.29	
		12	3257	fail	fail	
		8	3261	1.001	0.11	
		4	9652	fail	0.07	
B	52.15° N 4.07° E	Toroid	5228	0.9675	0.12	
		11	9680	Not fitted	0.11	
		7	9634	Not fitted	-0.02	
		3	3308	1.0740	0.05	
C	52.28°N 4.22° E	Toroid	6275	1.0308	0.13	Mooring moved to 52.20° N 4.15 ° E on the 1/10/90
		11	9643	Not fitted	0.15	
		7	6275	1.0308	0.13	
		3	9643	0.9723	0.10	
D	52.17°N 4.25° E	Toroid	6941			No data
		12	9632	1.0001	0.22	
		8	9650	Not fitted	0.20	
		4	7063	0.9726	0.07	

Table 3.4 Current meter details for 1992 survey

Mooring	Position	Height above bed (m)	Current meter No	*ff*	ΔT	Comments
A	52.21° N 4.23° E	Surface-1	05451264	Not fitted	Not fitted	S4 current meter
		Toroid	9903	0.9878	0.15	
		10	9909	1.0210	-0.22	No Velocity
		7	8247	0.9999	0.08	
		4	9419	1.0002	0.11	
B	52.28° N 4.07° E	Surface-1	05451261	Not fitted	Not fitted	Lost
		Toroid	9904	fail	0.10	
		10	9631	1.0403	0.16	
		7	7570	1.1223	0.25	
		4	9632	0.9788	-0.18	Velocities until day 256
C	52.37° N 4.17° E	Surface-1	05111113	Not fitted	Not fitted	S4
		Toroid	9418	0.9888	-0.05	
		10	8240	fail	fail	
		7	8249	fail	fail	
		4	6152	0.9702	0.13	No velocity
D	52.31° N 4.32° E	Surface-1	05111119	Not fitted	Not fitted	S4
		Toroid	9608	0.9765	0.17	
		10	9911	1.1167	0.23	
		7	6941	1.0985	0.19	
		4	5228	0.9715	-0.12	
E	52.28° N 4.23° E	Toroid	10525	1.1133	-0.10	
		10	10665	1.1739	0.25	
		7	10666	0.9762	0.09	
		4	9069	0.9978	0.08	No velocity

To obtain speed and direction the compass was previously calibrated by

Research Vessel Services, Barry. The accuracy to which the speed was measured is given by the manufacturer (Aanderaa,1992) as either ± 1 cms^{-1} or ± 2% of the speed, which ever is grater. The minimum measurable speed using an Aanderaa Recording Current Meter (RCM) is 1.1 to 1.5 cms^{-1}. For the velocity range measured in the Rhine ROFI the error in the compass was ± 5°.

The meters are balanced so that they are oriented vertically in the water column. The action of drag on the line and the subsurface buoyancy acts to deflect the line. The gimble mounting of the instrument allows an angle deflection of 27°, after which the instrument will no longer be oriented to the vertical and velocity measurements will be contaminated (Rippeth, 1993). Sharples (1992) found that the maximum tilt angle in Liverpool Bay, where velocities are stronger than those expected in the Rhine ROFI, was only 17°, so no problems of this kind should be expected in the present data set.

3.2.5 Acoustic Doppler Current meter Profiler (ADCP).

In recent years the ADCP has become an essential instrument for the oceanographer. It works by measuring the frequency of the backscattered acoustic energy from moving particles suspended in the water column, turbulence and density microstructure (RDI, 1986). The instrument transmits an acoustic pulse or ping at an oblique angle (usually 30° from the vertical) and the radial velocity relative to the transducer is obtained in small depth cells or "bins" by looking at the Doppler shift of the backscattered pulse. So, as in the case of the CODAR, to be able to obtain a velocity vector the instrument needs an array of at least two transducers. The ADCP has been used to measure velocities in two different ways: one is to measure velocities of part of the water column, while moored in one

point, as in the case of the bottom-mounted ADCPs and the other is to measure velocities while moving at a known speed, as in the of ship mounted ADCPs.

Although the best know ADCP is that developed by Rowe and Dinas Instruments (RDI), it is not the only one available. The Proudman Oceanographic Laboratory (POL) have developed their own system over the last few years. During the 1992 campaign both systems were used: a ship mounted a 150 kHz RDI ADCP onboard the Challenger and a 1 MHz POL bottom mounted ADCPs at each of the moorings A to D. The RDI instrument uses an array of four transducers to generate the three-dimensional vector field, although the vertical velocity is generally below the noise threshold. The POL system uses a bi-transducer array to resolve the horizontal components of velocity. The general characteristics of both systems are shown in table 3.6.

Table 3.6 ADCP characteristics

	Challenger RDI	Bottom mounted POL
Frequency	153.6 kHz	1 MHz
Sampling interval (min)	6	10
Bin size (m)	2	1.4
First bin (m)	6	3.9
Ping rate (Hz)	2	0.6
Short term error (cms^{-1})	2	1
Transducer missaligment (°)	1.5	N/A
Scaling factor	1.02	N/A

In the case of the bottom-mounted ADCP the calculation of the velocity

field is straightforward due to the fact that the instrument is static, while in the case of the ship mounted ADCP the instrument is mounted on a moving platform, so to obtain the absolute velocity of the water it is necessary to know the ship's velocity. In shallow waters, as it is the case in the present study, a separate acoustic pulse is used to determine the velocity of the ship relative to the bottom (Bottom tracking). The absolute velocity of the water is then achieved by subtracting this bottom velocity from the ADCP estimates of water velocity relative to the ship.

3.2.5.1 Theory of operation

The short term error in the ADCP is dependant on the number of pings in an ensemble, the depth bin and the frequency of the instrument. The formulae given by RDI (1986) to calculate the short term error is as follows:

$$\sigma_v = \frac{1.5\sqrt{2}\,c^2}{16\pi\, F D \tan\gamma \sqrt{N}} = \frac{1.6 \times 10^5}{f D \sqrt{N}} \qquad (3.2)$$

where c is the speed of sound, F the transmitting frequency (Hz), D the bin length (m), γ the inclination of the transducer from the vertical (30°) and N the number of pings transmitted during an averaging ensemble. A summary of the characteristics for the shipboard and bottom mounted ADCPs, including the short time error, are shown in table 3.6. The resolution reported from POL ADCPs is better than 4 cms^{-1} in speed and less than 10° in direction.

Errors in calculating the absolute velocities in ship-mounted ADCPs, arise from rotation movements (*e.g.* pitch and roll) and sensor head misalignment.

Errors due to pitch and roll for a vessel like the Challenger are negligible except under extremely rough seas (Lwiza, *et al.*, 1990). To test the system misalignment, comparisons between the Doppler measurements of the ship velocity against those estimated from navigation data, should be carried out. The correcting procedure has been suggested by Joyce (1989) and Pollard and Read (1989), as a rotation and scaling of the ADCP estimates of velocity as:

$$\begin{aligned} u_s &= A(u_A \cos\phi + v_A \sin\phi) \\ v_s &= A(u_A \cos\phi + v_A \sin\phi) \end{aligned} \qquad (3.3)$$

where u_s is the ship's velocity computed from GPS navigation data, u_A is the velocity of the ship measured by the ADCP, A is the scaling factor for the ADCP velocities to obtain the true velocities, and ϕ is the misalignment geometrical angle by which the Doppler transducers are rotated on installation. The corrections for the Challenger ADCP, as determined during the 1992 cruise, are a misalignment of $-1.5° \pm 0.5°$ and a scaling factor of 1.02 ± 0.01.

CHAPTER FOUR

DATA ANALYSIS

In this chapter we first review the basic analysis methods used to achieve the separation of the currents into their components and then present the essential ideas of Empirical Orthogonal Function analysis which we shall utilise in chapter 9.

4.1 Current analysis.

The measured currents are the result of three different forcing mechanisms operating together. In the Rhine ROFI, as for much of the northwest European shelf, the tide accounts for around 90% of the variance of measured currents, the rest being a combination of density driven flows and wind forcing (Durazo, 1993). The tidal currents can be extracted by the use of simple harmonic analysis providing that the time series is long enough, while wind driven velocities might be separated to first order by linear regression.

4.1.1. Harmonic Analysis.

The harmonic analysis is based on the idea that a current record can be interpreted as a Fourier series, where frequencies are determine from the astronomical arguments (Godin,1972). The time series of a single velocity component is written as:

$$u(t) = u_0 + \sum_{i=1}^{N} H_i \cos(\omega_i t - \theta_i)$$
$$= u_0 + \sum_{i=1}^{N} [b_i \cos\omega_i t + c_i \sin\omega_i t] \qquad (4.1)$$

where

$$H_i = \left[b_i^2 + c_i^2 \right]^{\frac{1}{2}}$$
$$\theta_i = \tan^{-1} \frac{c_i}{b_i} \qquad (4.2)$$

u_0, is the mean velocity over the observation period, H_i, ω_i and θ_i are the amplitude, frequency and phase lag of the i-th tidal constituent respectively. The number of harmonics N, is dependent on the length of the time series according to the Rayleigh criterion. To be able to resolve neighbouring tidal constituents, we require they should be separated by at least a complete period over the data span (Pugh, 1987). For example, to separate M_2 from S_2, we need a record of n cycles where

$$\mathbf{n\ M_2\ tidal\ cycles\ =\ (n+1)\ S_2 tidal\ cycles}$$

or

$$\mathbf{n\ 12.42\ =\ (n+1)\ 12.0\ \ hours}$$

solving for n will give us a minimum data length of 14.77 days to satisfactorily resolve the two tidal constituents independently. For the data sets with which we are concerned here, the records are of at least 15 days duration so that M_2 and S_2 can be separated in addition to O_1, K_1, N_2 and M_4.

To further investigate the structure of the tidal currents it is advantageous to

use the clockwise and anticlockwise rotary components. This form of counter rotating vectors is basic to the understanding the bottom Ekman layer dynamics and to calculate the ellipse characteristics, as explained in chapter 6. The rotary components can be calculate following Godin (1972) as:

$$
\begin{aligned}
Q_c &= \frac{1}{2}\left[u^2 + v^2 - 2uv\sin(\theta_v - \theta_u)\right]^{\frac{1}{2}} \\
Q_{ac} &= \frac{1}{2}\left[u^2 + v^2 + 2uv\sin(\theta_v - \theta_u)\right]^{\frac{1}{2}} \\
\theta_c &= \tan^{-1}\left[\frac{u\sin\theta_u + v\cos\theta_v}{u\cos\theta_u - v\sin\theta_v}\right] \\
\theta_{ac} &= \tan^{-1}\left[\frac{-u\sin\theta_u + v\cos_v}{u\cos\theta_u + v\sin\theta_v}\right]
\end{aligned}
\qquad (4.3)
$$

where u,v θ_u, θ_v are the amplitudes and phases for the east-west and north-south components of velocity respectively and Q_c, Q_{ac}, θ_c, θ_{ac} are the amplitudes and phases of the clockwise and anticlockwise rotary components respectively. The tidal ellipses are then calculated as:

$$
\begin{aligned}
M &= Q_{ac} + Q_c \\
m &= Q_{ac} - Q_c \\
\epsilon &= \frac{m}{M} \\
\Theta &= -\frac{1}{2}(\theta_{ac} - \theta_c) \\
\Phi &= \frac{1}{2}(\theta ac + \theta c)
\end{aligned}
\qquad (4.4)
$$

M and m are the semi-major and semi-minor axes respectively, while Θ and Φ are the phase and orientation of the semi-major axis. The quantity ε is the ellipticity, its value ranges between 1 (anti-clockwise rotation) and -1 (clockwise rotation), with rectilinear currents when $\varepsilon = 0$.

It is important to note that to be able to apply the harmonic analysis as

discussed above, it is necessary to have a time series of some variable for a single point. This is straightforward for moored and CODAR data, because the moored current meters are generating a time series at the same point, while the radar data has a more less regular coverage over space and time, although some grid points might be lost at times due to the sea state.

There are obvious problems, in applying this analysis, however when the observations are carried out from a moving platform (*i.e.* ship) and the data is recorded at different locations at different times. To overcome this problem, it is necessary to follow a survey strategy similar to that described by Simpson *et al.* (1990) and Lwiza *et al.* (1991), where the ship sails backward and forward on a straight line, so that the ADCP samples over the same point several times. In this way a time series can be created for that point, in a similar manner as that explained by Lwiza (1990). In order to remove the tidal signal, the duration of the time series must be at least one tidal cycle long (12.42 for M2) and it should contain at least 6 samples which should be well spaced over time.

4.1.1.1 Moving average harmonic analysis.

Recent studies on shelf seas (Maas and van Haren 1987, van der Giessen *et al.*, 1990 and Lwiza *et al.*, 1991) have indicated that the presence of stratification modifies the tidal velocity profiles. To study this effect a special case of the harmonic analysis has been applied to the mooring and CODAR time series. The analysis consisted in applying a semidiurnal (M_2) harmonic fit to short intervals of the time series (25 hours) in the form

$$\vec{U}(t_i) = (U(t_i),V(t_i)) = \frac{1}{2T}\int_{t_i}^{t_i+T} (u(t),v(t))\, e^{-i\omega t}\, dt \qquad (4.5)$$

where $U(t_i)$ and $V(t_i)$ will be the Fourier estimates of u(t) and v(t) for the i-th data value over a period 2T equal to 2 M2 tidal cycles (~25 hours).

This technique allows us to observe rapid changes in the semidiurnal constituents of tidal velocities and, therefore, to observe the modification in tidal dynamics due to stratification, as will be discussed in chapter 6.

4.1.2 Residual currents.

The residual currents were calculated simply by subtracting the tidal constituents of the currents from the measured velocities and then, to eliminate any effect from remaining tidal components, the velocities were filtered using a 19 hours Doodson filter (Pugh, 1987), with a frequency response as shown in figure 4.1.

As discussed at the beginning of this chapter, the residual currents are composed basically of density and wind driven currents. In order to estimate the wind effect at each level in the water column, in chapter 7 we follow Prandle and Matthews (1990) and express the residual velocities as a scaled and rotated function of the wind velocity and a steady non-wind-driven component, *i.e.*,

$$U_r(t) - U_0 = a\,W(t) \qquad (4.6)$$

where $U_r=u_r+iv_r$ is the velocity residual, $U_0=u_0+iv_0$ is the steady non wind-forced residual and $a=|a|e^{-i\theta}$ is a complex coefficient with scaling factor $|a|$ and veering

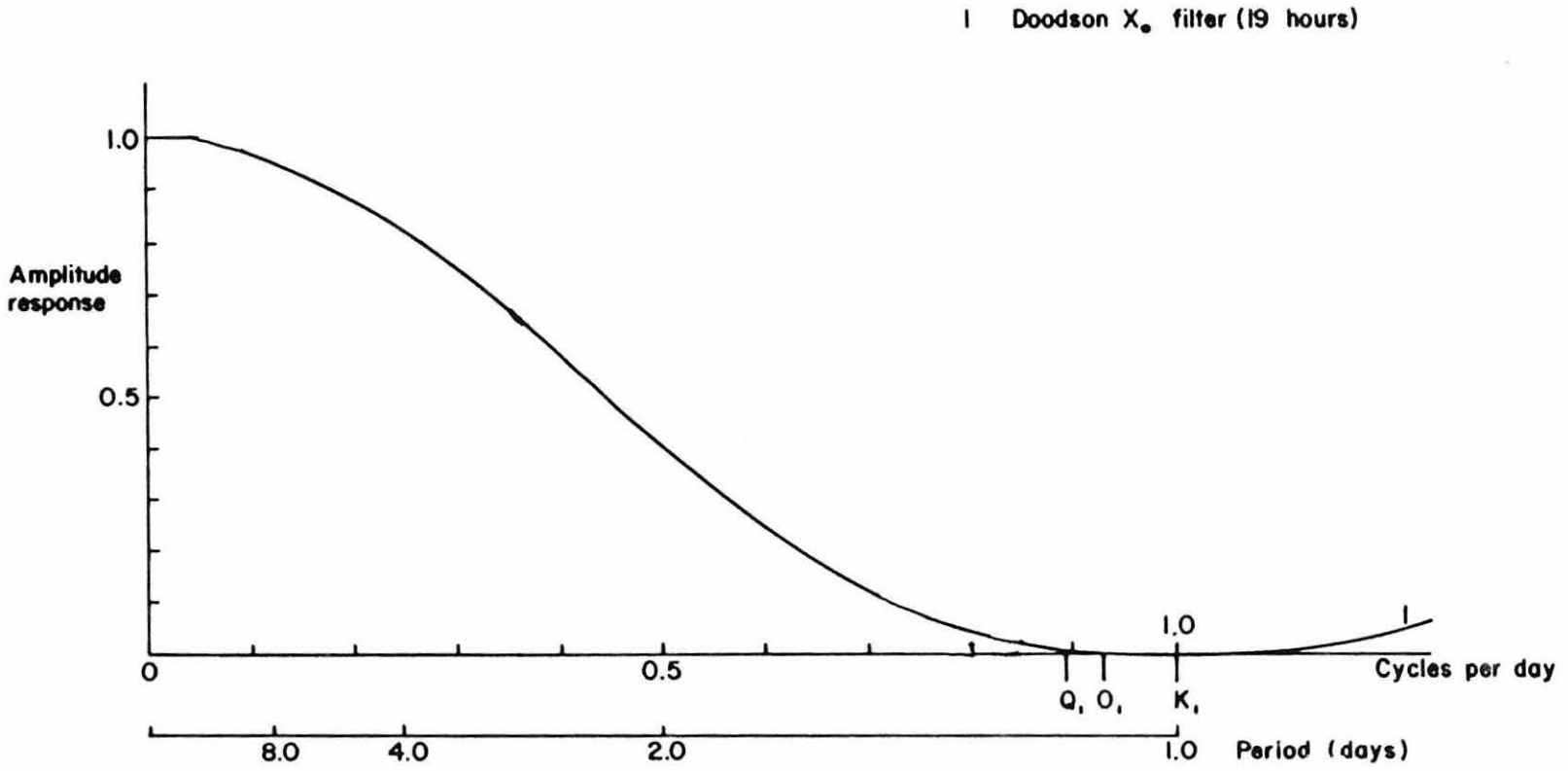

Figure 4.1 Characteristics of the 19 hour Doodson filter. Reproduced from Pugh (1987, page 418).

angle α of the current relative to the wind and $W=W_x+iW_y$ is the wind velocity. Equation (4.6) can be re written as

$$\begin{aligned} u_r &= u_0 + a_{11} W_x + a_{12} W_y \\ v_r &= v_0 + a_{21} W_x + a_{22} W_y \end{aligned} \qquad (4.7)$$

where $a_{11}=a\cos\theta=a_{22}$ and $a_{21}=a\sin\theta=-a_{12}$.

Values of non-wind-driven residuals and the a-coefficients were simultaneously obtained by a complex least-squares regression of wind and current velocities after both have been for filtered in the same way consistence.

4.2. Empirical Orthogonal Functions (EOF).

The Empirical Orthogonal Functions (EOF) analysis has become an important mathematical tool in the analysis of meteorological and oceanographical data. This technique has been used successfully for example in the study of frontal dynamics (Ou *et. al.*, 1988, Lagerloeff and Berstein, 1998 and Paden *et. al.*, 1991). The value of the technique is that it provides a unique decomposition of a space-time data set into two to sets of functions: one set over space and the other time, where the elements of each function are orthogonal to each other (Preisendorfer *et. al.*, 1981).

4.2.1. The analysis.

If we have a quantity A(x,t) it can be expressed as a matrix A_{mn} with dimensions M x N, where M is the number of spatially distributed points and N is the number of observations over time. The EOFs are traditionally calculated by

removing the time-average mean at each location so that the covariance matrix (C_{xy}), of dimension M x M, can be calculated:

$$A'(x,t) = A(x,t) - \frac{1}{N}\sum_{n=1}^{N} A(x,t_n) \tag{4.8}$$

$$C_{xy} = \frac{1}{N}\sum_{n=1}^{N} A'(x,t_n)\, A'(y,t_n) \tag{4.9}$$

where $A'(y,t_n)$ is the transpose of $A'(x,t_n)$.

The eigenvalues and eigenvectors are then found by solving

$$\lambda_i B_i = B_i C \tag{4.10}$$

where B_i is the dimensionless eigenvector forming the ith row of the matrix B and λ_i is the ith mode eigenvalue. The sum of the eigenvalues should be equal to the sum of the diagonal terms of the covariance matrix.

The data used to form the covariance matrix can be recovered by a linear combination of the eigenvectors B_i:

$$T'(x,t) = \sum_{n=1}^{N} a_n(t)\, B_n(x) \tag{4.11}$$

with modal amplitude $a_n(t)$ obtained by projecting the data onto each eigenvector

$$a_n(t) = \sum_{m=1}^{M} A'(x_m,t) B_n(x_m) \tag{4.12}$$

In this way the physical field A(x,t) has been solved into a set of orthogonal time series a(t) and orthogonal space series B(x). Frequently, most of the variability can be expressed in the first few modes, which then will be compared to other data fields to allow some physical interpretation of this statistical method (Davis, 1976). This method has been used in chapter 9 to relate the spatial survey with the temporal variability of the water column.

CHAPTER FIVE

DENSITY FIELD AND STRATIFICATION IN THE RHINE ROFI

5.1. Introduction

In this chapter we shall examine the space-time variation of stratification in the Rhine ROFI on the basis of the observations undertaken in the present study. These new results add considerably to the previous databases and provide, for the first time, both time series of water column stability at fixed points and rapid spatial surveys of stratification.

As explained in chapter 3 the observations were made during two major ship campaigns, one in September-October 1990 and the other in September 1992. Both experiments were planned so that there was at least one semi-monthly tidal cycle during the period of observations, as described in chapter 3. The main difference between the two experiments was the difference in meteorological conditions. In the 1990 experiment the windstress reinforced the contrast in stirring over the spring-neaps cycle; periods of strong winds coincided with the periods of spring tides, while light winds at neaps resulted in very low stirring (when strong stratification developed). In the 1992 experiment there were strong winds much of the time and the level of stratification was mainly controlled by the levels of wind stirring.

5.2. September-October 1990 experiment.

5.2.1. Time series of water column characteristics

Examples of the time series of salinity and temperature recorded at mooring A at the surface and at 12 meters deep are shown in figures 5.1 and 5.2. From the salinity record it can be seen that the near-bottom water (fig. 5.1b) has a more or less constant value of ~33 psu over the entire period of observations while the surface salinity (fig. 5.1a) is very variable over most of the record, with strong semidiurnal changes in salinity of up to 5 psu. The surface and bottom temperatures (fig. 5.2) show a decreasing trend, with temperatures falling from 16.2°C to 15 °C over the 24 days of observations, which is evidence of the strong surface cooling typical which occurs at this time of the year in the North Sea. The surface temperature also exhibits some semi-diurnal variability though it is less pronounce than in the case of salinity.

Stratification time series, shown as the difference between bottom and surface parameters are presented in figure 5.3. As expected in this area the density stratification is basically controlled by haline effects (de Ruijter *et al.*, 1992). The haline and density stratification clearly indicate two periods of strong stratification (days 269 to 277 and 285 to 290), with maximum stratification $\Delta\rho$=8 kgm^{-3}, equivalent to a potential energy anomaly ϕ=140 Jm^{-3}, separated by a period of almost complete mixing. The most striking feature of this data set is the strong semi-diurnal variability in stratification, which has an amplitude comparable to that of the mean stratification. From the plot of thermal stratification (fig. 5.3a) it is interesting to note that during the first period of observation the water column was thermally unstable, due to the strong cooling of the surface, while during the second period of stratification it became thermally stable. This period of thermal stability may be due to the fact that

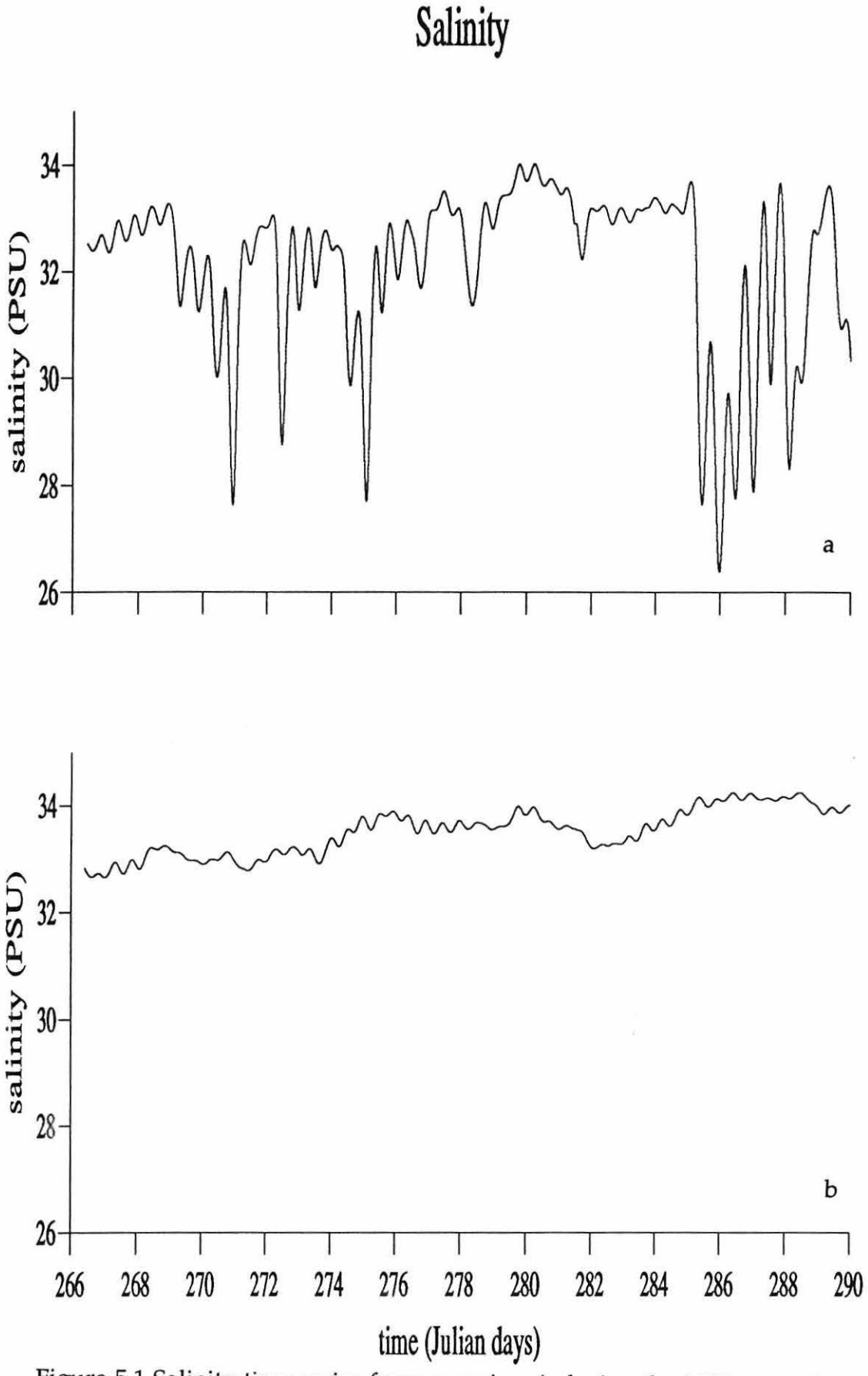

Figure 5.1 Salinity time series from mooring A during the 1990 campaign; a) surface, b) bottom.

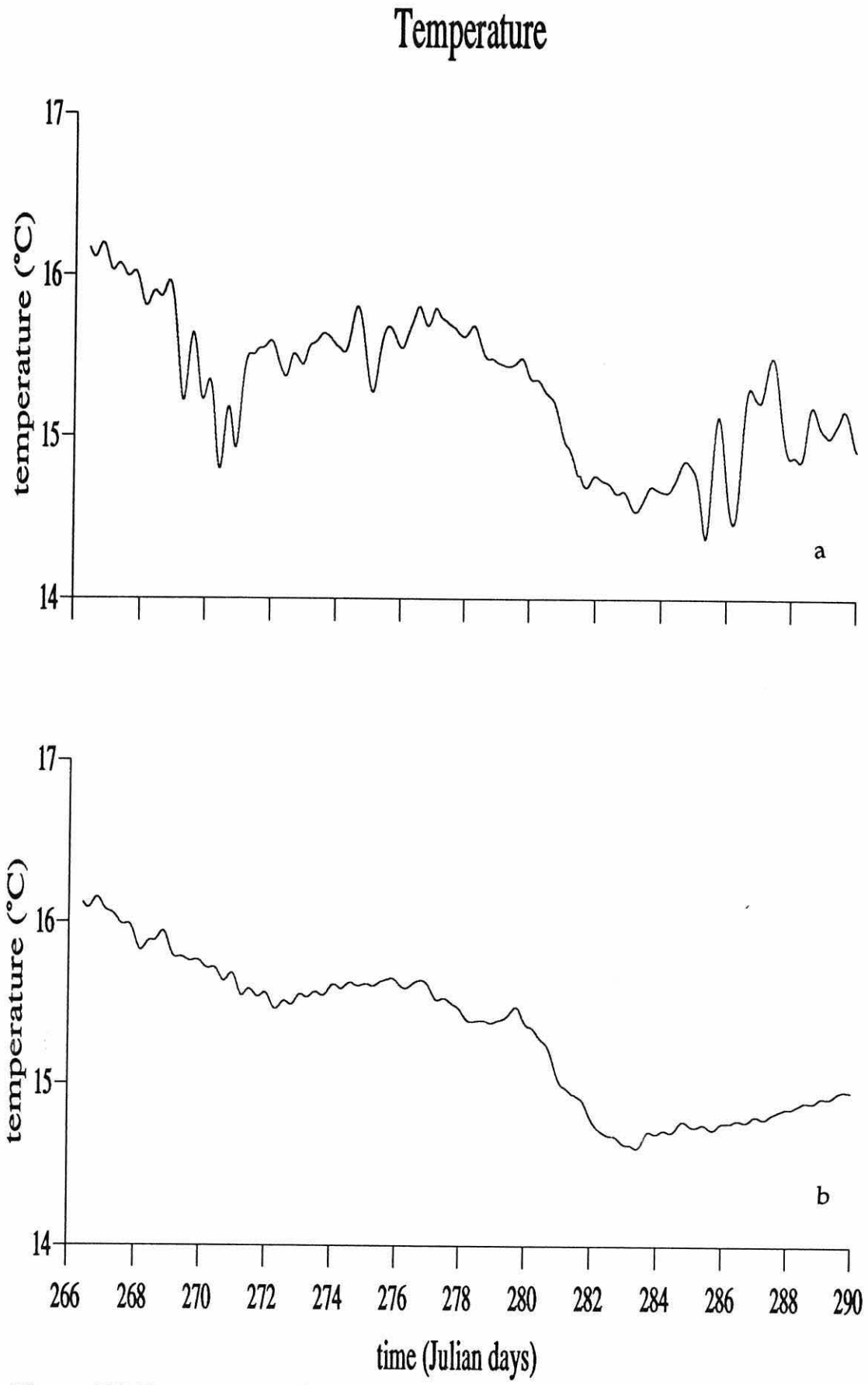

Figure 5.2 Temperature time series from mooring A during the 1990 campaign; a) surface, b) bottom.

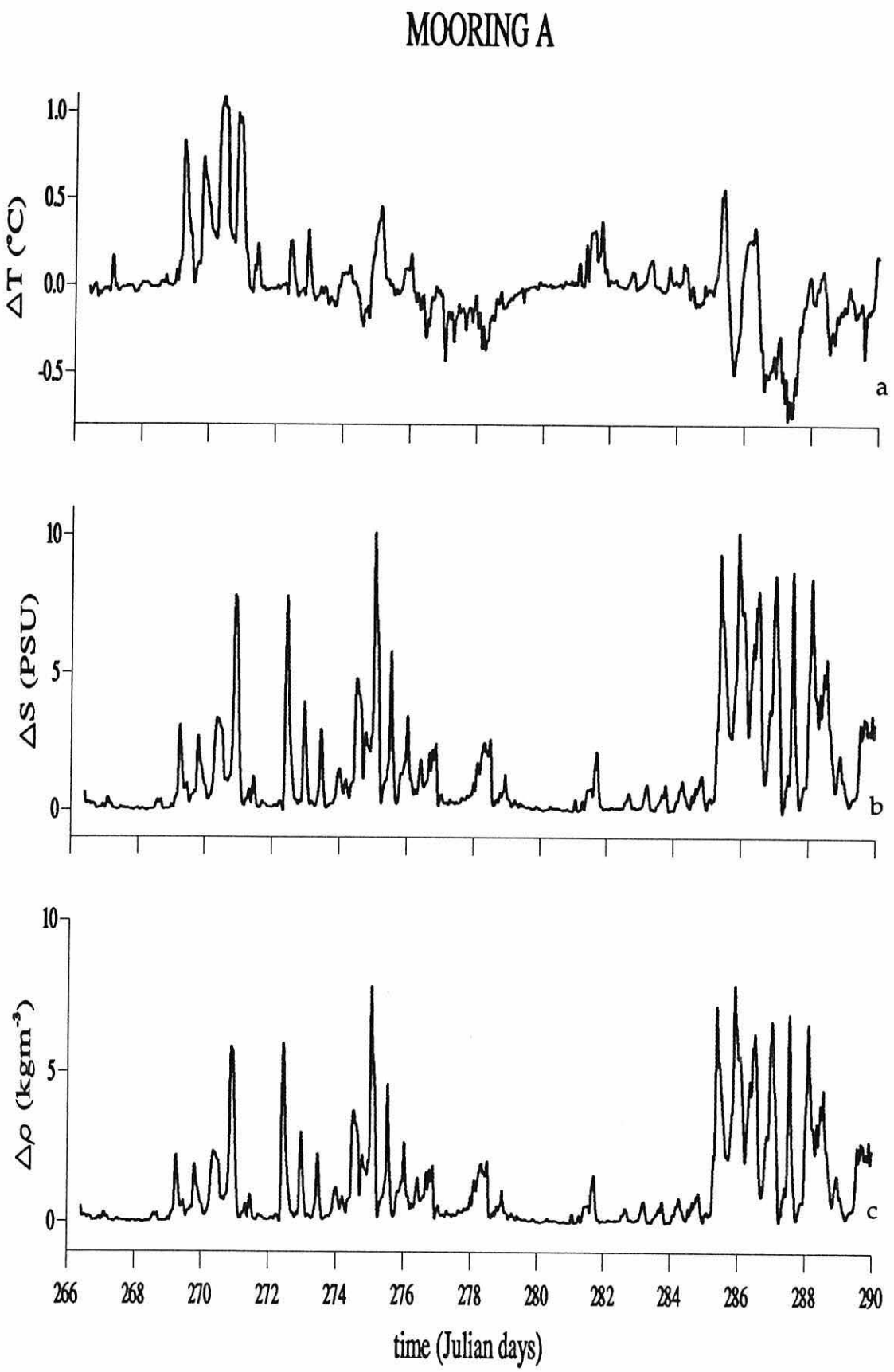

Figure 5.3 time series of bottom - surface characteristics for mooring A during the 1990 campaign. a) temperature, b) salinity and c) density.

from day 284 there is marked surface heating, as is indicated in fig 5.2.

The influence of mixing processes on stratification becomes evident when we plot the stratification time series alongside the possible stirring factors (fig. 5.4). The predicted tidal stirring cycle, evident in the tidal current (fig. 5.4a), was fortuitously augmented by wind- stress (fig. 5.4b) which acted to re-enforce vertical mixing during the central springs period (days 277-285) in contrast with the previous and subsequent neaps periods, when wind stirring was slight. These large changes in mixing are reflected in the water column stability as seen in the bottom-surface salinity difference (fig. 5.4c). The behaviour of the fortnightly stratification discussed earlier could the be explained as follows: the strong vertical mixing due to the combination of high wind and tidal stirring during the neap period (days 277 to 285) does not allow stratification to develop, while during the previous and later neaps period, when the wind-stirring was also slight, strong stratification is able to develop with values of $\Delta S>5$. An important feature to note is that during the two periods of stratification, we were able to observe strong semidiurnal oscillations in stratification.

Further strong evidence of the action of stirring and straining processes is apparent in the optical attenuation time series (fig. 5.4d). During springs when the stirring is strong, surface and bottom values are similar (~3 m^{-1}) and quarter diurnal variability is observed. Marked semidiurnal variability of the surface beam attenuance is observed during the periods of low turbulence, when the bottom attenuation reaches its minimum (0.8 m^{-1}).

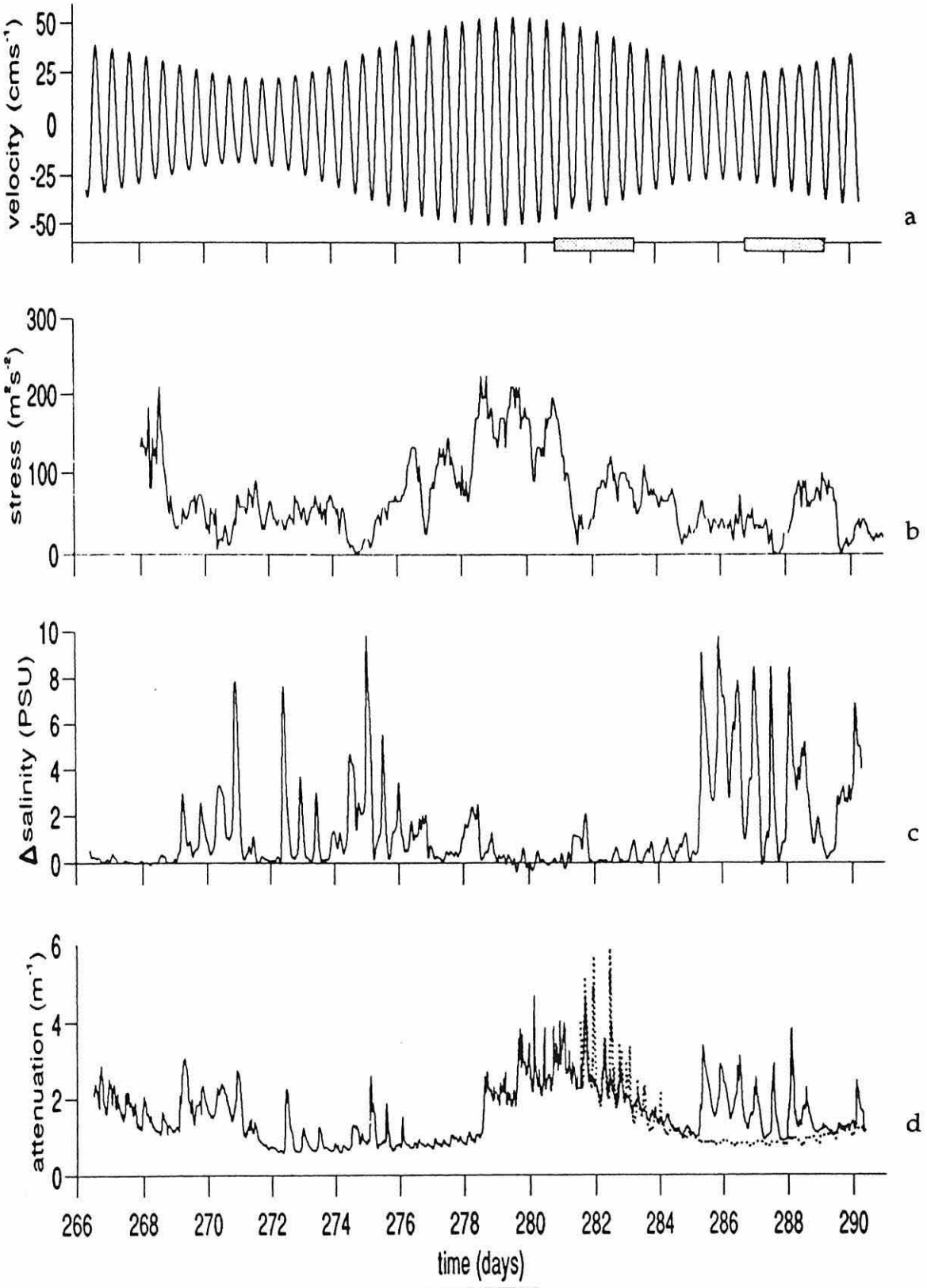

Figure 5.4 Mooring A time series: A) east-west tidal currents 4 m above the bed; b) windstress from the Hook of Holland; c) salinity difference between 1 and 16 below the surface; d) transmittance black line 1m deep dotted line 16 m deep.

5.2.2 Spatial distribution of water column structure.

From the surface distribution of properties shown in figures 5.5 and 5.6, we can observe that the horizontal changes of sea surface temperature (SST) (fig 5.5) are rather small (0.5°C) and variable in space, and do not appear to be related to the Rhine outflow either after springs (fig. 5.5a) or after neaps (fig 5.5b).

The change in density gradients is, therefore, mainly determined by the horizontal salinity distribution (fig. 5.6). The surface haline distribution exhibits a salinity deficit of up to 4 psu, confined to the coast in a narrow band of approximately 30 km in width. In consequence, horizontal density gradients are mainly in the cross-shore direction. The post-springs (fig. 5.6a) and post neaps (fig. 5.6b) surface salinities show a very similar distribution; the only difference is that in the post-neaps survey the isohalines have been displaced about 5 km off-shore relative to the post-springs position.

The strong influence of the Rhine as a nutrient source, as discussed in chapter 1, may be appreciated from the nitrate distribution (fig. 5.7). The nitrate contours closely follow those of the salinity behaviour, with high values up to 34 μM near the Rhine source and decreasing to low levels (< 2 μM) off-shore. A regression of nitrate on salinity shows a high degree of inverse correlation (R^2=0.78 with 36 degrees of freedom) pointing to the Rhine as the main source of nutrients.

The nature of the adjustment of the density field which occurs after a reduction in stirring is apparent from the repeated sections along the Noordwijk line (figs. 5.8 to 5.10). At post-springs when the vertical mixing is high there is complete

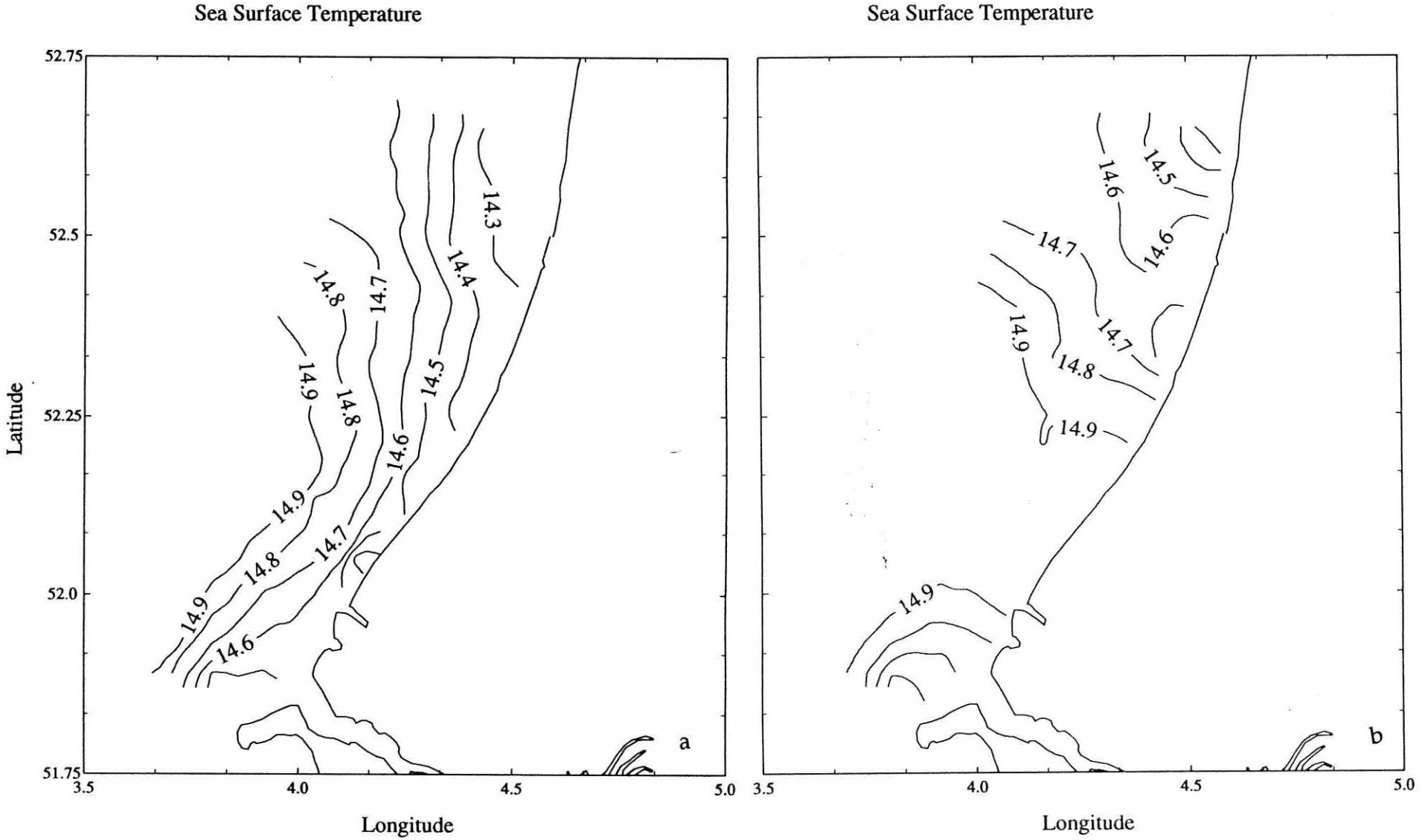

Figure 5.5 Sea surface temperature distribution for post-springs (a) and post-neaps (b).

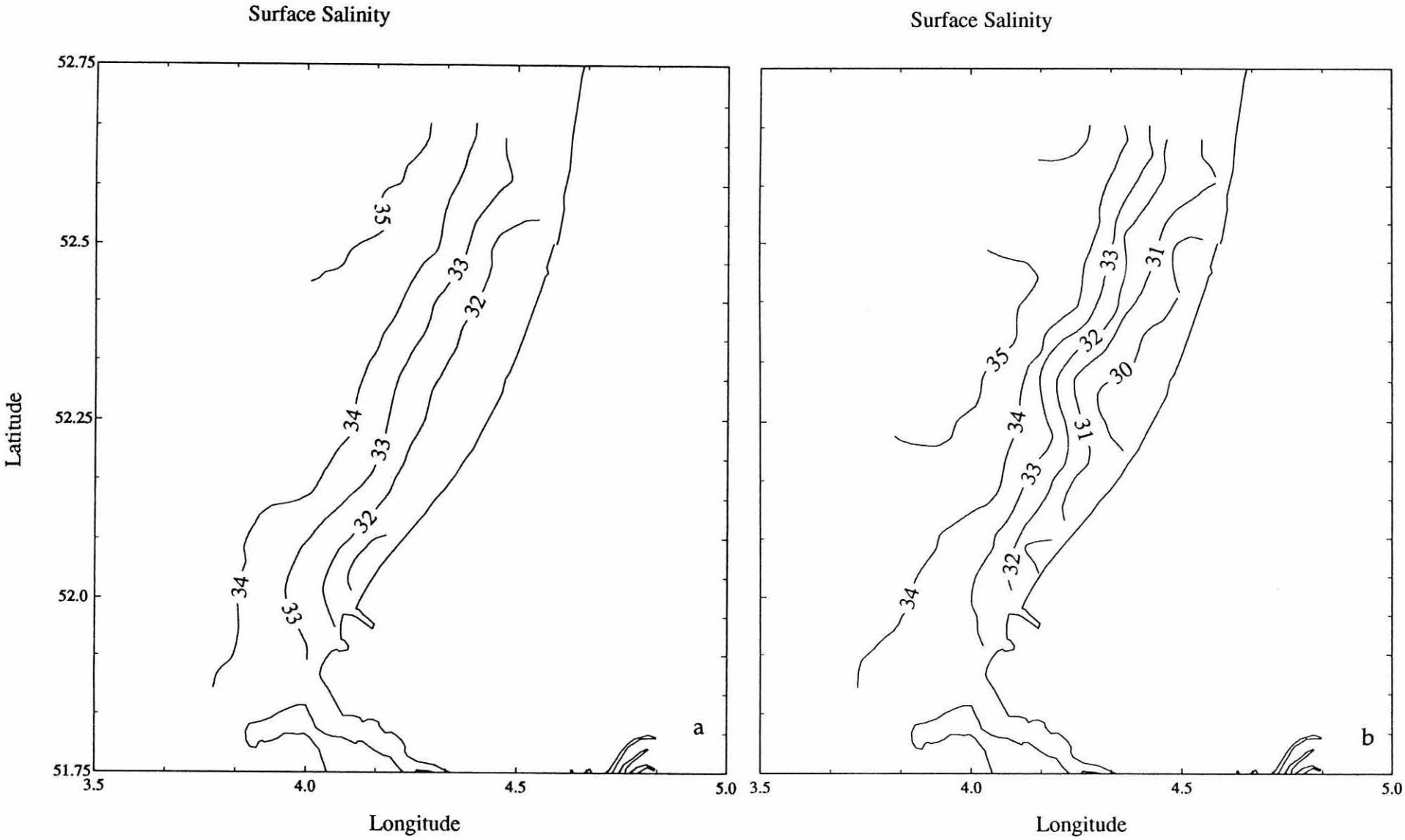

Figure 5.6 Surface salinity distribution for post-springs (a) and post-neaps (b).

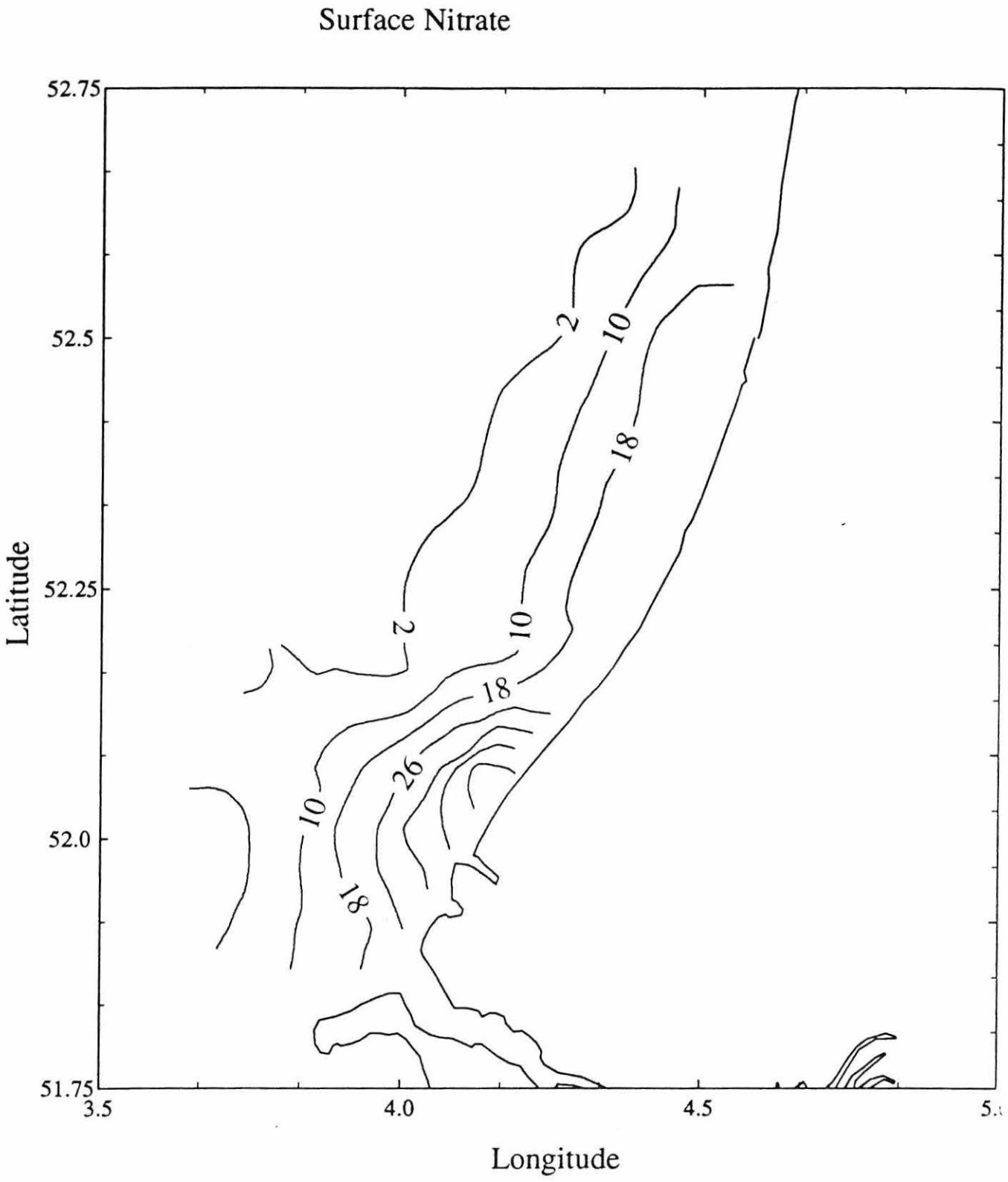

Figure 5.7 Surface Nitrate for the entire observation period.

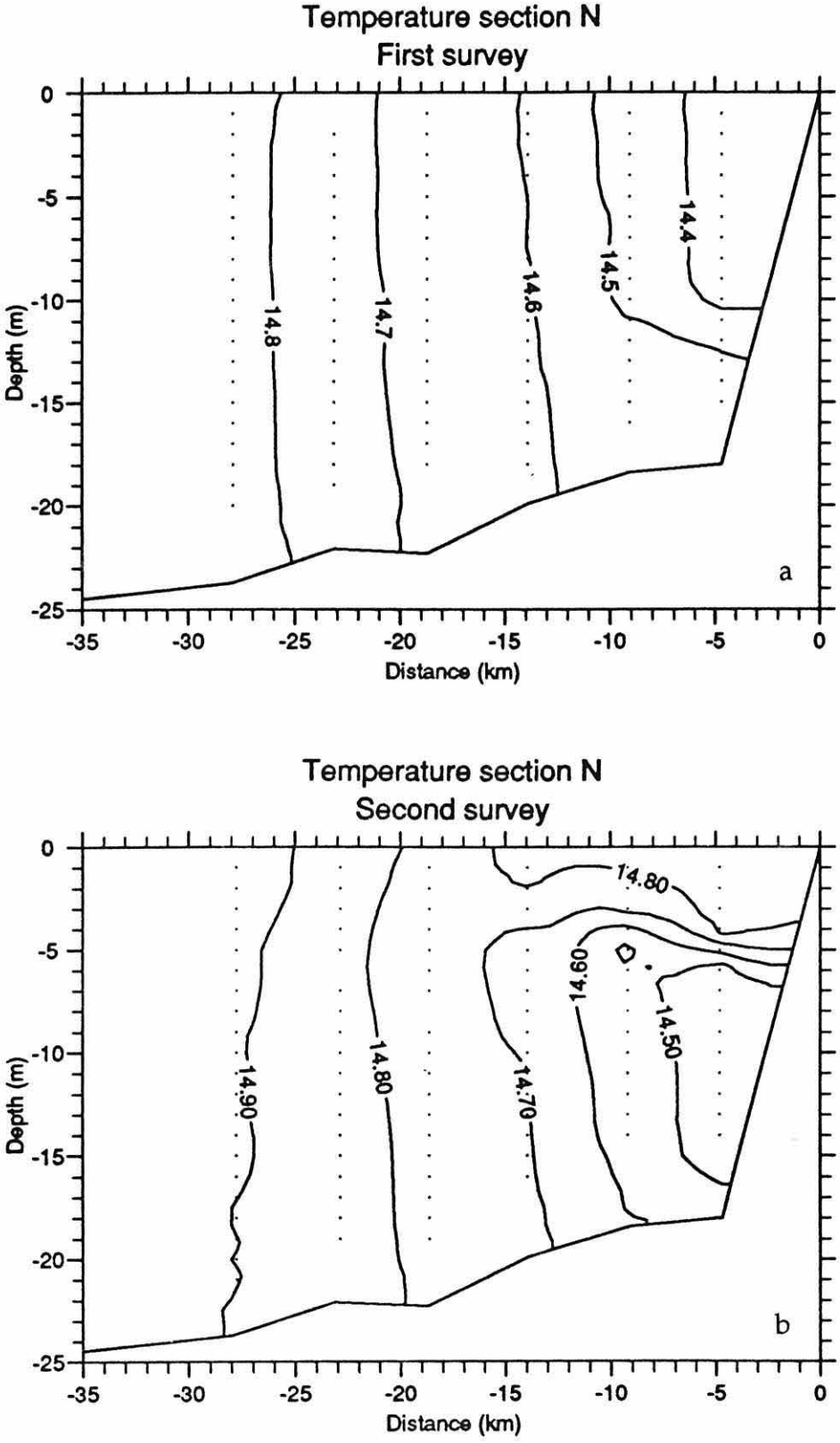

Figure 5.8 Temperature sections on the N (Noordwijk) transect. a) post-springs; b) post-neaps.

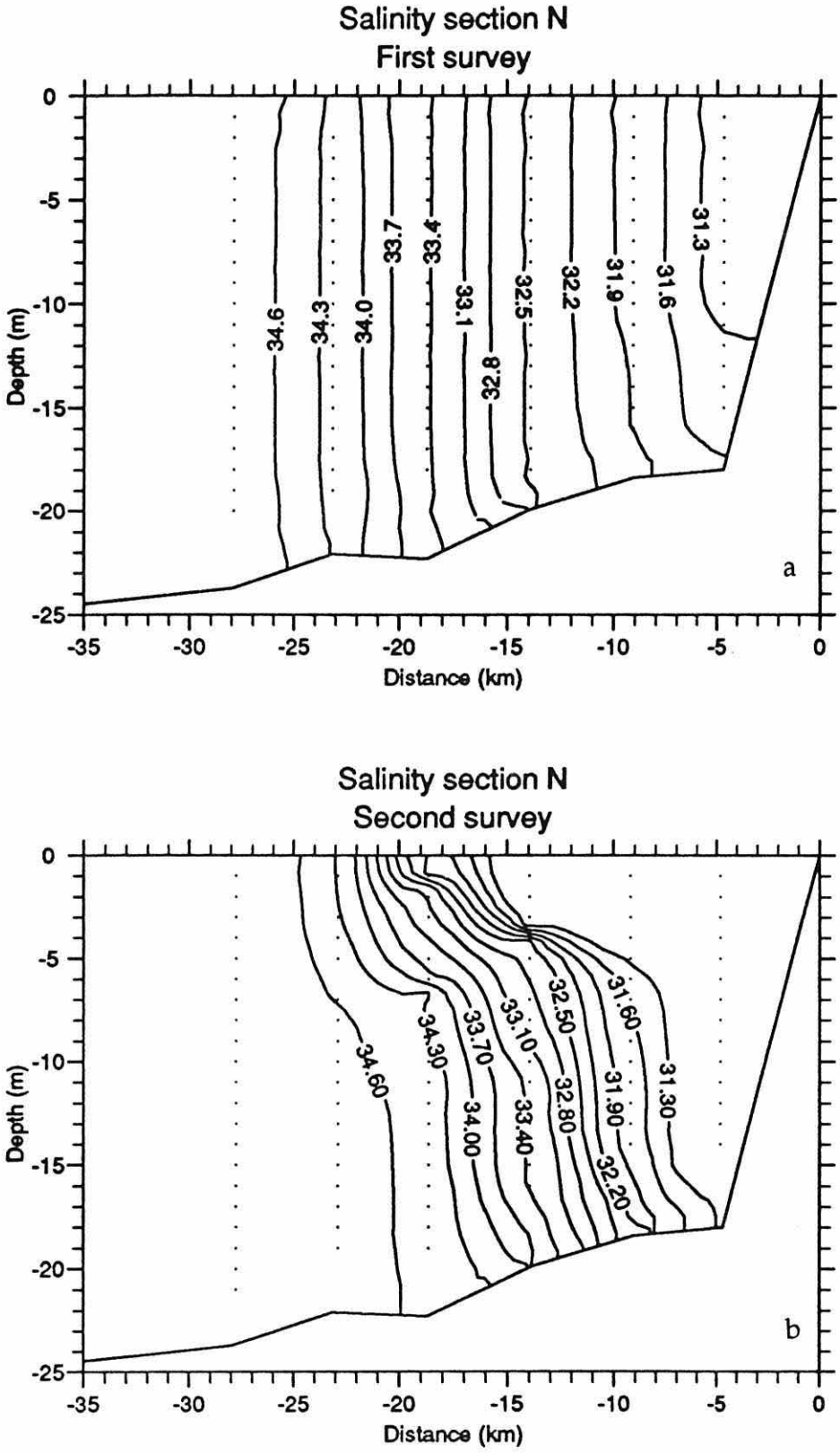

Figure 5.9 Salinity sections on the N (Noordwijk) transect. a) post-springs; b) post-neaps.

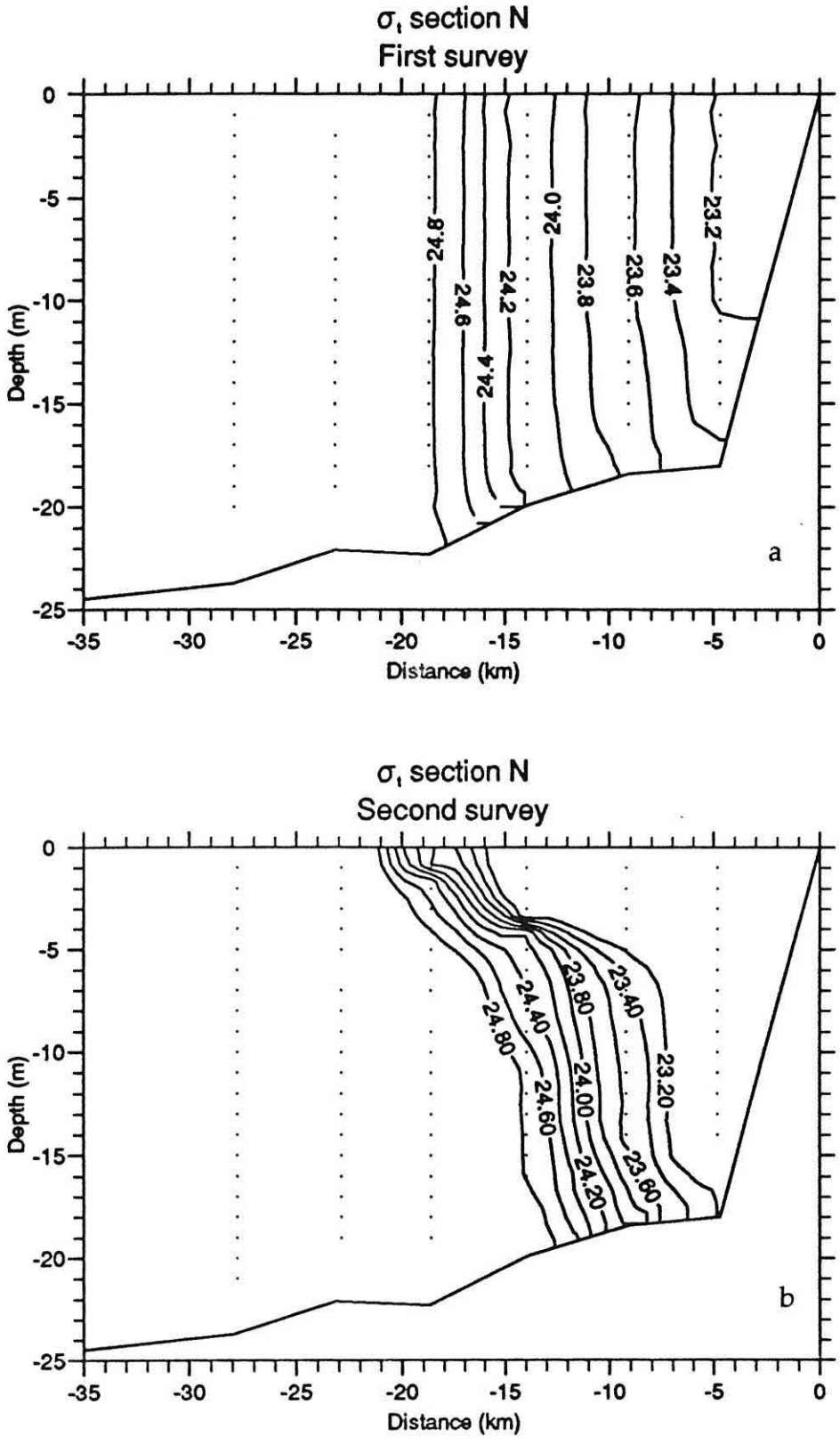

Figure 5.10 Density sections on the N (Noordwijk) transect. a) post-springs; b) post-neaps.

homogeneity, but at post-neaps when the vertical mixing decreases, the density gradients initiate a cross-shore flow similar to that observed in the Linden and Simpson (1988) experiment. However, the motion will be constrained due to the effect of the earths rotation.

The temperature distributions (fig. 5.8) also show a change in vertical structure, from completely homogeneous (fig. 5.8a) at post-springs to slightly stratified (fig. 5.8b) at post-neaps. The changes in horizontal and vertical distribution of temperature are probably influenced by the fact that the presence of haline stratification will limit the exchange with the atmosphere to a thin layer at the surface. The large increase in the total heat is an indication of advection of warmer water from the south.

The horizontal distribution of stratification may conveniently be represented as the potential energy anomaly ϕ. Figure 5.11a represents the situation after springs (days 281-283) where the water column was almost completely mixed over practically the whole survey area. Only in the immediate vicinity of the Rhine source is any significant stratification observed. Six days later, the post-neaps survey (fig. 5.11b) shows strong stratification, with ϕ up to 20 Jm^{-3}, extending out to 30 km from the coast and northwards from the Rhine source to the limit of the survey area.

Another indication of changes in mixing is given by the spatial distribution of suspended particulate matter (SPM) determined from CTD-deployed beam transmissometer. The contrast in re-suspension and vertical mixing between the two spatial surveys is represented in figure 5.12. With strong bottom stirring and vertical mixing that characterizes the post-springs survey, SPM concentration were high with typical values of 40-60 mgl^{-1} near the coast (fig 5.12a). A week later following neap

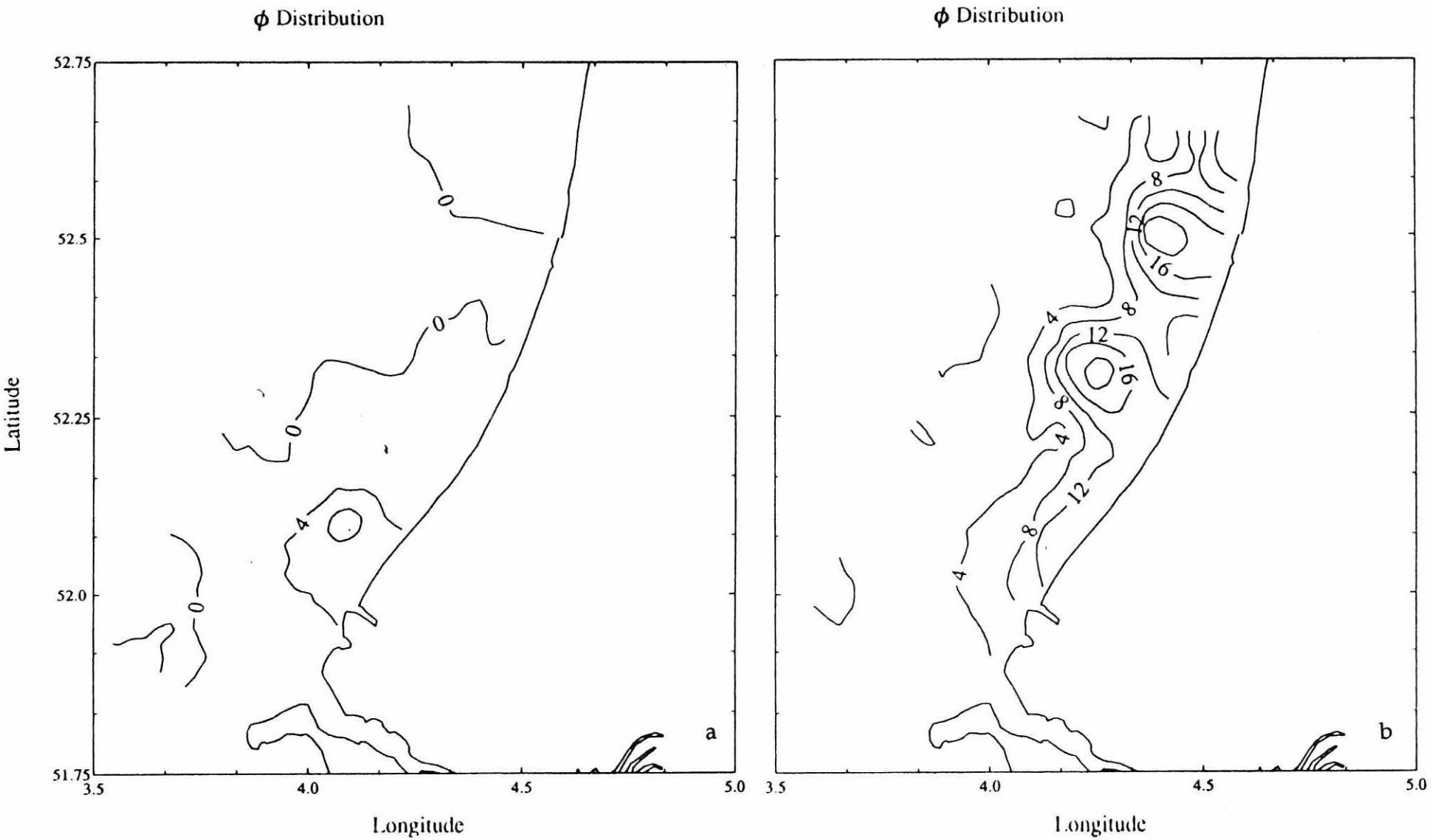

Figure 5.11 Distribution of potential energy anomaly ϕ in Jm^{-3}; a) post-springs; b) post-neaps.

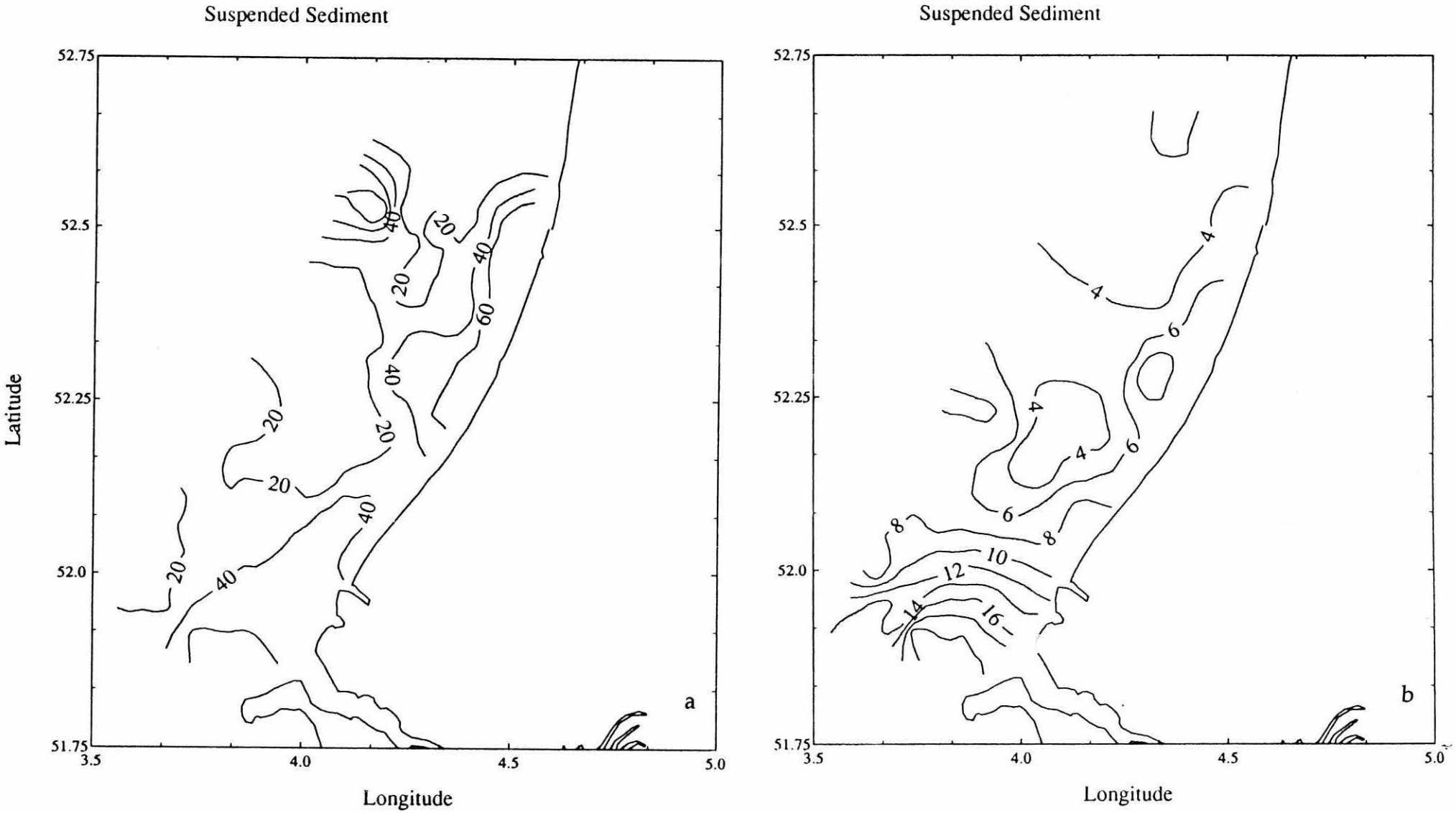

Figure 5.12 Surface total seston in mgl^{-1}. a) post-springs; b) post-neaps.

tides and a reduction in windstress, surface concentrations have fallen by almost an order of magnitude (to 4-6 mgl^{-1}).

5.3. September 1992 experiment.

5.3.1 Time series of water column structure.

The time series of surface and bottom salinity and temperature for moorings A, B, D, E are shown in figures 5.13 and 5.14. With them we can create a quasi-three-dimensional picture of the evolution of water column structure. In general we observe that salinity decreases as we approach the coast, with maximum stratification at moorings A and D and complete or almost complete homogeneity at mooring B. As expected, the surface salinity is less than bottom salinity so that stability is maintained. As in the 1990 experiment, semi-diurnal variability of surface salinity is greater at the surface than at the bottom where salinity remains more or less constant. The maximum of variability is observed near the coast at moorings A and D.

The temperature time series, from the 4 RCMs, show a tendency to decrease from 17 to 16.4 °C over the observation period, with strong increases in surface temperature of about 0.5 °C at day 254. This is probably due to intense thermal input to a very thin surface layer.

The evolution of water column stability is shown in figure 5.15. Maximum stability occurs near the coast (stations A and D) while stratification is almost negligible at mooring B about 20 km from the coast. Mooring E (~15 km from the coast) shows moderate stratification. At mooring A there are three periods of water column stability divided by two episodes of vertical homogeneity, while at mooring

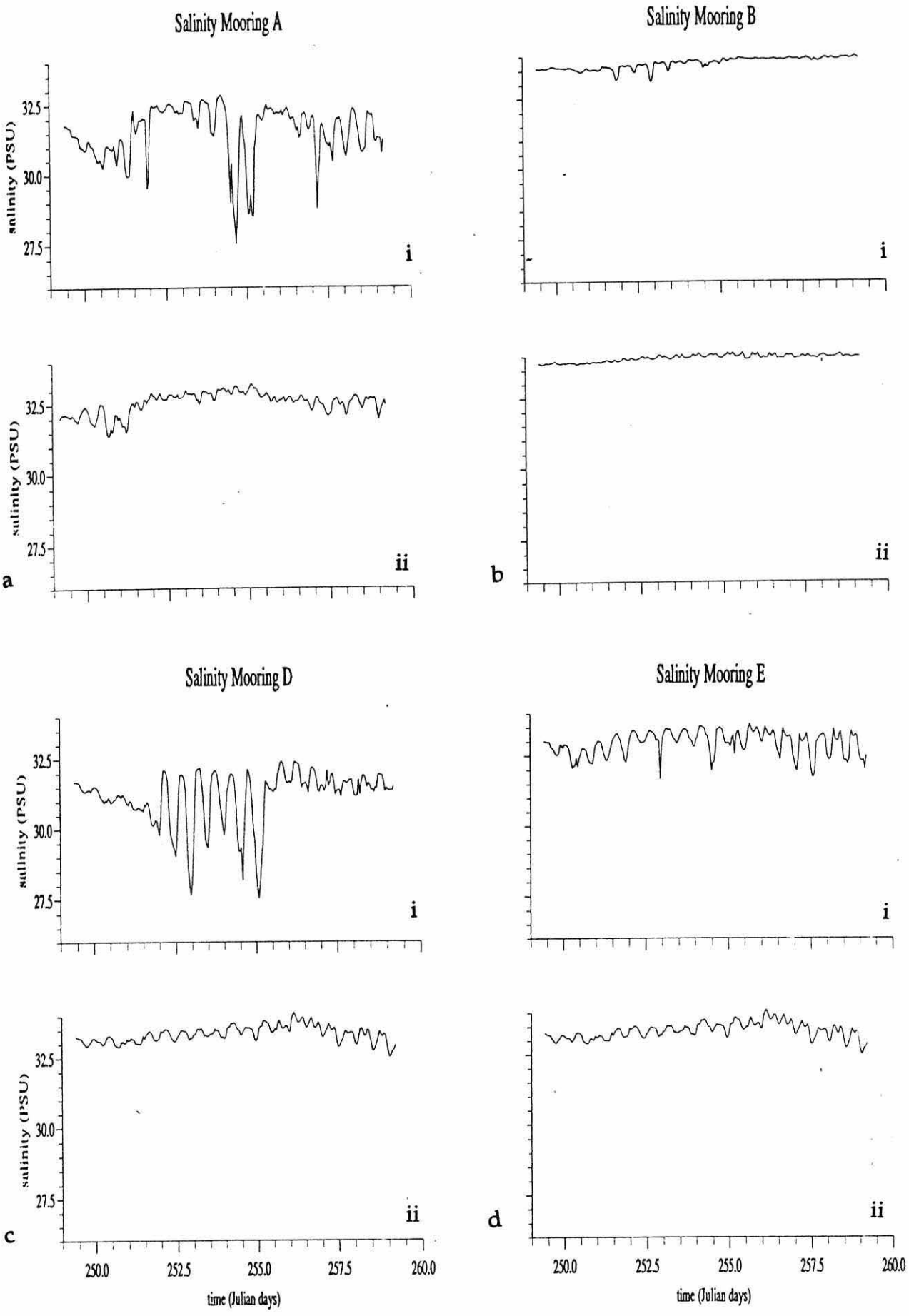

Figure 5.13 Salinity time series for 1992. a) mooring A; b) Mooring B; c) Mooring D; d) Mooring D. i) Surface (1 m), ii) bottom (16m).

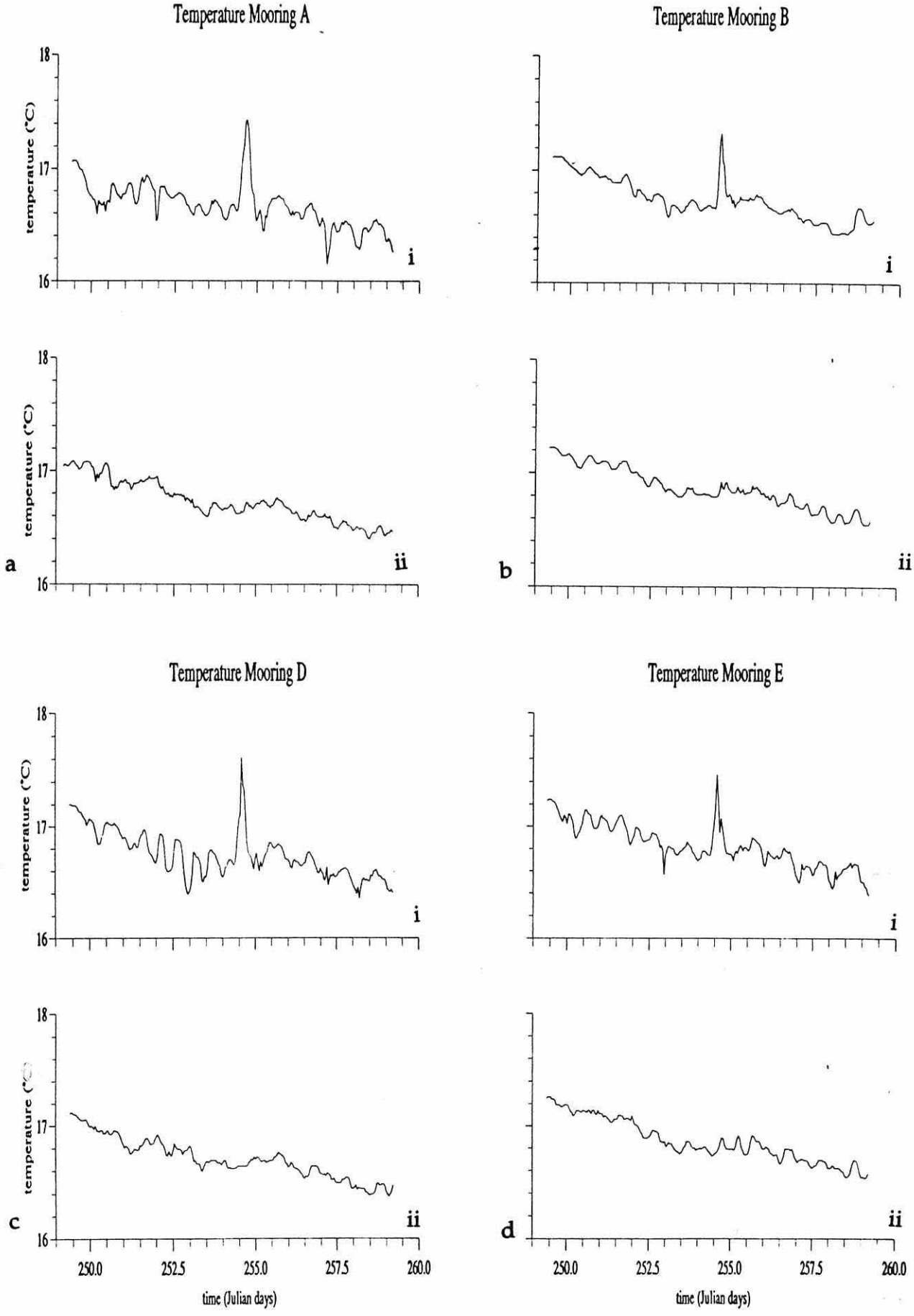

Figure 5.14 Temperature time series for 1992. a) mooring A; b) Mooring B; c) Mooring D; d) Mooring D. i) Surface (1 m), ii) bottom (16m).

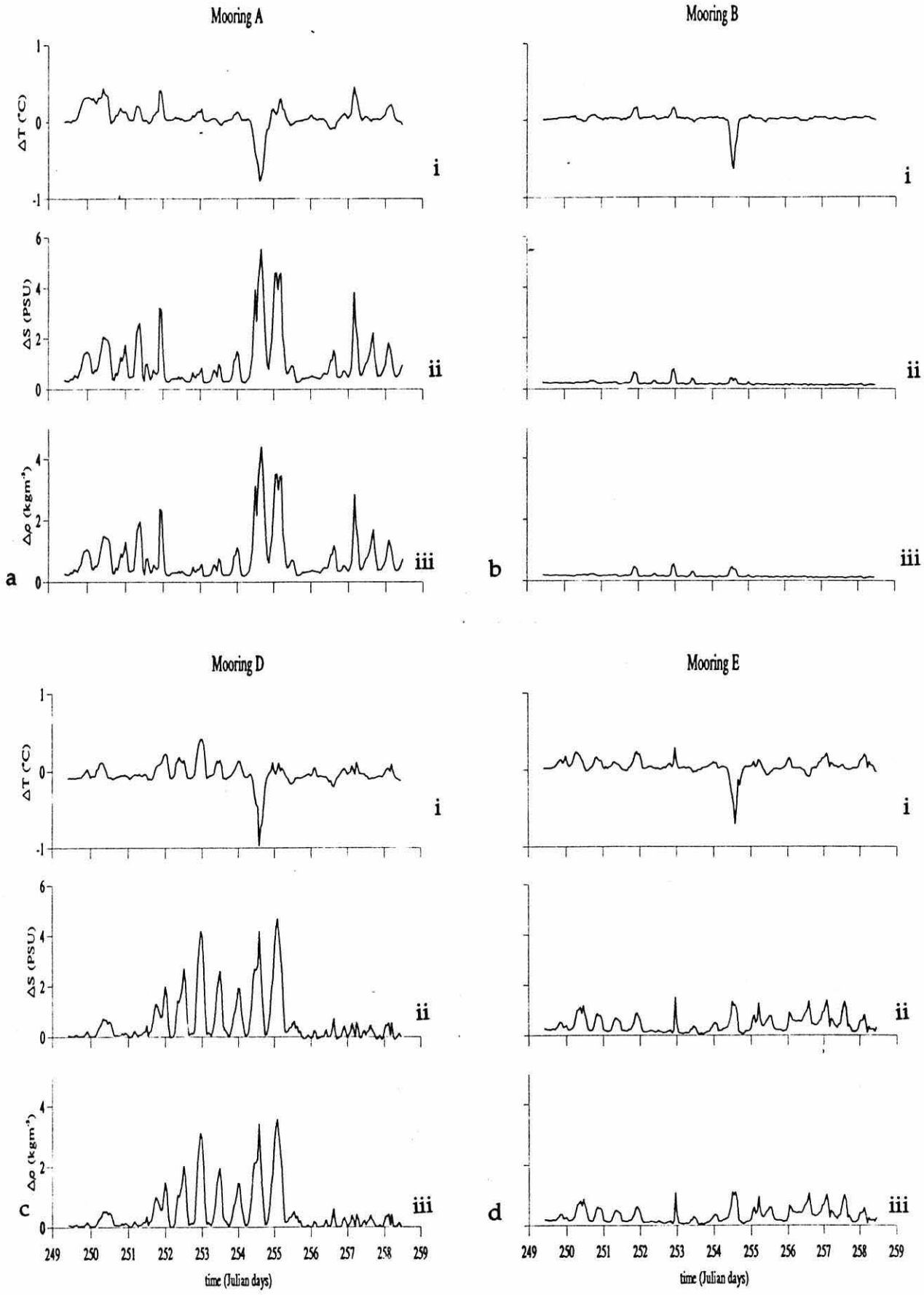

Figure 5.15 Time series of bottom - surface difference for the 1992 campaign. a) mooring A; b) Mooring B; c) Mooring D; d) Mooring D. i) temperature; ii) Salinity; iii) density.

D there was a central period of strong stratification from day 252 to about noon on day 255. Overall moorings A, D and E present a rather coherent picture; the decrease in stratification on mooring E should be related to the fact that it is located further off-shore than moorings A and D.

The difference between bottom and surface temperature shows slight thermal instability in all the moorings at most times, except at the period of strong stratification on day 254, where stable thermal stratification appears everywhere with $\Delta T \sim 1°C$. This is probably caused by strong heat flux between the atmosphere and a very thin sea surface layer, due to the onset of stratification.

The evolution of mixing and stratification is clearly related to the tidal and wind stirring (fig.5.16). The mixing energy from tidal mixing and tidal stirring has been calculated using the efficiency values from Simpson and Bowers (1981). The time series of tidal energy (fig. 5.16a) clearly show the spring-neaps cycle, with reduced stirring during neaps (days 249 to 252) and strong stirring at springs (days 255 to 258).

The stratification (fig. 5.16c) appears to be primarily controlled by the strong wind stirring (fig. 5.16b). Stratification was negligible at any time when the wind stirring exceeded 0.05 mWm^{-3}. Further on the regressions of the daily mean $\Delta\rho$ on the alongshore and cross-shore components of windstress and significant wave height (measured at he Noordwijk tower) demonstrate strong partial correlations with all 3 variables and explain 69% of the variance in the 12 day observational period reported here. Tidal stirring also makes a slowly varying contribution but is less important than wind stirring (fig 5.16). The most important feature in the stratification is, as in

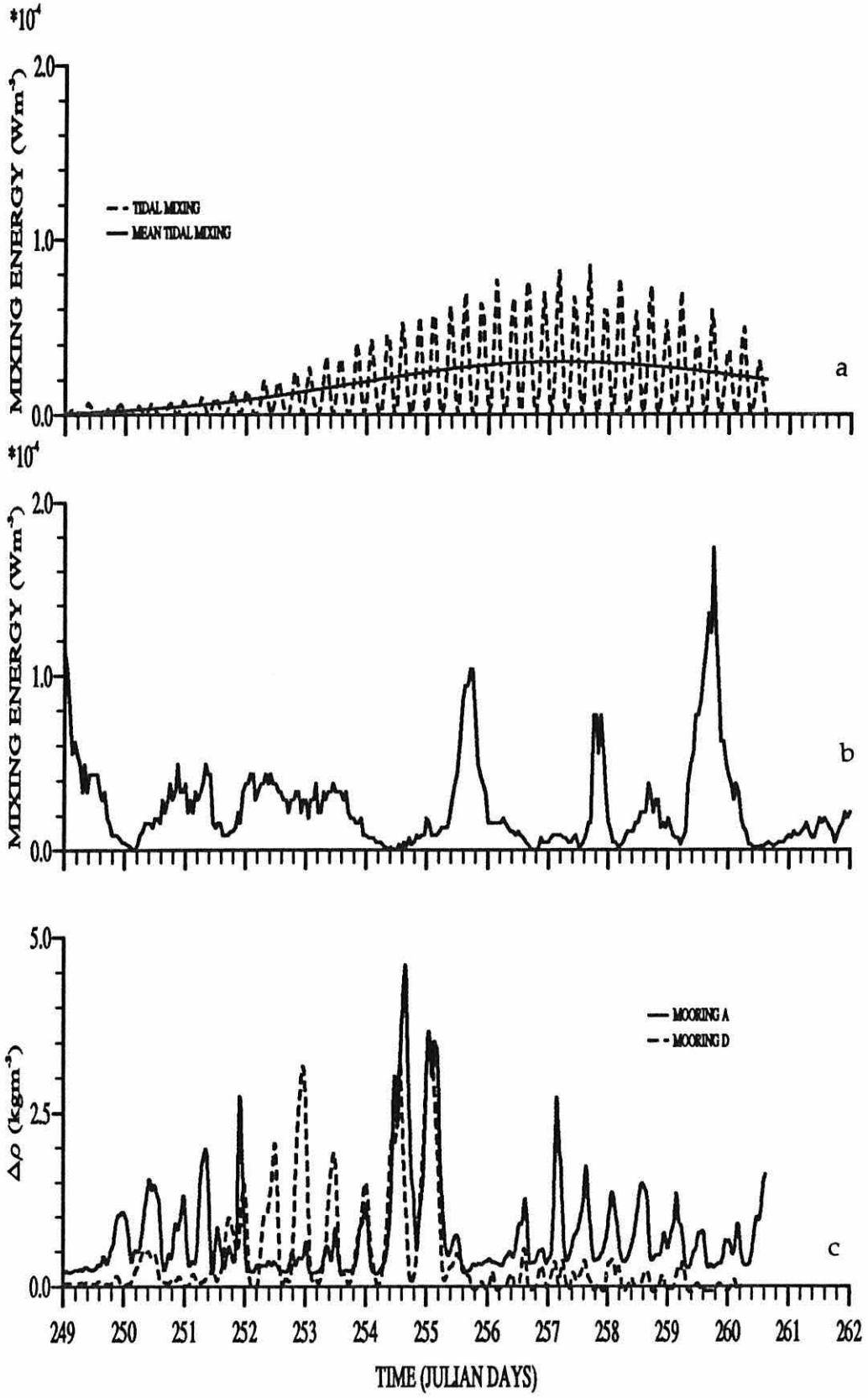

Figure 5.16 Time series of stirring power and stratification. a) tidal stirring power: instantaneous value (dashed) and daily mean (continuous) computed from current meter velocity at mooring A (4 m above the bed); b) wind stirring power calculated using data fro Noordwijk tower; c) stratification $\Delta\rho$, density difference between 1m and 16 m deep, continuous mooring A dashed mooring D.

the case of the 1990 experiment, the strong semi-diurnal variation in water column stability, which is present whenever there is stratification and has an amplitude comparable to that of the mean stratification.

5.3.2 Spatial distribution of water column structure.

In an attempt to achieve a space-time picture of the evolution of structure in the Rhine ROFI, a continuous spatial survey was carried out using the SEAROVER undulating CTD. Figures 5.17 to 5.19 show maps of surface distribution of temperature salinity and density respectively, during 3 different surveys. The first is formed from all the along-shore tracks and the rest are from repeated zig-zags along the coast, as explained in chapter 2.

Sea surface temperature exhibits little variability with gradients mainly in the cross-shore direction (fig. 5.17). Salinity and density (figs. 5.18 and 5.19), as in 1990, are strongly correlated confirming that the salinity field controls the density field in this ROFI. The density and salinity gradients are mainly oriented off-shore with fresher lighter water (S=29 psu; σ_t=21 kgm^{-3})near the coast and heavy saltier water (above 34 psu and above 24 kgm^{-3}) further offshore. The density and salinity gradients are intensified at about 15 km off the Dutch coast. This feature is better observed in figures 5.18b and 5.19b, during the day 255 when meteorological conditions were calm (fig. 5.16), so that the stirring will be at its lowest, allowing stratification to develop.

The stratification distribution, plotted as ϕ (equation 2.1), shows rather little stratification almost everywhere on all the surveys. In fig. 5.20a we find the strongest stratification, with a ϕ greater than 20 Jm^{-3} at about 100 km from the Rhine source.

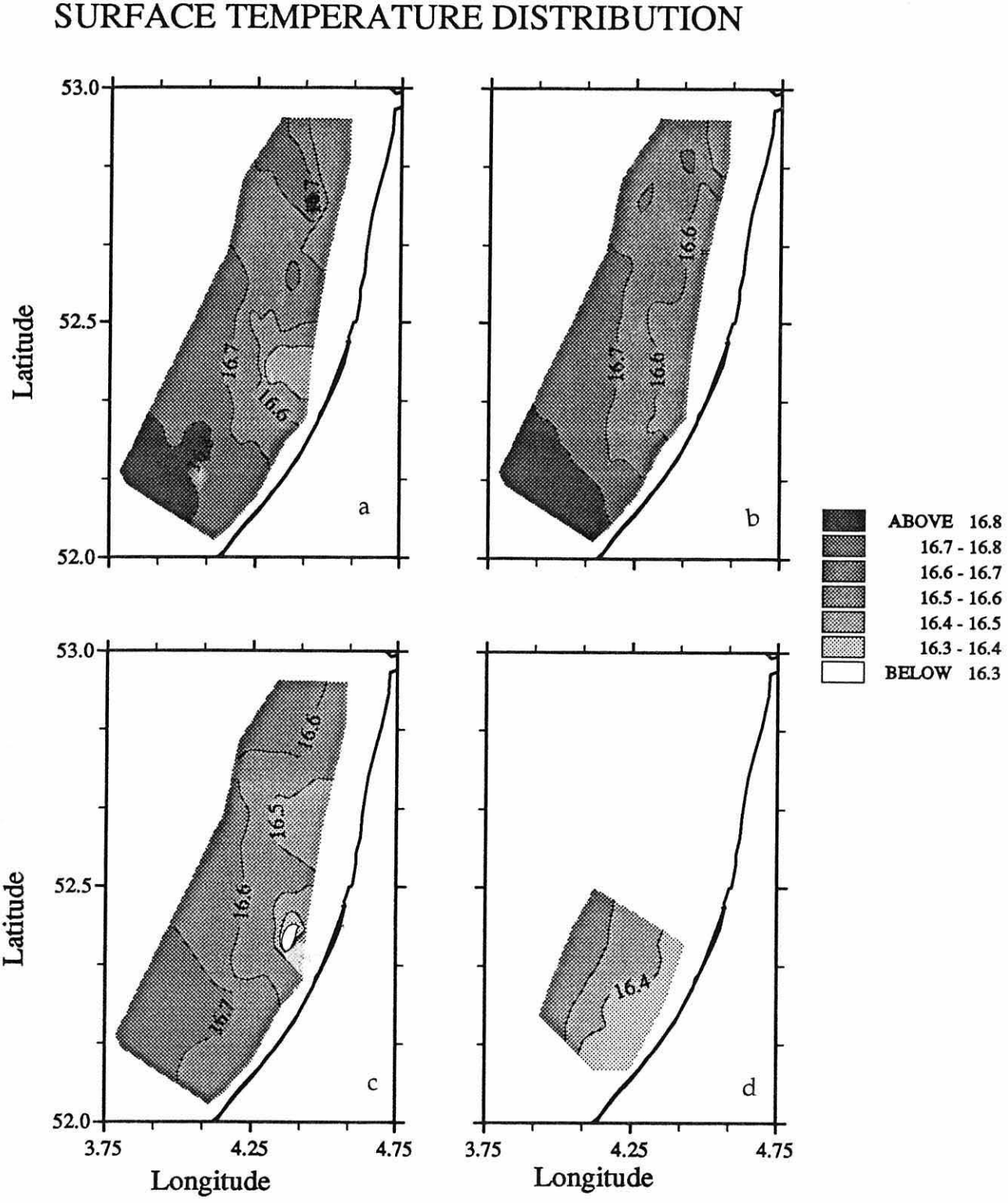

Figure 5.17 Sea surface temperature distribution in the Rhine ROFI for the 1992 campaign. a) 8 to 10 September (jdays 252-254); b) 11 September (jday 255); c) 12 September (jday 256); d) 15 September (jday 259).

from SEASOAR ?

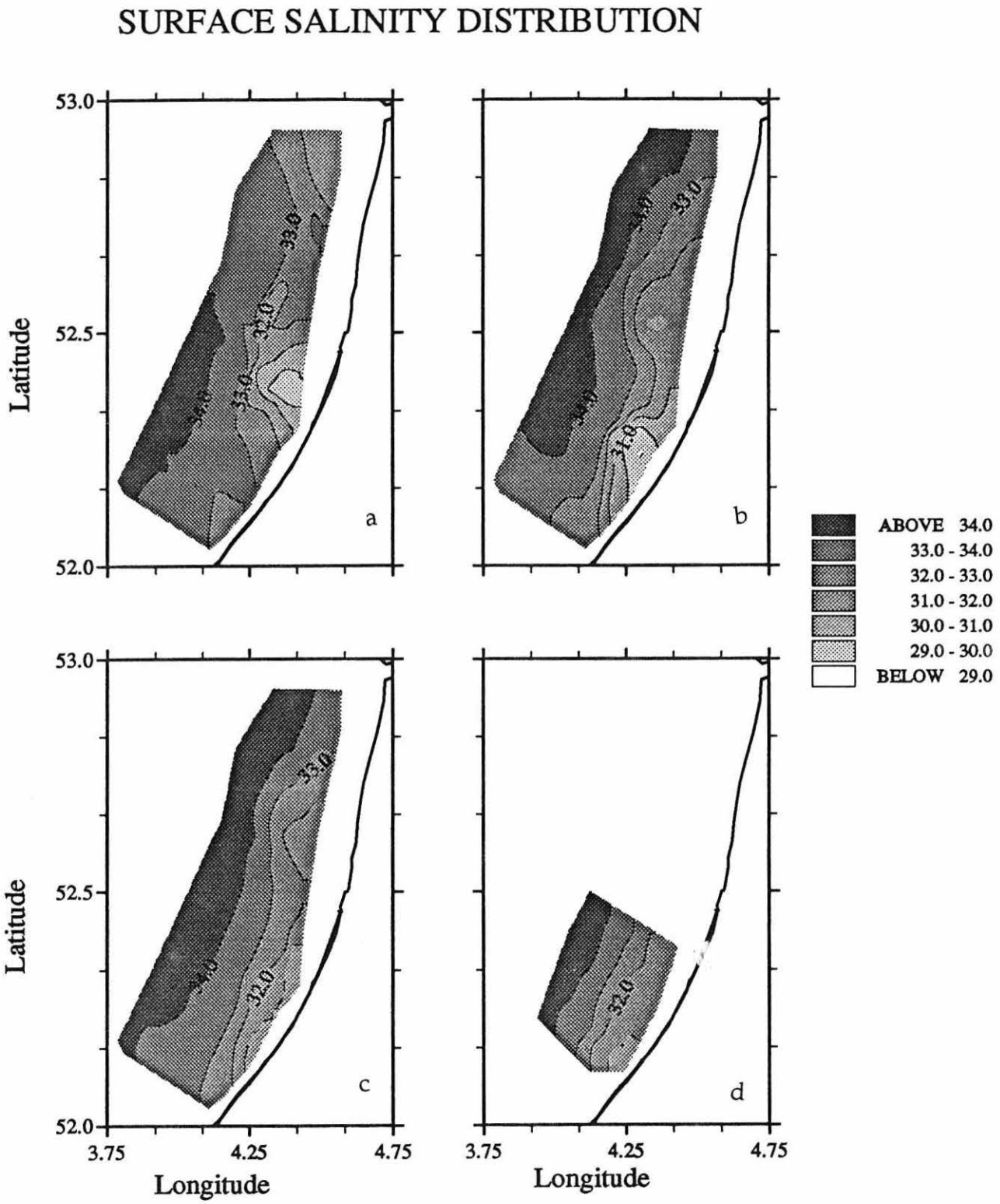

Figure 5.18 Surface salinity distribution in the Rhine ROFI for the 1992 campaign. a) 8 to 10 September (jdays 252-254); b) 11 September (jday 255); c) 12 September (jday 256); d) 15 September (jday 259).

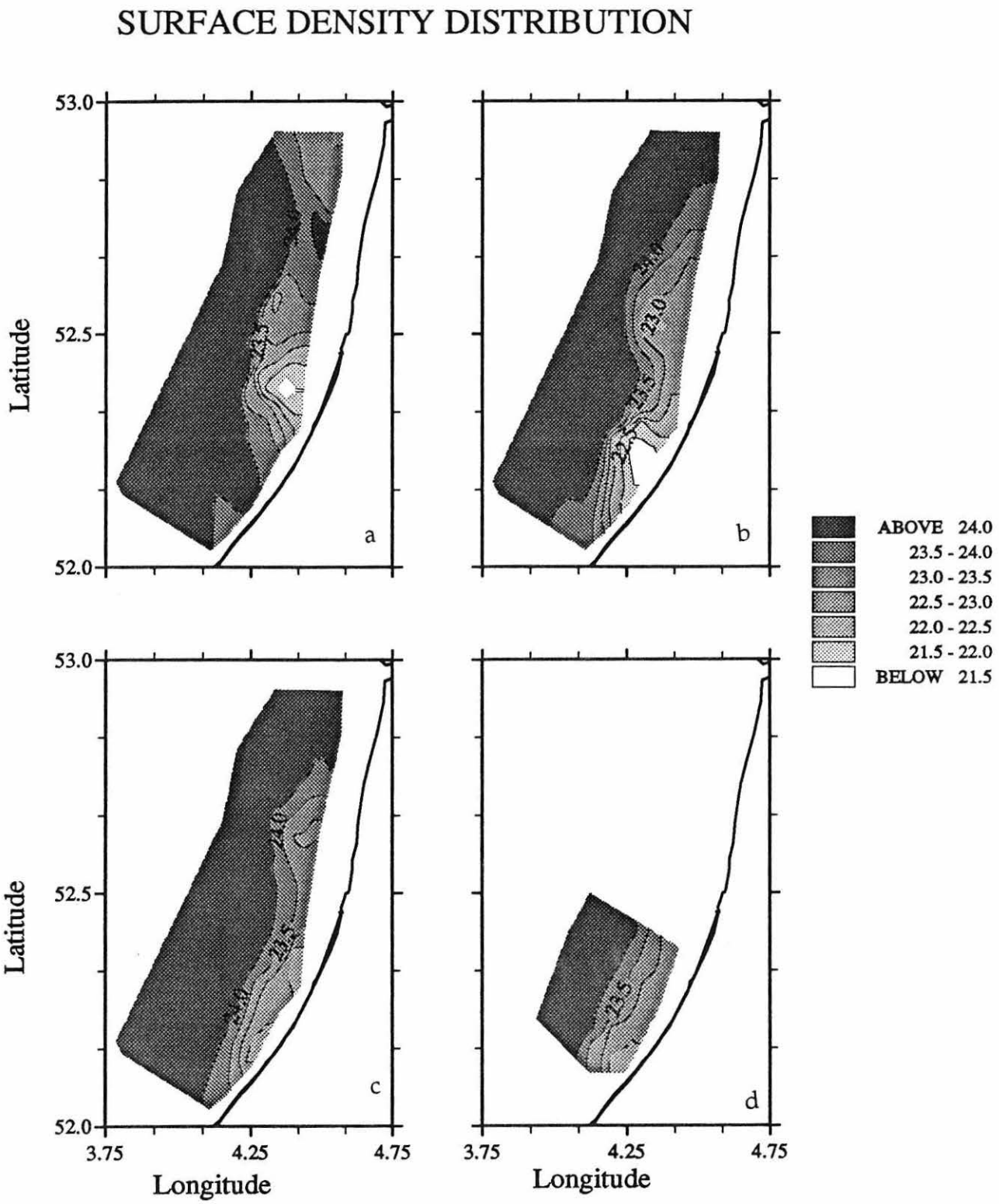

Figure 5.19 Surface density distribution in the Rhine ROFI for the 1992 campaign. a) 8 to 10 September (jdays 252-254); b) 11 September (jday 255); c) 12 September (jday 256); d) 15 September (jday 259).

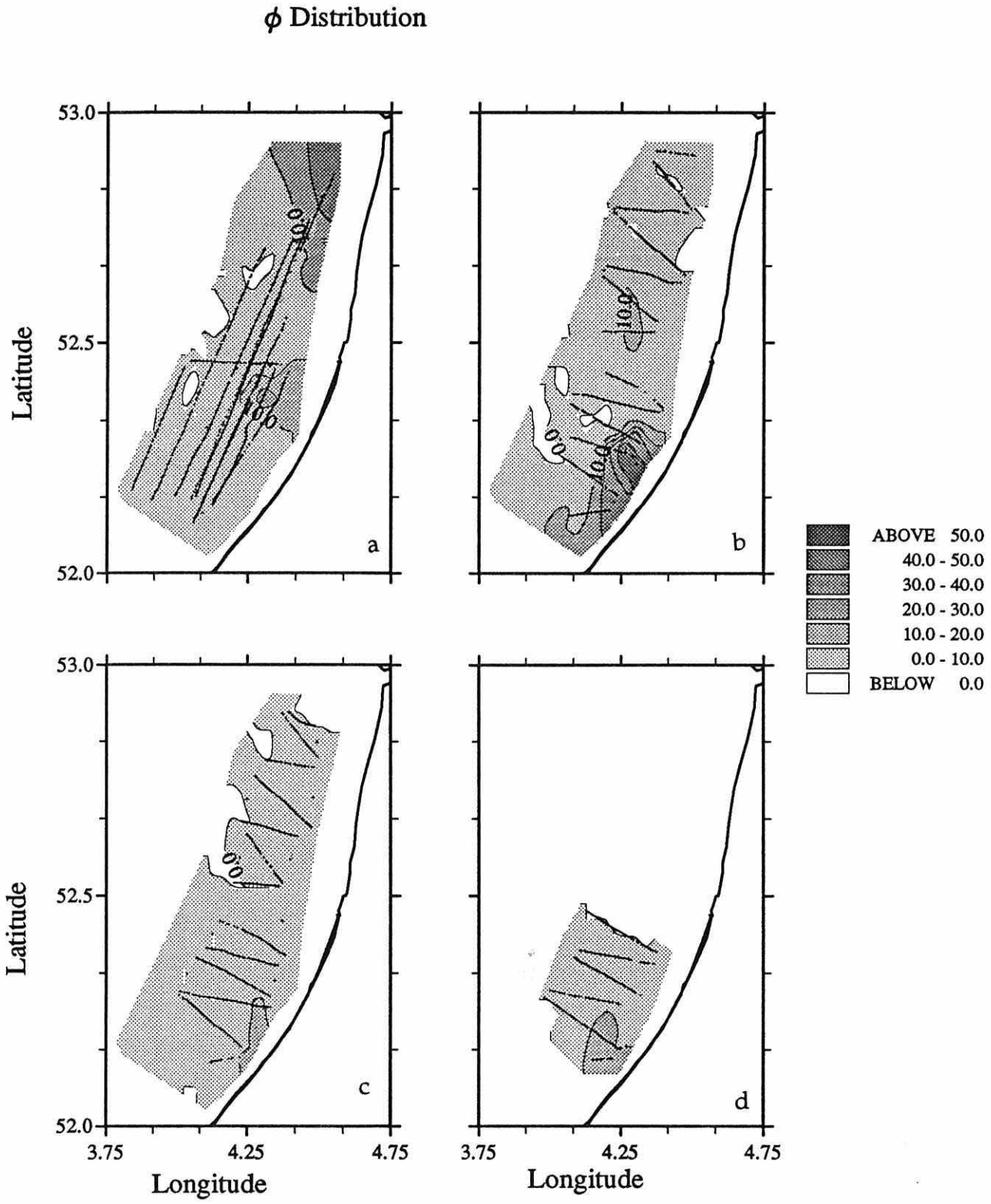

Figure 5.20 Potential energy anomaly (ϕ) distribution in the Rhine ROFI for the 1992 campaign. a) 8 to 10 September (jdays 252-254); b) 11 September (jday 255); c) 12 September (jday 256); d) 15 September (jday 259).

The rest of the stratification maps exhibit the strongest stratification near the Rhine source, with values of ϕ of the order of 50 Jm^{-3} on the 11 September 1992 (day 255) (fig. 5.20b), while during the next day (fig.5.20c) the stratification becomes negligible everywhere, as for day 259 (fig. 5.20d).

A clearer picture of short-term variability is observed in a series of density sections following the line in front of Noordwijk (fig. 3.4) during day 261, when the stirring was low (fig. 5.16). The evolution of stratification over half a tidal cycle is observed in figure 5.21 which shows how the water column changes from almost complete mixing (fig. 5.21a) to strongly stratified in about seven hours (figs. 5.21b,c,d).

5.4 Interpretation and discussion.

From the observations presented above it has become clear that the Rhine outflow generates a ROFI system in the North Sea, with a spatial coverage of about 30 km off-shore and at least 100 km along-shore. In this area as expected the main input of buoyancy will be due to the freshwater discharge of the Rhine.

During the two survey periods, it has been observed that the stratification is controlled by the level of stirring energy present in the system. During the 1990 survey it appeared to be a clear semi-monthly cycle of stratification which might be attributed to the fortnightly cycle of tidal stirring although the fortuitous correlation between wind speed and tidal velocity make it difficult to assess the importance of each component of vertical stirring. Numerical simulations for that period suggest the need of strong wind stirring to bring the water column to complete mixing (Luyten *et al.*, 1994). For the case of the 1992 study it has become evident that the strong wind

stirring is the dominant factor in controlling water column stability.

The process by which the stratification develops is that during low levels of stirring the vertically homogeneous density gradients (fig. 5.21a) collapse under gravity, travelling off-shore (fig. 5.21) until limited by rotation. The initial offshore flow is deflected into an along-shore coastal current in which the transverse pressure gradients are, to first order, in geostrophic balance, with an isopycnal displacement of about 1.5 Rossby radii as predicted by Ou's (1983) two-layer geostrophic model, which for the present case will be about 5 km (fig. 5.10b).

A clear pattern present in both experiments is the strong semidiurnal switching of stratification, present in the time series whenever stratification is present. This strong semi-diurnal signal is clear evidence of the importance of the interaction between tidal straining and the horizontal density gradients as an important process in the development of freshwater stratification. This mechanism has also been proposed by Simpson *et al.*, 1990 to explain observations in Liverpool Bay. It has also been observed in the Merbok estuary by Uncles *et al.*, 1992.

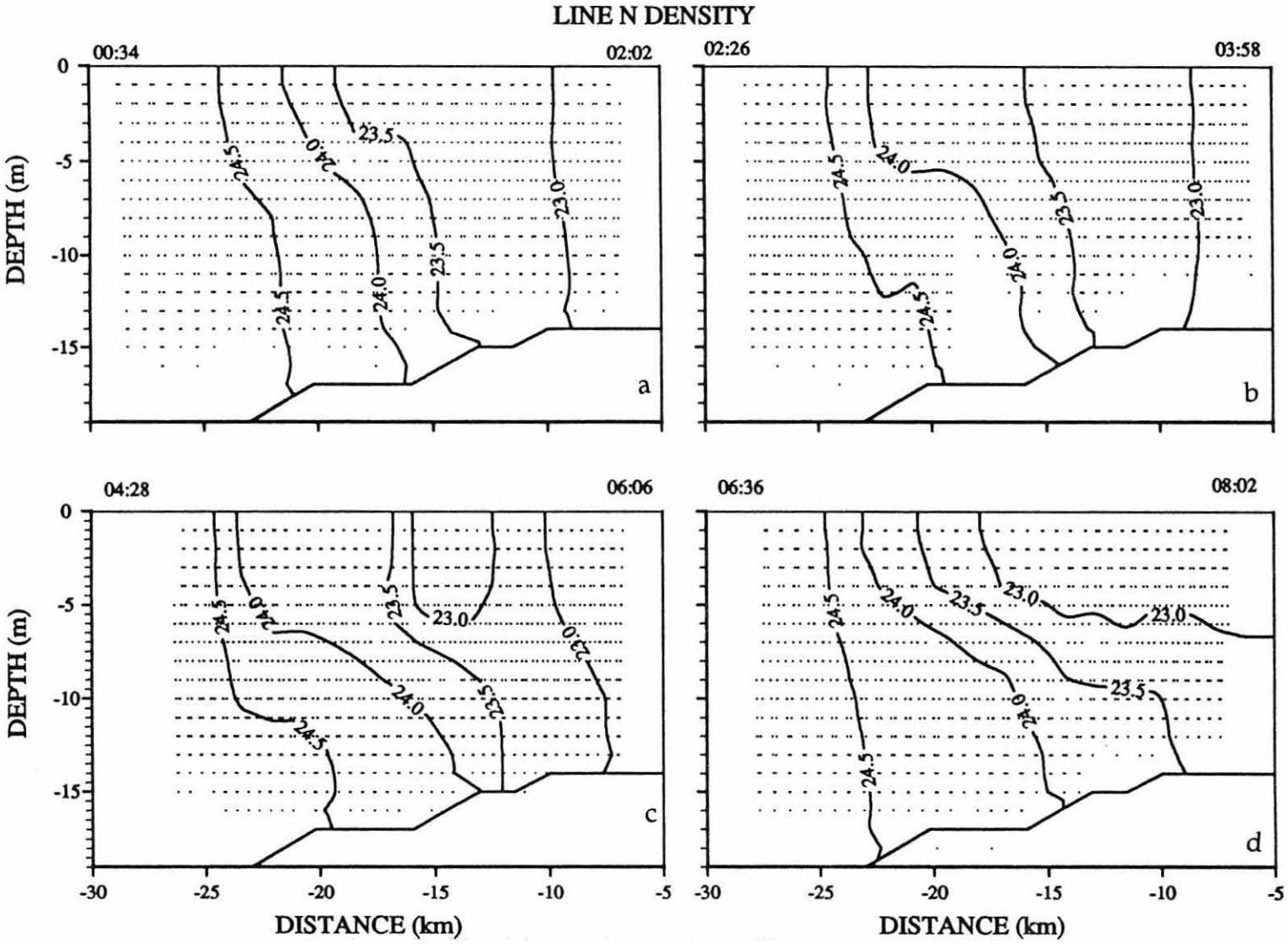

Figure 5.21 Density sections on jday 261 (17 September 1992). a) between 00:34 and 02:26 hrs; b) at low water, between 02:26 and 03:58 hrs; c) between 04:28 and 06:06; d) at high water between 06:36 and 08:02.

CHAPTER SIX

TIDAL FLOW

6.1. Introduction.

We now proceed to consider the form of the tidal flow and present some results concerning the configuration of the tidal ellipses which have emerged from this study. We shall see that this new information on the ellipticity and its variation through the water column, is crucial in understanding the short term variation of stratification.

Thanks to availability of state-of-the-art instrumentation we have been able to construct an extensive picture of the tidal distribution and its evolution in time. The use of HF radar CODAR has enabled us to map the currents in the top 1m of the water column and this, combined with data from current meters permitted us to construct time series of velocity profiles. At the same time, the use of bottom-mounted ADCPs in the 1992 campaign allowed us to create time series of high resolution velocity profiles within 3m from the bottom and surface. The time evolution of tidal currents was achieved by applying a moving average harmonic analysis, described in chapter 4, where an M_2 fit was applied to short intervals of the time series (25 hours).

6.2. Spatial mapping of ellipse properties.

A summary picture of the M_2 and S_2 horizontal distribution of surface tidal currents for the 1990 experiment, based on HF radar CODAR data is shown in figure 6.1. The M_2 tidal ellipses (fig. 6.1a) are oriented parallel to the coast, with increasing clockwise ellipticity ($\varepsilon \sim -0.3$) near the coast. At about 20 km from the coast the ellipses become degenerate and further away they show a weak anticlockwise rotation ($\varepsilon \sim 0.08$), while the semi-major axis is more or less constant at about 0.8 ms^{-1}.

The S_2 ellipses are also more or less oriented parallel to the coast with a semi-major axis of the order of 0.25 ms^{-1}, the ellipticity and orientation behave very similarly to that of the M_2 harmonic, with strong negative ellipticity near the coast and becoming more positive with distance from the coast, but the region where the ellipses rotate clockwise is limited to about 15 km off-shore. A striking difference from the M_2 constituents that the orientation of the tidal ellipses veers to the east as the coast is approached.

6.3 Vertical structure of the tidal currents.

The vertical distributions of the principal tidal components for moorings B and D are show in tables 6.1 and 6.2 respectively. In general the magnitude of the tidal ellipses decreases with depth while the ellipticity becomes less anti-clockwise with height above the bed. If we combine these results with those of the CODAR data, we can observe how the ellipticity changes from strongly anti-clockwise near the bottom (~0.2) to clockwise (~-0.1) at the surface.

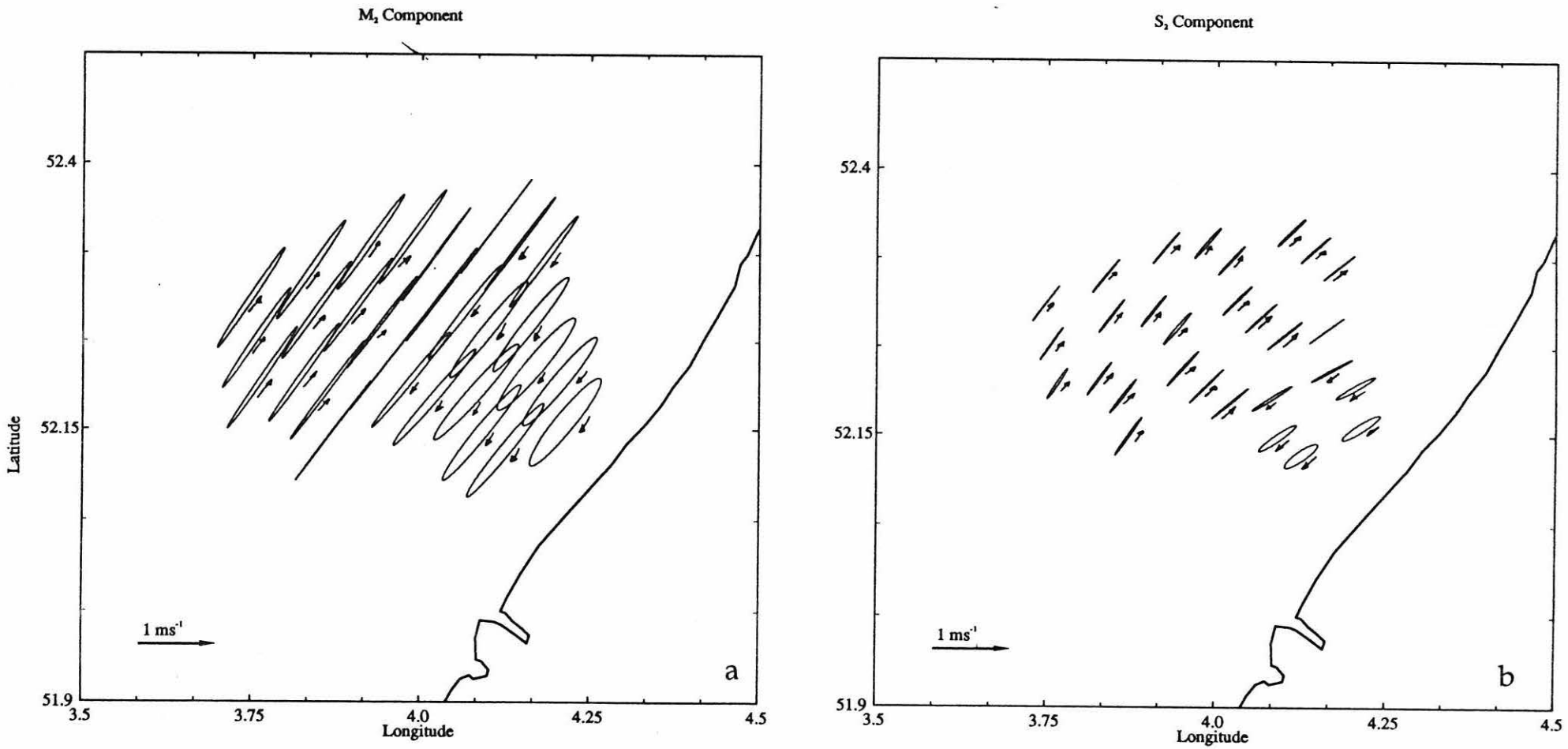

Figure 6.1 Surface distribution of tidal ellipses from CODAR observations, between the 7 and 18 October 1990 (Julian days 280 to 291). a)M_2, b) S_2.

Table 6.1 Tidal ellipse characteristics for mooring B (1990)

height (m)	Constituent	semi-major axis (ms^{-1})	ellipticity	phase (°)	orientation (°)
CODAR	M_2	0.8000	-0.1090	66.499	52.528
	S_2	0.276	0.008	90.163	36.596
12	M_2	0.5055	0.0221	72.6826	52.3710
	S_2	0.1830	0.0418	120.4626	51.5548
8	M_2	0.5043	0.0640	71.9142	53.6919
	S_2	0.2075	0.0059	118.1879	54.7783
4	M_2	0.4018	0.2105	61.7349	42.8105
	S_2	0.1470	-0.0152	122.1021	40.4174

Table 6.2 Tidal ellipse characteristics for mooring D (1990)

height (m)	Constituent	semi-major axis (ms^{-1})	ellipticity	phase (°)	orientation (°)
CODAR	M_2	0.7220	-0.0830	61.748	51.208
	S_2	0.267	-0.134	84.503	36.596
9	M_2	0.5219	-0.0260	73.7246	45.3214
	S_2	0.2053	0.0341	126.2892	44.9386
6	M_2	0.4323	0.0857	72.3275	47.7220
	S_2	0.1835	0.0484	311.3102	237.3147
3	M_2	0.3365	0.2298	64.5592	47.5852
	S_2	0.1413	0.0051	308.4465	242.2493

The vertical distribution of tidal characteristics for the 1992 experiment, from the ADCPs at moorings A and B, are shown in figures 6.2 to 6.3. The behaviour of the M_2 characteristic is somewhat different between mooring A in the stratified area and B in the mixed region (fig. 6.2). The semi-major axis for mooring A shows a general tendency to increase with height, while for the case of mooring B it shows a maximum at mid water (~ 8 m height). The semi-major axis is also about 40 % greater

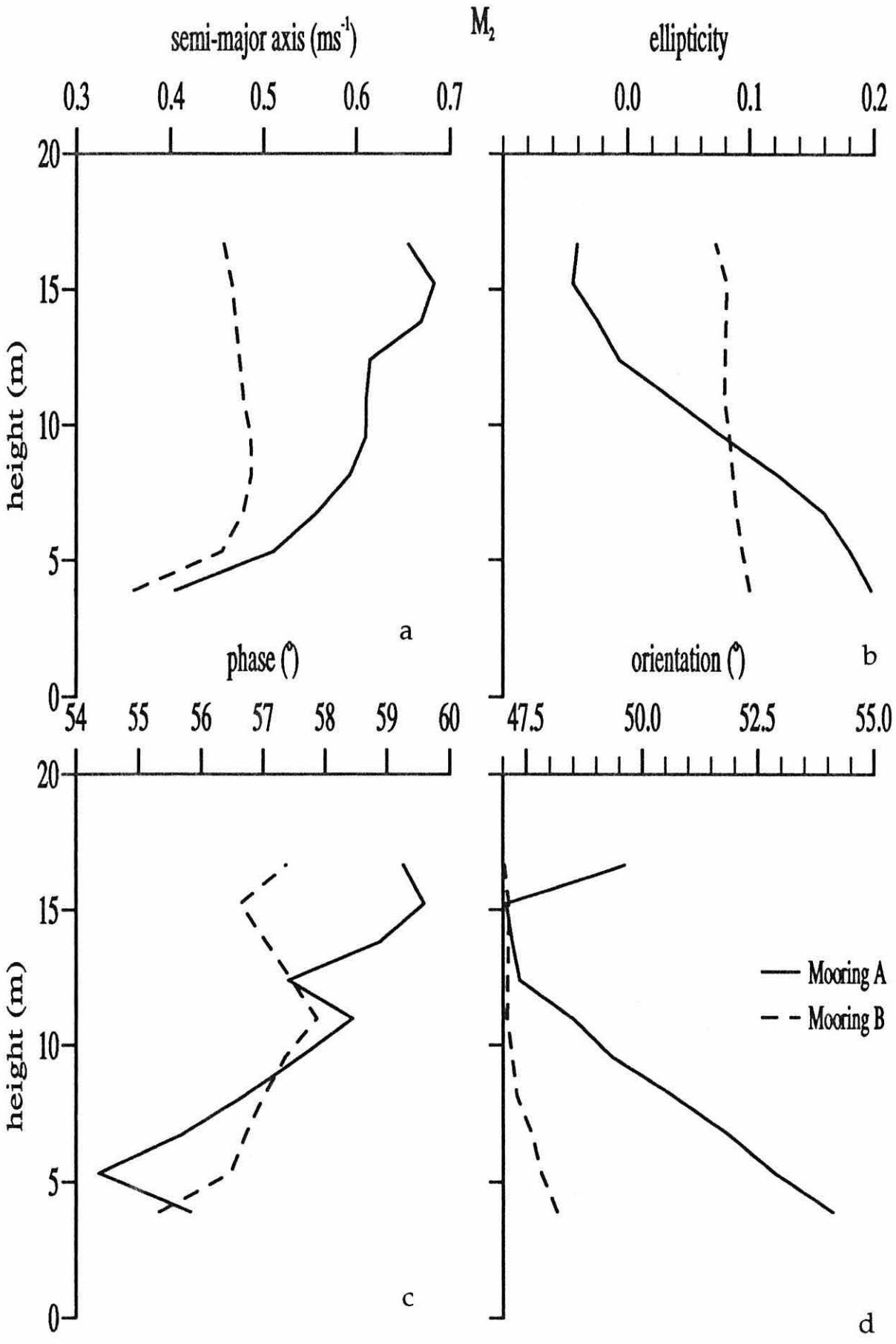

Figure 6.2 M_2 tidal ellipses profiles, from bottom-mounted ADCPs at mooring A (continous) and mooring B dashed, from 2 to 17 September 1992 (Julian days 248 to 261). a) semi-major axis, b) ellipticity, c) phase and d) orientation.

in mooring A except near the bottom boundary (fig. 6.2a). The ellipticity for mooring B decreases only slightly with height, having a value close to 0.08 through the water column, while there is strong decrease in ellipticity for mooring A (fig. 6.3b). The surface ellipticity value is -0.04 and near the bottom is 0.2; this means that the ellipses have changed from strongly anticlockwise near the bottom to slightly clockwise near the surface, with degenerate ellipses at about 12 m height. Another difference is that the semi-major axis orientation in mooring A changes approximately 5° between bottom and surface while the changes in orientation in mooring B are negligible (fig. 6.2d). The behaviour for S_2 is similar (fig. 6.3).

The different behaviour of the tidal ellipses, particularly the change in ellipticity and orientation, between mooring A and mooring B are due to the fact that mooring A is inside the stratified area while mooring B is not. The effect of stratification over the tidal ellipses is to decouple the clockwise boundary layer, this will be explained in more detail in the next sections.

The ellipse characteristics for section N have been derived from hull-mounted ADCP data collected during 25 hours between Julian day 260 and 261. The results for M_2 are plotted in figure 6.4, showing the same general characteristics described from the mooring and CODAR data: the magnitude of the semi-major axis increases with height (fig. 6.4a), while the ellipticity decreases (fig. 6.4b). The main difference is that there is no evidence of negative ellipticity, due to the fact that the ADCP does not sample the water column above the pycnocline.

6.4. The effect of stratification on the tidal current profiles.

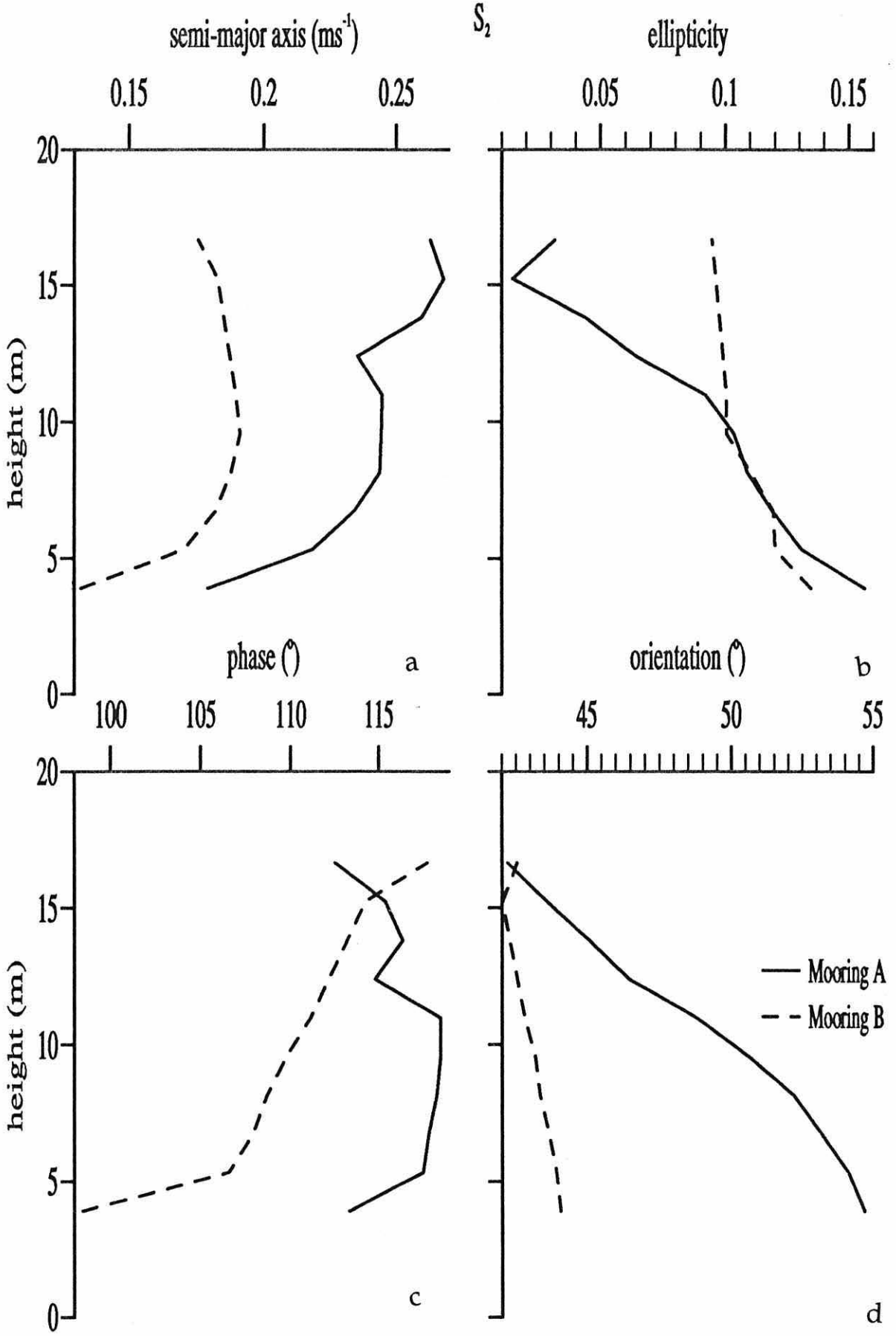

Figure 6.3 S_2 tidal ellipses profiles, from bottom-mounted ADCPs at mooring A (continous) and mooring B dashed, from 2 to 17 September 1992 (Julian days 248 to 261). a) semi-major axis, b) ellipticity, c) phase and d) orientation.

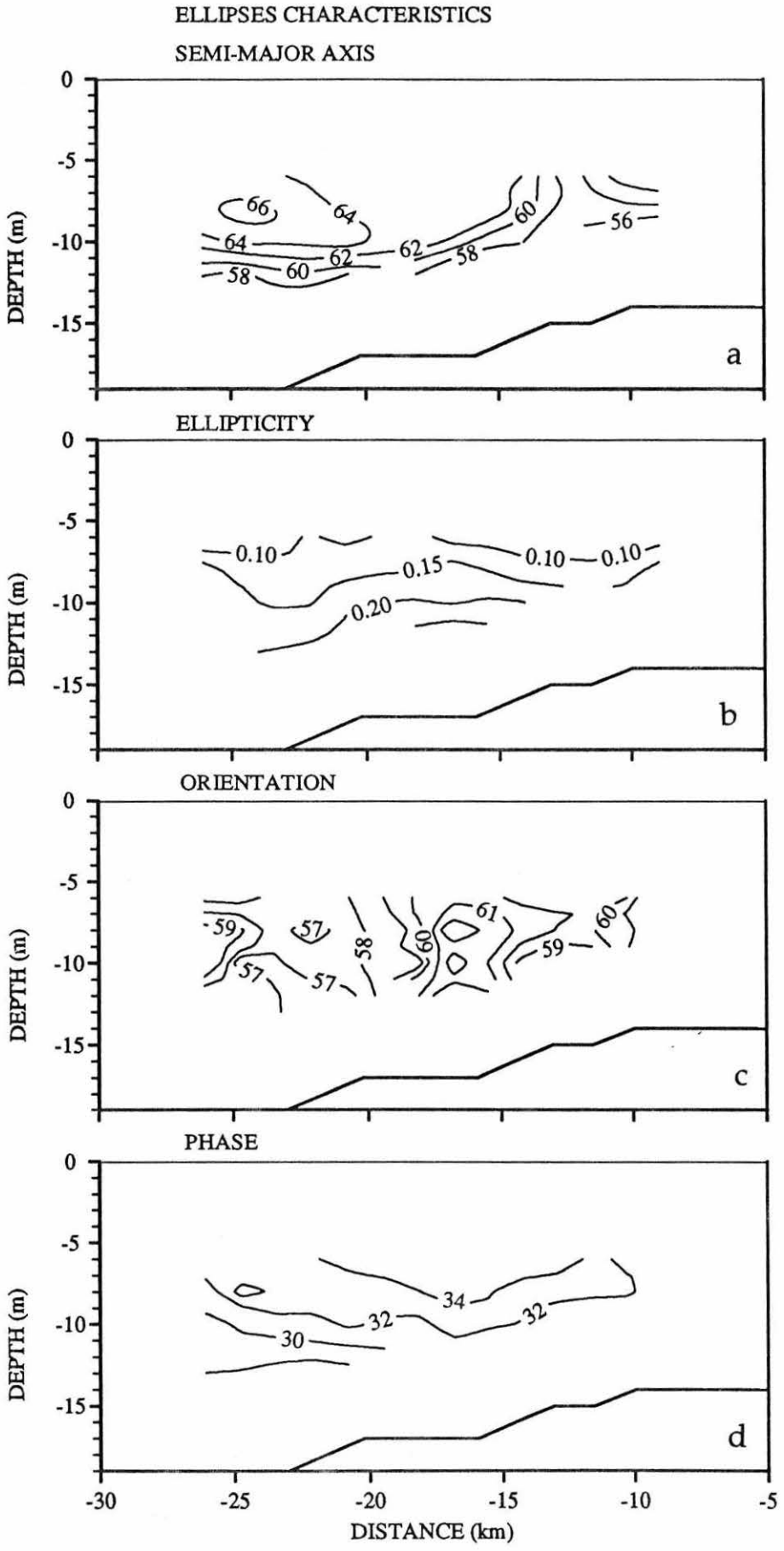

Figure 6.4 Tidal ellipses distribution allong line N from ship-mounted ADCP on Julian day 261. a) semi-major axis; b) ellipticity; c) orientation; d) phase.

The advantage of using HF radar is that apart from getting a large coverage in the horizontal, we are also able to measure the true surface velocity, within the first meter of the water column (Barrick *et al.*, 1977), so that, even in the case of a very shallow pycnocline, we will be able to see the effect that stratification has on the tidal currents.

We may illustrate the strong influence of stratification by dividing the time for which the CODAR was operating into mixed and stratified periods ($\Delta S>3$). During the former, the tidal ellipses are all close to being degenerate (fig. 6.5a), but during the stratified period the tidal ellipses become more circular with a clockwise sense of rotation inside the ROFI. Outside the stratified area, the ellipses remain almost degenerate with a slight anticlockwise rotation (fig. 6.5b). It is interesting to note from figure 6.5b, how the region where the tidal ellipses are degenerate (*i.e.* the boundary between clockwise and anticlockwise rotation) coincides with the ROFI frontal region.

Furthermore, if we combine the current meter data with the HF data, we are able to generate a profile of the tidal currents. To asses the time evolution of the ellipses, we divided the data into 25 hour periods and then proceeded to apply a harmonic analysis for M_2 as explained in chapter 4. The time-depth variation of the tidal ellipse at mooring B are presented in figure (6.6). During well-mixed conditions (*e.g.* days 280 to 285) the general pattern is of near bottom anticlockwise rotation decreasing with height above the bed, until the surface ellipses have become almost completely degenerate with very little anticlockwise rotation. However from day 285, with the onset of stratification, the surface tidal ellipses become strongly clockwise while the bottom layer remains anticlockwise and the near bottom ellipticity even increases. Another interesting feature is that the orientation of the ellipses varies with stratification, the surface ellipses change their orientation slightly to the east relative

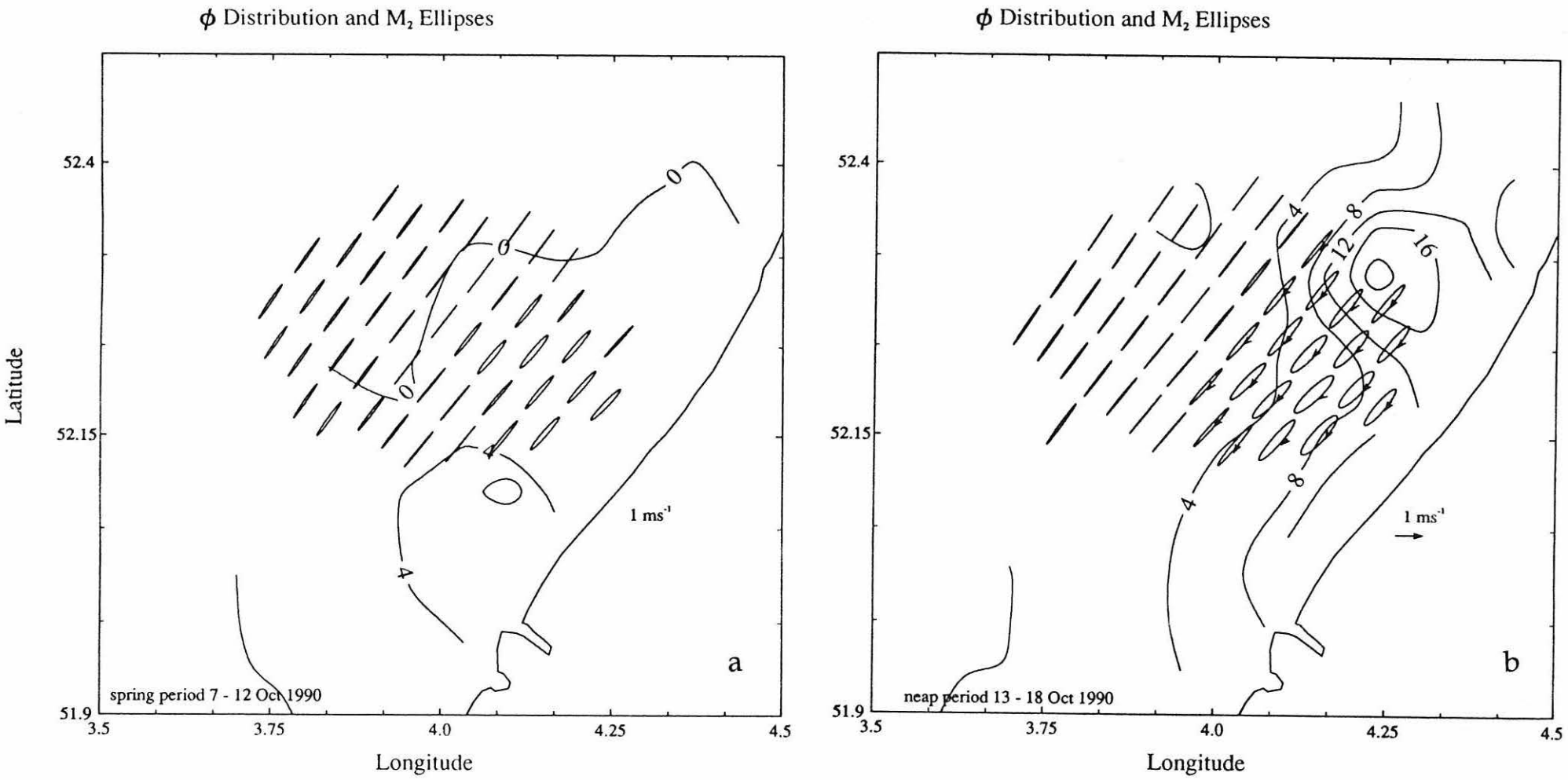

Figure 6.5 Spatial distribution of the surface semi-diurnal tidal ellipses during mixed (a) and stratified (b) conditions, as mapped by the HF radar CODAR.

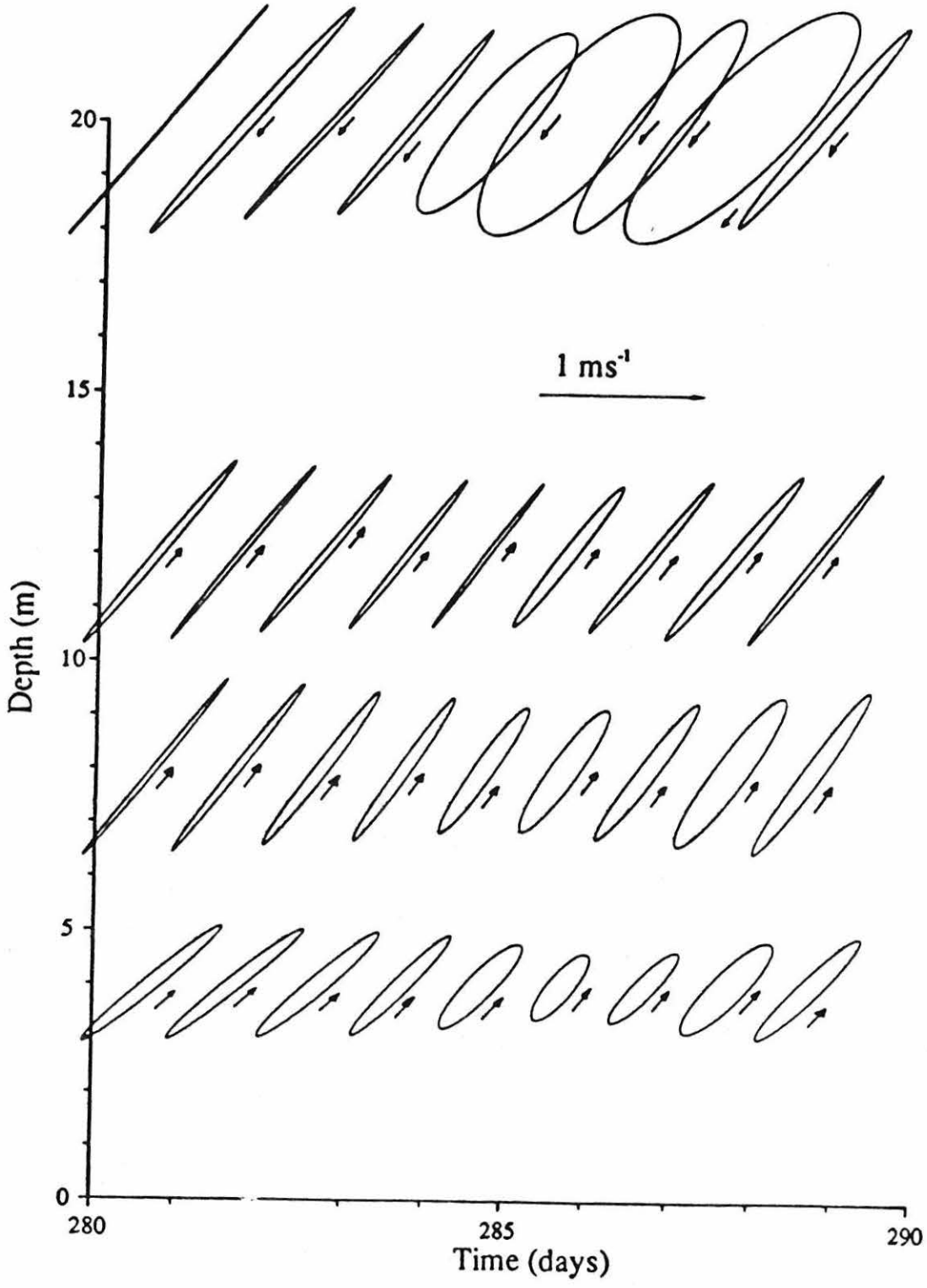

Figure 6.6 Vertical structure of tidal ellipses at a location 19 km from the coast on the Scheveningen transect during the 1990 campaign. Surface currents are from CODAR and subsurface from current meters at mooring B. Note the change between mixed and stratified conditions on day 285.

to the bottom ellipses. This has also been observed in the RWS mooring 3 km from the coast (Visser *et al.*, 1994).

Similar behaviour is observed in the horizontal, as the time evolution of tidal ellipses plotted against distance from the coast is shown in figure 6.7. The ellipses inside the stratified area between 5 and 20 km from the coast, show moderate positive ellipticity at the beginning of the observations but become strongly clockwise with the onset of stratification on day 285. They revert to being anticlockwise again on day 291 when the water column has re-mixed. The ellipses nearest to the coast, at 5 km, show more pronounced effects of stratification, with larger ε and tend to be oriented more eastward than those further offshore.

Although during the 1992 campaign we did not have the surface measurements from the HF radar, the use of high frequency bottom-mounted ADCPs allowed us to observed the currents within 3m from the surface and hence to be in the surface layer which has a depth of 5m under normal circumstances. ADCP also gives us a better vertical resolution. These time series of velocity profiles were analyzed in the same manner as the time series of the CODAR and current meters in the 1990 campaign.

Time series of the vertical profile of tidal currents at moorings A and B moorings are presented in figures 6.8 and 6.9 respectively. Figure 6.8 shows the profile for mooring A which was stratified during part of the observational period (fig. 6.8a); clear evidence of changes in the ellipse properties with time and depth are observed. The semi-major axis is oriented approximately parallel to the coast with an angle of about 45°at the surface and slightly increasing with depth to about 60° near the bed (fig. 6.8d). The semi-major axis at the surface is about 60% larger than at the

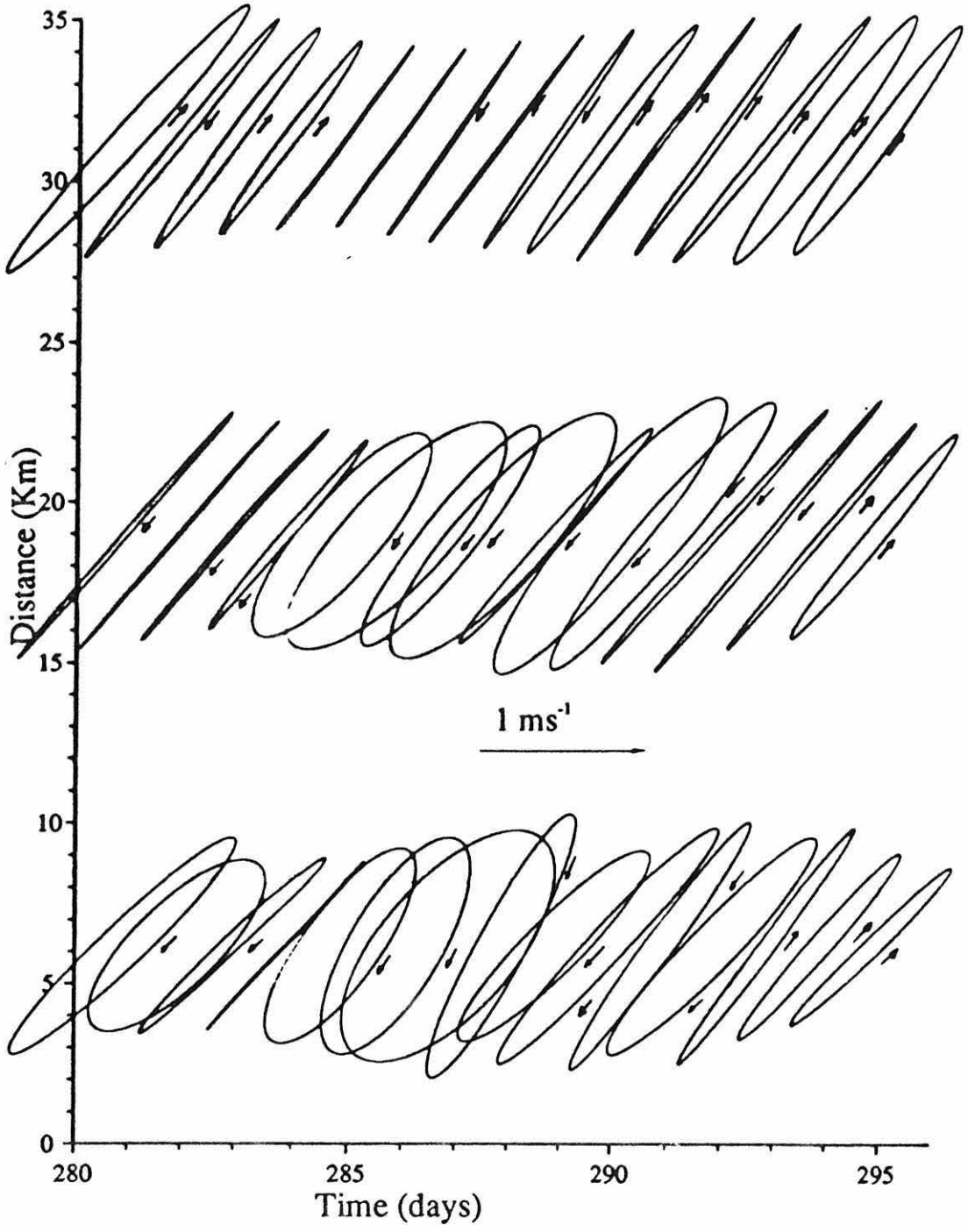

Figure 6.7 cross-shore eveolution of the tidal ellipses from CODAR data at 5 20 and 30 km off-shore, from CODAR observations.

bottom, with surface values greater than 0.8 ms^{-1} (fig. 6.8c). It is also clear that the bottom ellipses rotate anti-clockwise (ε~0.2), while the surface ellipses rotate clockwise (ε~-0.2) at times (fig. 6.8b).

In the stratification time series, plotted as the difference between bottom and surface density (fig. 6.8a), we note three periods in which stratification was present, from day 250 to 252, between days 254 and 255 and from day 256 to day 259. The effect of stratification is apparent in the presence of stronger negative ellipticity near the surface, with values of about -0.2, while the negative values of ellipticity are not apparent during periods of complete or almost complete mixing. This means that during periods of stratification the surface current is rotating clockwise, while the bottom current is anti-clockwise.

Another apparent effect is the increase of the surface maximum current, specially during the periods centred on day 255 and on day 258. This should be interpreted carefully, however, due to the fact that this period coincide with spring tides when stronger currents are expected, although the homogeneous case does not show such a large surface velocity.

In the case of mooring B (fig. 6.9) where stratification is negligible throughout the observational period (fig. 6.9a), the vertical profile of tidal currents behave in accordance with the theory for the homogeneous case (*i.e.* Prandle, 1982). There is no strong vertical structure at any time in ellipticity, there are almost degenerate ellipses everywhere in the entire water column , with slightly stronger anticlockwise rotation near the bottom ($\Delta\varepsilon$~0.05) (fig. 6.9b). The semi-major axis (fig 6.9c) has maximum near the surface during the first three days, but from day 252 on there is a weak maximum

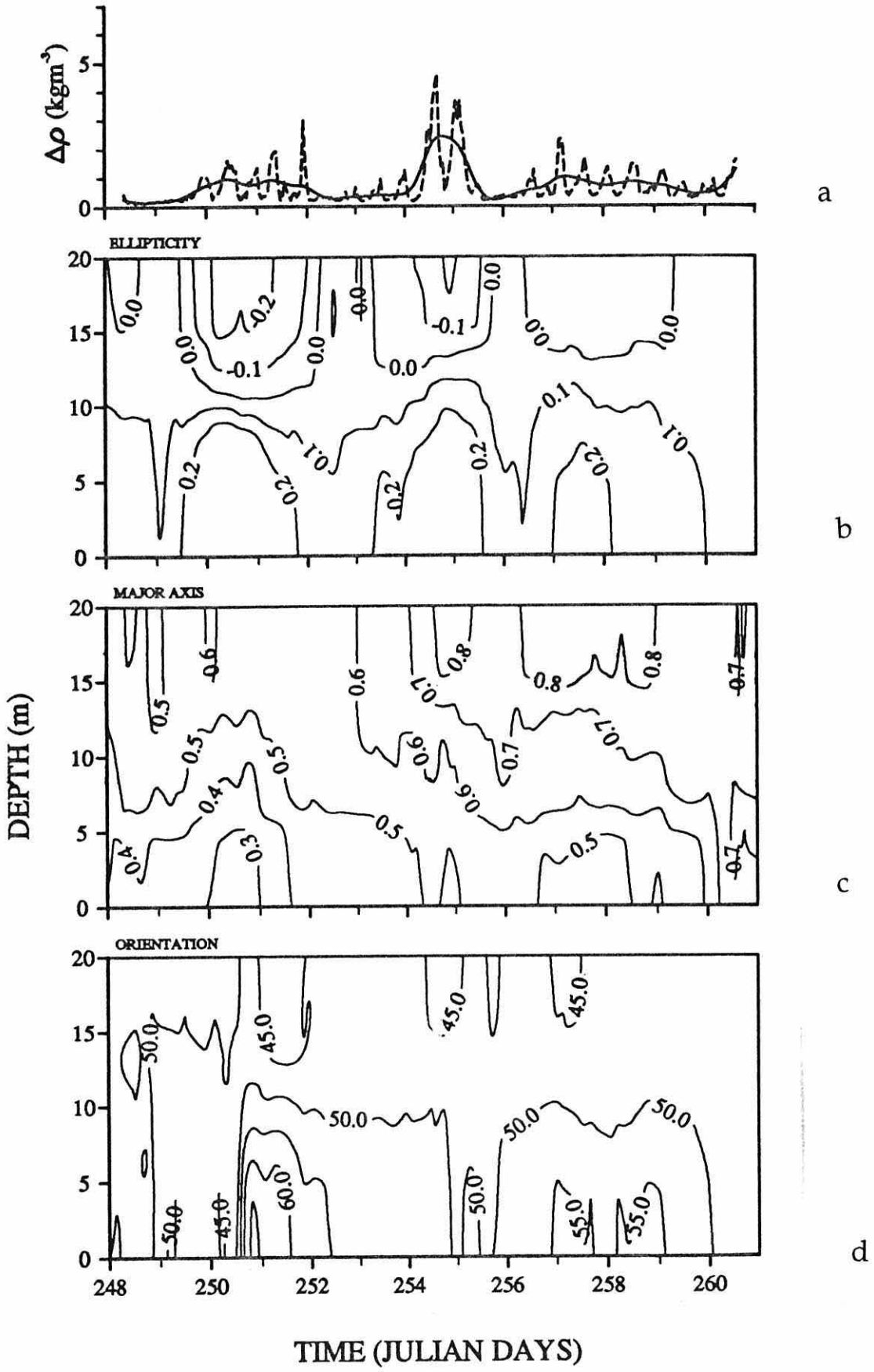

Figure 6.8 Time series of ellipse characteristics and water column stratification at mooring A (20 deep). (a) The density difference between bottom and top current meters; the continuous line represent the mean stratification averaged over two tidal periods while the dashed line is the instantaneous value. (b) Ellipticity ε from bottom mounted ADCP data. (c) Semi-major axis of the ellipse in ms^{-1}. (d) Orientation of the ellipse major axis in degrees (positive anti-clockwise from the east).

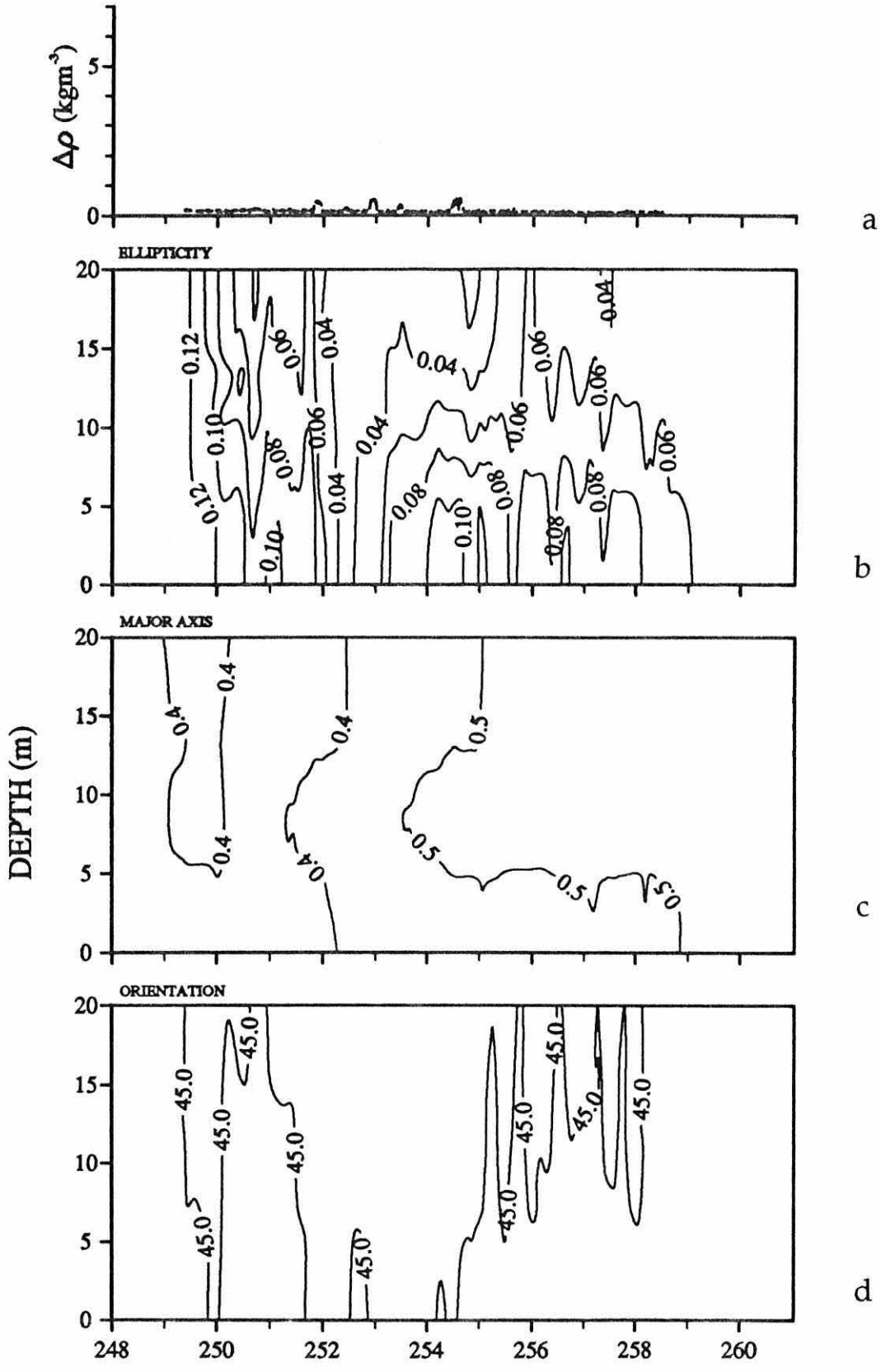

Figure 6.9 Time series of ellipse characteristics and water column stratification at mooring b (20 deep). (a) The density difference between bottom and top current meters. (b) Ellipticity ε from bottom mounted ADCP data. (c) Semi-major axis of the ellipse in ms^{-1}. (d) Orientation of the ellipse major axis in degrees (positive anti-clockwise from the east).

in mid-water, at a depth of about 12 m. This could be explained using homogenous theory (Prandle, 1982) : when the value of the eddy viscosity is small the pressure gradient and the stress gradient may be in phase. Similar profiles have been observed during January in the North Sea (Howarth,1994).

6.5. Interpretation.

We need to consider the problem of tidal flow in two directions on a rotating frame (the Earth) under the influence of frictional stresses. The motion, in which the particle trajectories are elliptical in form, may be decomposed into anti-clockwise and clockwise components. The characteristic boundary layer thickness for these two components is given by (Prandle, 1982a):

$$\delta_{-} \sim \left(\frac{2 N_z}{(\omega - f)} \right)^{\frac{1}{2}}$$

for clockwise motion and

$$\delta_{+} \sim \left(\frac{2 N_z}{(\omega + f)} \right)^{\frac{1}{2}}$$

for anti-clockwise motion, where ω is the frequency of the tidal constituent (M_2 for this case), N_z is the eddy viscosity and f the Coriolis parameter. Outside these bottom boundary layers the tidal oscillation is not influenced by frictional stresses and is depth independent.

At the latitude of the Rhine ROFI, f~1.15 x 10^{-4} s^{-1} is close to ω= 1.41 x 10^{-4} s^{-1},

so that

$$\frac{\delta_+}{\delta_-} = \left(\frac{\omega - f}{\omega + f}\right)^{\frac{1}{2}} \approx 0.3$$

The very different scales for the clockwise and anticlockwise boundary layers accounts for the general tendency for rotation of the current ellipse to become more clockwise with increasing distance from the seabed. Fig. 6.10a illustrates this for the case of equal clockwise and anti-clockwise components at the surface which produces a degenerate ellipse with rectilinear tidal flow. Near the bed the boundary layer structure reduces the clockwise component U_c relative to the anti-clockwise U_{ac} so that the resultant ellipse exhibits anti-clockwise rotation.

Consider next what happens when the water column becomes stratified while the tidal forcing remains the unchanged (fig. 6.10b). The effect of water column stability is to reduce the eddy viscosity N_z in the vicinity of the pycnocline with the consequence that the upper layer is largely de-coupled from frictional influence. The surface current ellipse thus acquires a clockwise rotation, while the near bottom current ellipse becomes more anti-clockwise due to the restriction of the frictional influence to the layer below the pycnocline, as we have observed.

6.6 Summary.

The combined results from the 1990 and 1992 campaigns exhibit strong evidence of the influence of stratification over the tidal currents. From the CODAR

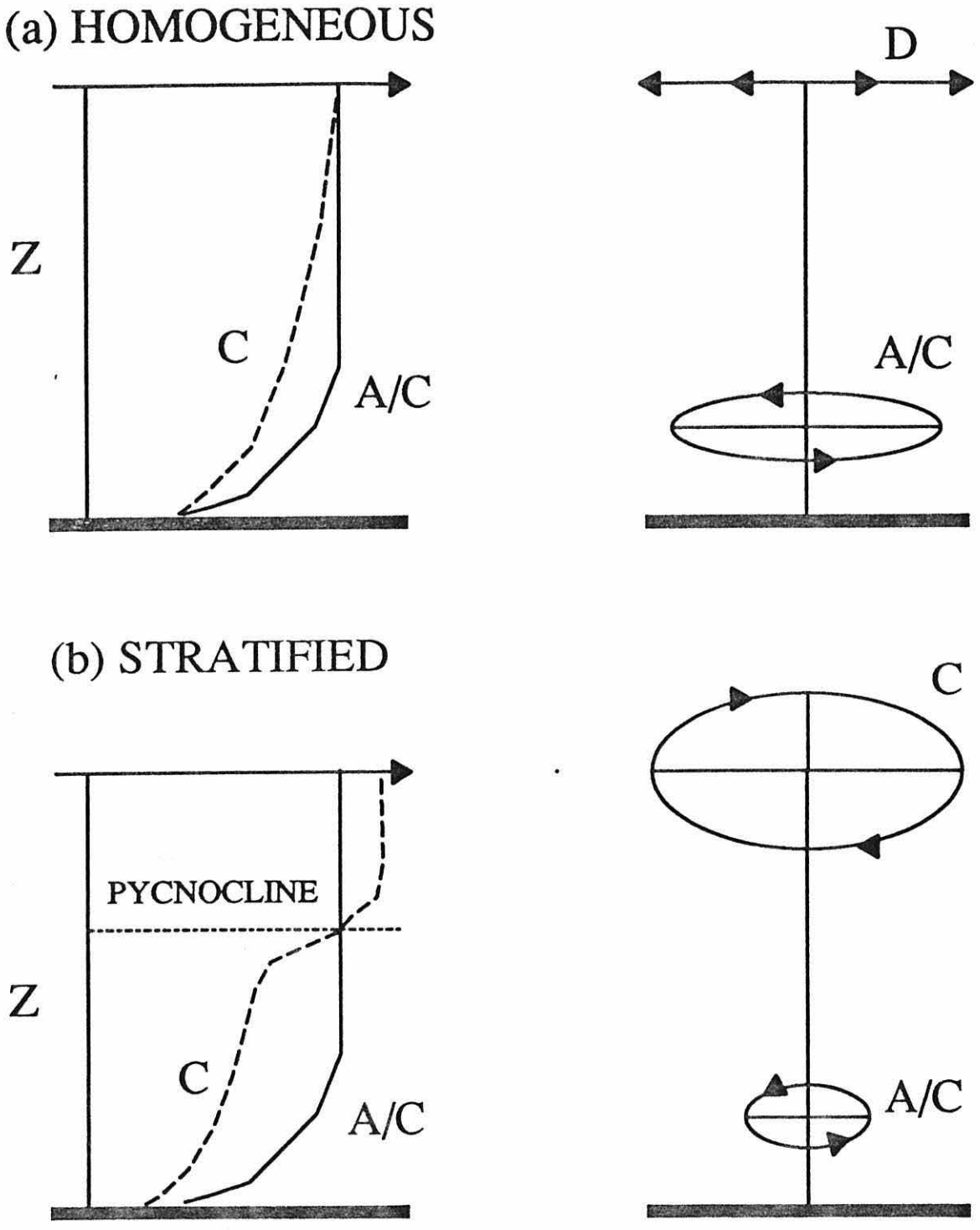

Figure 6.10 Schematic of the vertical profile of the clockwise and anti-clockwise rotary components and ellipse configuration. a) for the homogeneous case when N_z is constant. b) for the stratified case when N_z is reduced at the pycnocline.

observations the region in which the effect of stratification is felt has been delimited to about 20 km off-shore, which is the same length of the ROFI. Inside the ROFI the ellipticity changes from clockwise at the surface to anti-clockwise at the bottom, while outside the stratified area the ellipses are anti-clockwise throughout the water column and tend to be degenerate at the surface. At the outer boundary of the ROFI, the tidal ellipses become degenerate.

Inside the ROFI the tidal velocity profile changes with time due to the changes in water column stability. Both the 1990 and 1992 data sets suggest a close correlation of the changes in ellipticity (ε) and stratification. This can be explained by the changes in N_z, due to stability and stirring, which control the level of coupling between surface and bottom layers and that this change in coupling influences the clockwise and anti-clockwise motions to a different extent.

CHAPTER SEVEN

WIND-DRIVEN FLOW

7.1. Introduction.

According to Giessen *et al.* (1990), the subtidal circulation in the Dutch coastal zone is driven by wind and buoyancy as well as by tidal rectification. In this chapter we will attempt to determine the wind-related low frequency currents and subtract them from the non-tidal flow to obtain the residual.

The method used to analyze the wind forcing, which has been discussed in chapter 4 was first used by Prandle (1987). It is based on Ekman's idea that the windstresses generates a circulation which is proportional to them and rotated due to the effect of the earth rotation. The method uses a complex least squares technique to find the transfer factor (A) and the angle of rotation (θ).

The complex least squares technique was applied to the 1990 CODAR data to map the surface wind effect and to the 1992 bottom-mounted ADCP data to observe the wind effect behaviour in the vertical.

7.2. Surface Currents.

The surface currents, for 1990, gathered by the CODAR, show a transfer factor A=3% near the coast to about 20 km off-shore, where A decreases to 2% (fig. 7.1a).

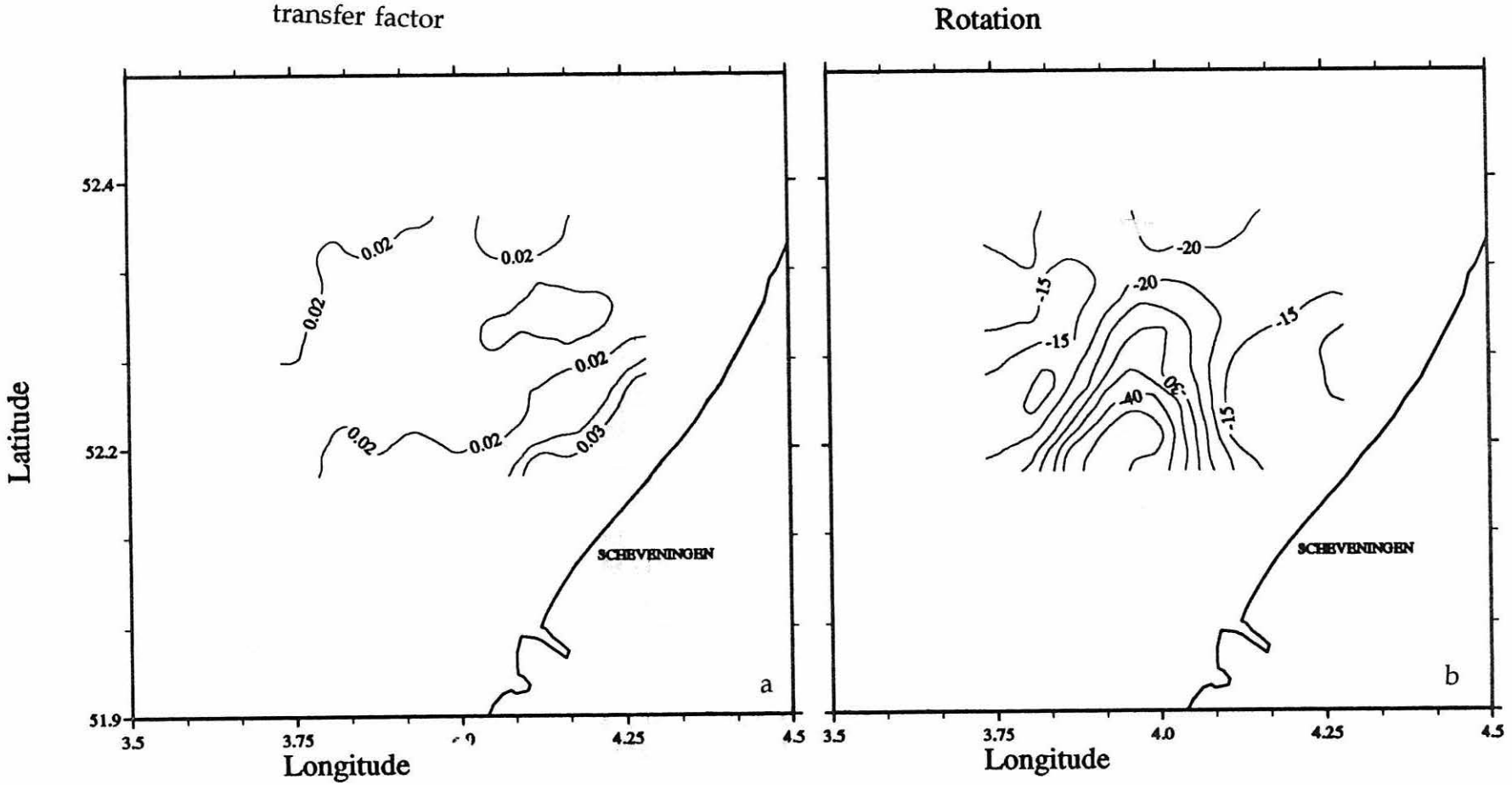

Figure 7.1 Wind analysis for surface currents mapped by CODAR, from 7 to 23 October 1990. a) Transfer factor; b) rotation.

The rotation angle (fig. 7.1b) lies between 15° and 45° clockwise, with the maximum values in a "tongue" located in the centre-south of the CODAR area.

The percentage of the explained variance (R^2) ranges between 55% in the stratified zone and 80% in the mixed area, with the isolines bunching near the haline frontal area (fig. 7.2).

7.3 Vertical structure.

For the bottom-mounted ADCP data collected in 1992 the profile of A (fig. 7.3a), for mooring A in the stratified area, shows a decrease from 1.2% near the surface to 0.45% near the bottom with a relative minimum at mid water (12m), while for the mooring B in the mixed region the transfer factor ranges between 0.35 and 0.5 % with a maximum at mid water (7.3a). The veering angle for mooring A exhibits (7.3b) changes between 70°, at the top bin 4m from the surface, to 140°, in the bottom bin. For the mixed region (mooring B), there is less variation with the veering changing from 100° near the surface to 140°at about 4m from the bottom.

Interesting results are present in the values of R^2 (fig. 7.4), with relatively high values near the surface (30%), decreasing to less than 15% at a depth of 4m and then rapidly increasing to about 35% at about 12 m deep followed by a decrease below 6m. This is characteristic of both moorings, although the mid-water minimum is not as marked in the mixed region.

7.4. Discussion.

In general we can say that the surface currents are rotated to the right of the

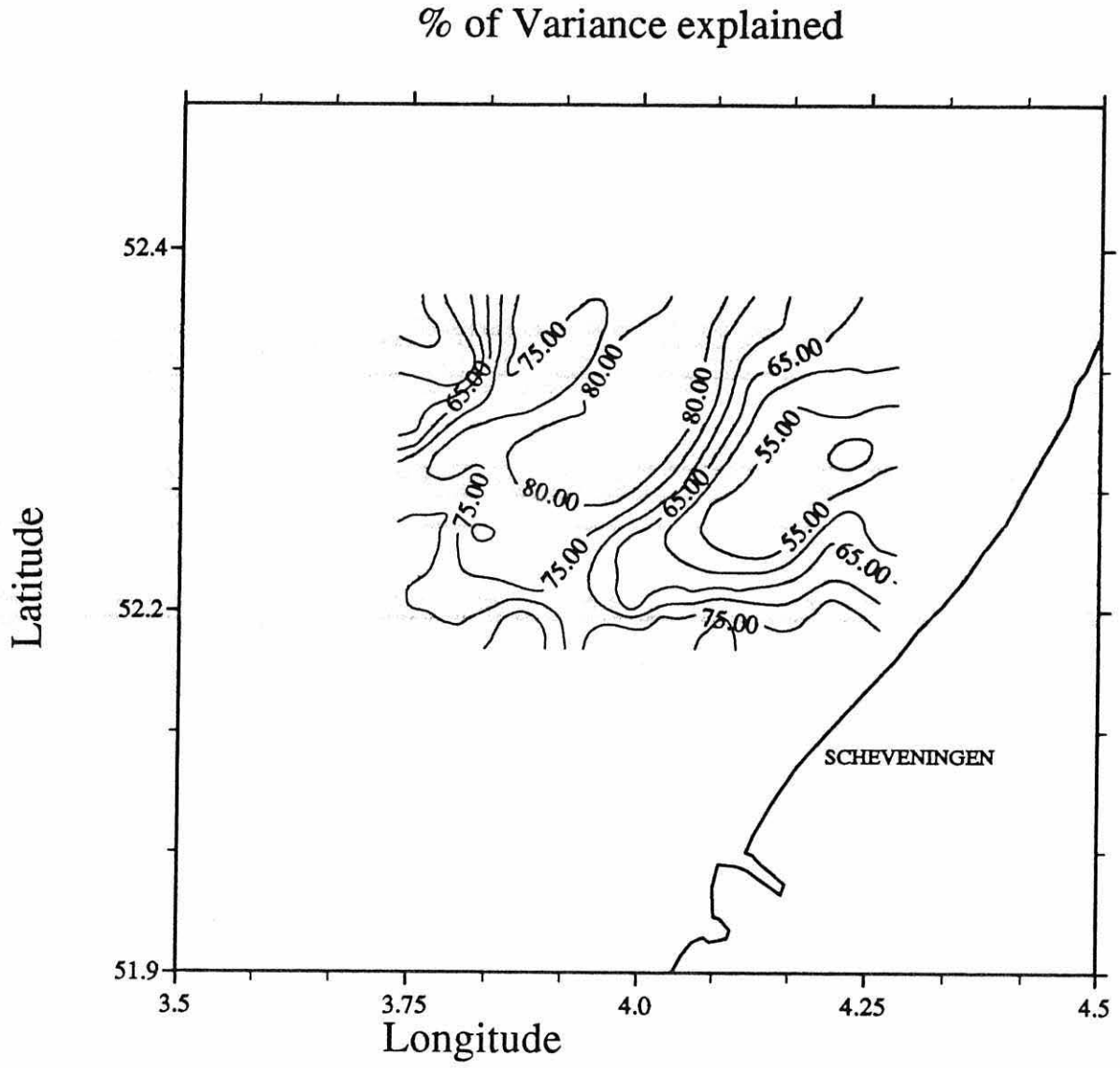

Figure 7.2 Percentage of variance, of the non-tidal currents, explained from the wind analysis.

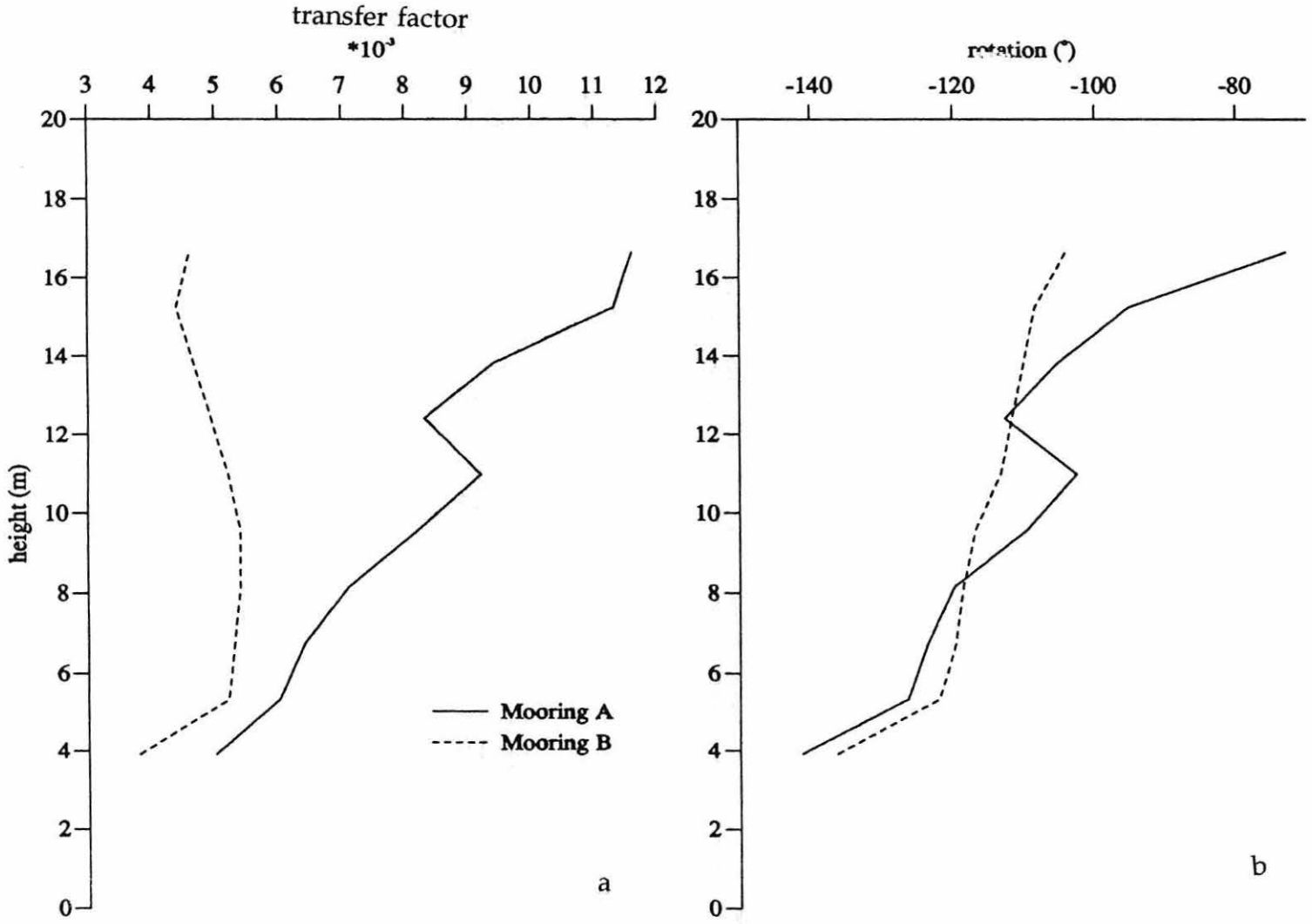

Figure 7.3 Vertical profile of the wind transfer function from moorings A (continuous) and B (dashed) bottom-mounted ADCPs, from 2 to 17 September 1992. a) transfer factor; b)rotation.

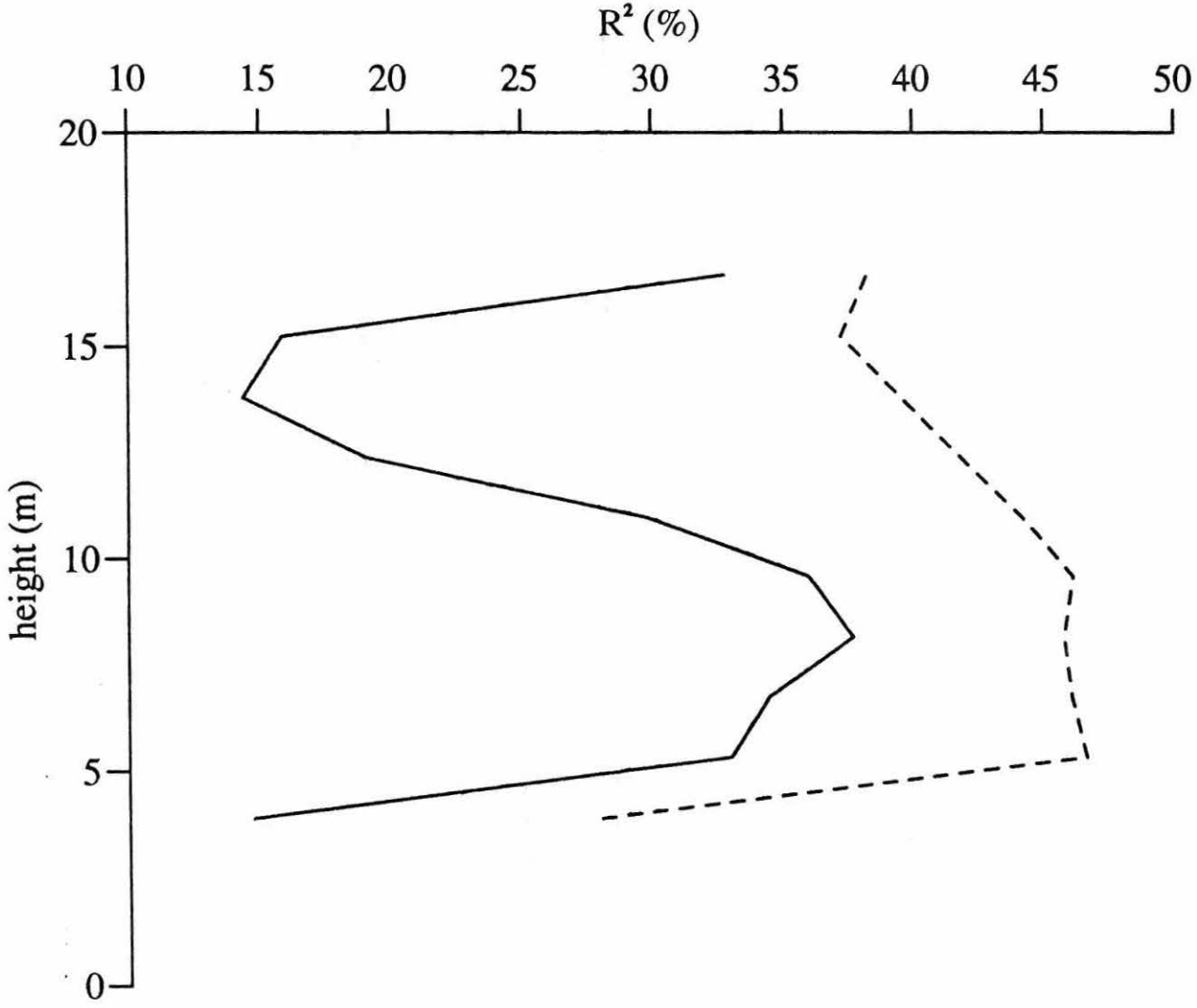

Figure 7.4 Vertical distribution of the explained variance from the wind analysis of non-tidal currents at moorings A (continuous) and B (dashed), from 2 to 17 September 1992.

wind between 15° and 45°, and decreasing with depth. The near-bottom currents almost oppose the wind (Δ~140°). The transfer function of the wind ranges between 2% at the surface to 0.3% near the bottom. The above results are in fair agreement with Ekman theory and with previous observations in the North Sea by Prandle, 1987; Prandle and Matthews, 1990.

Some differences are apparent between the stratified and mixed regions, in both the horizontal and vertical distribution. The surface maps suggest that the transfer factor is larger inside the stratified area, while the explained variance is lower. This suggests that the presence of stratification concentrates the wind effect in the surface layer. The vertical profiles of reduction factor and rotation angle exhibit different behaviour in the stratified and mixed areas. The stratified area (mooring A) has a surface-bottom difference of 0.8% for the reduction factor and of 70° for the rotation angle, in contrast with the mixed case (mooring B) where the vertical changes in transfer factor and rotation angle are smaller (*i.e.* ΔA~0.015% and Δθ~40°).

The effect of stratification is to decouple the bottom layer from the wind effect. In consequence there is a reduction in the transfer function and the explained variance near the pycnocline. The effect of stratification in decoupling the wind-induced currents can be observed directly in the subtidal currents from the RWS current meters for the mooring 3 km from the coast on the M section (fig. 7.5). At the start of the time series the water column is mixed and there is strong correlation between the wind, the near surface currents and the near bottom currents. However, with the onset of stratification about 6 days later the bottom residual current is largely decoupled from the surface flow, while the surface currents and wind remain correlated.

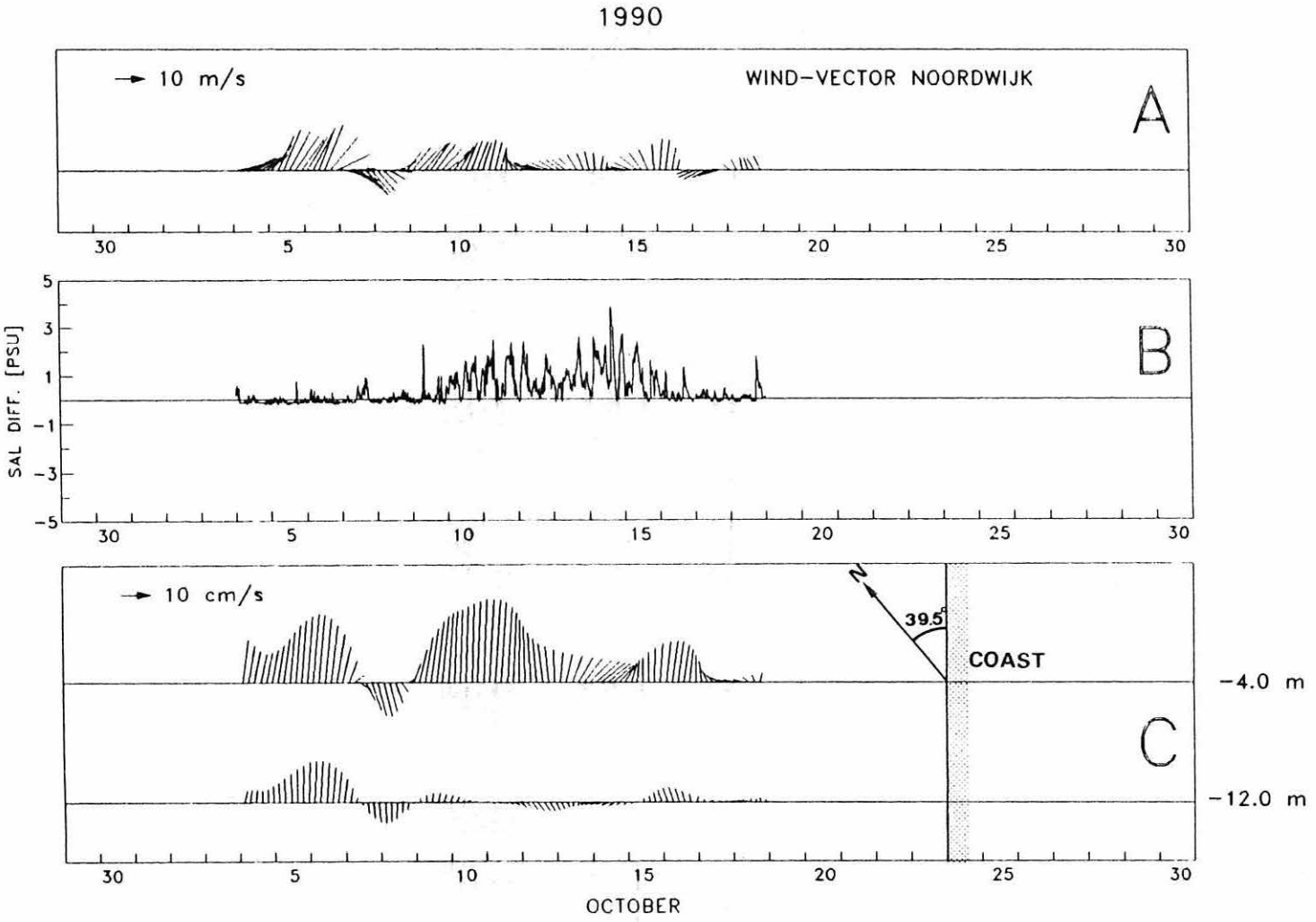

Figure 7.5 Time series 3 km from the coast from 3 to 18 October 1992. a) wind vector at Noordwijk 10 m above the ground; b) Salinity difference between 5 and 9 m deep; c) Current residuals at 4 and 12 m deep. Both wind and currents have been rotated clockwise through 39.5°, so that the vector lie parallel and perpendicular to the coast. as indicated in panel c.

Proximity to the bottom boundary reduces the transfer factor and the explained variance, in accordance with previous observation and analytical models (Prandle, 1987; Prandle and Matthews, 1990).

CHAPTER EIGHT

DENSITY-DRIVEN FLOW

8.1. Introduction.

In the previous chapters we have managed to extract the tidal and wind influence on the velocities in the Rhine ROFI, so the only components left should be those due to tidal rectification and the density-driven circulation.

The horizontal density gradients maintained by the input of freshwater from the Rhine tend to drive an estuarine circulation in the ROFI. The influence of variable tide and wind stirring, however, modulates this flow as illustrated in the laboratory experiments of Linden and Simpson (1988). At the scale of the Rhine ROFI, the flow is further complicated by the influence of the Earth's rotation, which limits the cross-shore transport. Under conditions of geostrophic balance, the cross-shore density gradients drive an along-shore flow, forming a coastal current flowing from the estuary source with the land on its right (looking down current) in the northern hemisphere, as described in chapter 1. The Rhine ROFI is, however, a very shallow region, so that bottom friction becomes important and the balance is not completely geostrophic. A solution for such flows, given by Heaps (1972), has been discussed in more detail in chapter 2.

The strong gradients at the outer edge of the coastal current constitute the ROFI frontal region in which we might expect strong horizontal convergence. Such

convergence has been observed in tidal mixing fronts using HF radar (OSCR) and ship-borne ADCP data (Hill *et al.*, 1993); and is also suggested by remote sensing in the Rhine ROFI (Ruddick *et al.*, 1994).

In this chapter the remaining residual currents (after removing the wind effect), will be considered as the baroclinic circulation. We will try to locate the position of the convergence zone and the frontal jet, as well as making comparisons with theoretical profiles (Heaps, 1972).

8.2 Horizontal distribution of the residual currents.

As we have discussed in the previous chapter, the wind accounts for a considerable percentage of the variance of the flow, especially at the surface. Figure 8.1a shows the total non-tidal residual currents in which we can observe a more or less coherent structure in the entire CODAR domain. The currents near the coast appeared to be 2 or 3 times greater than the currents off-shore and in a coast-parallel direction, except near to the coast and at the northern boundary of the domain. In the mixed region the currents are much smaller and generally to the north. Once we have removed the wind forcing (fig 8.1b), the currents in the stratified region become more coast-parallel to the north-east, while in the mixed region, the residual flow is very weak and variable in direction.

If we separate the flow into its cross- and along-shore components, for the 1990 CODAR observations (fig 8.2), we clearly observe both the coastal jet and the convergence zone. The off-shore component of velocity (fig. 8.2a),suggests a main convergence zone at about 24 km off-shore. The velocities range between 5 cms^{-1} off-

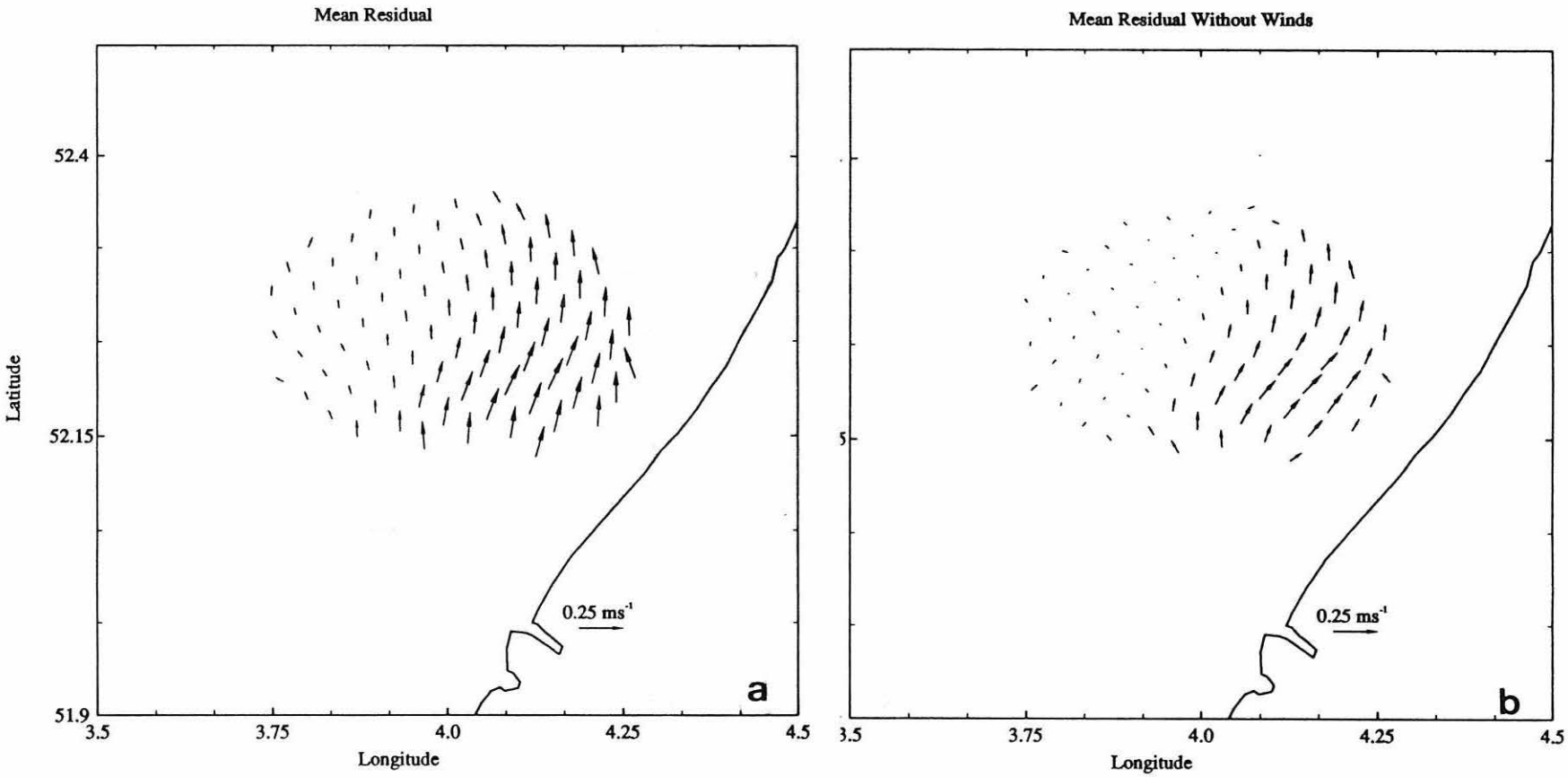

Figure 8.1 Surface Velocity vectors mapped by IFM CODAR from 7 to 23 October 1990. a) total long term residual; b) after removing the wind driven flow.

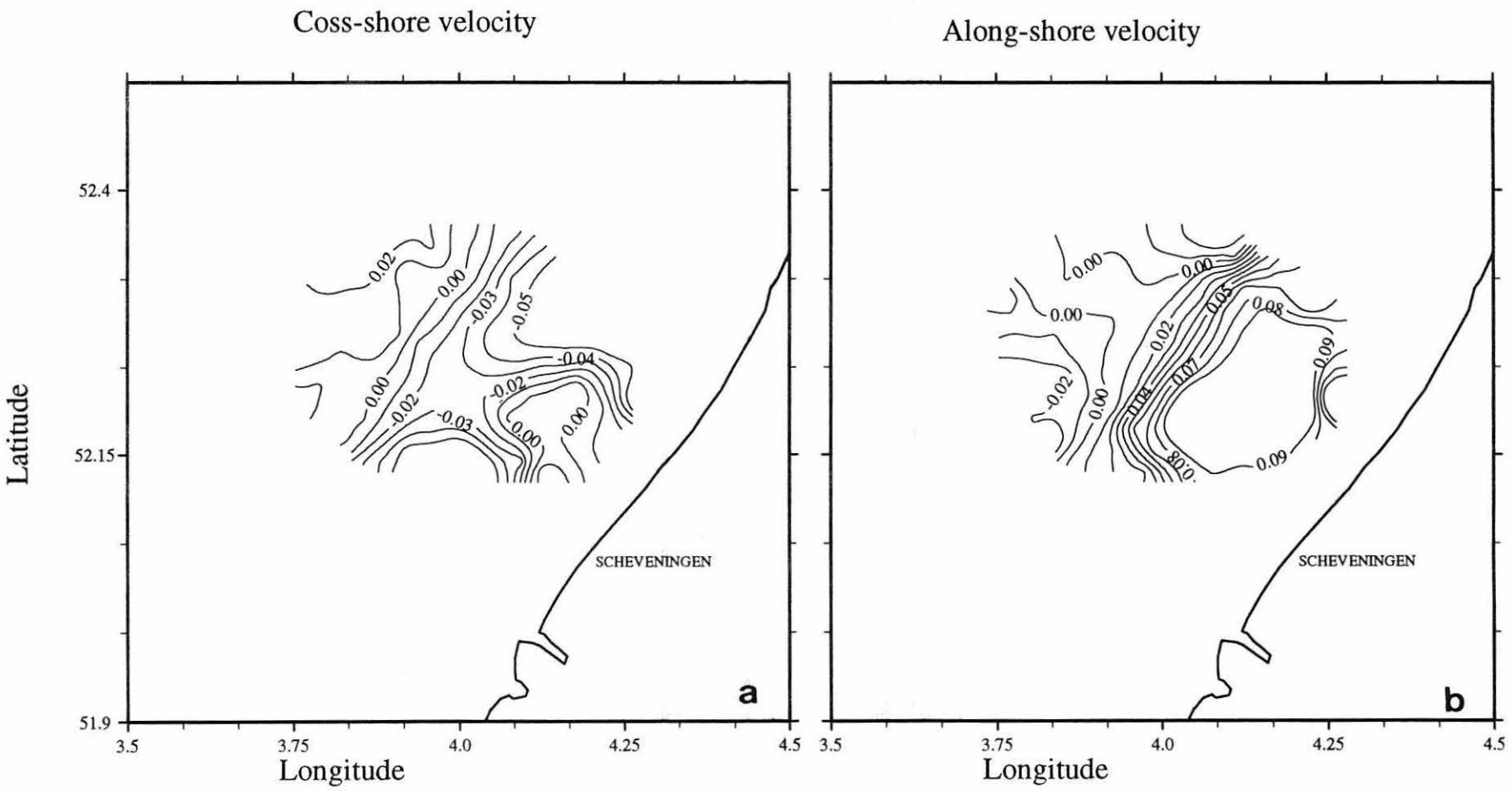

Figure 8.2 Surface velocity components after removing the wind driven component, between 7 to 23 October 1990. a) off-shore; b) along-shore.

shore near the coast, to 2 cms^{-1} coastward in the open sea. This convergence should be related to the ROFI frontal region. A small divergence region is observed at about 5 km offshore near the southern boundary of the CODAR domain,with a range in velocities between -2 and 1 cms^{-1}.

The coastal jet is clearly apparent in figure 8.2b. It is located between 10 and 20 km off-shore and has a magnitude of ~9 cms^{-1}. Beyond the jet there is a region of marked shear, with changes in velocity of about 8 cms^{-1} in 10 km.

We should note that the boundary of the jet coincides with the convergence zone at a distance of the order of 20 km off-shore, which is the approximate position of the Rhine ROFI frontal region during 1990 campaign.

8.3 Vertical structure of the residual current.

Estimates of the long term residual current profile should be available from mooring data from the 1992 campaign. If the main driving force of the currents is the density gradients, the velocities should be comparable to those proposed by the theoretical model of Heaps (1972). The residual flow vectors from the bottom-mounted ADCPs are compared with Heaps (1972) in figures 8.3 and 8.4. The Heaps profile is calculated using a depth of 20 m, a density gradient $\frac{1}{\rho}\frac{\partial \rho}{\partial x} = 2 \times 10^{-7}$ m^{-1} and $N_z = 2.5 \times 10^{-3}$ $m^2 s^{-1}$.

The data for mooring A (fig. 8.3) shows a fair correlation between observed and

theoretical velocity profile, and as expected the values of the residual after removing the wind are closer to the Heaps model. The main deviation from the expected values of velocity are near the bottom for the along-shore component. This is probably due to the tidal rectification residual.

For the case of mooring B (fig 8.4), outside the density gradient influence there is no similarity between the Heaps profile predicted and the observed profile of velocity, when using parameters for the Rhine ROFI. The velocity shows little variation in the vertical and has an amplitude between 1 and 2 cms^{-1}, which is similar to the value of the tidal residual predicted by vertically integrated models (Prandle, 1984) so we can assume that the residual in this mooring is entirely due to tidal rectification. We can also assume that the tidal residual will be more or less the same at the two mooring positions. Hence, we can the subtract the observations from mooring B from those of mooring A to obtain the pure density driven circulation (fig.8.5). However, for the cross-shore component there is little change, due to the fact that the main tidal residual in this area of the North Sea is oriented along the coast (see chapter 1). For the along-shore component there is clearly an improvement in the agreement between the observed data and the Heaps profile, especially near the bottom.

The Heaps (1972) approximation does not consider stratification so it will only give a first order approximation of the density driven currents in the Rhine ROFI. A different approach which allows for stratification, but does not consider friction may be achieved by geostrophic balance as given in the thermal wind equation:

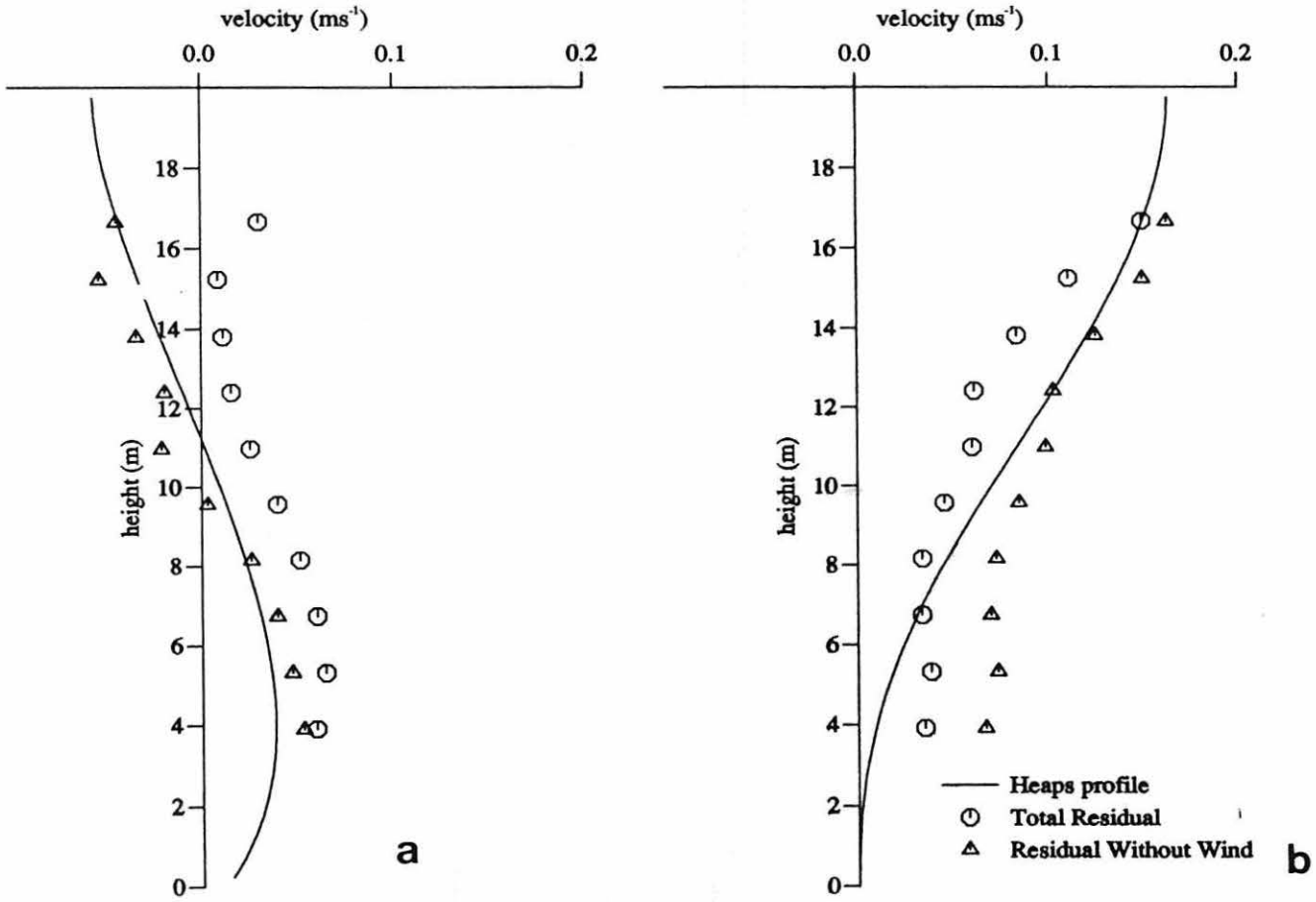

Figure 8.3 Vertical distribution of velocity as observed by the POL bottom-mounted ADCP at mooring A, between 2 and 17 September 1992; a) is the cross-shore component; b) is the along-shore component. Continuous line is the Heaps profile; octagons are the observed total long term residual; triangles are the observed long term residuals after removing the wind component.

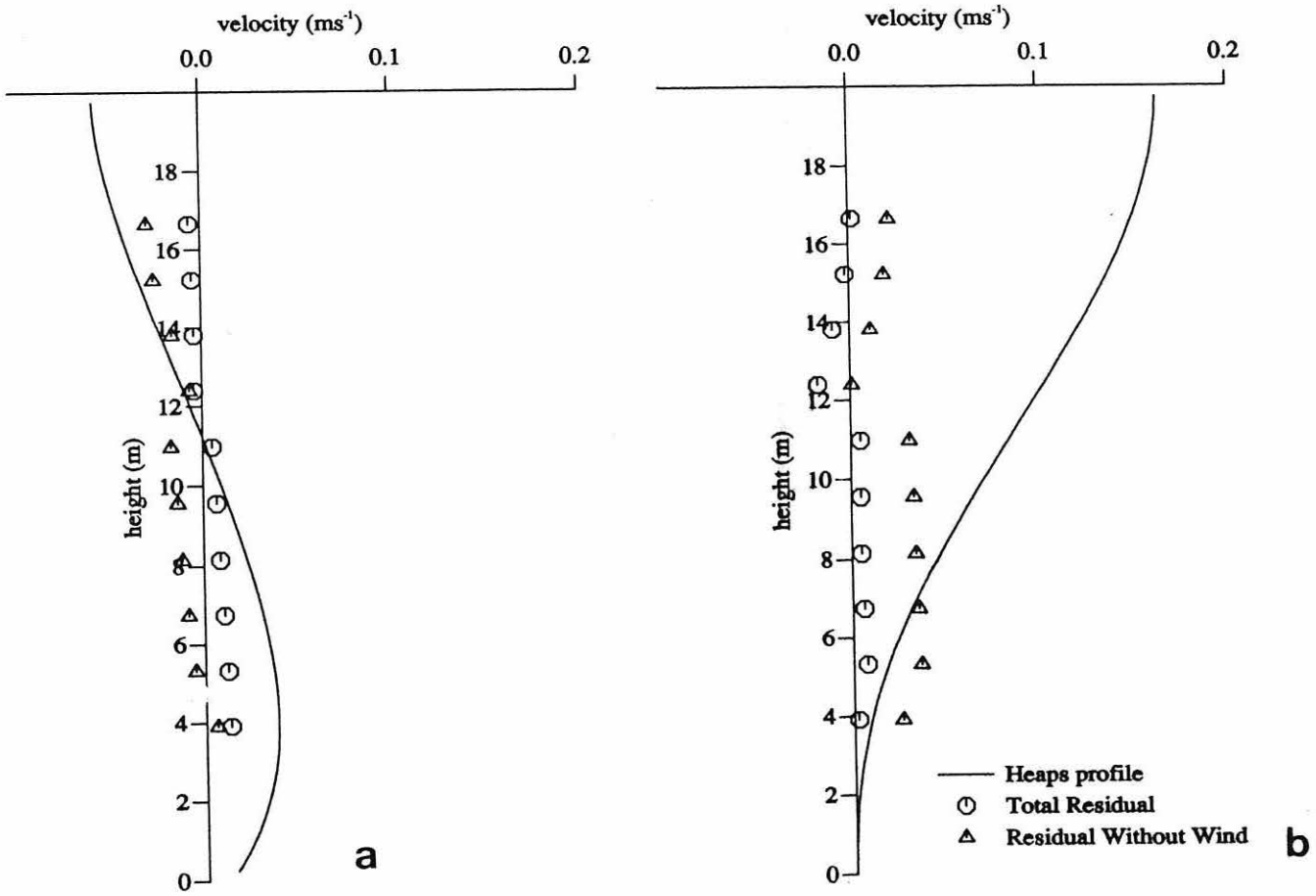

Figure 8.4 Vertical distribution of velocity as observed by the POL bottom-mounted ADCP at mooring B, between 2 and 17 September 1992; a) is the cross-shore component; b) is the along-shore component. Continuous line is the Heaps profile; octagons are the observed total long term residual; triangles are the observed long term residuals after removing the wind component.

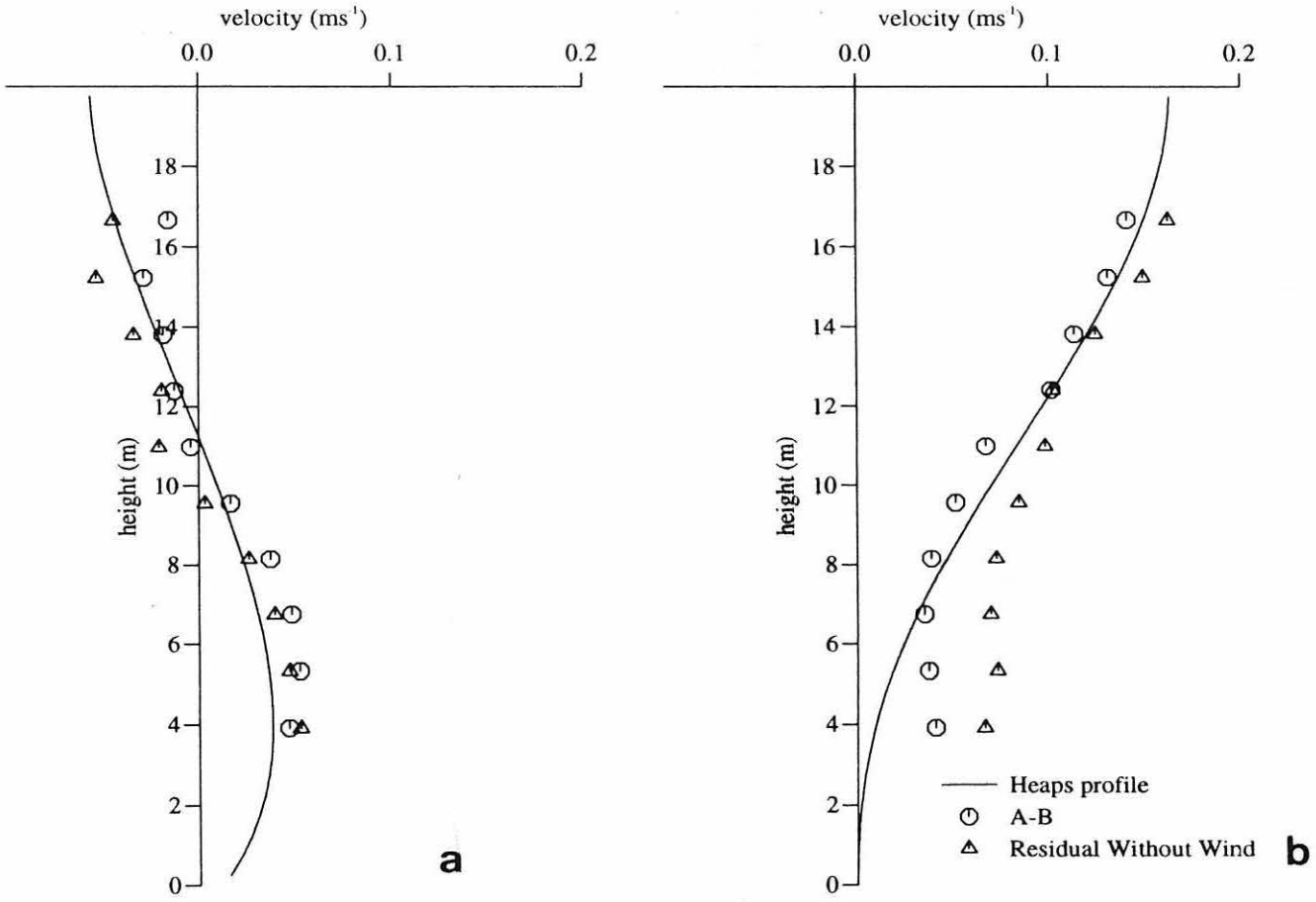

Figure 8.5 Vertical distribution of velocity as observed by the POL bottom-mounted ADCP at mooring B, between 2 and 17 September 1992; a) is the cross-shore component; b) is the along-shore component. Continuous line is the Heaps profile; octagons are the difference between observations at mooring A and at mooring B after removing the wind component; triangles are the observed long term residuals after removing the wind component.

$$\frac{\partial v}{\partial z} = -\frac{g}{\rho f}\frac{\partial \rho}{\partial x}$$

with v=0 level at the bottom.

The water column structure in the Rhine ROFI is stratified, at least during part of the tidal cycle. Figure 8.6b shows the mean water column structure at line N during a 25 hours between Julian days 260 and 261. The geostrophic flow (fig. 8.6a) shows strong shear between the bottom and surface (~ 10 cms^{-1}) and it is in qualitative agreement with observations using the ship-mounted ADCP (fig. 8.7).

8.4 Summary.

In general we can say that the freshwater from the Rhine creates a region of strong cross-shore density gradients which drive a quasi-geostrophic flow similar to that explained by Heaps (1972), but with additional effects from stratification. The density driven flow takes the form of a strong coastal jet extending about 20 km off-shore and with a maximum velocity of about 10 cms^{-1}. There is a related cross-shore convergence zone at 24 km off-shore. Outside the ROFI area the residual flow is weak and does not show any preferential direction.

The vertical distribution of velocity inside the ROFI area is explained, to a first order by Heaps (1972) quasi-geostrophic velocity profile. The strong density gradients generate a flow with strong alongshore velocities of the order of 18 cms^{-1} and moderate cross-shore component of about 5 cms^{-1}.

Evidence of the importance of stratification in driving the flow has been

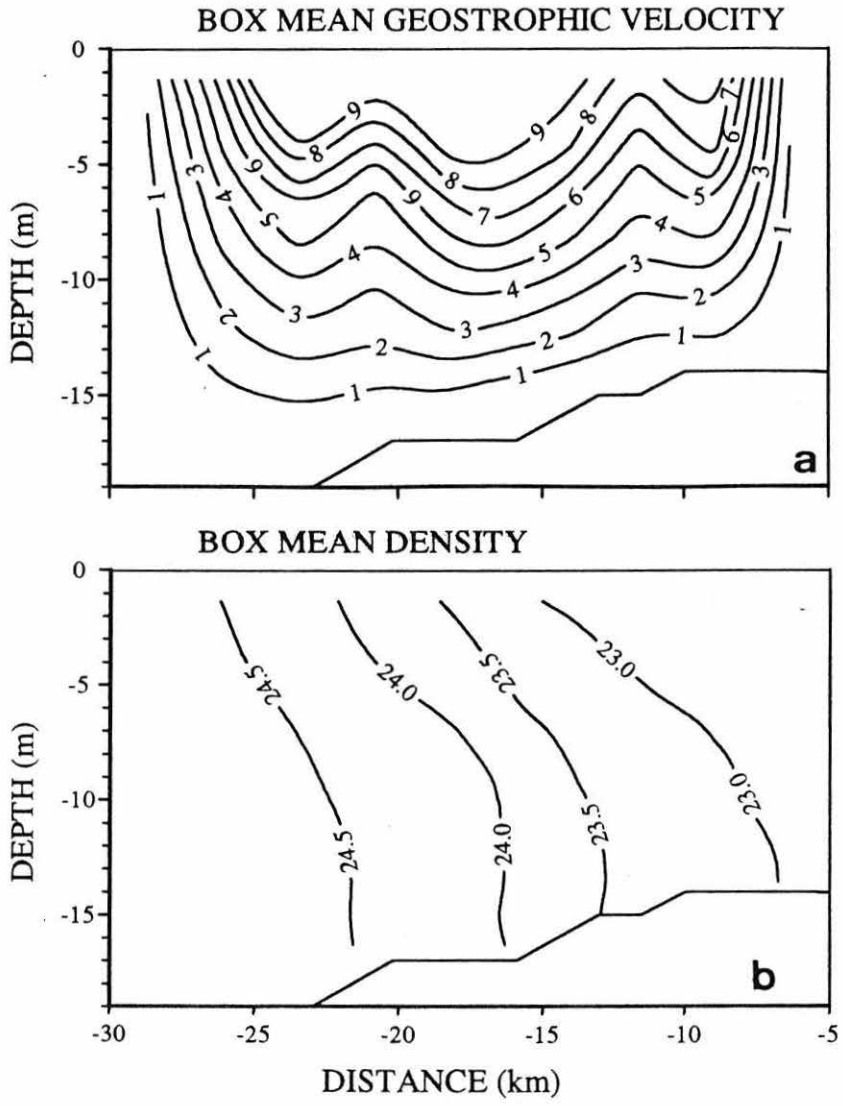

Figure 8.6 Geostrophic velocity calculated using the density structure from the 25 hours SEAROVER survey at line N on days 260 and 261 1992, reference to the bottom. a) mean geostrophic velocity; b) mean density structure.

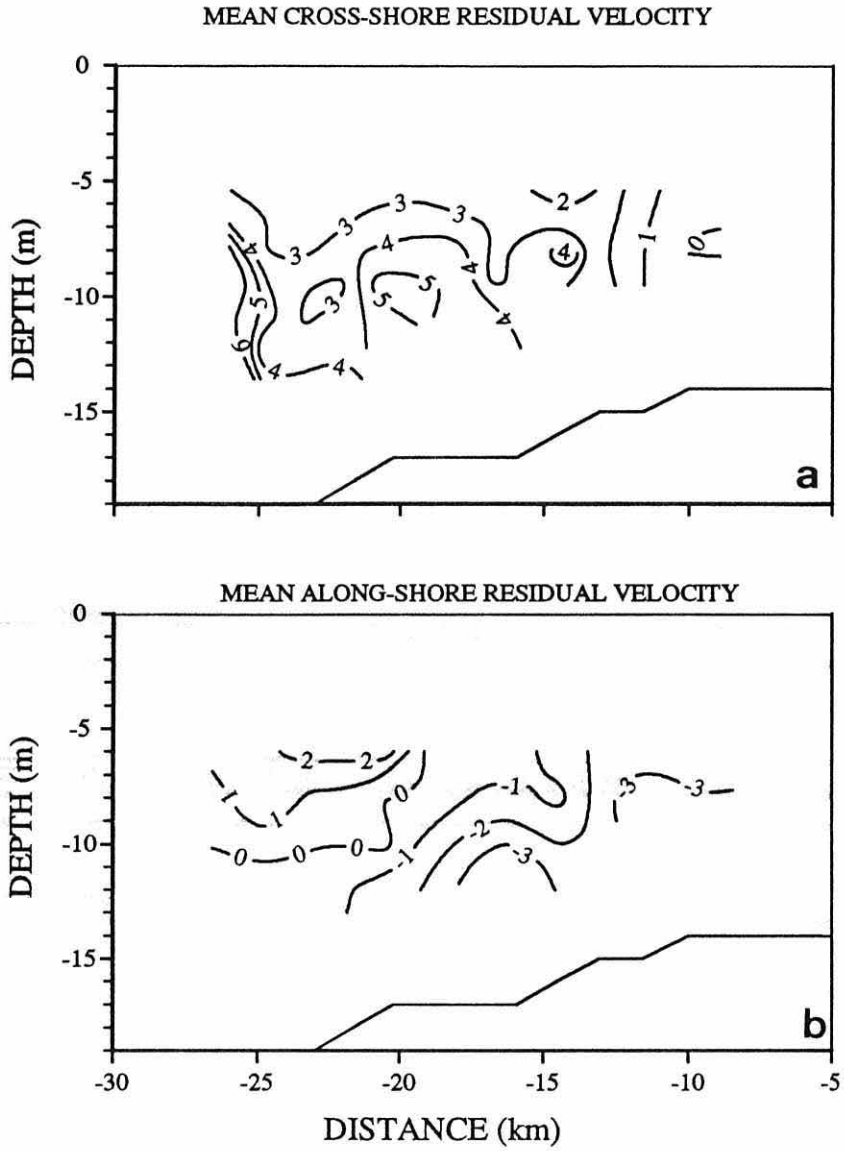

Figure 8.7 Velocities from the ship-mounted ADCP at line N between days 260 and 261 1992. a) cross-shore component; b along-shore component.

observed in the thermal wind calculations which predicts a vertical shear of about 10 cms^{-1} inside the ROFI.

CHAPTER NINE

SYNTHESIS

9.1. Introduction.

In this chapter we try to combine observations from chapters 5 and 6 and use them to elucidate the way in which the various processes involved interact to explain some of the complexity in the observed pattern of variability in structure, and in particular the occurrence of marked semi-diurnal variability in stratification. This will clarify the role of tidal straining as an important source of stratification in the region and will allow some conclusions about the origin of the cross-shore component of tidal shear to be drawn.

9.2 Space-time evolution of stratification.

In chapter 5 we discussed the rapid variability in water column stability and have addressed the problem of interpreting the quasi-synoptic sections and maps due to the effect that this variability could have in the ROFI area.

In the presentation of the SEAROVER survey data above, we have had to assume that the evolution of the temperature and salinity fields during the survey period can be neglected in constructing quasi-synoptic sections and maps. In many situation this forms a reasonable basis for interpreting the data, especially if we have evidence from fixed sensors that the time development of the structure is slow in

relation to the timescale of the survey.

It is clear from the observations in fig 5.16 that in the vicinity of the moorings there is a significant evolution of the density field even on short time scales due to the marked semi-diurnal variation in column structure. If this pattern of variation is a general characteristic of the stratified region, it would seem that time-dependent changes will be interpreted as spatial structures in mapping exercises. In order to test the notion that there is a general semidiurnal oscillation under stratified conditions, we have combined the SEAROVER data with the mooring data for the same period in fig 9.1. Surface to bottom density differences observed by the SEAROVER system when inside the ROFI (i.e. within 15 km of the coast) are plotted as a time series in parallel with $\Delta\sigma_t$ from mooring A. There is a significant coherence between the envelope of the SEAROVER data and the mooring observations which strongly suggests that the semi-diurnal oscillation is a general characteristic of the ROFI. Some differences in the phase of the data from fixed and moving sensors may be expected due to the change in the phase in tidal processes over the area.

In trying to explain the space-time evolution of stratification, we have applied an EOF analysis technique to the stratification observed by the SEAROVER. The density difference values were interpolated onto a 1 km by 1 hour grid. The result of this analysis should allow us to separate the space-time observations into two sets of functions: one over space, the other over time.

The EOF results (fig. 9.2) show that the only mode above noise level was the first mode with 75.30 % of the explained variance. The temporal function of the first mode (fig. 9.2a) appears to be related to the stratification and straining. If we compare

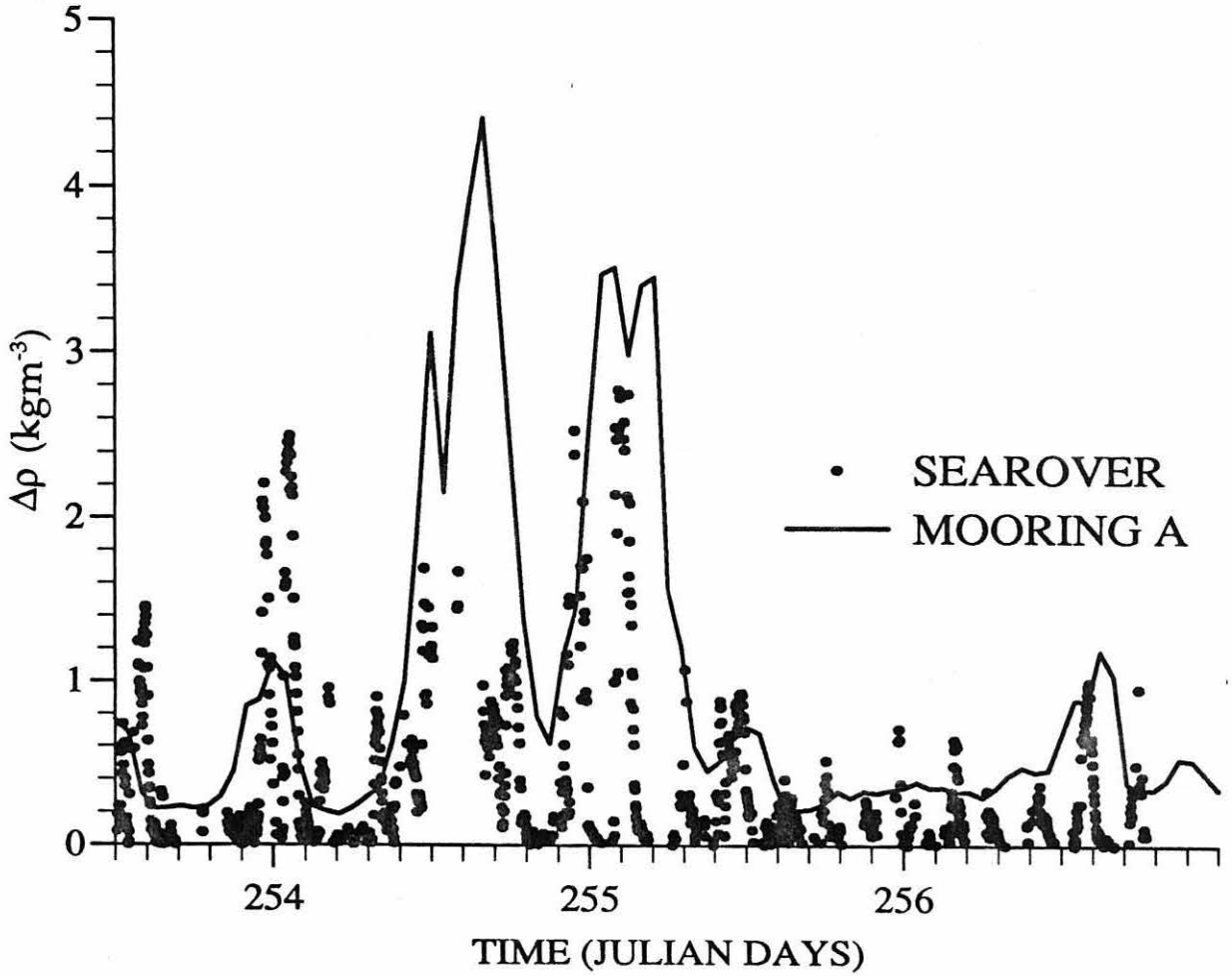

Figure 9.1 Time series of stratification expressed as the density difference between 1 m and 12 m deep. continuous line correspond to data from mooring A and the dots correspond to data from the SEAROVER inside the stratified area (15 km from the coast).

it with the mooring time series showed in figure 9.1 it is clear that the peak value from the temporal function corresponds with the peak in stratification on day 255. As the stratification decreases due to the combined effect of wind and tidal stirring the value of the temporal function also decreases. Two smaller peaks of stratification are present on days 255 and 256 which are also in agreement with the temporal function. Probably the most interesting result of the EOF analysis is that the temporal eigenvector (fig. 9.2b) indicates the width of the ROFI area and helps to define the frontal region. The temporal eigenvector exhibits large values (~0.4) near the coast and increasing off-shore, having a maximum at 14 km from the coast, and then rapidly decreasing to values of almost zero at 16 km offshore. This region of rapid change between 14 and 16 km from the shore is the frontal region for the mean period of study and the maximum in the vicinity of it will be a maximum in stratification, probably due to the intensification of the density gradients near the frontal region.

9.3 Interaction between mean water column stability and tidal shear in the production of semi-diurnal switching of stratification in the Rhine ROFI.

Semi-diurnal variations in water-column stability of this kind have been previously identified in other ROFI and estuarine regimes (Bowden and Sharaf el din (1966), Uncles(1992)), Simpson *et al.*, 1991) and attributed to the influence of tidal straining (Simpson et al. 1990). The amplitude of the semi-diurnal variation in the Rhine ROFI is, however, considerably greater in relation to the mean amplitude than in previously observed cases. Reference to the 1990 observations shows similar behaviour as illustrated in figure 5.4 with even larger oscillations in salinity stratification (amplitude ~ 4 salinity units) than we observe in the 1992 measurements.

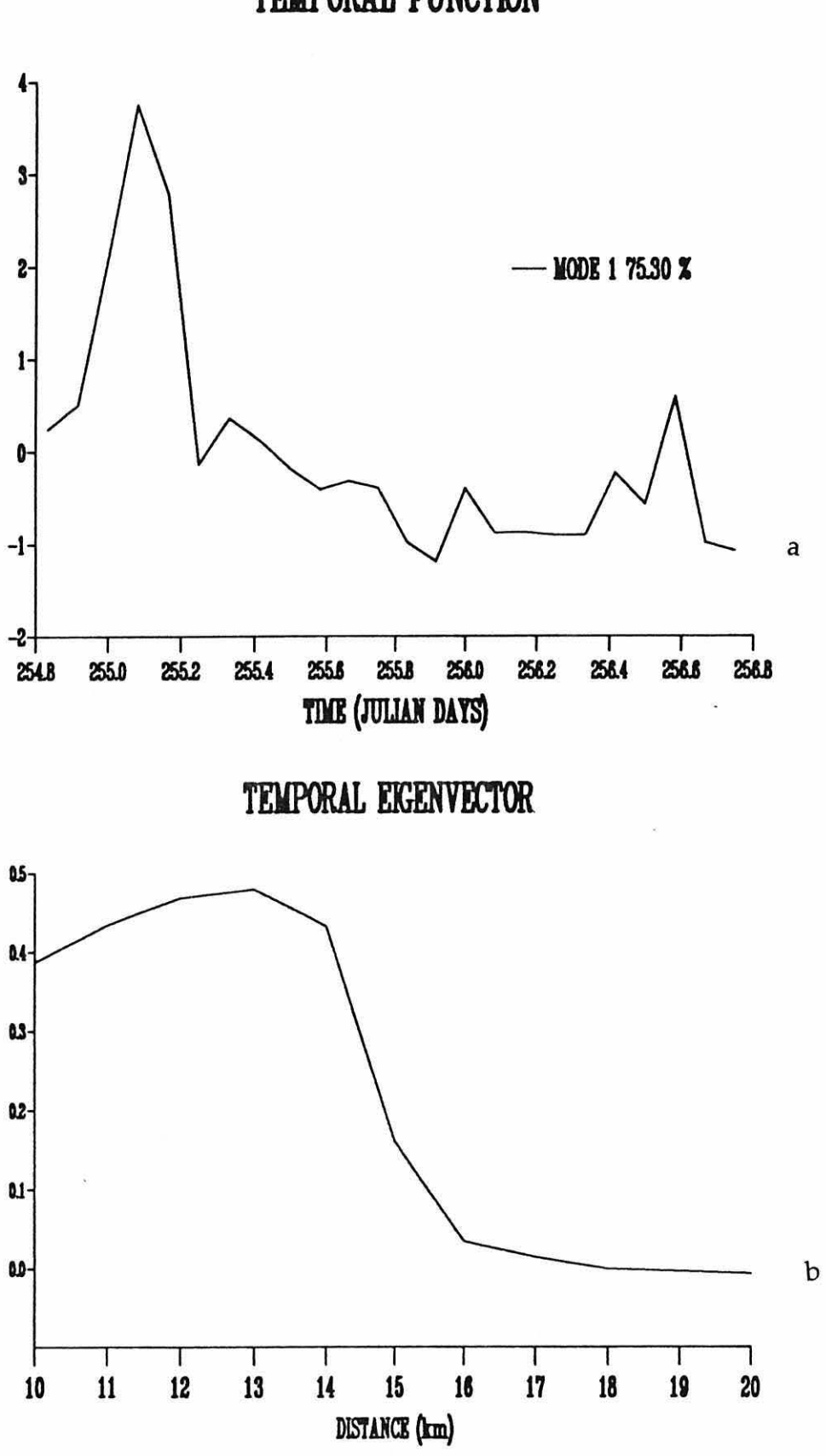

Figure 9.2 EOF mode 1, with 75.3 % of the variance explained, from the cross-shore density stratification as observed by the SEAROVER. a) is the temporal function; b) is the eigenvector.

The question then arises as to the role of tidal straining in the present case and whether or not other mechanisms are involved. As a first step in answering these questions we have plotted in fig 9.3 the density stratification alongside the relative tidal displacement (the cross-shore "straining") between surface and bottom water over a 4 day period. This, the more important of the two tidal straining components, has been computed in two different ways. In fig 9.3a a predicted shear displacement is obtained from tidal velocity constituents derived from harmonic analysis over the full duration of the record and shows that the straining signal has an amplitude of 1.5 km and is somewhat advanced in phase relative to the two large oscillations of $\Delta\rho$ on days 254-255.

In fig 9.3b the actual relative tidal displacement has been calculated by high pass filtering the ADCP data for the 4 day period. Prior to midday on day 255, there was a strong enhancement of the straining with a relative displacement of 7 km between current meters at depths of 4m and 16m. Following the onset of intense wind mixing on day 255 (fig 9.3c), the tidal shear signal was greatly reduced. These changes in the straining signal are clearly reflected in the $\Delta\rho$ variation suggesting that straining is the primary process driving the semi-diurnal stratification cycle.

Neglecting the effects of mixing we may estimate the range of $\Delta\rho$ from straining alone according to:

$$\Delta\rho = \Delta X \frac{\partial\rho}{\partial x} \qquad (9.1)$$

For a typical cross-shore gradient of 2.5 kg m^{-3} per km and relative displacement ΔX= 7 km, we have $\Delta\rho \sim$ 1.75 kg m^{-3} which is of the right order though somewhat less than the observed value on day 254. This may be due to our under-

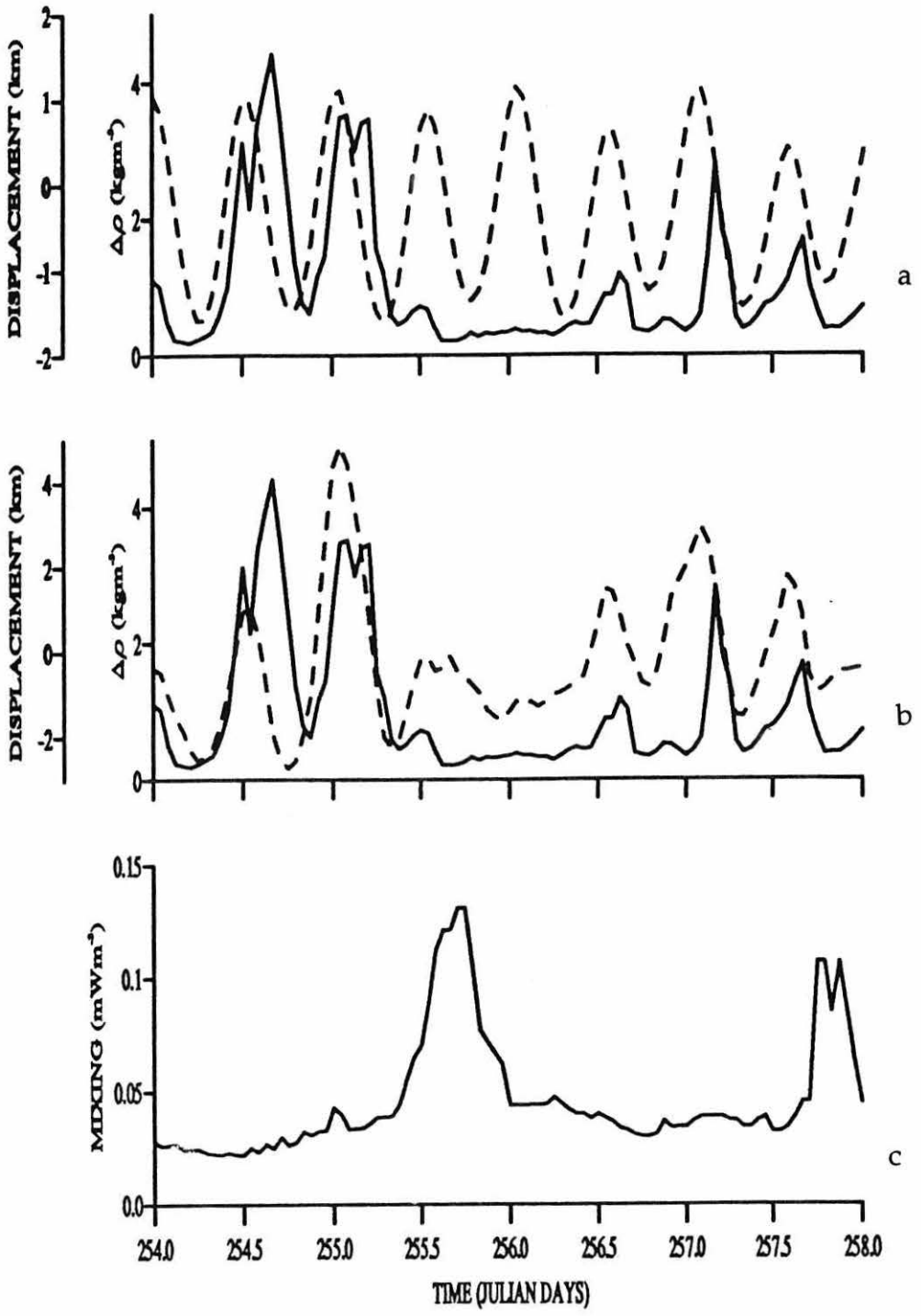

Figure 9.3 Tidal straining and periodic stratification:
(a) time series of stratification (continuous line) and tidal displacement (dashed line); the displacement is calculated using 6 tidal constituents (M2, S2, N2, O1, K1, M4) from the top bin (3m deep) relative to the bottom bin (17m deep) from a 1.2 MHz ADCP at mooring A; positive displacement is off-shore;
(b) as a but the displacement is calculated from the high-pass-filtered velocities.
(c) estimates of the combined wind and stirring power for the same period.

estimating the effective straining since the upper ADCP bin is 4m below the surface while the surface density is measured at 1m depth and previous measurements of surface currents indicate the presence of significant near-surface shear. As well as increasing the amplitude of the tidal straining, the missing component of near surface shear may also be responsible for the apparent phase lag between the stratification and the straining although mixing effects may be involved in delaying the time of maximum stratification. We also have to consider that the amplitude of the density gradient varies during the observational period by up to five times the mean value.

9.4 Conceptual model.

A striking feature of the observations is the relatively large cross-shore straining which evidently operates during periods of stratification and which provides the primary drive for the semi-diurnal oscillation. This straining with a relative displacement of surface and bottom waters of ~ 7 km is large in relation to the average amplitude of the cross-shore tidal flow. It appears to be associated with the change in the shape of the tidal ellipse which is brought about by the development of mean stratification as discussed in chapter 6. Whereas at times of complete vertical mixing, the tidal ellipses are close to being degenerate (i.e. near rectilinear motion) when the system stratifies the surface ellipses exhibit pronounced clockwise motion while the near-bed flow becomes more anti-clockwise in character. The result is a strong increase in the cross-shore shear in the flow which produces the large relative displacements observed.

It should be noted that the phase of the tidal straining in relation to the elevation is quite different in this case from that observed in Liverpool Bay (Simpson

et al., 1991) where the tidal motion is almost a pure standing wave and minimum stratification tends to occur close to high water. In the present case (fig 9.4), the tide is better described by a Kelvin wave travelling to the north east along the Dutch coast and the maximum alongshore current occurs near local HW. The phase of the cross-shore shear during times of stratification is such that minimum stability occurs near low water.

On the basis of the above results we hypothesise that the mechanism responsible for the strong semi-diurnal variability in stratification involves the sequence of interactions illustrated in figure 9.5. Following a period of complete vertical mixing, when the isopycnals are vertical (fig. 9.5a), the density gradients start to relax under gravity as in the laboratory experiments of Linden and Simpson (1988). This relaxation is constrained by the effect of the earth's rotation, generating a coast-parallel flow (fig. 9.5b) as in the models of Ou(1983 and 1984). The stratification then induces changes in the tidal ellipses by de-coupling the surface and bottom layers, so that surface ellipses acquires clockwise rotation and the bottom ellipses anti-clockwise. The consequence is a strong cross-shore component of tidal shear (fig. 9.5c). The resulting off-shore tidal straining initiates oscillations in stability which combine with the mean stratification to give the observed pattern of stability variation with the system coming close to complete mixing in each tidal cycle. When the combined effect of wind and tidal stirring increases again (fig. 9.5d), vertical exchange is enhanced and the off-shore tidal shear is suppressed as the ellipses revert to near degenerate form and the stratification is broken down.

The analysis of the spatial survey suggests that the above series of processes are characteristic of the ROFI area. This region (~20 km wide) will be stratifying and

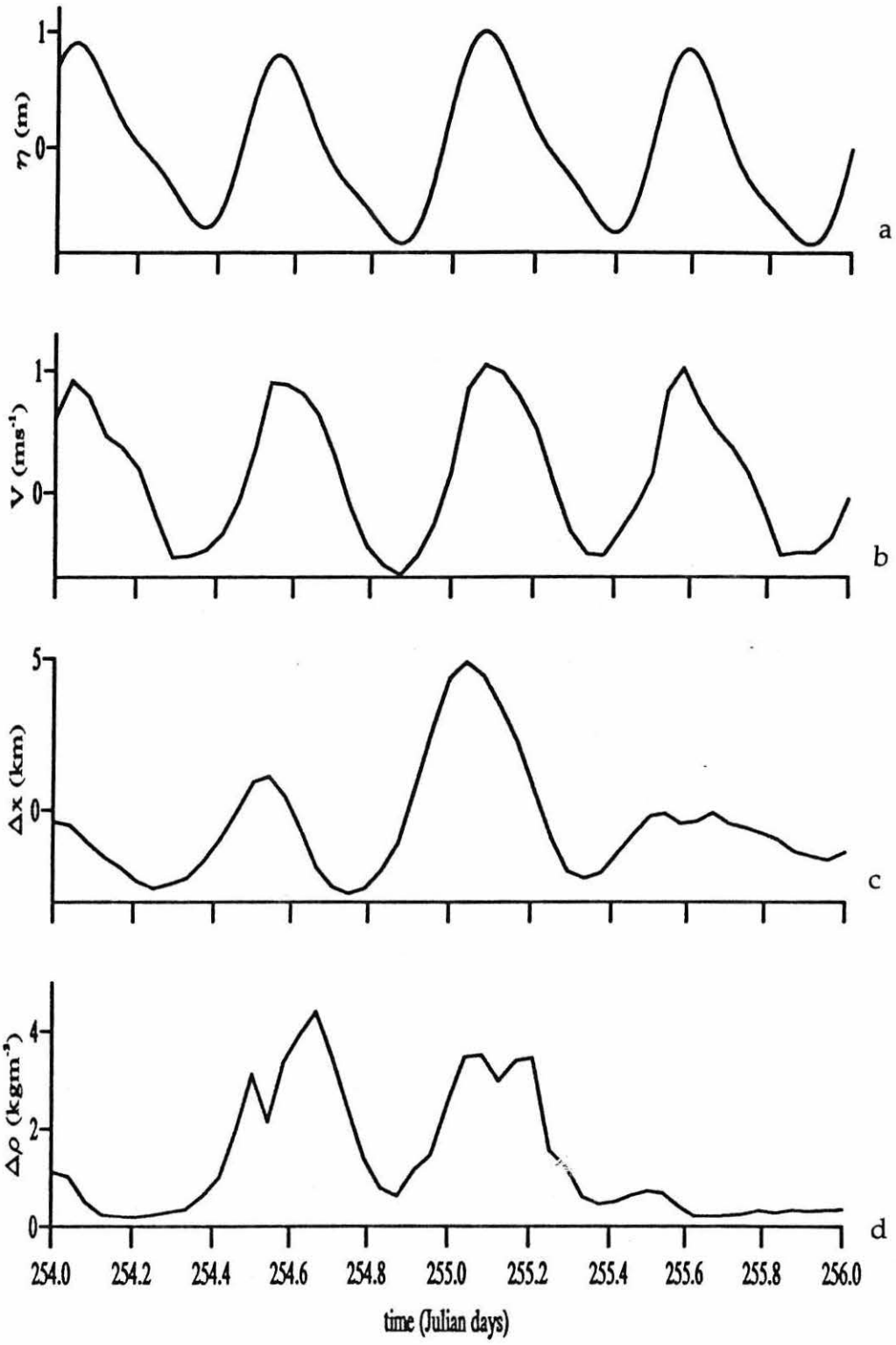

Figure 9.4 The relation between straining and the propagation of the tidal wave from measurements at mooring A:

(a) tidal elevation
(b) alongshore velocity v
(c) relative displacement between 4m and 16m.
(d) density difference

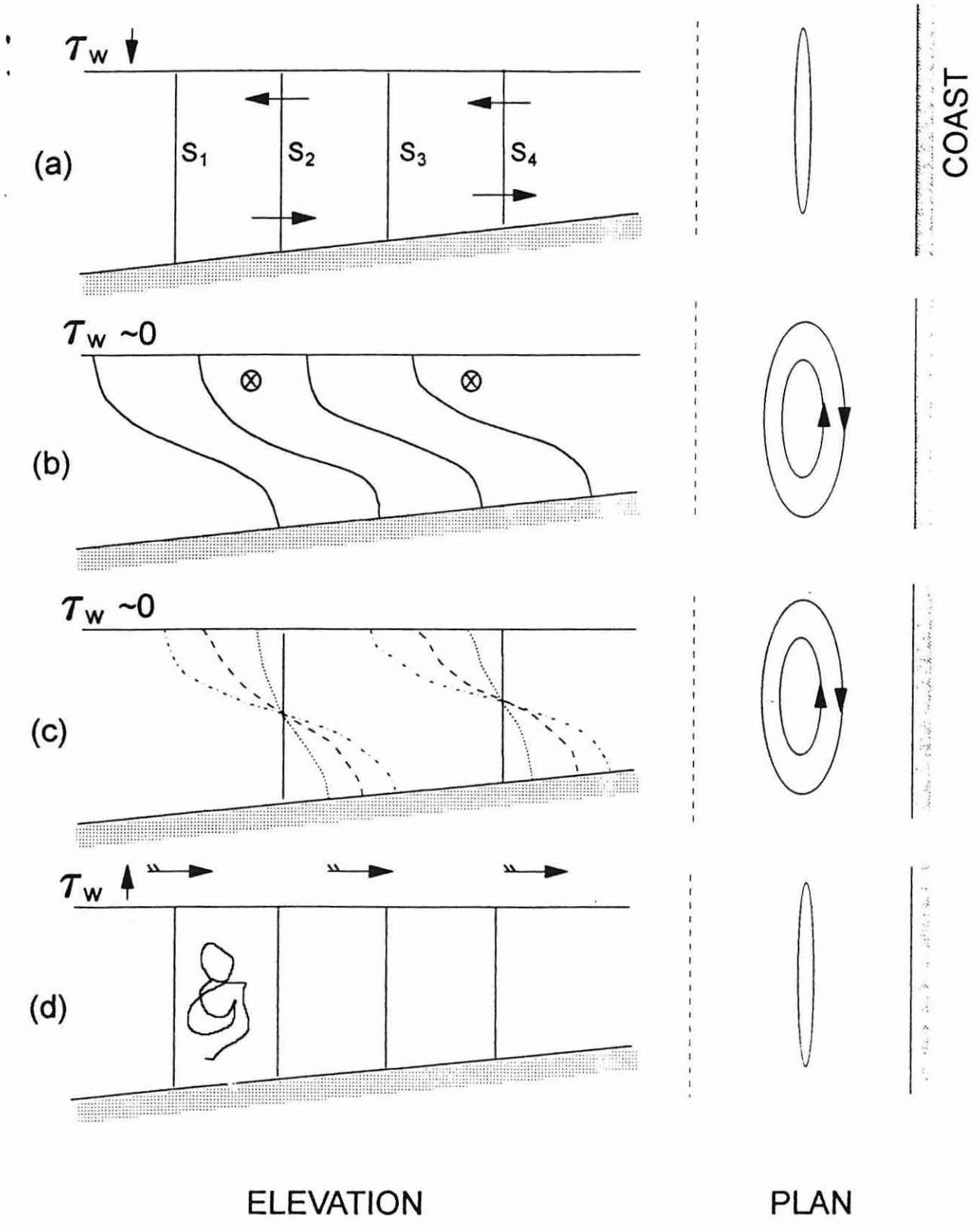

Figure 9.5 Process summary schematic showing the changes in ellipse format at surface and bottom due to the onset of stratification and the resulting semi-diurnal oscillations in stability driven by tidal straining. The symbolic windstress is shown in an arbitrary direction.

mixing over each tidal cycle, with a time lag between the south-west and the north-east of the up to 3 hours, due to the typical phase change along the Dutch coast.

CHAPTER TEN

MODELLING OF PROCESSES IN THE RHINE ROFI.

10.1. Introduction.

The modelling and understanding of the different processes involved in the ROFIs has become a goal of the modern coastal oceanographers. The simplified analytical models of the density driven currents in estuaries (Hansen and Rattray, 1965) and coastal region (Heaps, 1972), have been available for over two decades. The results have been combined with the ideas of mixing and stratification to produce a prescriptive model to asses the importance of different processes in the production and fate of haline stratification in ROFIs (Simpson *et al.*, 1991).

Recently, so-called "point models" have been extensively used to investigate the interaction of stratification, mixing and straining in ROFI systems. We shall make use of such a model (Simpson and Sharples, 1992) to test the hypothesis implied in the conceptual model of stratification outlined at the end of chapter 9.

10.2 The numerical model.

10.2.1 The equations of motion.

The model uses an explicit scheme to integrate the equations of motion:

$$\frac{\partial u}{\partial t} = -\frac{1}{\rho}\frac{\partial P}{\partial x} + fv + \frac{\partial}{\partial z}\left(N_z \frac{\partial u}{\partial z}\right) \qquad (10.1)$$

$$\frac{\partial v}{\partial t} = -\frac{1}{\rho}\frac{\partial P}{\partial y} - fu + \frac{\partial}{\partial z}\left(N_z \frac{\partial v}{\partial z}\right) \qquad (10.2)$$

with x and y positive in the cross- and along-shore directions respectively, and z increasing positively from the seabed. The second term on the right is the usual Coriolis forcing, and the third term is the effect of friction between the layers in transporting momentum vertically through the water column, with N_z the coefficient of vertical eddy viscosity.

The horizontal pressure gradient terms in equations (10.1) and (10.2) are given by:

$$\frac{1}{\rho}\frac{\partial P}{\partial x} = g\left(\frac{\partial \eta}{\partial x}\right)_{tidal} + g\frac{\partial \bar{\eta}}{\partial x} + g(h-z)\frac{\partial \rho}{\partial x} \qquad (10.3)$$

and similarly for the y component. The first term on the right of equation (10.3) is a tidally oscillating sea surface slope, the second two terms represent the effect of a depth-invariant horizontal density gradient in setting up a mean surface slope and driving a depth-dependent density circulation. Calculation of the mean surface slope is achieved by specifying a zero net flow condition in the cross-shore direction, in such way that

$$\frac{\partial \bar{\eta}}{\partial x} = \gamma \frac{h}{\rho}\frac{\partial \rho}{\partial x} \qquad (10.4)$$

where the parameter γ is chosen to make the net cross-shore transport equal zero.

Horizontal advection and vertical diffusion of salinity and temperature at each level are controlled by

$$\frac{\partial(s,T)}{\partial t} = -u\frac{\partial(s,T)}{\partial x} + \frac{\partial}{\partial z}\left(K_z\frac{\partial(s,T)}{\partial z}\right) \qquad (10.5)$$

where $\partial(s,T)/\partial x$ are the horizontal salinity and temperature gradients, assumed depth independent and taken from observations. K_z is the coefficient of vertical eddy diffusivity. There is no flux of salt or heat through the sea bed, and no net flux of salt at the surface. Surface heating is specified in terms of observed values of solar radiation, air temperature, relative humidity and wind speed following Gill (1982, p34). Density ρ is derived from temperature and salinity using the standard equation of state (UNESCO, 1981).

A level 2 turbulence closure scheme is used to calculate vertical profiles of N_z and K_z as functions of local stability (Mellor and Yamada (1974)) via

$$N_z = S_M lq \quad ; \quad K_z = S_H lq \qquad (10.6)$$

where q^2 is the turbulent kinetic energy, l is a mixing length and S_M and S_H are stability functions which depend on the local gradient Richardson number (for details, see Sharples and Simpson 1994).

10.2.2. The forcing.

Most of the forcing of the model is derived from observations. The density gradients are calculated from mooring data, while the surface heating exchange is from KNMI meteorological stations. In the 1990 simulation the solar radiation, air temperature and relative humidity are from Valkenburg, while the wind data is from the Hook of Holland. For the 1992 simulation the wind, air temperature and relative humidity are from the Noordwijk tower and the solar radiation from Valkenburg.

The surface elevation and surface slope for 1990 is calculated using values of tidal constituents from a 2-D barotropic model of the North Sea (Proctor and Smith, 1991), while for the 1992 simulation it was derived from sea level measurement from water level recorders.

10.3 Results.

10.3.1 1990 simulation.

The 1990 simulation (fig. 10.1) shows two periods of strong stratification at the beginning (between Julian day 269 and Julian day 276) and end (J285 to J290) of the observational period, with an intermediate period of negligible stratification (Julian day 277-285). This has been explained in chapter 5 as the result of periods of increased stratification due to neap tides and calm winds from Jday 269 to Jday 277 and from Jday 285 to Jday 290, while the mixed period is the result of intense stirring due to spring tides and augmented due to strong winds of the order of 25 ms^{-1}. In both of the stratified periods there is a strong semi-diurnal variability in stratification, showing clear indication of tidal straining. The amplitude of the stratification from the

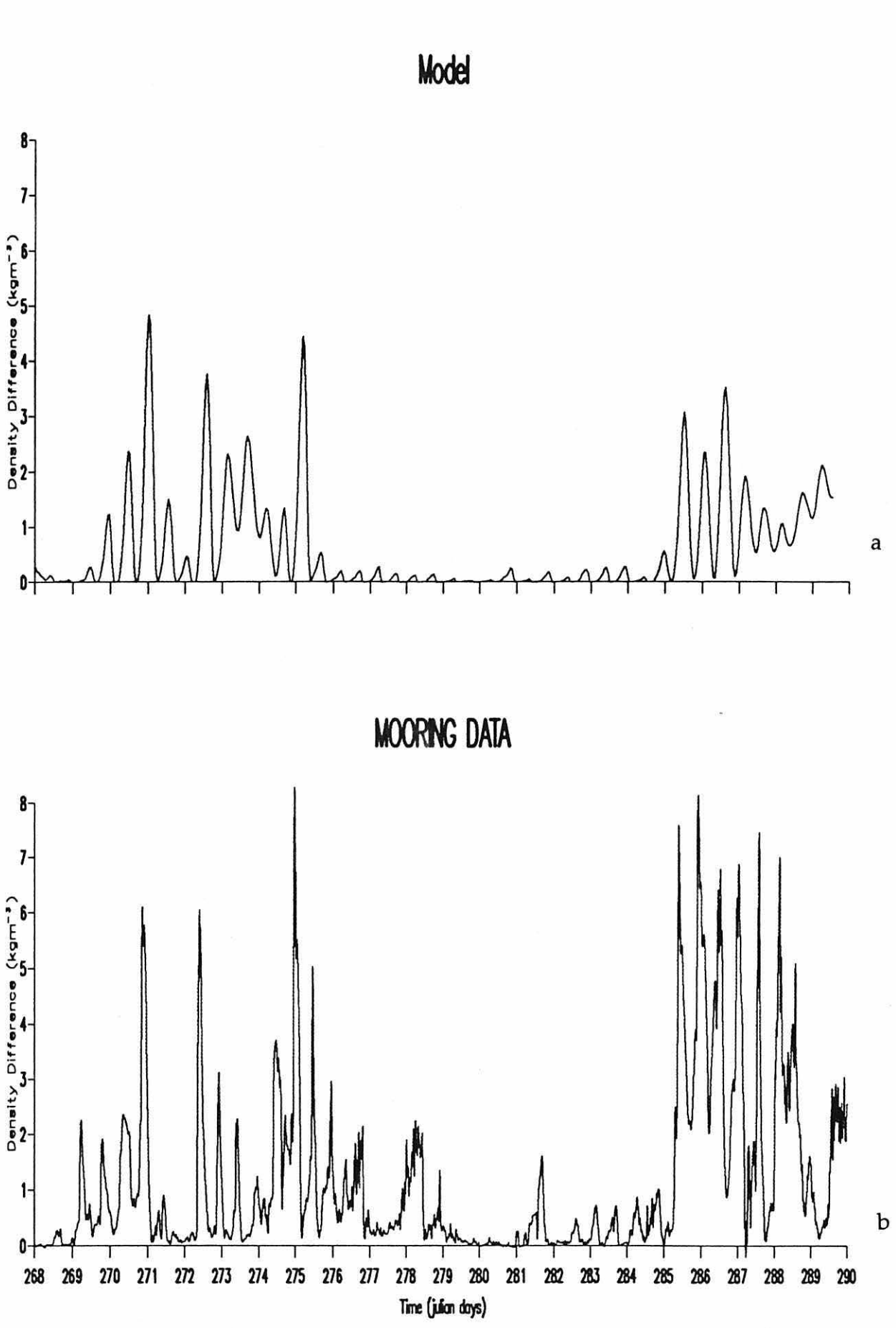

Figure 10.1 Time series of stratification for the 1990 campaign. a) from observations; b) from simulation.

simulation is about 60% of that of the observed data and slightly out of phase with stratification occurring about two hours earlier in the observed than in the simulated data. However, in general the envelope of the simulated stratification and the strong semi-diurnal variability is in accordance with the observations

A further comparison between the vertical density structure from a 25 hours anchor station at mooring B at the end of the observational period and the model (fig. 10.2), reveals only a fair qualitative agreement. The observations show complete mixing at the start, while stratification is already present in the simulation. The model appears to have a better agreement during second half of the observations, although the pycnocline appears deeper in the model than in the observations.

The effect of stratification on the tidal currents and especially in the distribution of ellipticity and rotational sense is in agreement, at least to first order, to that discussed in chapter 6 (fig. 10.3). It shows stronger clockwise (negative) rotation at the surface than at the bottom, with higher values of ellipticity at the surface during periods of stratification (from day 285) than during mixed conditions. The model fails to reproduce the anticlockwise rotation below a height of 15m although anti-clockwise motion is present at the bottom during periods of stratification.

10.3.2 1992 simulation.

Figure 10.4a,b shows the time series of stratification for the observations and the model. As in the 1990, case there is a good degree of correspondence between the two with the model exhibiting the main features of the observations, notably the two strong maxima in $\Delta\rho$ on Jdays 254-255 which are simulated with satisfactory timing

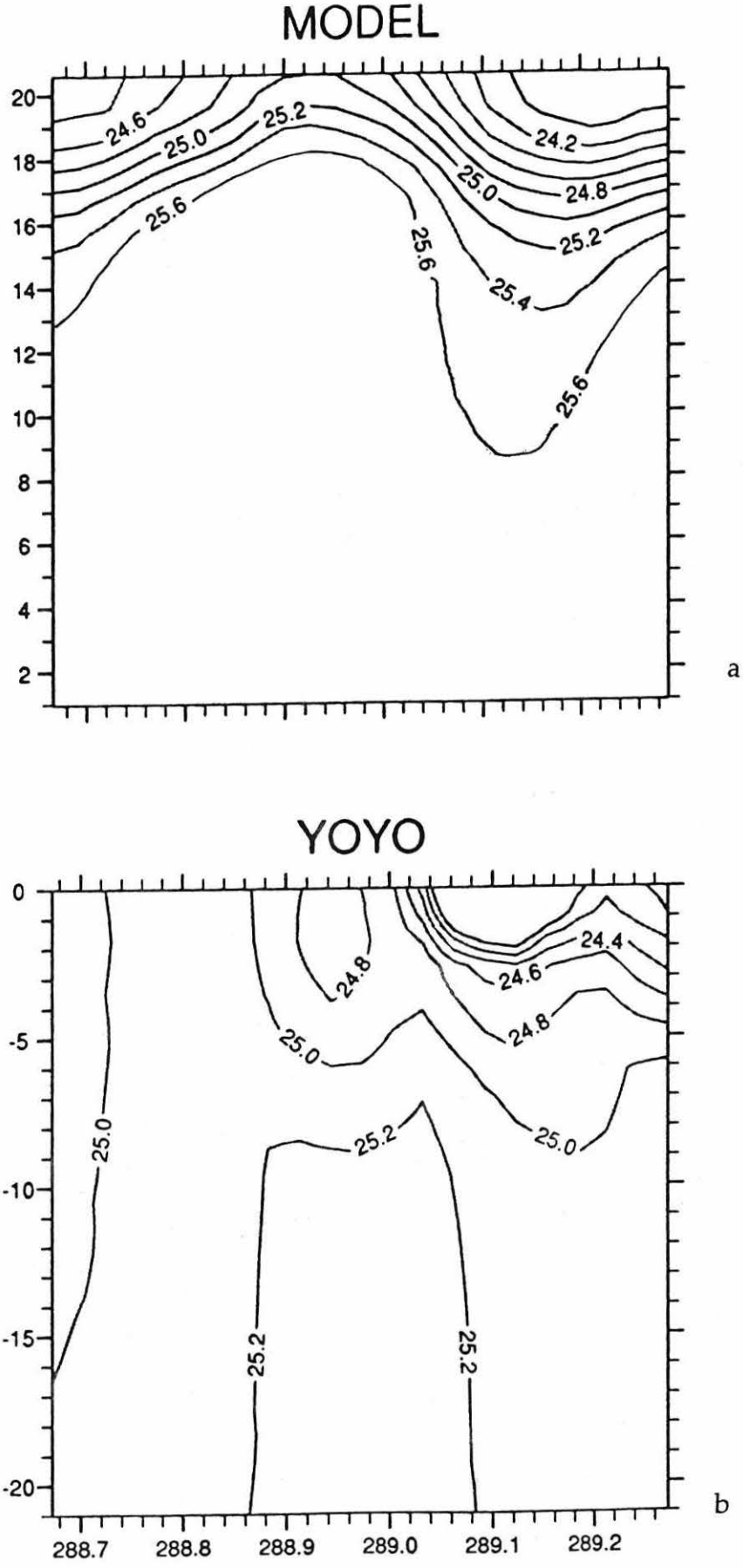

Figure 10.2 Density evolution over 1 tidal cycle. a) modelled; b) observed

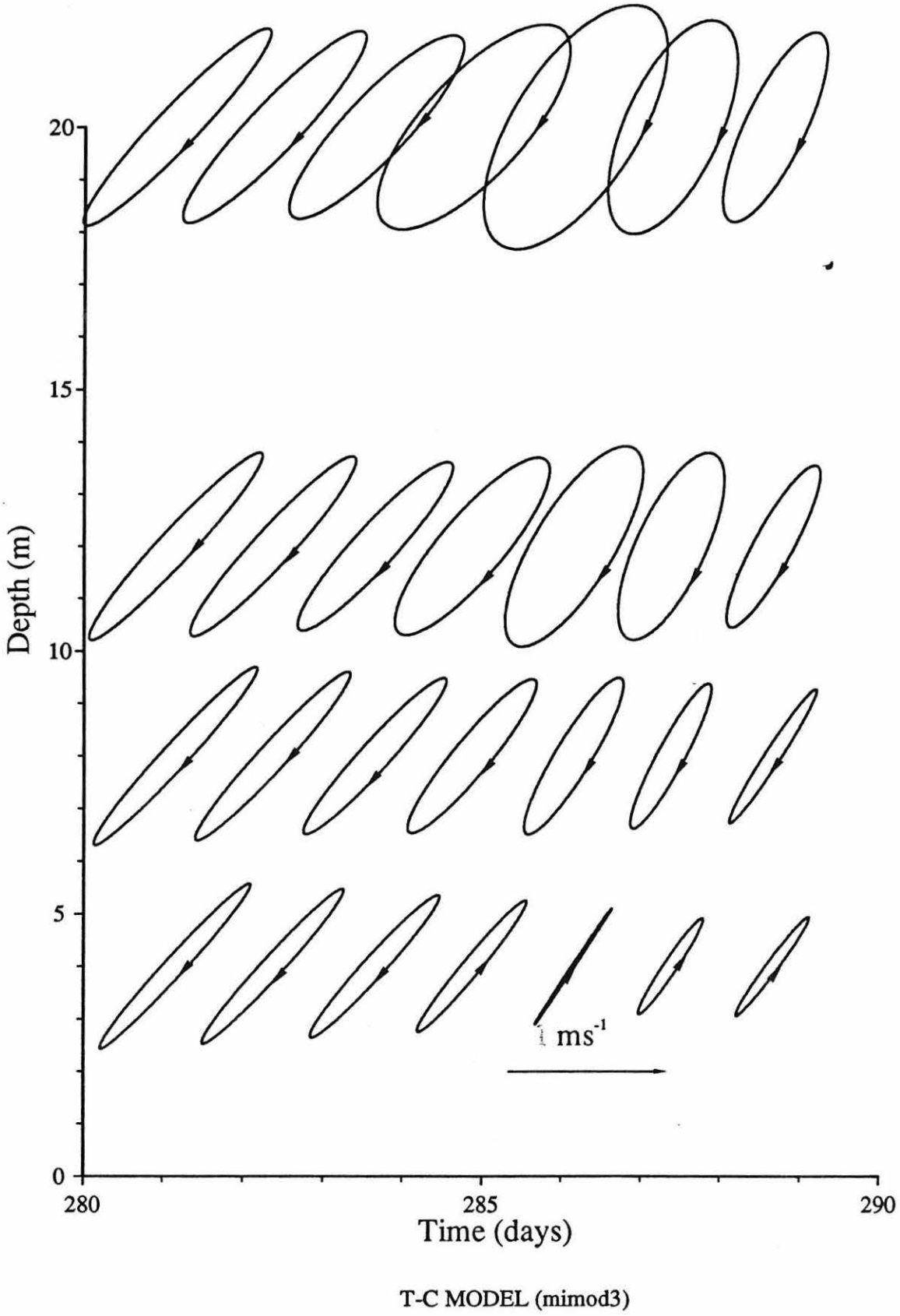

Figure 10.3 Tidal ellipses time series from model simulations for the 1990 data.

and magnitude. The preceeding and following periods of near zero stability are also reproduced by the model.

The model confirms the operation of the cross-shore straining mechanism in driving the semi-diurnal oscillations of stability, as discussed in chapter 9. In figures 10.4c,d we see that the differential displacement between surface and bottom predicted by the model are of comparable magnitude and similar phasing to those observed. The suppression of tidal straining by enhanced vertical mixing is clearly apparent, if somewhat, exaggerated in the model results.

The increase in cross-shore displacement, *i.e.* tidal straining, during periods of stratification is due to the modification in the ellipse properties. Hence, if the relative tidal displacement in figures 10.4c,d are in approximate agreement, it is expected that the tidal ellipses will also be comparable. In figure 10.5 we see fair agreement between model and observations, in amplitude distribution and timing of ellipses characteristics and stratification. The major axis is large at the surface from day 254, which will coincide with the springs period, while the ellipticity is negative during stratified periods with $\varepsilon \sim -0.2$. The difference in stratification and straining during periods of strong stirring might be due to the fact that the model overestimates the anticlockwise rotation during these periods in comparison with the observations. The values of phase and orientation are similar to those from the observed cross-shore and along-shore currents.

10.3 Discussion.

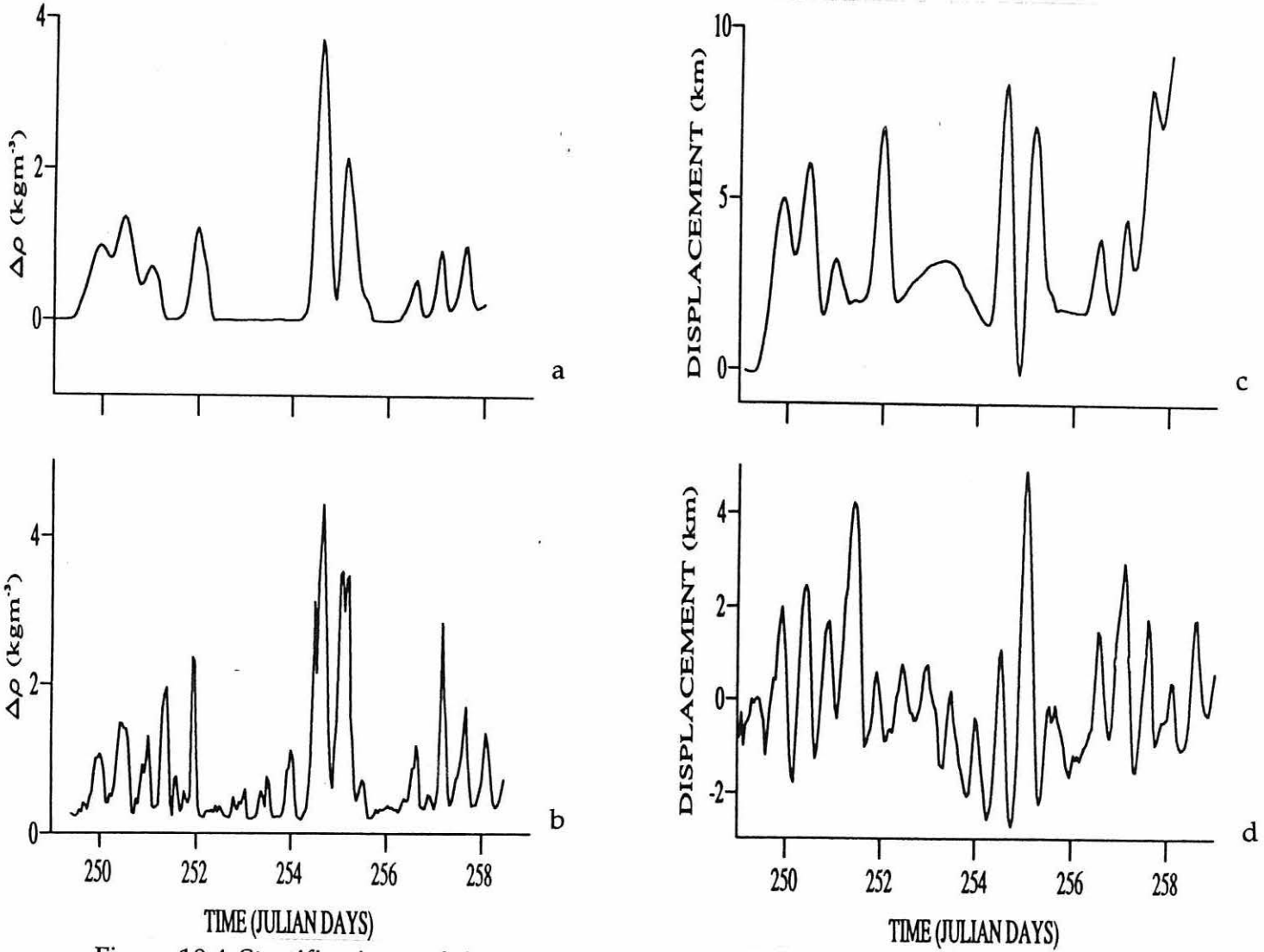

Figure 10.4 Stratification and displacement from the 1-dimensional turbulence closure model, for the 1992 observations:

Density stratification from the model (a) and observations (b)

Relative displacement from the model (c) and observation (d)

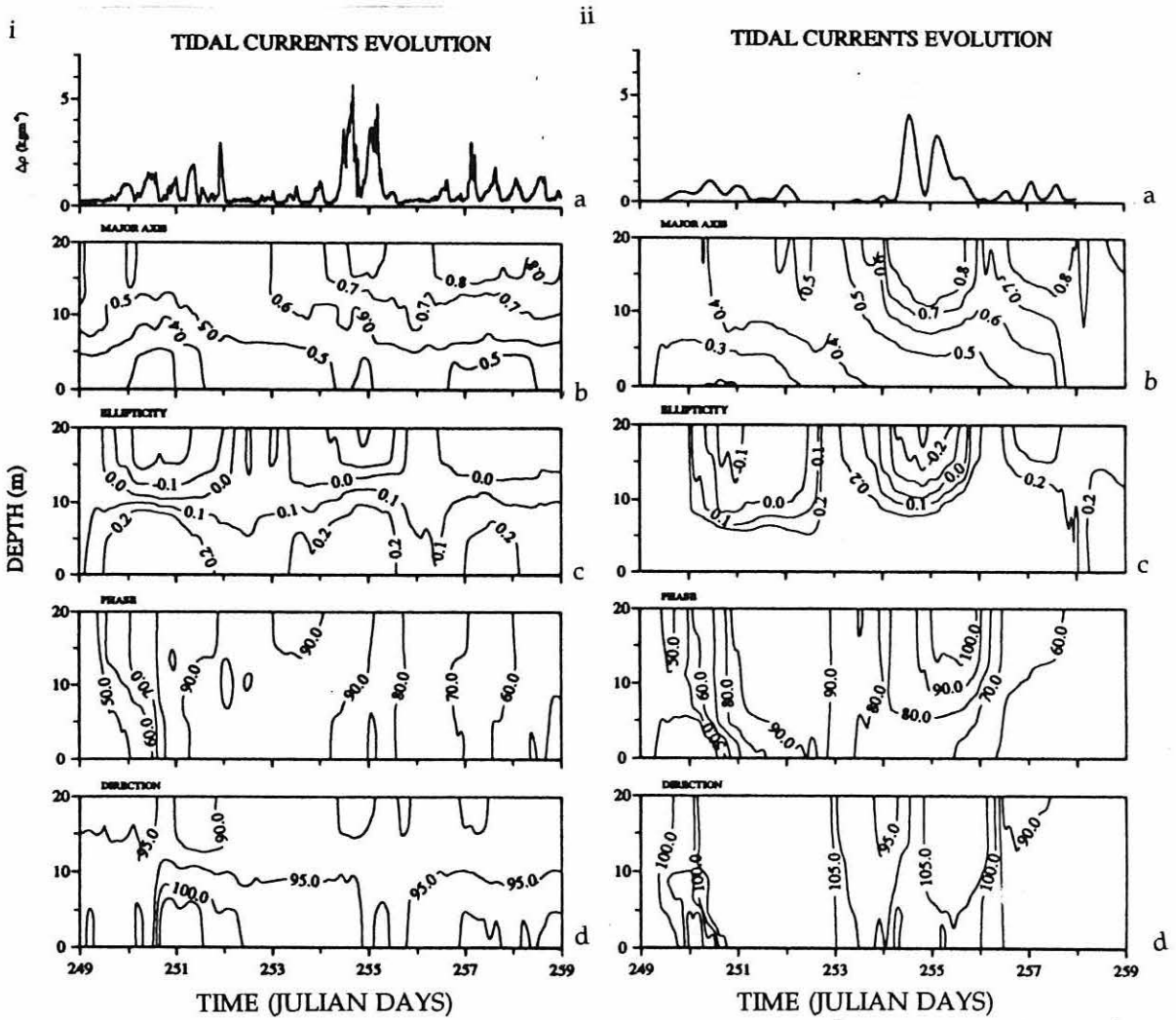

Figure 10.5 Stratification and tidal ellipses from the 1-dimensional turbulence closure model, for 1992 observations. i) are the observations and ii) are the model results. a) stratification; b) semi-major axis; c) ellipticity; d) phase and e) orientation.

The model results appear to confirm the hypothesis proposed in chapter 9, that the stratification in the Rhine ROFI is the result of the competition between the buoyancy input from the density gradients and the stirring from tides and wind. It also confirms the role of the modification of the tidal ellipses by the mean stratification, in the generation of semi-diurnal stratification.

The stratification in the observations and the model appears to follow the general pattern of stirring; with strong stratification when the combined tidal and wind stirring are low and almost, or complete, mixing when the stirring is high.

Another striking feature of both observations and model results is the relatively large cross-shore straining which evidently operates during periods of stratification and which provides the primary drive for the semi-diurnal oscillation. This straining with a relative displacement of surface and bottom waters of ~ 7 km is large in relation to the average amplitude of the cross-shore tidal flow. It appears to be associated with the change in the shape of the tidal ellipse which is brought about by the development of mean stratification as reported on the basis of the 1990 observations in Visser *et al.*(1994). Whereas at times of complete vertical mixing, the tidal ellipses are close to being degenerate (i.e. near rectilinear motion), when the system stratifies, the surface ellipses exhibit pronounced clockwise motion while the near-bed flow becomes more anti-clockwise in character.

The difference between the observations and the model may be partly attributed to the inadequate specification of the driving forcing. For example, the amplitude and phase in the stratification, as well as the vertical profile of tidal velocity, are much better simulated for the 1992 simulation than for the 1990. The

barotropic model used to drive the surface elevation and slope for the 1990 simulation, does not give accurate enough predictions of tidal amplitudes and phase in the Dutch coastal zone, with phase difference between observations and model which can be as much as 30° (Howarth personal communication). By contrast for the 1992 simulation the slope data should be very accurate as they are taken from the observations using the water level recorders. There are also better estimates of density gradients during 1992 than during 1990 because of the improved instrument performance and calibration.

CHAPTER ELEVEN

SUMMARY AND DISCUSSION

11.1. Introduction.

The substantial results presented in this work have been possible thanks to the collaborative nature of the project which involved Rijkswaterstaat, IFM Hamburg and the University of Wales Bangor. The availability of state-of-the-art instrumentation has enable us to get a deeper insight into the processes involved in ROFI systems and the subtle nature of the 2 way interaction between water column structure and flow. In this chapter I will present a summary of the principal findings, discuss their importance for the processes in this, and other, ROFIs and indicate the direction of future research.

11.2 Summary of principal findings.

•The observations confirm the existence of a ROFI regime extending Northwards along the Dutch coast to more than 100 km from the Rhine source and out to about 30 km from the coast.

•The currents in the Rhine ROFI are tidally dominated, but they have important wind and density driven components. The wind driven component exhibits behaviour akin to Ekman theory with a transfer function of the order of 2%.

•The density driven component of velocity is similar to Heaps (1972) velocity profile. But some modifications in the flow are observed due to the presence of stratification.

•The presence of stratification intensifies the wind response in the surface layer while decoupling the bottom layer. In consequence, the explained variance and transfer function are strong near the surface and decrease near the pycnocline with an inverse relation near the bed.

•Stratification also modifies the behaviour of the tidal ellipses. The presence of the pycnocline decouples the surface and bottom layers. The clockwise and anti-clockwise motions are decoupled to a different degree so that, whenever there is stratification, the tidal ellipses become more clockwise at the surface and more anti-clockwise at the bottom.

•The observations in this work and numerical simulations by Luyten *et al.* (1994) and Souza and James (1994) suggest that mixing in the Rhine ROFI is frequently dominated by wind and waves stirring.

•If we start with a period of complete vertical mixing when the isolines are vertical, as the stirring decreases the density gradients start to relax under gravity as in the Linden and Simpson (1988) experiments, but they are limited by the earth's rotation as indicated in Ou's (1983) model.

•The stratification then modifies the tidal ellipses by decoupling the bottom and surface layers. This results in strong cross-shore tidal straining which interacts

with the cross-shore density gradients and produces the strong semi-diurnal variability in stratification. This semi-diurnal switching of stratification will be repeated every tidal cycle until there is an increase in turbulent kinetic energy which will bring the water column back to vertical homogeneity.

•The point model embodies the central hypothesis about controls on stratification in the Rhine ROFI. It serves to confirm the hypothesis to the extent that it successfully reproduces the observations, for both the 1990 and 1992 data.

11.3. Discussion.

11.3.1. Currents.

The density driven currents have the typical behaviour of coastal currents, namely a strong coastal jet with along-coast velocities, in this case of the order of 0.10 ms^{-1}, and a convergence region, here located at about 20 km off-shore and velocities of the order of 0.02 ms^{-1}. The position of both the convergence and jet region appear to represent the boundary to the Rhine ROFI frontal region. The vertical distribution of velocity (fig. 8.5) suggests that the currents inside the ROFI area behave similarly to that prescribed by Heaps (1972) analytical model while outside the ROFI (fig 8.4) the velocities are small (~1 cms^{-1}) and homogeneous in the vertical, suggesting that they are the tidal rectification component of velocity.

A summary of the relative importance of each of current components can be made in terms of the kinetic energy (K.E):

$$K.E. = \frac{1}{2}\rho \bar{U}^2$$

$$= \frac{1}{2}\rho \{U_{tid} + U_{wind} + U_{\rho} + U_{tidrect}\}^2$$

If the components are uncorrelated the total tidal kinetic energy (T.K.E.) will be simply the addition of each individual component of the kinetic energy:

$$T.K.E = (K.E.)_{tid} + (K.E.)_{wind} + (K.E.)_{\rho} + (K.E.)_{tidrect}$$
$$T.K.E = \frac{1}{2}\rho U_{tid}^2 + \frac{1}{2}\rho U_{wind}^2 + \frac{1}{2}\rho U_{\rho}^2 + \frac{1}{2}\rho U_{tidrect}^2$$

using typical values for the Rhine ROFi this becomes

$$328 + 20 + 15 + 0.2 = 365 \text{ Jm}^{-3}$$

indicating that the currents are tidally dominated, with significant wind and density gradient components, while the contribution of tidal rectification is negligible.

11.3.2. The effect of stratification on the tidal ellipses.

The observations of the polarisation of tidal currents reported in chapter 6 are consistent with the explanation given in section 6.5, in terms of boundary layer theory. The essential mechanism, which has also been demonstrated in two layer models for example by Maas and van Haren(1987) and Visser et al.(1994), is that changes in N_z due to stability and stirring control the level of coupling between surface and bottom layers and that this change in coupling influences the clockwise and anti-clockwise motions to a different extent. If this basic explanation of our observations in terms of boundary layer dynamics is correct, we might expect that there should be a consistent relationship between the changes in polarisation through the water column and the levels of water column stability and stirring. Such a

possibility is also suggested by the close correlation of the changes in ε and stratification apparent in figures 6.5 to 6.8.

I have tested for such a general relationship by plotting the surface to bottom contrast in ellipticity, for both the 1990 and 1992 campaigns, versus a bulk Richardson number defined as:

$$\mathbf{Ri_0} = \frac{\mathbf{g\,h\,\Delta\rho}}{\mathbf{\rho\,U^2}}$$

where $\Delta\rho$ is the surface to bottom density difference and U is the amplitude of the tidal current, which varies over the spring-neaps cycle. The results (fig 11.1) show that there is a reasonably consistent relationship between $\Delta\varepsilon$ and Ri_0 although with greater variability at larger Richardson number.

The results for 1990 data cover a wider range of Ri_0 but indicate the same form of relationship as that of the 1992 data, with closely comparable slopes for $Ri_0 < 0.5$. At higher Ri_0, there are indications that the slope decreases with ε eventually reaching an upper limit. Increasing scatter at higher Ri_0 may be due to differences in the form of stratification (e.g. the depth of the pycnocline) which are not reflected in the bulk density difference component of Ri_0. Similarly, some variability will be attributable to variations in wind stirring which is not included in the shear component of Ri_0.

It is important to note that although the analysis technique used here may introduce some temporal variability in the ellipse characteristics, due to the interaction of the M_2 and S_2 harmonics during the spring-neaps cycle, such changes would be in

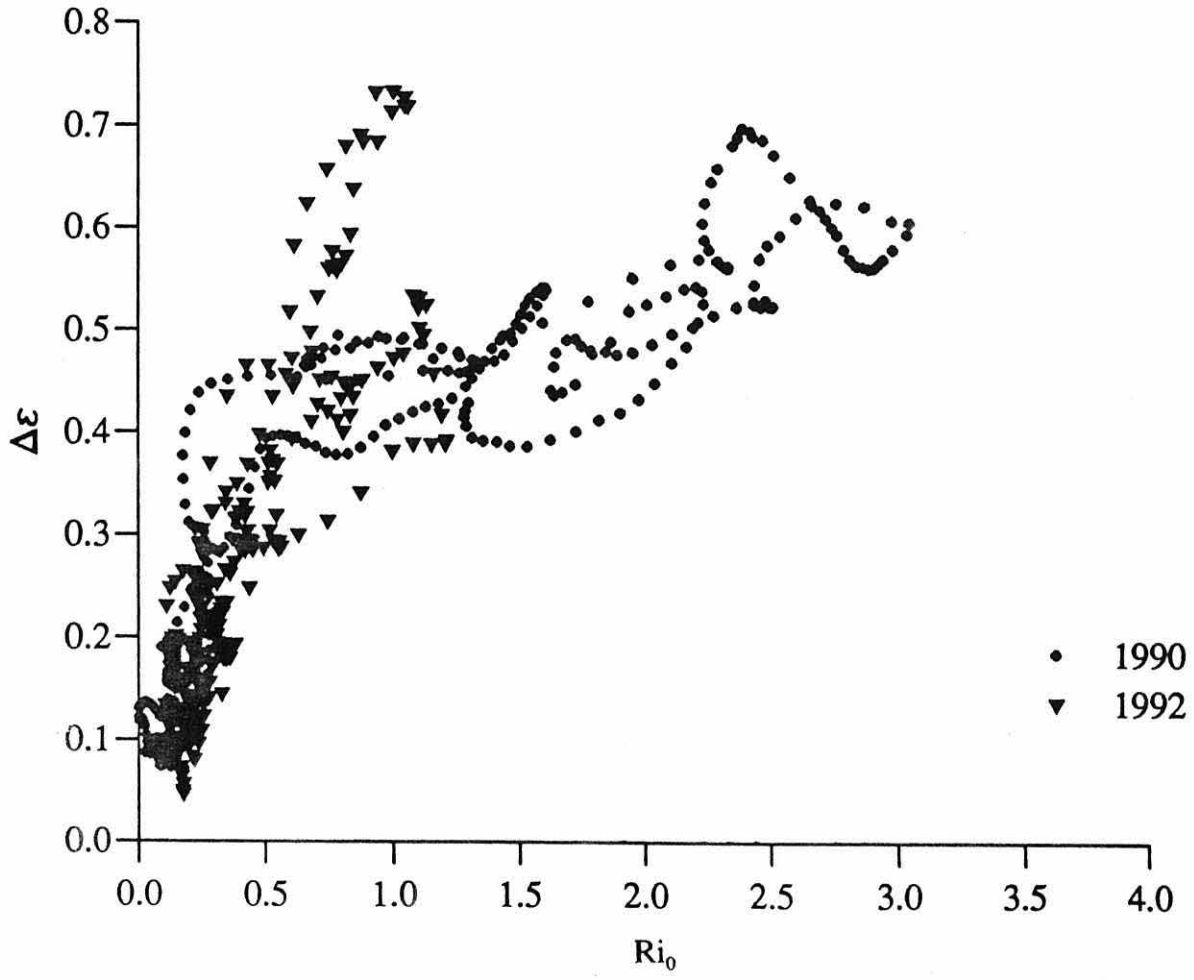

Figure 11.1 Relationship between bottom-surface ellipticity difference ($\Delta\varepsilon$) and bulk Richardson number Ri_0 for September 1992 data (▾) and October (Jdays 280 to 290) 1990 data (·).

both the stratified and mixed regimes. The striking differences between figure 6.8 and figure 6.9, in ellipticity and orientation, indicates that the changes observed in figure 6.8 are due to the effect of stratification. The only change which could be attributed to the interaction of M_2 and S_2 tidal constituents is a temporal variation in phase through the spring-neaps cycle (see for example Simpson *et al.*, 1991).

11.3.3. Controls on stratification on the Rhine ROFI system.

In general it can be said that stratification in the Rhine ROFI system is the result of competition between the effect of stirring due to wind, waves and tides against the buoyancy input due to tidal straining and density driven currents. This interaction has been explained in chapter 9 and summarized in figure 9.5, where it is clear that when the combined stirring due to wind waves and tides is high the isopycnals are vertical. When the stirring decreases the density gradients relax generating an cross-shore transport which is limited by the effect of rotation and generates a typical coastal current. The presence of water column stability then modifies the tidal ellipses, as discussed above and generates a strong off-shore component of tidal shear which then interacts with the horizontal density gradients generating a strong semi-diurnal component of stratification.

The relaxation is a function of the strength of the density gradients and the turbulent kinetic energy available. For example, the Rhine ROFI frontal region in 1990 was located at about 20 km off-shore in contrast with its position in 1992 at about 15 km. This difference could be due to the fact that during the 1990 campaign the periods of calm winds coincided with post-neaps tides resulting in periods of very low stirring in contrast to the 1992 campaign when light winds corresponded with

spring tides so that there was some tidal stirring working against the relaxation. The difference in buoyancy input between the two surveys is readily represented in the form of the internal Rossby radius of deformation ($Ro=(g'h_1)^{1/2}/f$) which is about 5km for the 1990 campaign and 3.2 km for the 1992 campaign. It is interesting to note that the ratio between the 1990 and the 1992 Rossby radii is similar to the ratio between the position of the frontal region between 1990 and 1992 campaigns, with a value of approximately 1.5.

11.3.4. Contrast with other ROFIs

The Rhine ROFI behaves similarly to other ROFIs in the general way in which stratification is generated by the competition between buoyancy input and stirring. However they are also some more subtle differences present. As an example of these differences a comparison between the Rhine ROFI and Liverpool Bay will be discussed in this section.

The main difference between the Rhine ROFI system and other ROFIs, such as Liverpool Bay, is that although semi-diurnal oscillations in stratification are present, they are relatively small in comparison with the mean stratification, while in the Rhine ROFI the mean and semi-diurnal components of stratification are of similar magnitude. This difference is due to the fact that in the Rhine ROFI the major axis of the tidal ellipses is oriented normal to the main density gradient, so that when the stratification modifies the tidal ellipses, it enhances the tidal shear along the direction of the main density gradient vector, as confirmed by the point model in chapter 10. In contrast in Liverpool bay the major axis is oriented with the main density gradient, so when the stratification modifies the tidal ellipses the shear enhancement is

perpendicular to the density gradients and therefore with no direct effect on the semi-diurnal stratification.

In Liverpool Bay the tide behaves almost as a pure standing wave, while in the Rhine ROFI it behaves like a progressive Kelvin wave. This creates a difference in the timing of the maximum stratification. In the case of Liverpool Bay the maximum stratification is at low water while in the Rhine ROFI it is at high water (fig 9.4).

Another difference is that stirring in Liverpool bay is tidally dominated while for the Rhine ROFI wind and tidal stirring are a very important component.

11.4. Generalization of processes in a 2-dimensional model.

The strong tidal straining present in the Rhine ROFI is a general feature of any ROFI at mid latitudes and relatively shallow waters, in which the tides behave as a Kelvin wave travelling along-shore and the horizontal density gradients are perpendicular to the coast. Recent numerical simulations using a 2-d slice (x-z) model (Souza and James, 1994) illuminate the operation of the mechanisms involved. Figure 11.2 show a series of salinity sections from the model: at 27 hours (fig. 11.2a), 3 hours after high water, the water column shows moderate stratification; at low water (fig. 11.2b) the water column has become homogeneous. But a quarter of a tidal cycle later the water column starts to re-stratify (fig. 11.2c), reaching its maximum at high water (fig. 11.2d). These change correlate closely with the SEAROVER observations shown in figure 5.21.

The current distribution associated with the above density structure is shown in figure

Figure 11.2 Salinity distribution from the slice model at different times in a tidal cycle. (a) 3 hours after high water, (b) at low water, (c) 3 hours after low water and (d) at high water. Simulation times are above each pane. Note that the tidal states are chosen to be comparable to those of the SEAROVER sections.

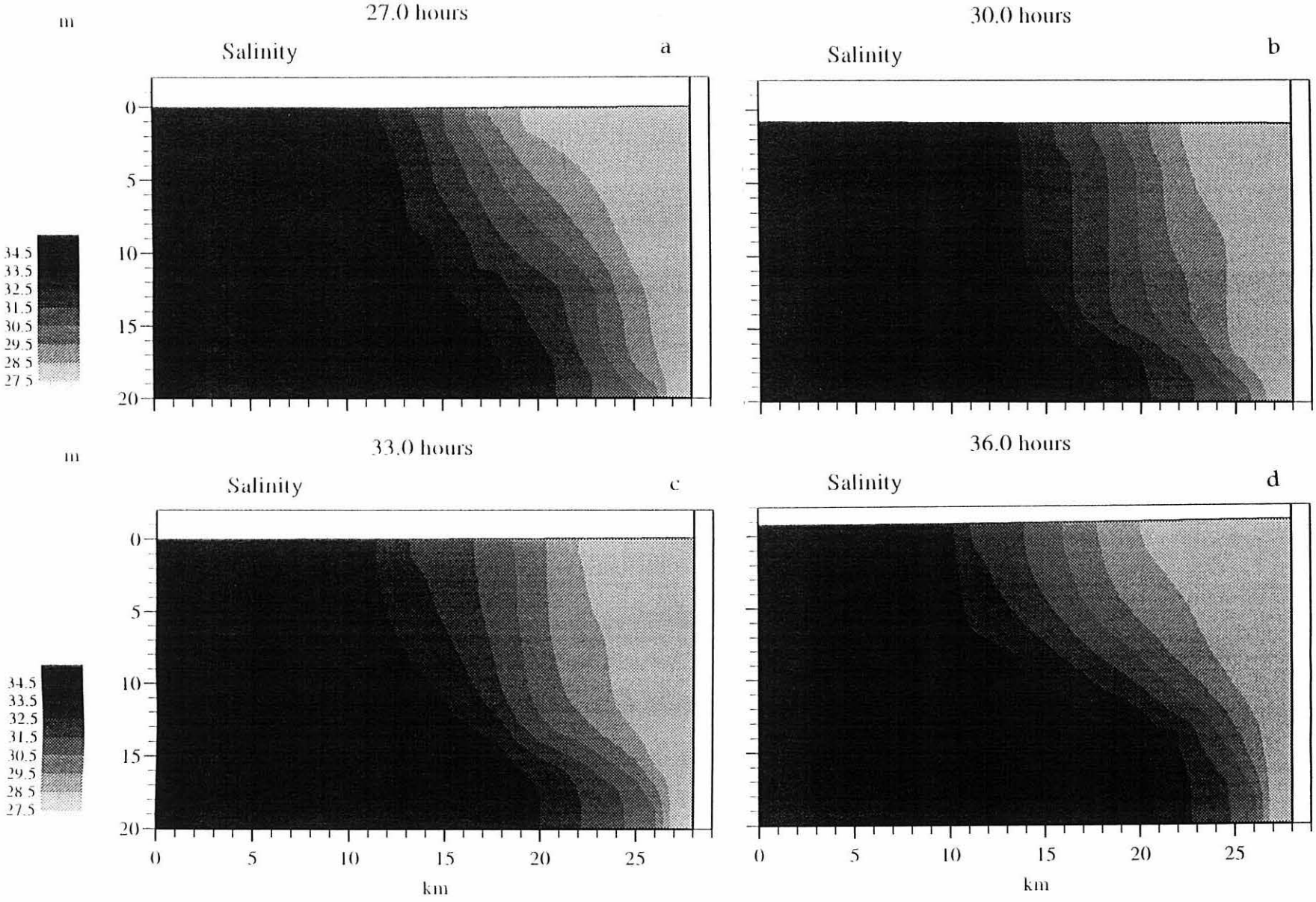
m
27.0 hours
Salinity
a
0
5
10
15
20
34.5
33.5
32.5
31.5
30.5
29.5
28.5
27.5
30.0 hours
Salinity
b
m
33.0 hours
Salinity
c
0
5
10
15
20
0
5
10
15
20
25
km
36.0 hours
Salinity
d
0
5
10
15
20
25
km

Figure 11.3 Same as figure 11.2 but for the current field. Contours show the alongshore component of velocity, while the vectors show the cross-shore and vertical components, all in ms^{-1}.

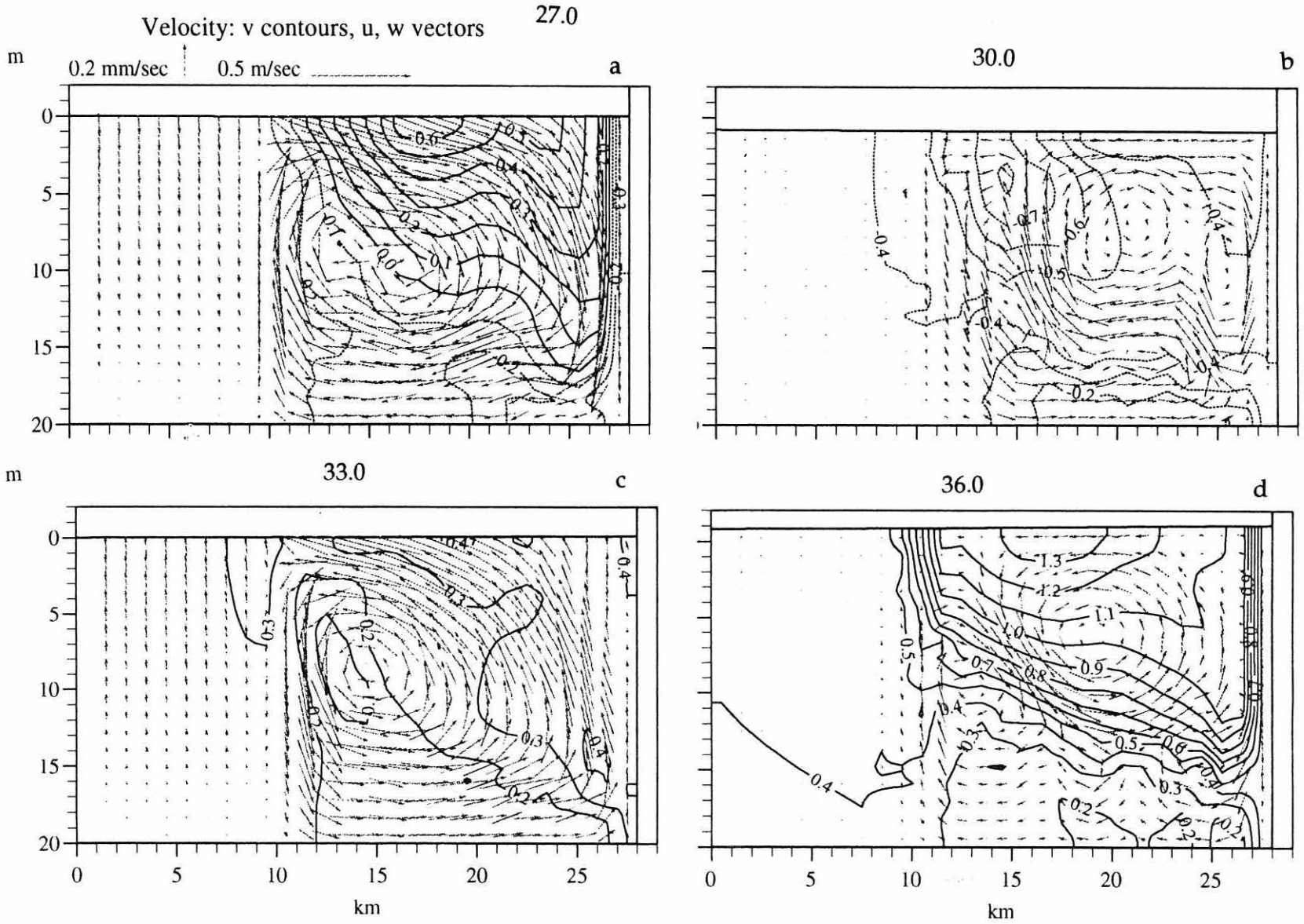
Velocity: v contours, u, w vectors
0.2 mm/sec
0.5 m/sec
27.0
a
30.0
b
33.0
c
36.0
d
m
km

11.3. The velocity distributions show that both along- and cross-shore velocities have a maximum inside the stratified area, bounded at approximately 10 km. This stratified region shows a strong cross-shore shear, which is not apparent in the mixed region. The cross-shore shear is maximum when the tidal elevation is equal to that of the mean sea level, while the maximum velocities are at high and low water.

11.5. Future work.

This work has allowed us to gain a clear understanding of the main physical processes involved in ROFI systems. The subtle way in which water column stability interacts with the flow has been elucidated and has been tested in a point model which has been successful in reproducing the observations. To gain further understanding of this ROFI system, both observations and model would need to be refined.

The observations could be improved by making simultaneous quasi-synoptic observations of velocity and structure on a cross-shore line using an undulator and a towable ADCP, so that near surface velocities could be measured. This way the effect of tidal straining could be better observed in a representative slice of the ROFI., while the model should include both the effect that the coast and the wave stirring have on the stratification.

There is strong evidence (*e.g.* fig. 11.4) of the importance of wave mixing as discussed in chapter 5, where a regression of $\Delta\rho$ on the along-shore, cross-shore wind and wave height explained 69% of the observed variance. The present model does not include the effect of wave mixing and it is clear from the above results that wave

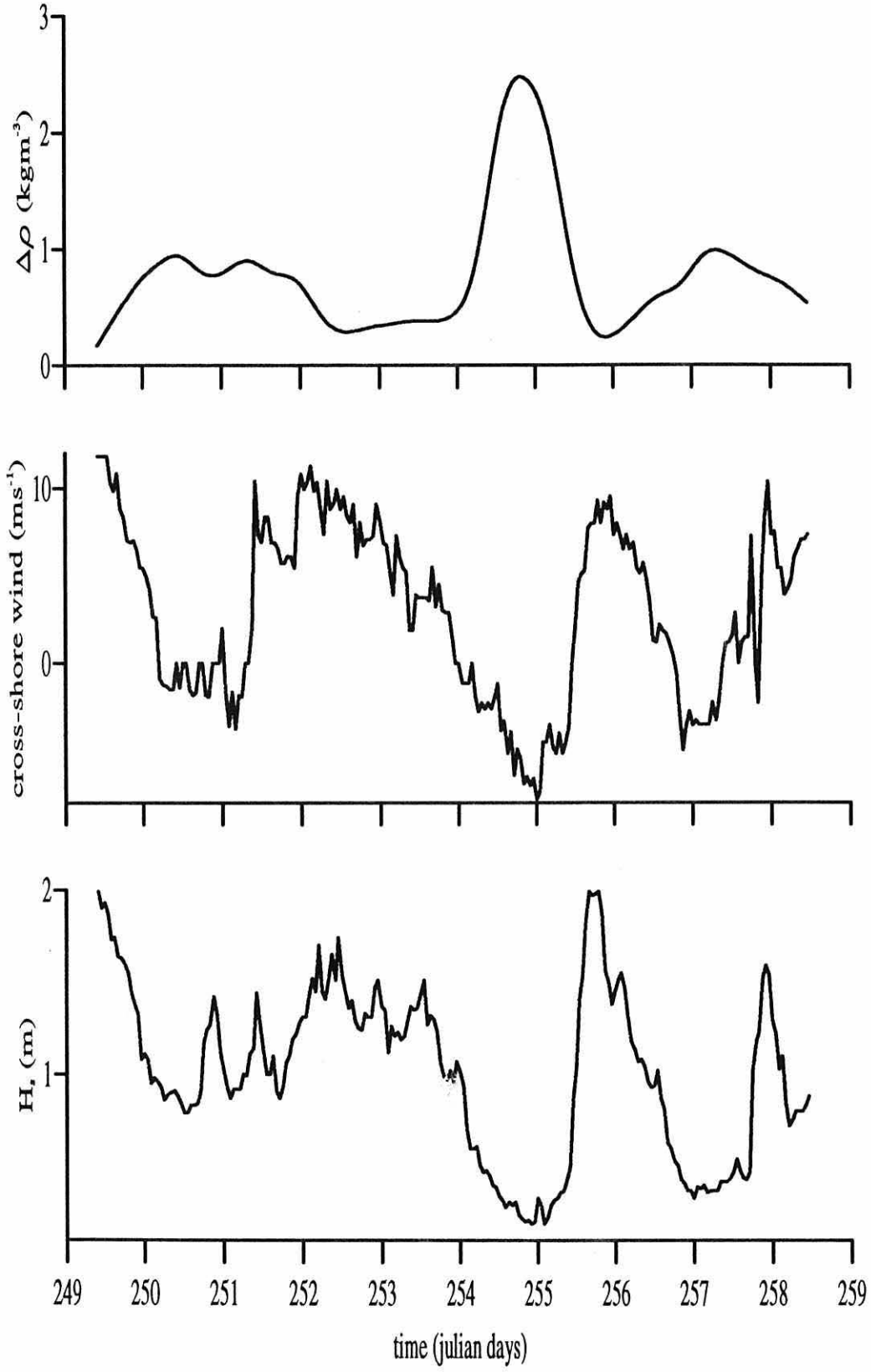

Figure 11.4 Relation between stratification (a), cross-shore wind (b); and waves (c).

mixing should be included in the model to assess its importance in controlling stratification.

Since the model is 1-dimensional, it omits any influence of the coast line on the structure and dynamics. The coast has the effect of enhancing or reducing stratification due to upwelling and downwelling (Munchow and Garvine, 1993). This brings an asymmetric influence of the wind on stratification that can only be included in a two-dimensional model similar to that of Souza and James (1994).

Such 2-d models represent a necessary intermediate step towards the development of validated 3-d models for ROFI systems. Full simulation of Physics will ultimately be required as basics for water quality models on which the rational management of ROFIs will depend.

REFERENCES

Aanderaa (1992). RCM 7 & 8 operating manual, technical description no 159.

Argote, M.L., A. Amador and C. Morales (1985). Variacion estacional de estratificacion en la region norte del Golfo de California. Memorias Reunion Anual 1985, Union Geofisica Mexicana, 334-338.

Barrick, D.E., M.W. Evans and B.L. Weber (1977). Ocean surface currents mapped by radar. Science 198, 138-144.

Beardsley, R.C., R. Limeburner, Hu Dunxin, Le Kentang, G.A. Cannon and D.J. Pashinki. (1994). Structure of the Changjiang river plume in the East China Sea during June 1980. personal communication 243-260.

Bowden, K.F. (1953). Note on wind drift a channel in the presence of tidal currents. Proceedings of the Royal Society, London A219, 426-446.

Bowden, K.F. and L.A. Fairbairn (1952). A determination of the frictional forces in a tidal current. Proceedings of the Royal Society, London A214, 371-392.

Bowden, K.F. and S.H. Sharif El Din. (1966). Circulation and mixing processes in the Liverpool Bay area of the Irish Sea. Geophys. J. Royal Astro. Soc., london 11, 279-292.

Davis, R.E. (1976). Predictability of sea surface temperature and sea level pressure anomalies over the North Pacific Ocean. J. Phys. Ocean. 6, 249.

De Ruijter, W.P.M., A. Van der Giessen and F.C. Groendijk (1992). Current and density structure in the Netherlands coastal zone. In: Dynamics and exchanges in Estuaries and the Coastal Zone. (ed. D. Prandle). AGU, Washington D.C. 40, 255-276.

Durazo, R. (1993). Horizontal circulation and diffusion at tidal fronts. Ph.D. Thesis University College of North Wales pp146.

Garret, C.J., J.R. Keeley and D.A. Greenberg (1978). Tidal mixing versus thermal stratification in the Bay of Fundy and Gulf of Maine. Atmosphere-Ocean 16, 403-423.

Garvine, R.W. and J.D. Monk (1974). Frontal structure of a River plume. J. Geophys. Res. 79, 2251-2259.

Gill, A.E. (1982). Atmosphere-Ocean Dynamics. Academic press. New York

662pp.

Glorioso, P.D. (1987). Temperature distribution related to shelf-sea fronts on the Patagonian Shelf. Cont. Shelf. Res. 7, 27-34.

Godin, G. (1972). The analysis of tides. Liverpool University press, Liverpool

Griffith, R.W. and P.F. Linden (1981). The stability of buoyancy driven coastal currents. Dynamics of Atmospheres and Oceans 5, 281-301.

Halliwell, A.R. (1973). Residual drift near the sea-bed in Liverpool Bay: an observational study. Geophys. J. Royal Astro. Soc., London 32, 439-458.

Hansen, D.V. and M. Rattray (1965). Gravitational circulation in straits. J. Mar. Res. 23(2), 1994-121.

Heaps, N.S. (1972). Estimation of density currents in Liverpool area of Irish Sea. Geophys. J. R. Ast. Soc. 30, 415-432.

Hill, A.E., I.D. James, P.F. Linden, J.P. Matthews, D. Prandle, J.H. Simpson, E.M. Gmtrowicz, D.A. Smeed, K.M.M. Lwiza, R. Durazo, A.D. Fox and D.G. Bowers (1993). Dynamics of tidal mixing fronts in the North Sea. Phil. Trans. R. Soc. Lond. A343, 431-446.

Howarth, M.J. (1994). The effect of stratification on tidal current profiles. Cont. Shelf. Res. (submitted)

Johns, B and P. Dyke (1972). The structure of the residual flow in an off-shore tidal stream. J. Phys. Ocean. 2, 72-79.

Joyce, T.M. (1989). On in situ 'calibration' of shipboard ADCP's. J. Atmos. Ocean. Tech. 6, 169-172.

Lagerloef, G.S.E. and R.L. Bernstein (1988). Empirical orthogonal function analysis of advanced very high resolution radiometer surface temperature patterns in Santa Barbara Channel. J. Geophys. Res. 93 (C6), 6863-6873.

Linden, P.F. and J.E. Simpson (1988). Modulated mixing and frontogenesis in shallow seas and estuaries. Cont. Shelf. Res. 8(10), 1107-1127.

Luyten, PJ., E. Deleersnijder, J. Ozer and K.G. Ruddick (1994). Presentation of a family of turbulence closure models for stratified shallow water flows and application to the Rhine outflow region. Cont. Shelf. Res. (submitted).

Lwiza, K.M.M. (1990). A study of tidal front dynamics using ADCP. Ph.D. Theis, University College of North Wales

Lwiza, K.M.M., D.G. Bowers and J.H. Simpson (1991). Residual and tidal flow at a tidal mixing front in the North Sea. Cont. Shelf Res. 11, 1379-1395.

Maas, L.R.M. and J.M. Van Haren (1987). Observations on the vertical structure of tidal and inertial currents in the central North Sea. J. Mar. Res. 45, 239-318.

McClimans, T.A. (1978). Fronts in fjords. Geophys. Astrophys. Fluid. Dyn 11, 23-24.

Mellor G.L. and P.L. Durbin (1975). The structure and dynamics of the ocean surface mixed layer. J. Phys. Ocean. 5, 718-728.

Mellor G.L. and T. Yamada (1974). A heirarchy of turbulence closure models for planetary boundary layers. J. Atmos. Sci. 31, 1791-1806.

Munchow, A. and R.W. Garvine (1993). Buoyancy and wind forcing of a coastal current. J. Mari. Res. 51, 293-322.

Ou, H.W. (1983). Some-two layer models of shelf-slope front: Geostrophic adjustment and its maintenance. J. Phys. Ocean 13, 1798-1808.

Ou, H.W., F. Aikman III and R.W. Hougton (1988). Complex empirical orthogonal function analysis of thermistor chain data near a shelf-slope front. Cont. Shelf Res. 8, 711-728.

Paden, C.A., M.R. Abbott and C.D. Winant (1991). Tidal and atmospheric forcing of the upper ocean in the Gulf of California. J. Geophys. Res. 96(C10), 18337-18359.

Pingree, R.D. and D.K. Griffiths (1978). Tidal fronts on the shelf seas around the British Isles. J. Geophys. Res. 83, 4615-4622.

Pollar, R. and J. Read (1989). A method for calibration ship mounted acoustic Doppler profilers and limitations of gyro compasses. J. Atmos. Ocean. Tech 6, 859-865.

Prandle, D (1982). The vertical structure of tidal currents. Geophys. Astrophys. Fluid Dynamics 22, 29-49.

Prandle, D (1987). The fine-structure of nearshore tidal and residual circulation revealed by H.H. radar surface current measurements. J. Phys. Ocean. 17, 231-245.

Prandle, D. (1984). A modelling study of Mixing of 137Cs in the European Continental Shelf. Phil. Trans. R. Soc. Lond. A343, 405-421.

Prandle, D. and J. Matthews (1990). The dynamics of nearshore surface currents generated by tides, wind and horizontal density gradients. Cont. Shelf Res. 10, 665-681.

Preisendorfer, R.W., F.W. Zweirs and T.P. Barnett (1981). Foundations of principal component selection rules. SIO Refernce series 81-4, pp 192.

Proctor, R. and J.A. Smith (1991). The depth - average residual circulation on the North West European Shelf August 1988 - October 1989. Proudman Oceanographic Laboratory, report No 20

Pugh, D.T. (1987). Tides Surges and Mean Sea-Level. John Wiley and Sons pp472.

Ramster, J.W. (1971). A long-term current meter station in Liverpool Bay. ICES C.M. 1971 Hydrographic Committee Document No. C:8.

RDI (1986). Rd-Vm accoustic Doppler current meter profiler, operation and maintenance manual.

Rippeth, T.P. (1993). Control of tratification in a fjordic regime (the Clyde Sea). Ph.D. Thesis, University College of North Wales

Ruddick, K.G., E. Deleersnijder, T De Mulder, P.J. Luyten (1993). A model study of the Rhine discharge front and circulation. Tellus (submitted)

Sharples, J. (1992). Time dependent stratification in regions of large horizontal gradient. Ph. D. Thesis, The university College of North Wales. 137.

Sharples, J. and J.H. Simpson (1994). Semi-diurnal and longer period stability cycles in the Liverpool Bay R.O.F.I. Cont. Shelf. Res. (in Press)

Simpson J.H. and I.D. James (1986). Coastal and estuarine fronts. In: Baroclinic processes on continental shelves. Coastal and Estuarine Sciences 3 (ed. N.K. Mooers) 63-93.

Simpson J.H., J. Brown, J.P. Matthews and G. Allen (1990). Tidal straining, density currents and stirring in the control of estuarine stratification. Estuaries 12, 129-132.

Simpson, J.H. and D. Bowers (1984). The role of tidal stirring in controllimg the seasonal heat cycle in shelf areas. Annals. Geophys. 2 6, 411-416.

Simpson, J.H. and D. Bowers (1981). Models of stratification and frontal movement in the shelf seas. Deep Sea Res. 28, 727-738.

Simpson, J.H. and J. Sharples (1992). Dynamically-active models in the prediction of estuarine stratification. In: Dynamics and exchanges in Estuaries and the coastal zone. (ed. D. Prandle). AGU, Coastal and estuarine sciences 40, 101-113.

Simpson, J.H. and J. Sharples (1994). Does Earth's rotation influence the location of shelf sea fronts?. J. Geophys. Res. 99C2, 3315-3319.

Simpson, J.H. and J.R. Hunter (1974). Fronts in the Irish Sea. Nature 250, 404-406.

Simpson, J.H., C.M. Allen and N.C.G. Morris (1978). Fronts on the continental shelf. J. Geophys. Res. 83, 4615-4622.

Simpson, J.H., J. Sharples and T.P. Rippeth (1991). A prescriptive model of stratification induce by freshwater runoff. Estuarine Coastal Shelf. Sci. 33, 23-35.

Souza, A.J. and I.D. James (1994). A two-dimensional model of tidal straining in the Rhine ROFI. Cont. Shelf. Res. (submitted)

Uncles, R.J., J.E. Ong and W.K. Gong (1990). Observation and analysis of a stratification-destratification event in a tropical estuary. Estuarine Coastal and Shelf Sci. 31, 651-655.

Uncles, R.J., W.K Gong and J.E. Ong (1992). Intratidal fluctuations in stratification within a mangrove estuart. Hydrobiologia 247, 163-171.

UNESCO (1981). Tenth report of the Joint Panel on Oceanographic Tables and Standards. UNESCO Technical papers in Marine Science 36, pp. 24..

Van Alphen, J.S.L.J., W.P.M. de Ruijter and J.C. Borts (1988). Outflow and three-dimensional spreading of the Rhine river in the Netherlands coastal zone. In: Physical Processes in Estuaries (ed. J. Dronkers and W. Van Leusen). Berlin. Springer Verlag 560 pp. 70-92.

Van der Giessen, A., W.P.M. de Ruijter and J.C. Borst (1990). Three-dimensional current structure in the Dutch coastal zone. Netherlands J. Sea Res. 25(1/2), 45-55.

Van Pagee, J.A., H. Gerritsen and W.P.M. de Ruijter (1986). Transport and water quality modelling in the southern North Sea in relation with coastal pollution research and control. Wat. Sci. Tech. 18, 245-256.

Visser, A.W., A.J. Souza, K. Hessner and J.H. Simpson (1993). The influence of water column stratification on tidal current profiles in a ROFI system. Oceanlogogica Acta (submited)

Wright, L.D. and J.M. Coleman (1971). Effluent expansion and interfacial mixing in the presence of a salt wedge, Mississippi River Delta. J. Geophys. Res. 76, 8649-8661.

Yanagi, T. (1980). A coastal front in the Sea of Iyo. J. Ocean. Soc. Japan. 35, 253-260.

APPENDICES

A1 The turbulence closure scheme.

The turbulence closure scheme used here to calculate the vertical profiles of eddy viscosity (N_z) and eddy diffusivity (K_z) is a level 2 formulation based on Mellor and Yamada (1974) with the transfer functions as

$$N_z = S_M lq \quad ; \quad K_z = S_H lq \tag{A1.1}$$

where S_M and S_H are stability functions which are functions of the flux Richardson number following (Mellor and Yamada 1974; Sharples and Simpson, 1994)

$$S_M = B_1^{-\frac{1}{3}} \frac{(1 - R_{fc}^{-1} R_f)(1 - R_{f1}^{-1} R_f)}{(1 - R_f)(1 - R_{f2}^{-1} R_f)} \tag{A1.2}$$

$$S_H = \frac{B_1^{-\frac{1}{3}}}{P_r^N} \frac{(1 - R_{fc}^{-1} R_f)}{(1 - R_f)} \tag{A1.3}$$

R_{fc} is a critical value of R_f and R_{f1} and R_{f2} are constants. P_r^N is the turbulent Prandtl number for homogeneous conditions and here is assumed equal to the unity, while B_1 is a laboratory-determined constant of the closure scheme. R_f is the local flux Richardson number, calculated from the local gradient Richardson number (R_i) via

$$R_f = \frac{1}{2}\left\{R_{f1} + R_i R_{f1} R_{f2}^{-1} - \left[\left(R_{f1} + R_i R_{f1} R_{f2}^{-1}\right)^2 - 4 R_{f1} R_i\right)^{\frac{1}{2}}\right\} \tag{A1.4}$$

The values of the constants (R_{fc}, R_{f1},R_{f2}) have been taken from a recent re-calibration of the Mellor-Yamada scheme by Hamrick (unpublished lecture notes):

$$R_{fc} = \frac{1}{6} \; ; \quad R_{f1} = \frac{1}{4} \; ; \quad R_{f2} = \frac{1}{5} \; ; \quad B_1 = 15.0 \qquad \textbf{(A1.5)}$$

The mixing length l must be specified independently and according to Mellor and Yamada is the most arbitrary aspect of the method. The simplest method is used here, following the formulation of Yalin (1972) and justified by Davies (1990). The length scale is calculated directly, without being related to the turbulent intensity from:

$$l(z) = \kappa z\left(1 - \frac{z}{h}\right)^{\frac{1}{2}} \qquad \textbf{(A1.6)}$$

with h the water depth, κ is the von Karman constant and z the height above the bed. The length scale has a parabolic shape, biased towards the surface and decreasing towards both the bottom and the surface to include the effect of the nearby boundaries.

The turbulent intensity, q (ms^{-1}), is calculated in the level two by assuming a local equilibrium between shear and buoyancy production of turbulent kinetic energy, and dissipation:

$$N_z\left[\left(\frac{\partial u}{\partial z}\right)^2 + \left(\frac{\partial v}{\partial z}\right)^2\right] + K_z\left(\frac{g}{\rho}\frac{\partial \rho}{\partial z}\right) = \frac{q^3}{B_1 l} \qquad \textbf{(A1.7)}$$

Although simple to implement, the level 2 scheme has the weakness of

preventing all vertical transports above a critical Richardson number, in this case $R_i=1/3$, which is physically unrealistic (Simpson and Sharples, 1994). This can conveniently be overcome by introducing a background viscosity bellow which N_z and K_z are not allowed to fall. The suitable value for this background appears to be dependent on the physical characteristics of the environment to which the model is being applied. Some examples of values of background viscosity are $1.7\text{-}2.0\times10^{-5}$ (Mellor and Durbin, 1981) and 5.0×10^{-5} m^2s^{-1}.

A2. Boundary conditions.

The boundary conditions for the momentum equations for the bottom boundary, is consider as quadratic stress, so that:

$$\tau_{bx} = -k\rho\,(u_1^2 + v_1^2)^{\frac{1}{2}}\,u_1 \qquad \textbf{(A2.1)}$$

$$\tau_{by} = -k\rho\,(u_1^2 + v_1^2)^{\frac{1}{2}}\,v_1 \qquad \textbf{(A2.2)}$$

in the x and way direction respectively, with the quadratic friction coefficient $k=3\times10_{-3}$, and u_1 and v_1 as the u and v components of velocity near the bed.

The surface boundary condition consider the wind stress at the sea surface:

$$\tau_{sx} = \rho_a k_s (u_w^2 + v_w^2)^{\frac{1}{2}}\,u_w \qquad \textbf{(A2.3)}$$

$$\tau_{sy} = \rho_a k_s (u_w^2 + v_w^2)^{\frac{1}{2}}\,v_w \qquad \textbf{(A2.4)}$$

where again the x and y suffices represent the direction in which the stress is acting, ρ_a is the air density equal to 1.25 kgm^{-3}, k_s the surface drag coefficient ($k_s=1.4\times10^{-3}$), and u_w and v_w are the wind velocity components in the x and y direction respectively.

There is no flux of salt or heat through the seabed and no net flux of salt at the surface. Surface heating is specified in terms of observed values of solar radiation, air temperature, relative humidity and wind speed following Gill (1982, p34) and Elliott

and Clarke (1991):

$$Q_T = Q_S(1 - \alpha) - (Q_B + Q_H + Q_E) \qquad \textbf{(A2.5)}$$

where Q_T is the net heat flux (Wm^{-2}), Q_S is the incoming short wave radiation (Wm^{-2}), α is the sea surface albedo (0.06), Q_B is the outgoing long wave heat flux (Wm^{-2}), Q_H is the sensible heat flux (Wm^{-2}) and Q_E is the evaporative heat flux (Wm^{-2}).

Long wave radiation

$$Q_B = E_M \sigma (T_s + 273)^4 (0.39 - 0.05 E_A^{1/2}) (1 - 0.6 C^2) \qquad \textbf{(A2.6)}$$

where E_M is the emissivity of the sea surface (0.985), σ is the Stephan's constant (5.6×10^{-8} $Wm^{-2}K^{-4}$), T_S is the sea surface temperature (°C), E_A is the vapour pressure of air (mbar), and E_W is the saturated vapour pressure at sea surface (mbar) which is used to compute the evaporative heat loss, and C is the fractional cloud cover.

E_W and E_A were calculated using

$$E_W = 10^{\frac{0.7859 + 0.03477 T_S}{1 + 0.00412 T_S}} \qquad \textbf{(A2.7)}$$

and

$$E_A = RH\, E_W \qquad \textbf{(A2.8)}$$

where RH is the relative humidity of moist air.

Sensible heat flux

$$Q_H = C_H \rho_A C_P W(T_S - T_A) \quad \text{(A2.9)}$$

where C_H is the Stanton number, ρ_A is the air density (1.25 kgm^{-3}), C_P is the specific heat of air (1004 $Jkg^{-1}K^{-1}$), W is the wind speed (ms^{-1}) and T_A is the air (°C).

Evaporative heat flux

$$Q_E = C_E \rho_A W(Q_W - Q_A) L_T \quad \text{(A2.10)}$$

where C_E is the Dalton number, Q_W is the specific humidity of air at the temperature of the sea surface, Q_A is the specific humidity of air at the air temperature, and L_T is the latent heat of vaporization of water given by

$$L_T = 2.6 \times 10^6 - 2.3 \times 10^3 T_S \quad \text{(A2.11)}$$

Q_W and Q_A were calculated using

$$Q_A = \frac{0.62 E_A}{P - 0.38 E_A} \quad \text{(A2.12)}$$

and

$$Q_W = \frac{0.62 E_W}{P - 0.38 E_W} \quad \text{(A2.13)}$$

where P is the atmospheric pressure in milibars.

A3 The finite difference scheme.

The model is one-dimensional and simulate the changes in velocity and density profile. The water column is split into a number of discrete depth elements which are equally spaced, with the values of velocity and density specified in the middle of the grid point, while the eddy diffusivity and eddy viscosity defined in the lower extreme of the of the grid cell (Sharples, 1992), as shown in figure A3.1.

The model is written in finite difference form, with a forward difference in time and central difference in the vertical. To keep the code simple, the integration of the equations of motion is done in a explicit manner. This puts a strong limitation on the time step which has to comply with the stability condition

$$\Delta t < \frac{1}{2}\frac{(\Delta z)^2}{N_z} \qquad \textbf{(A3.1)}$$

with Δt the time step and Δz as the depth interval. For the Rhine ROFI the model simulations have been done using a 2m depth interval and a time step of 5s, complying with the stability condition for values of N_z up to 4 m^2s^{-1}.